ANALYSIS OF HEAT TRANSFER, STABILITY, AND DYNAMICS OF CZOCHRALSKI AND LIQUID ENCAPSULATED CZOCHRALSKI GROWTH OF SEMICONDUCTOR MATERIALS

Vol. 1

by

JEFFREY J. DERBY

B.S., California Institute of Technology
(1981)

M.S.C.E.P., Massachusetts Institute of Technology
(1982)

Submitted to the Department of Chemical Engineering
in partial fulfillment of the requirements
for the degree of

DOCTOR OF PHILOSOPHY

at the

MASSACHUSETTS INSTITUTE OF TECHNOLOGY

June 1986

© Massachusetts Institute of Technology 1986

Signature of Author ______________________________
Department of Chemical Engineering
April 11, 1986

Certified by ______________________________
Robert A. Brown
Thesis Supervisor

Accepted by ______________________________
William M. Deen
Chemical Engineering Graduate Officer

Vol. 1
MASSACHUSETTS INSTITUTE OF TECHNOLOGY

JUN 0 3 1986

ARCHIVES

LIBRARIES

ANALYSIS OF HEAT TRANSFER, STABILITY, AND DYNAMICS OF CZOCHRALSKI AND LIQUID ENCAPSULATED CZOCHRALSKI GROWTH OF SEMICONDUCTOR MATERIALS

by

JEFFREY J. DERBY

Submitted to the Department of Chemical Engineering
on April 11, 1986 in partial fulfillment of the
requirements for the degree of Doctor of Philosophy in
Chemical Engineering

ABSTRACT

Most of the crystalline silicon used today by the electronics industry is produced by the Czochralski (CZ) process, where a single-crystal rod is solidified as it is withdrawn from a pool of melt, and the liquid encapsulated Czochralski (LEC) process is a promising method of producing III-V compounds, such as gallium arsenide and indium phosphide. The quality of the semiconductor crystals produced by both of these methods depends on careful control of the crystal radius, solidification interface shape, and the thermal history of the material grown from the melt. The objective of this research is to accurately model these crystal growth systems and apply the insight gained from this effort toward improving the quality of the semiconductor crystals grown by these two methods.

Capillarity and heat transfer determine the shape of the crystal boules grown by the CZ and LEC methods and the stability of these processes. This research addresses the complete description of heat transfer and interface shapes as a complex, nonlinear moving-boundary problem. A quasi-steady-state model is described in which the field and boundary equations are solved simultaneously by an innovative finite-element/Newton scheme for the temperature field in the melt, crystal, and encapsulant, the position of the melt/crystal interface, the shapes of the melt and encapsulant menisci, and the quasi-steady crystal radius. A dynamic thermal-capillary model is also presented which accounts for heat transfer, capillarity, and the evolution of crystal shape. The differential/algebraic equations derived from a finite element discretization of the energy balance and interface conditions are integrated in time by an implicit technique which uses Newton's method to solve the nonlinear algebraic equation set at each time step. The linear stability analysis of quasi-steady-states which follows naturally in this framework is formulated.

Results are presented for small-scale systems with thermophysical properties characteristic of silicon and gallium arsenide. Quasi-steady-state results demonstrate the sensitivity of the processes to changes in growth parameters and the importance of capillarity

in setting overall heat transfer and the size of the crystal. Reasonable temperature fields and interface shapes are predicted, and the response of the quasi-steady radius to different crystal pull rates closely matches an experimentally-derived correlation. Radiation from the system surfaces is a major factor in setting overall heat transfer, and the radiative character of the encapsulant in LEC growth crucially affects the sensitivity of that process to changes in operating parameters.

Linear stability analyses of temperature fields and crystal shapes calculated for the idealized growth of silicon from a melt of constant level and a long crystal show that the CZ process is inherently stable for a wide range of growth rates and heater temperatures. This parameter range is bound by a locus that marks limit points in the steady-states; steady-state operation at parameter values larger than the critical values is not possible.

The importance of the batchwise nature of the CZ process is demonstrated through the coupling of the quasi-steady results with those from the linear stability analysis and the fully transient simulation. Three disparate time scales characterize heat transfer, crystal shape changes, and the variations in the heat transfer environment caused by the dropping melt level during batch growth. The short, heat transfer time scale is successfully decoupled from the long transient caused by the decreasing melt level in an augmented quasi-steady model for the calculation of processing strategies for the control of crystal radius and melt/crystal interface shape. The complete description of the dynamic evolution of crystal shape is accessed through growth simulations with the fully transient thermal-capillary model.

Two fundamentally different mechanisms are observed which produce oscillations in the crystal radius. An inherent oscillatory mode is found for situations where low temperature gradients exist in the CZ system. The presence of these oscillations is confirmed by fully transient simulations. In addition, controller-induced dynamics are shown to produce undulating crystal shapes when integral control is used in an attempt to maintain a constant-diameter crystal during a growth run.

A thorough understanding of fundamental heat transfer interactions in conventional and liquid encapsulated Czochralski crystal growth has resulted from this research. This work has also lead to one of the most complex models ever put forth for the description of the CZ and LEC systems, yet it is does not account for the detailed radiation heat transfer among system surfaces nor the effects of convective heat transfer in the melt and encapsulant. However, this research establishes a basis for the addition of these phenomena to future models.

Thesis Supervisor: Dr. Robert A. Brown

Title: Professor of Chemical Engineering

Acknowledgements

I would like to acknowledge financial support from the National Science Foundation through a Graduate Fellowship for the first three years of my graduate education. I also wish to thank AT&T Bell Laboratories, particularly the late J. Nielson, for the initial funding of this research, and the Defense Advanced Research Projects Agency (DARPA) for continued support.

I owe a debt of gratitude to my research advisor, Professor R.A. Brown, for his constant support and seemingly endless enthusiasm. His boundless energy and curiosity will undoubtedly influence me throughout my career and life. I would also like to thank the members of my committee, Professor W.M. Deen, Dr. F.T. Geyling, Professor A.T. Patera, Professor G. Stephanopoulos, and Professor A.F. Witt, for their technical assistance. Special thanks to F.T. Geyling for the Bell Laboratories connection and to Professors W.M. Deen and J.W. Tester for their support as educators and advisors.

Thanks go out to all of the students and friends who made my experience at M.I.T. a special one. My fellow students, particularly those sharing the office of 66-256, provided many hours of enlightened conversation and just plain fun. I would especially like to thank the coffee club brats, Jeff Atherton, Phil Sackinger, and Peter Adornato, for their friendship and willingness to discuss topics ranging from technical aspects of research to mundane facts of everyday life. Paul Thomas provided invaluable support through software development. The viscoelastic types two doors down also provided a nice change of pace; thanks to Sue Muller and John Lawler. My stay at M.I.T. was enriched by participation on the 66ers, a great volleyball team.

I could not have completed my 20-odd years of schooling without the encouragement and support of my parents, and I may not ever have gotten out of school without the aid and urging of my wife, Ann, to whom I dedicate this thesis. Her support was unfailing through the dark stages of this research when I was confined to my cage and ordered to finish. Thanks for caring for the beast, honey!

Table of Contents

Abstract..2

Acknowledgements..4

Figures and Tables..8

Chapter 1. Introduction....................................20

1.1 Electronic Materials...................................22

1.2 Crystal Growth...27

1.3 The Czochralski Process................................34

1.4 Previous Work..41
1.4.1 Process Modeling.....................................42
1.4.2 Process Control and Stability........................48

1.5 Thesis Outline...50

Chapter 2. Thermal-Capillary Model of CZ and LEC Growth.............52

2.1 Heat transfer in the CZ and LEC systems...................52

2.2 Quasi-Steady-State Formulation............................66

2.3 Transient Formulation.....................................75

Chapter 3. Numerical Methods...............................83

3.1 Finite Element Method.....................................84

3.2 Quasi-Steady-State Formulation............................91
3.2.1 Discretization by the Galerkin Finite Element Method.....95
3.2.2 Iterative Solution with the Newton-Raphson Method......103

3.3 Transient Formulation....................................110
3.3.1 Spatial Discretization.................................111
3.3.2 Temporal Discretization................................121

3.4 Linear Stability Formulation.............................126

Chapter 4. Quasi-Steady-State Results....133

4.1 Initial Results for LEC Gallium Arsenide Growth....134
4.1.1 Calculations....134
4.1.1.1 Pull Rate....142
4.1.1.2 Encapsulant Volume....152
4.1.1.3 Heat Transfer Boundary Conditions....156
4.1.2 Discussion....161

4.2 CZ Silicon and LEC Gallium Arsenide Growth....165
4.2.1 Calculations for CZ Growth of Silicon....168
4.2.1.1 Meniscus Shape....173
4.2.1.2 Melt Volume and Crucible Wall....175
4.2.2 Calculations for LEC Growth of Gallium Arsenide....184
4.2.2.1 Radiative Character of Encapsulant....186
4.2.2.2 Pull Rate....188
4.2.2.3 Encapsulant Volume....193
4.2.2.4 Melt Volume....193
4.2.3 Discussion....196

4.3 Processing Strategies....199
4.3.1 Methodology....205
4.3.2 Calculations....208
4.3.2.1 Diameter....210
4.3.2.2 Diameter and Interface Deflection....213
4.3.3 Discussion....219

Chapter 5. Transient Results and Stability....224

5.1 Quasi-Steady Operating States....225
5.1.1 Pull Rate....238
5.1.2 Heater Temperature....246
5.1.3 Ambient Temperature....250

5.2 Linear Stability....254

5.3 Transient Simulation....259
5.3.1 Dynamic Transitions between Steady States....259
5.3.2 Dynamic Growth Simulation....266

5.4 Dynamics of Control....275
5.4.1 Proportional Control....277
5.4.2 Integral Control....279
5.4.3 Proportional-Integral Control....287
5.4.4 Quasi-Steady Processing Results....290

5.5 Discussion....292

Chapter 6. Final Remarks....................................297

6.1 Quasi-Steady-State Results..........................297

6.2 Stability and Transient Results.....................299

6.3 Future Research Directions..........................304
6.3.1 Radiation...304
6.3.2 Fluid Flow..305

6.4 Postscript..306

References...310

Appendix A...321

Nomenclature
Thermophysical Properties

Appendix B...330

A Fully Implicit Method for the Simulation of the One-dimensional Solidification of a Binary Alloy, J.J. Derby and R.A. Brown, 1986, Chem. Eng. Sci. 41(1), 37-46.

Figures and Tables

Fig. 1.1 Electron drift velocity as a function of applied electric field for Gallium Arsenide, Indium Phosphide, and Silicon (Rode and Roper, 1985)....................................23

Fig. 1.2 Projected markets for silicon and gallium arsenide devices (Burmeister, 1983)..25

Fig. 1.3 Schematic diagram of directional solidification..........28

Fig. 1.4 Melt crystal growth. (a) Horizontal Boat. (b) Vertical Bridgman-Stockbarger. (c) Floating Zone.................30

Fig. 1.5 Melt crystal growth. (a) Edge-defined film-fed growth. (b) Czochralski growth...................................31

Fig. 1.6 Liquid Encapsulated Czochralski crystal growth...........33

Fig. 1.7 (a) Experimental dislocation distribution in a gallium arsenide wafer. (b) Calculated thermal stress patterns. (Jordan et al., 1980)...................................37

Fig. 2.1 Heat transfer mechanisms in an LEC system................53

Fig. 2.2 Black body spectral emissive power distribution distribution at 1511 K superimposed on transmission spectrum of solid B_2O_3 (220 ppm H_2O) at room temperature (RASA Industries, 1981)..61

Fig. 2.3 Schematic diagram for thermal-capillary model............68

Fig. 2.4 Schematic diagram for fully transient thermal-capillary model..76

Fig. 2.5 Detail of tri-junction dynamics..........................80

Fig. 3.1 Lagrangian quadratic basis functions in a unit element...88

Fig. 3.2 Isoparametric mapping of a biquadratic element...........92

Fig. 3.3 Sample finite element mesh for converged solution........96

Fig. 3.4 Characteristic "arrow" structure of Jacobian matrix for a free-boundary problem.................................105

Fig. 3.5 Convergence for a typical calculation using the finite-element/ Newton method for the solution of the quasi-steady-state thermal-capillary model....109

Fig. 4.1 Schematic diagram of prototype LEC system for calculations of Section 4.1....135

Fig. 4.2 Sample finite element mesh used for LEC gallium arsenide calculations of Section 4.1. Mesh contains 320 elements and 1361 nodes. There are a total of 1415 unknowns for this system....140

Fig. 4.3 Isotherms and interface shapes for reference case (parameters listed in Tables 4.2 and 4.3). The finite element mesh used in this calculation is shown in Fig. 4.2. Isotherms for all plots of Section 4.1 are incremented by 23K ($\Delta\Theta = 1.5 \times 10^{-2}$)....141

Fig. 4.4 Changes in isotherms and interface shapes with increasing pull rate. All other parameters are held fixed at those listed in Tables 4.2 and 4.3....145

Fig. 4.5 Finite element meshes for the isotherms and interface shapes shown in Fig. 4.4....146

Fig. 4.6 Convergence of finite element solution with Newton iterations for calculations shown in Fig. 4.4....147

Fig. 4.7 Variation of axial temperature profiles along centerline ($r = 0$) and at the crystal radius ($r = R$) for pull rates of Fig. 4.4....148

Fig. 4.8 Variation of crystal radius as a function of pull rate. All other parameters were held fixed at reference values. The dashed curves represent the relations of Billig (1955), eq. (4.1), and Kim et al. (1983), eq. (4.2)....150

Fig. 4.9 Changes in isotherms and interface shapes with the volume of the encapsulant layer. All other parameters are held fixed at the values listed in Tables 4.1 and 4.2....153

Fig. 4.10 Variation of axial temperature profiles along centerline ($r = 0$) and crystal radius ($r = R$) with increasing depth of the encapsulant....154

Fig. 4.11 Changes in isotherms and interface shapes with increase in ambient temperature. All other parameters are held fixed at those of reference case....157

Fig. 4.12 Variation of isotherms and interface shapes with decrease of convective heat transfer coefficient (Biot number). All other parameters are held fixed at the values listed in Tables 4.1 and 4.2....................................159

Fig. 4.13 Changes in isotherms and interface shapes with a decrease in surface emissivities (Radiation numbers). (a) Reference case, Ra_i = 0.8. (b) All Ra_i = 0.4. (c) $Ra_{1,3}$ = 0.4 and $Ra_{2,4}$ = 0.8. All other parameters are held fixed at those of reference case...160

Fig. 4.14 Schematic diagram of prototype LEC system for calculations of Section 4.2..166

Fig. 4.15 Sample finite element mesh used for LEC gallium arsenide calculations of Section 4.2. Mesh contains 94 elements for a total of 461 unknowns.............................167

Fig. 4.16 Interface shapes and isotherms for reference configuration for CZ growth of silicon and ambient temperature profile used in calculation. Isotherms are spaced in 30K intervals around the melt/crystal interface. Shaded regions denote solid...172

Fig. 4.17 Variation of isotherms and interface shapes resulting from changes in equilibrium growth angle Φ_{ms}. All other parameters are held fixed at the values listed in Table 4.8........174

Fig. 4.18 Changes in isotherms and interface shapes with decreasing melt volume for CZ growth of Si using a uniform ambient temperature profile. All other parameters are held fixed at those of reference case..............................176

Fig. 4.19 Changes in isotherms and interface shapes with decreasing melt volume for CZ growth of Si using the ambient temperature profile for the shallow crucible (z_h = 0.75). All other parameters are held fixed at those of reference case....178

Fig. 4.20 Changes in isotherms and interface shapes with decreasing melt volume for CZ growth of Si using the ambient temperature profile for the deep crucible (z_h = 1.0). All other parameters are held fixed at those of reference case...............179

Fig. 4.21 Variation of axial temperature profiles along the centerline (r = 0) and at the crystal radius (r = R) for the three melt volumes of Fig. 4.19 (CZ growth of Si using the ambient temperature profile for the shallow crucible)...........181

Fig. 4.22 Variation of crystal radius as a function of melt volume and as a function of heater position (the location of the top of the hot crucible in the ambient temperature distribution, z_h)..183

Fig. 4.23 Interface shapes and isotherms for reference configuration of CZ growth of silicon and hypothetical CZ growth of gallium arsenide, both with uniform ambient temperature profiles. Differences in ambient temperatures are indicated in the figure..185

Fig. 4.24 Variation in isotherms and interface shapes for changing radiative character of the encapsulant layer for LEC growth of GaAs using the uniform ambient temperature profile. All other parameters are held fixed at those listed in Table 4.8. (a) Hypothetical CZ growth (no encapsulant). (b) LEC with transparent encapsulant. (c) LEC with opaque encapsulant..187

Fig. 4.25 Changes in isotherms and interface shapes with pull rate for LEC growth of GaAs with a uniform ambient temperature profile. The encapsulant layer is taken to be perfectly transparent, and all other parameters are held fixed at those listed in Table 4.8................................189

Fig. 4.26 Variations in isotherms and interface shapes with pull rate for LEC growth of GaAs with a uniform ambient temperature profile. The encapsulant layer is taken to be completely opaque, and all other parameters are held fixed at those listed in Table 4.8....................................190

Fig. 4.27 Normalized crystal radius (radius divided by value obtained for zero pull rate, Pe = 0.) plotted as a function of pull rate for LEC growth of GaAs with a uniform ambient with all other parameters held fixed at reference values listed in Table 4.8. Data points are shown for cases of no encapsulant, transparent encapsulant, and opaque encapsulant. The solid and dashed curves represent the best fits to the correlation of Kim et al. (1983)...................192

Fig. 4.28 Changes in isotherms and interface shapes with encapsulant volume for LEC growth of GaAs with a uniform ambient temperature profile. The encapsulant layer is taken to be perfectly transparent, and all other parameters are held fixed at those listed in Table 4.8................................194

Fig. 4.29 Variations in isotherms and interface shapes with encapsulant volume for LEC growth of GaAs with a uniform ambient temperature profile. The encapsulant layer is taken to be completely opaque, and all other parameters are held fixed at those listed in Table 4.8....................................195

Fig. 4.30 Changes in isotherms and interface shapes with decreasing melt volume for LEC growth of GaAs using the ambient temperature profile for the deep crucible (z_h = 1.0). The encapsulant layer is taken to be completely opaque, and all other parameters are held fixed at those of reference case..............197

Fig. 4.31 Variation of a process parameter (or control variable), such as pull rate used to maintain constant crystal diameter, throughout a growth run to different time scale fluctuations in CZ process..200

Fig. 4.32 Crystal radius and melt/crystal interface deflection for CZ silicon growth as a function of melt volume. All other parameters held constant. Results are presented for both the shallow crucible and uniform ambient temperature distributions..209

Fig. 4.33 Isotherms and interface shapes for cases of Figs. 4.32 and 4.34 for melt volumes of V_m = 3.1416, 2.6, 2.2, and 1.8. (a-d) No control. (e-h) Pull rate used to control diameter. Isotherms are spaced in 30K intervals around the melt/crystal interface, and shaded regions denote solid silicon..211

Fig. 4.34 Pull rate and interface deflection for CZ silicon growth as a function of melt volume when pull rate is designated as a control parameter to set crystal radius at R = 0.5 (R:Pe). Results are presented for both the shallow crucible and uniform ambient temperature distributions...........212

Fig. 4.35 Pull rate and bottom ambient temperature control of CZ silicon growth as a function of melt volume; control parameters act to set crystal radius at R = 0.5 and melt/crystal interface deflection at Δ = -0.0509 (R,Δ:Pe,$\Theta_{a,b}$). Results are presented for the shallow crucible temperature distribution.......215

Fig. 4.36 Isotherms and interface shapes for different processing strategies of Figs. 4.35, 4.37, and 4.38 for melt volumes of V_m = 3.1416, 2.6, 2.2, and 1.8. (a) Initial case. (b-d) (R,Δ:Pe,$\Theta_{a,b}$). (e-g) (R,Δ:Pe,Θ_c). (h-j) (R,Δ:$\Theta_{a,b}$,Θ_c)..216

Fig. 4.37 Pull rate and crucible wall temperature control of CZ silicon growth as a function of melt volume (R,Δ:Pe,Θ_c). Radius and interface deflection held constant at values of R = 0.5 and Δ = -0.0509. Results are presented for the shallow crucible temperature distribution......................218

Fig. 4.38 Bottom ambient and crucible wall temperature control of CZ silicon growth as a function of melt volume (R,Δ:$\Theta_{a,b}$,Θ_c). Radius and interface deflection held constant at values of R = 0.5 and Δ = -0.0509. Results are presented for the shallow crucible temperature distribution...........220

Fig. 5.1 Schematic diagram of prototype CZ system for calculations of Chapter 5..226

Fig. 5.2 Isotherms and interface shapes for reference case of $V^*=1.0$ (parameters listed in Tables 5.1 and 5.2) and case with identical operating parameters except $V^*=2.8$. Isotherms for all plots of Chapter 5 are incremented by 15K with alternating thin and thick contours....................229

Fig. 5.3 Biquadratic finite element meshes used for CZ silicon calculations of Section 5.1 for case of pull rate $V^*=1.0$.....231

Fig. 5.4 Biquadratic finite element meshes used for CZ silicon calculations of Section 5.1 for case of pull rate $V^*=2.8$.....232

Fig. 5.5 Quasi-steady crystal radius as a function of crystal top position for the high-gradient reference case parameters listed in Tables 5.1 and 5.2 for CZ growth of silicon. Solutions at solid points on curve are shown in Fig. 5.6..236

Fig. 5.6 Changes in quasi-steady isotherms and interface shapes with increasing crystal top position for CZ growth of silicon. All other parameters are held fixed at those of the high-gradient reference case..................................237

Fig. 5.7 CZ silicon growth quasi-steady operating curves of crystal radius as a function of pull rate for three heater-ambient temperature settings. All parameters except pull rate were held fixed at the reference values listed in Tables 5.1 and 5.2. The solutions at the points denoted by solid circles are shown in Figs. 5.8-5.10; results of linear stability analyses are given in Fig. 5.18 for the states denoted by the open circles..............................239

Fig. 5.8 Changes in isotherms and interface shapes with increasing pull rate for CZ silicon growth with $\Theta_a=0.85$ and $\Theta_h=1.1497$ corresponding to the solid circles on the high-gradient operating curve of Fig. 5.7. All other parameters are held fixed at those listed in Tables 5.1 and 5.2........241

Fig. 5.9 Changes in isotherms and interface shapes with increasing pull rate for CZ silicon growth with $\Theta_a=0.875$ and $\Theta_h=1.1278$ corresponding to the solid circles on the medium-gradient operating curve of Fig. 5.7. All other parameters are held fixed at those listed in Tables 5.1 and 5.2........242

Fig. 5.10 Changes in isotherms and interface shapes with increasing pull rate for CZ silicon growth with $\Theta_a=0.95$ and $\Theta_h=1.0486$ corresponding to the solid circles on the low-gradient operating curve of Fig. 5.7. All other parameters are held fixed at those listed in Tables 5.1 and 5.2........243

Fig. 5.11 Expanded view of region near melt/crystal interface for solutions near the limit point on the operating curves of Fig. 5.7...245

Fig. 5.12 Quasi-steady CZ silicon growth operating curves of crystal radius as a function of heater temperature for pull rate $V^*=1.0$ and two ambient temperature settings. Initial points (R=0.5) on operating curves are the same states represented on the pull rate operating curve of Fig. 5.7. All parameters except heater temperature were held fixed at the reference values listed in Tables 5.1 and 5.2. The solutions at the points denoted by solid circles are shown in Figs. 5.13 and 5.14..247

Fig. 5.13 Changes in isotherms and interface shapes with increasing heater temperature for CZ silicon growth with $\Theta_a=0.95$ and $V^*=1.0$ corresponding to the solid circles on the dashed operating curve of Fig. 5.12. All other parameters are held fixed at those listed in Tables 5.1 and 5.2........248

Fig. 5.14 Changes in isotherms and interface shapes with increasing heater temperature for CZ silicon growth with $\Theta_a=0.85$ and $V^*=1.0$ corresponding to the solid circles on the solid operating curve of Fig. 5.12. All other parameters are held fixed at those listed in Tables 5.1 and 5.2........249

Fig. 5.15 Quasi-steady CZ silicon growth operating curves of crystal radius as a function of ambient temperature for pull rate $V^*=1.0$ and two heater temperature settings. Initial points (R=0.5) on operating curves are the same states represented on the pull rate operating curve of Fig. 5.7. All parameters except ambient temperature were held fixed at the reference values listed in Tables 5.1 and 5.2. The solutions at the points denoted by solid circles are shown in Figs. 5.16 and 5.17..251

Fig. 5.16 Changes in isotherms and interface shapes with increasing ambient temperature for CZ silicon growth with $\Theta_h=1.1497$ and $V^*=1.0$ corresponding to the solid circles on the solid operating curve of Fig. 5.15. All other parameters are held fixed at those listed in Tables 5.1 and 5.2........252

Fig. 5.17 Changes in isotherms and interface shapes with increasing ambient temperature for CZ silicon growth with $\Theta_h=1.0486$ and $V^*=1.0$ corresponding to the solid circles on the dashed operating curve of Fig. 5.15. All other parameters are held fixed at those listed in Tables 5.1 and 5.2........253

Fig. 5.18 Results of linear stability analyses performed for the states denoted by the open circles on the operating curves of Fig. 5.7. Left column plots show disturbance evolution for each case; right column shows semi-log plots for the same disturbance...255

Fig. 5.19 Real part of maximum system eigenvalue as a function of pull rate for the three operating curves of Fig. 5.7. Crossings of zero axis indicate exchange of stability between solutions; negative values represent inherently stable solutions. Oscillations in disturbance vector evolution are seen in states denoted by open circles..............257

Fig. 5.20 Crystal radius at tri-junction as a function of time for dynamic response of quasi-steady solution to step change in pull rate. Results are shown for the initial state denoted by the open circle on the upper branch of high-gradient operating curve in Fig. 5.7, with Θ_a=0.85, Θ_h=1.1497, and V^*_0=2.7. At τ=0, the pull rate was stepped instantaneously to V^*=3.0, 2.5, or 2.0 with all other parameters are held fixed at those listed in Tables 5.1 and 5.2. Solutions at solid circles are shown in Fig. 5.21.................261

Fig. 5.21 Changes in isotherms and interface shapes for transient simulation of continuous-processing CZ silicon growth system with the high-gradient conditions of Θ_a=0.85 and Θ_h=1.1497. Solutions correspond with the solid circles on the curves of Fig. 5.20 and show response of system to initial step change of pull rate to value shown for each case. All other parameters are held fixed at those listed in Tables 5.1 and 5.2..262

Fig. 5.22 Crystal radius at tri-junction as a function of time for dynamic response of quasi-steady solution to step change in pull rate. Results are shown for the initial state denoted by the open circle on the low-gradient operating curve in Fig. 5.7, with Θ_a=0.95, Θ_h=1.9486, and V^*_0=3.5. At τ=0, the pull rate was stepped instantaneously to V^*=3.0 or 2.5 with all other parameters are held fixed at those listed in Tables 5.1 and 5.2. Solutions at solid circles are shown in Fig. 5.23.................................264

Fig. 5.23 Changes in isotherms and interface shapes for transient simulation of continuous-processing CZ silicon growth system with the low-gradient conditions of Θ_a=0.95 and Θ_h=1.0486. Solutions correspond with the solid circles on the curves of Fig. 5.22 and show response of system to initial step change of pull rate to value shown for each case. All other parameters are held fixed at those listed in Tables 5.1 and 5.2..265

Fig. 5.24 Crystal radius as a function of time for the dynamic simulation of batchwise CZ silicon growth. Results are shown for the tri-junction radius in a fully transient run with all parameters held fixed at those listed in Table 5.4 and for the quasi-steady radius obtained by steady-state calculations. Solutions corresponding to the solid points are shown in Figs. 5.25 and 5.26 for the fully transient simulation and the quasi-steady calculations, respectively.........269

Fig. 5.25 Changes in isotherms and interface shapes with time for the fully transient CZ silicon batch growth simulation. Solutions correspond to the solid circles shown in Fig. 5.24. All parameters are held fixed through the run at those listed in Table 5.4....................................273

Fig. 5.26 Changes in isotherms and interface shapes with time for the quasi-steady-state CZ silicon batch calculations. Solutions correspond to the solid squares shown in Fig. 5.24. At each time shown, crystal top position and melt volume were obtained from the values obtained from the fully transient simulation. All parameters except crystal top and melt volume are held fixed through the run at those listed in Table 5.4..274

Fig. 5.27 Crystal radius at tri-junction as a function of time for fully transient batchwise growth simulations. Results of proportional (P) control strategies with different gain values are shown. Strategies use eq. (5.7) to adjust heater temperature in an attempt to maintain a constant crystal radius of R=0.5 throughout the run.....................278

Fig. 5.28 Crystal radius at tri-junction as a function of time for fully transient batchwise growth simulations. Results of integral (I) control strategies with different gain values are shown. Strategies use eq. (5.8) to adjust heater temperature in an attempt to maintain a constant crystal radius of R=0.5 throughout the run.....................280

Fig. 5.29 Isotherms and interface shapes for transient simulation of a controlled CZ silicon batch growth system with the integral controller of eq. (5.8) employed with gain g_I=4.0. Solutions are shown at various points during growth run. All parameters except for heater temperature are held fixed at those listed in Table 5.4............................282

Fig. 5.30 Finite element meshes for the isotherms and interface shapes shown in Fig. 5.29....................................283

Fig. 5.31 Crystal radius at tri-junction and heater temperature as functions of time for the dynamic simulation of a CZ silicon batch growth run with the integral controller of eq. (5.8) employed with the gain set at g_i=4.0. All parameters except heater temperature are held fixed at those listed in Table 5.4..284

Fig. 5.32 Crystal radius at tri-junction and heater temperature as functions of time for the transient simulation of a continuous-processing CZ silicon run with a constant melt volume. The integral controller of eq. (5.8) was employed with the gain set at g_i=4.0. All parameters except heater temperature are held fixed at those listed in Tables 5.1 and 5.2 for the high-gradient reference case. A small step decrease in heater temperature was imposed initially....286

Fig. 5.33 Crystal radius at tri-junction as a function of time for fully transient batchwise growth simulations. Results of proportional-integral (PI) control strategies with different gain values are shown. Strategies use eq. (5.9) to adjust heater temperature in an attempt to maintain a constant crystal radius of R=0.5 throughout the run.............288

Fig. 5.34 Crystal radius at tri-junction as a function of time for fully transient batchwise growth simulations. Results of proportional-integral (PI) control strategies with different gain values are shown. Strategies use eq. (5.9) to adjust heater temperature in an attempt to maintain a constant crystal radius of R=0.5 throughout the run.............289

Fig. 5.35 Heater temperature as a function of time for fully transient batchwise growth simulation with PI control (g_p=2.0, g_i=10.0) compared with results obtained by quasi-steady processing calculations. Open squares denote processing calculations in which an approximate correction for the batch-induced increase in the melt/crystal interface growth rate was made. Solutions at selected times are shown for the transient simulation and the quasi-steady calculations in Figs. 5.36 and 5.37, respectively..................................291

Fig. 5.36 Changes in isotherms and interface shapes with time for a fully transient CZ silicon batch growth simulation with effective PI control on heater temperature. Solutions correspond to the selected points along the solid curve of Fig. 5.35...293

Fig. 5.37 Isotherms and interface shapes for the quasi-steady CZ silicon processing strategies calculated for crystal top position and melt volume corresponding to the batch growth time shown. Solutions are shown for the batch-corrected calculations at selected open squares plotted in Fig. 5.35..294

Fig. 6.1 Comparison of crystal shape resulting from transient simulation of CZ silicon growth under low temperature gradient conditions to experimentally grown gallium arsenide by LEC method under similar conditions (Elliot et al., 1984). Undulating crystal shapes caused by inherent oscillatory responses in system are seen....................................301

Fig. 6.2 Crystal resulting from a transient simulation of batchwise CZ silicon growth using an integral controller and an experimentally grown CZ germanium crystal in a system exhibiting servo-loop instability (Bardsley et al., 1977b). Oscillating crystal radius in both systems is the result of controller-induced dynamics....................................303

Table 1.1 Classification of thermal models for CZ and LEC crystal growth...43

Table 3.1 Functional forms of Lagrangian biquadratic basis functions in unit element coordinate system........................90

Table 4.1 Material properties and physical constants for LEC gallium arsenide calculations of Section 4.1....................136

Table 4.2 Dimensionless groups for LEC gallium arsenide calculations of Section 4.1...138

Table 4.3 Operating parameters for LEC gallium arsenide calculations of Section 4.1...139

Table 4.4 Results of mesh refinement..............................143

Table 4.5 Results for calculations with varying crystal pull rate..151

Table 4.6 Variations of melt/crystal interface deflection, crystal radius, and interfacial temperature gradient with the depth of the encapsulant layer...............................155

Table 4.7 Thermophysical properties and parameters for Si and GaAs calculations of Section 4.2............................169

Table 4.8 Dimensionless groups used in reference cases for Si and GaAs calculations of Section 4.2.......................170

Table 4.9 Process constraints and variables for Czochralski growth..202

Table 4.10 Temperature gradients for calculations without control and with the four processing algorithms for crystal radius and interface shape control presented in Section 4.3....221

Table 5.1 Thermophysical properties and parameters used for CZ silicon calculations of Chapter 5..............................227

Table 5.2 Operating parameters and dimensionless groups used in reference cases for CZ silicon quasi-steady and transient continuous-processing calculations of Chapter 5...................228

Table 5.3 Results of mesh refinement for the quasi-steady solutions shown in Fig. 5.2 and the meshes displayed in Figs. 5.3 and 5.4...234

Table 5.4 Operating parameters and dimensionless groups characterizing the quasi-steady initial condition used for the dynamic CZ silicon simulations of batchwise growth in Chapter 5..267

Table A.1 Nomenclature..322

Table A.2 Thermophysical properties for gallium arsenide..........327

Table A.3 Thermophysical properties for silicon..................328

Table A.4 Thermophysical properties for boric oxide (B_2O_3), graphite, and quartz (SiO_2)...................................329

Chapter 1. Introduction

Chemical engineering fundamentals are being successfully applied to complex problems in the semiconductor and electronics industry. These applications range from fabricating electronic devices to processing bulk semiconductor materials and involve disciplines spanning the fields of chemical kinetics, thermodynamics, and transport phenomena. One particularly challenging problem is the fabrication of the high purity, crystalline electronic materials which are used as substrates for electronic devices. This research focuses on understanding two important methods for the production of electronic materials, crystal growth by the Czochralski (CZ) and liquid encapsulated Czochralski (LEC) processes.

The Czochralski process has been used with great success for more than three decades in the electronics industry for the growth of silicon crystals. However, the fundamentals of the method are not quantitatively understood, and the extrapolation of past empirical techniques for CZ silicon growth to the growth of gallium arsenide by the liquid encapsulated Czochralski process has yielded poor results. These and similar problems have motivated this research; we hope to model the CZ and LEC methods and thus better understand the interactions of heat transfer and capillarity which control the stability and dynamics

of these systems.

Modeling Czochralski and liquid encapsulated Czochralski crystal growth is a very difficult task, and previous efforts have simplified the problem to the point where the "idealized" model bears little resemblance to the real process. In an effort to capture the essential physics involved in these growth methods, we take a comprehensive approach in which we model heat transfer simultaneously with determination of system boundaries, such as the melt/crystal interface, the melt meniscus, and the shape of the crystal. Traditional mathematical techniques are not readily applied to a problem of this complexity, so we have developed a novel numerical approach which employs the finite-element method and a sophisticated Newton-Raphson iteration technique. This model and the insight it provides on the workings of the CZ and LEC processes are the major results of this work and are described in this thesis.

In the following sections of this introductory chapter, we examine the materials of interest to the electronics industry and the relevant materials processing issues involved in their production. We present the major techniques for growing these crystalline substrates and then focus on the process of interest in this research, the Czochralski method. Previous efforts of modeling this complex process are discussed, and in the last section of this chapter, we briefly outline the contents of the remainder of the thesis.

1.1 Electronic Materials

Silicon (Si) has formed the backbone of the solid-state electronics industry for over two decades and is used almost exclusively in the fabrication of semiconductor devices. The development of integrated circuits (IC's) on single wafers of crystalline silicon allowed for the miniaturization of many electronic systems and led to work on much smaller devices using the principles of large- and very-large-scale integration (LSI and VLSI). Along with these advances came the concomitant need for high quality silicon substrate upon which to fabricate microcircuits. Silicon promises to remain the major material used by the industry due to the great success of process engineering for LSI and VLSI circuits and as further development of silicon devices continues.

Another electronic material of particular interest is gallium arsenide (GaAs) which is currently used in a variety of optoelectronic devices such as light emitting diodes, solid state lasers, and optical communication circuits. Promising applications for GaAs devices include the development of high speed microwave devices and ultra-high speed integrated circuits. These applications take advantage of the low-field mobility and high electron velocity of GaAs, features which can be used to produce circuits which are almost an order-of-magnitude faster than their silicon-based counterparts (Rode and Roper, 1985). The electron drift velocity is plotted as a function of applied electric field strength in Fig. 1.1 for gallium arsenide, indium phosphide, and silicon. The development of large-scale integrated circuits fabricated

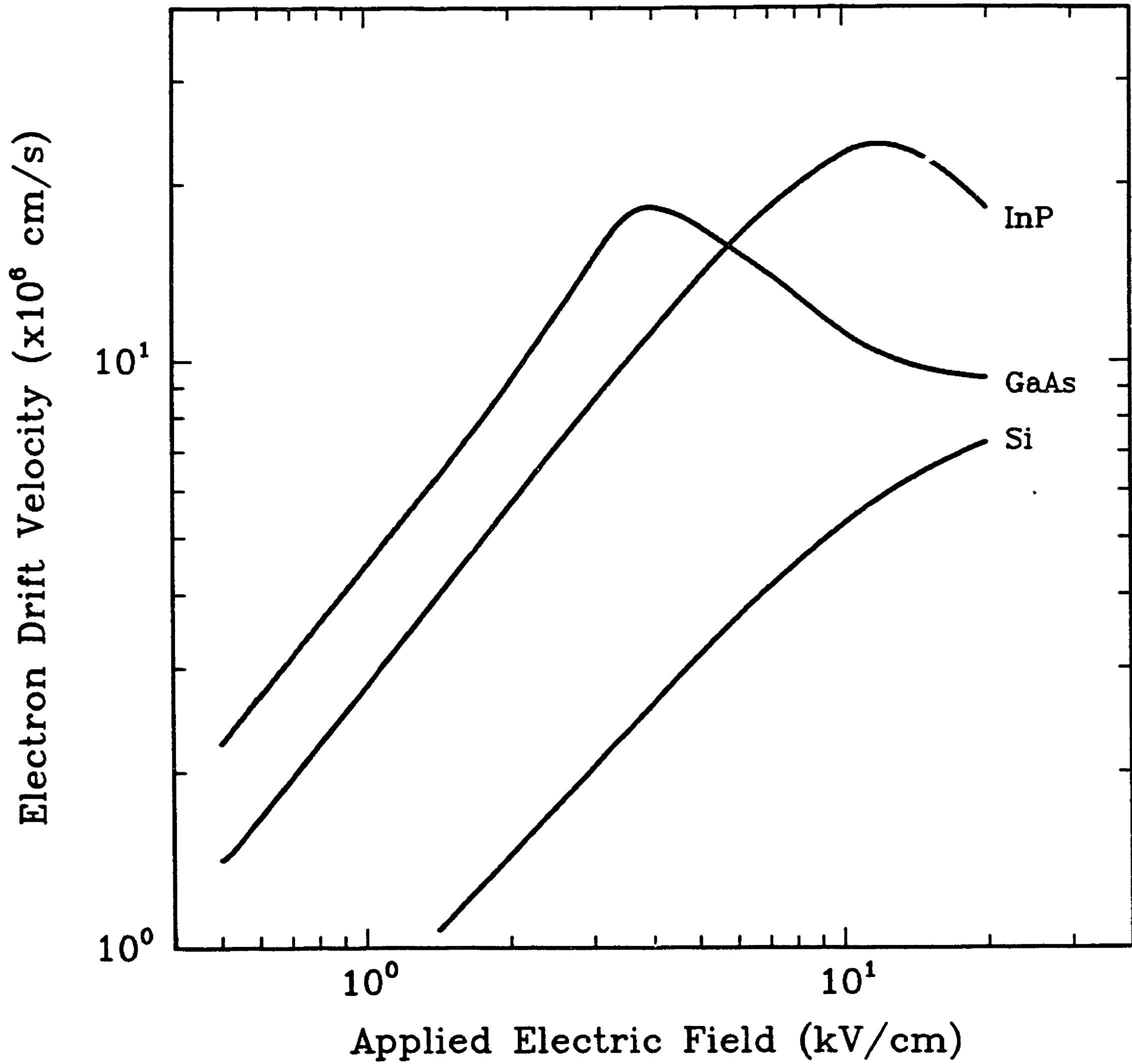

Fig. 1.1 Electron drift velocity as a function of applied electric field for Gallium Arsenide, Indium Phosphide, and Silicon (Rode and Roper, 1985).

on gallium arsenide substrate is particularly important for the next generation of high speed supercomputers (Robinson, 1983).

The projected market for silicon and gallium arsenide devices is depicted in Fig. 1.2 (Burmeister, 1983). While the sales of silicon devices is projected to nearly double from 1983 to 1986, the growth in the market for GaAs devices is expected to increase almost fifty-fold for the same period. Both of these trends rely on the development of devices with increased complexity and decreased size, issues which depend on substrate quality and availability and on advances in the processing techniques used to fabricate devices (Rode and Roper, 1985). The huge increase in the market for gallium arsenide devices hinges on the assumption that knowledge derived from silicon technology can be readily applied to the production of gallium arsenide devices. A major obstacle to the development of this new device technology is the current lack of success in fabricating sufficient quantities of high-quality GaAs substrate.

Several factors affect the quality of semiconductor substrate used in electronic devices. The material must be extremely pure, since even trace amounts of impurities significantly alter the electronic properties of the material. Usually, impurity concentrations are lower than the parts per billion level. This issue is not a major obstacle to the production of electronic materials and has been largely solved by careful attention to the quality of the raw materials used in crystal growth and the cleanliness of the growth apparatus.

A more difficult factor to control is the overall uniformity of the material. Impurities or "dopants", usually boron or phosphorus,

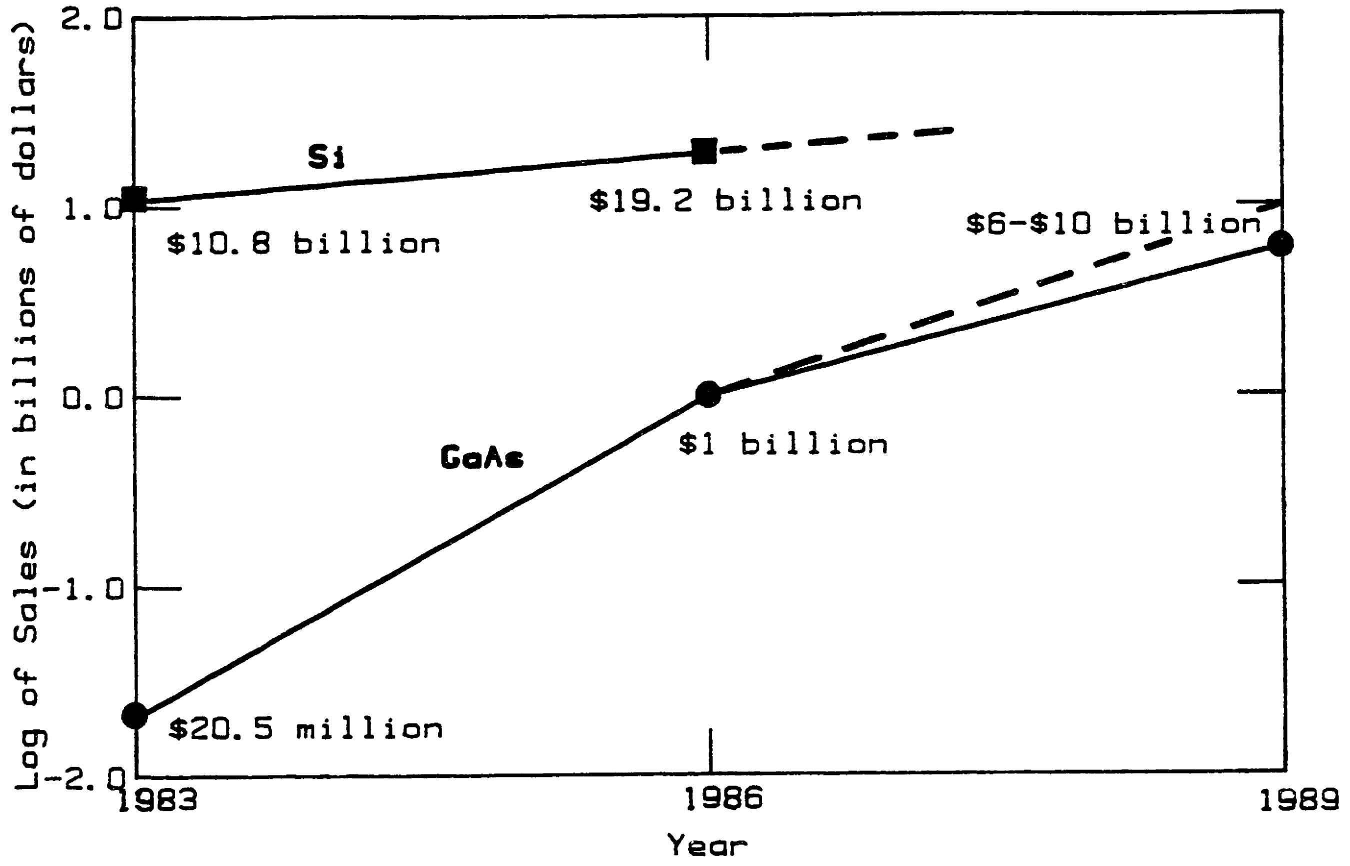

Fig. 1.2 Projected markets for silicon and gallium arsenide devices (Burmeister, 1983).

are often added to silicon to produce a substrate of desired properties, and it is important to maintain a relatively uniform distribution of these dopants throughout the silicon crystal. Similarly, alloys and stoichiometric materials, such as gallium arsenide, consist of two or more elements. The precise ratio of elements must be constant in the resulting substrate. Ideally, the composition of the substrate is homogeneous over a macroscopic scale. The control of the distribution of species in the crystal is directly related to the spatial composition of the liquid or vapor phase adjacent to the solid and thus depends on understanding the mass transport phenomena during crystal growth.

Related to the issue of purity and stoichiometry is the crystallinity of the substrate; the optimum substrate should possess a perfect crystalline array. Any disruption of this array, for example dislocations or defects, can affect the electronic properties of the material. Dislocations can occur during the growth of the crystal or in the device fabrication process and are caused by effects which are too numerous to mention here; see, for example, Ghandhi (1983). Dislocation densities are reported in units of the number of defects/cm^2 and represent the surface density of dislocations in a wafer cut from a the substrate. These dislocations are often measured by etching the crystal wafer in a suitable solvent and visually counting the number of etch pits. Silicon is uniformly grown "dislocation free", i.e. with etch pit densities (EPD) of less than 200/cm^2. In contrast, gallium arsenide wafers commonly exhibit etch pit densities of 10^4-10^5/cm^2.

When an electronic circuit is fabricated on the surface of a crystalline wafer, the surface properties of the wafer must be spatially

uniform to insure the proper functioning of all the individual components of the circuit. The presence of a defect on the wafer surface can cause the failure of a device which falls on or near the defect, especially if the size of the device is comparable to the size of the defect. Therefore the density of defects becomes a crucial parameter in very-large-scale integration (VLSI) as device dimensions become smaller and smaller. As device dimensions shrink, crystal quality must at the same time increase in order to maintain acceptable circuit yields.

1.2 Crystal Growth

There are a variety of means of fabricating the high-purity single-crystal electronic materials needed for device production. These materials can be produced by careful control of gas-solid reactions or of liquid-solid phase transitions. Although gas-solid deposition techniques are able to produce crystalline material of very high quality, the processes are very slow and thus not well suited for the production of the needed quantities of substrate. Therefore the most common means of substrate production is by the "directional solidification" of semiconductor melts. This method involves the application of a precise temperature gradient across a melt to achieve the controlled uni-directional growth of a single crystal, as detailed schematically in Fig. 1.3.

Several melt crystal growth techniques, all forms of directional solidification, are presented schematically in Figs. 1.4 and 1.5. In the Horizontal Boat or Horizontal Bridgman method, semiconductor

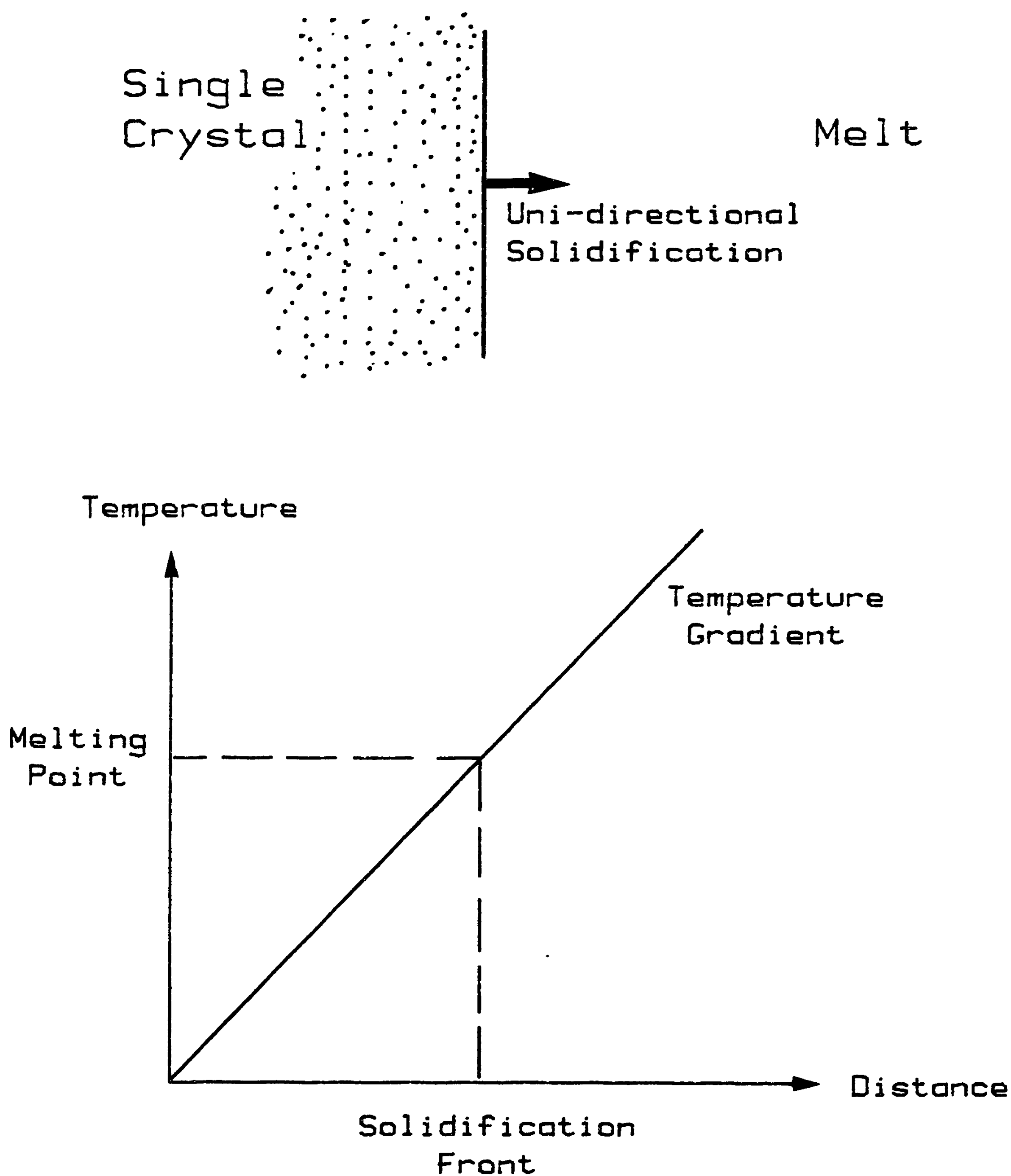

Fig. 1.3 Schematic diagram of directional solidification.

material is melted in a trough-shaped boat and is then solidified by slowly moving the boat through a temperature gradient maintained by a special furnace. This method is relatively simple and inexpensive; however, intense free convection can develop in the melt due to the temperature gradient imposed along the length of the boat. Convection can adversely affect crystal quality by altering the macroscopic distribution of solutes in the resulting crystal. In an effort to minimize convection in the melt, the Vertical Bridgman or Bridgman-Stockbarger process was developed. This technique is similar to the Horizontal Boat method except that the ampoule containing the substrate is lowered vertically through the furnace. In this manner the imposed thermal gradient tends to stabilize the configuration with hot melt above the cooler solidifying melt. A disadvantage shared by both methods is caused by the use of an ampoule to contain the melt. If the thermal expansion characteristics of the crystal differ from those of the ampoule, thermoelastic stresses develop as the crystal cools. These stresses can cause the formation of unwanted dislocations and grains in the solid. Additional limitations to these methods can arise from the incompatibility of substrate and ampoule materials.

Several crystal growth techniques have been developed which do not use an ampoule; instead the crystal supports itself as it is withdrawn directly from the melt. These techniques are called free-meniscus or meniscus-controlled methods since the shape and size of the crystal are determined by a solidification interface connected to the melt bulk by a melt/gas meniscus. The Floating Zone technique for crystal growth consists of passing a polycrystalline semiconductor rod through

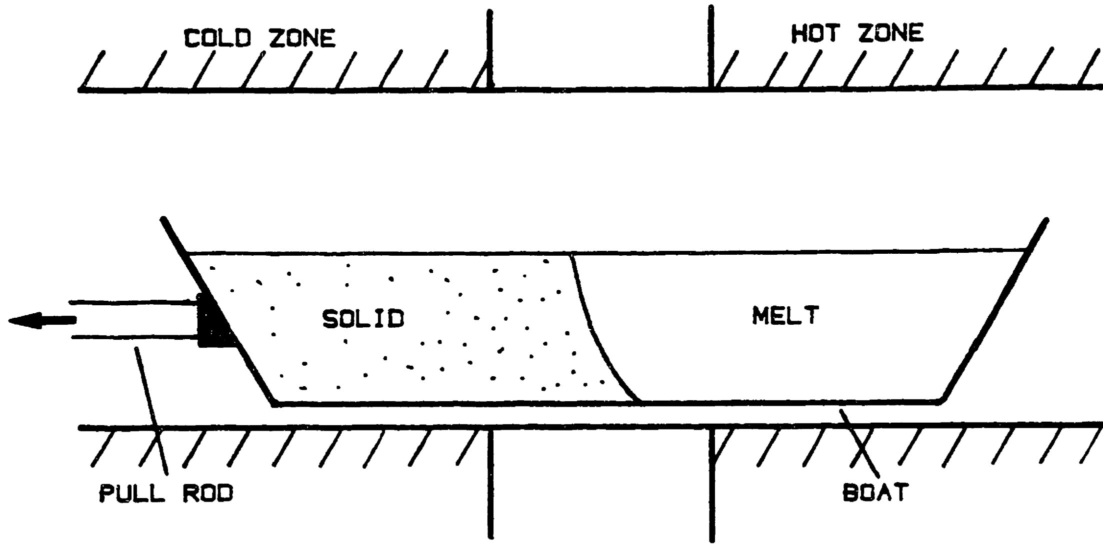

(a)

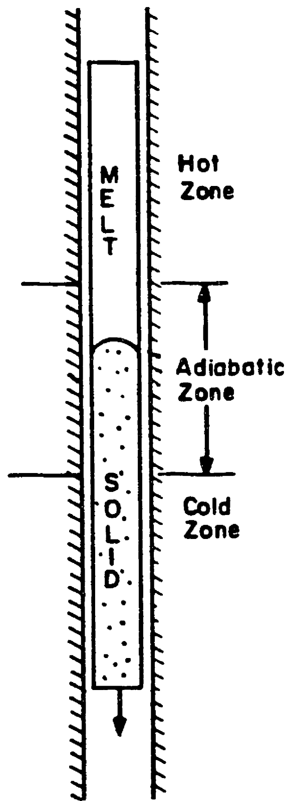

(b)

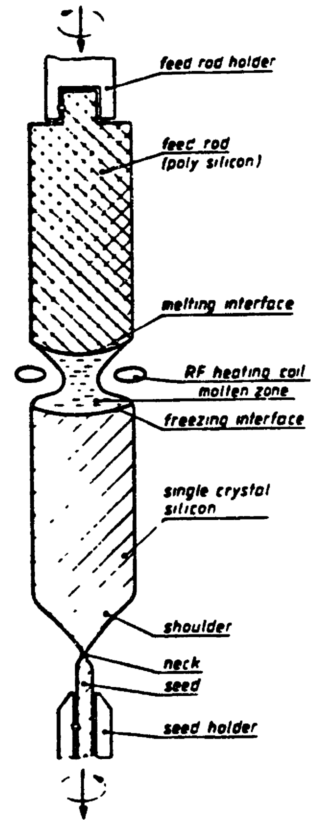

(c)

Fig. 1.4 Melt crystal growth. (a) Horizontal Boat. (b) Vertical Bridgman-Stockbarger. (c) Floating Zone.

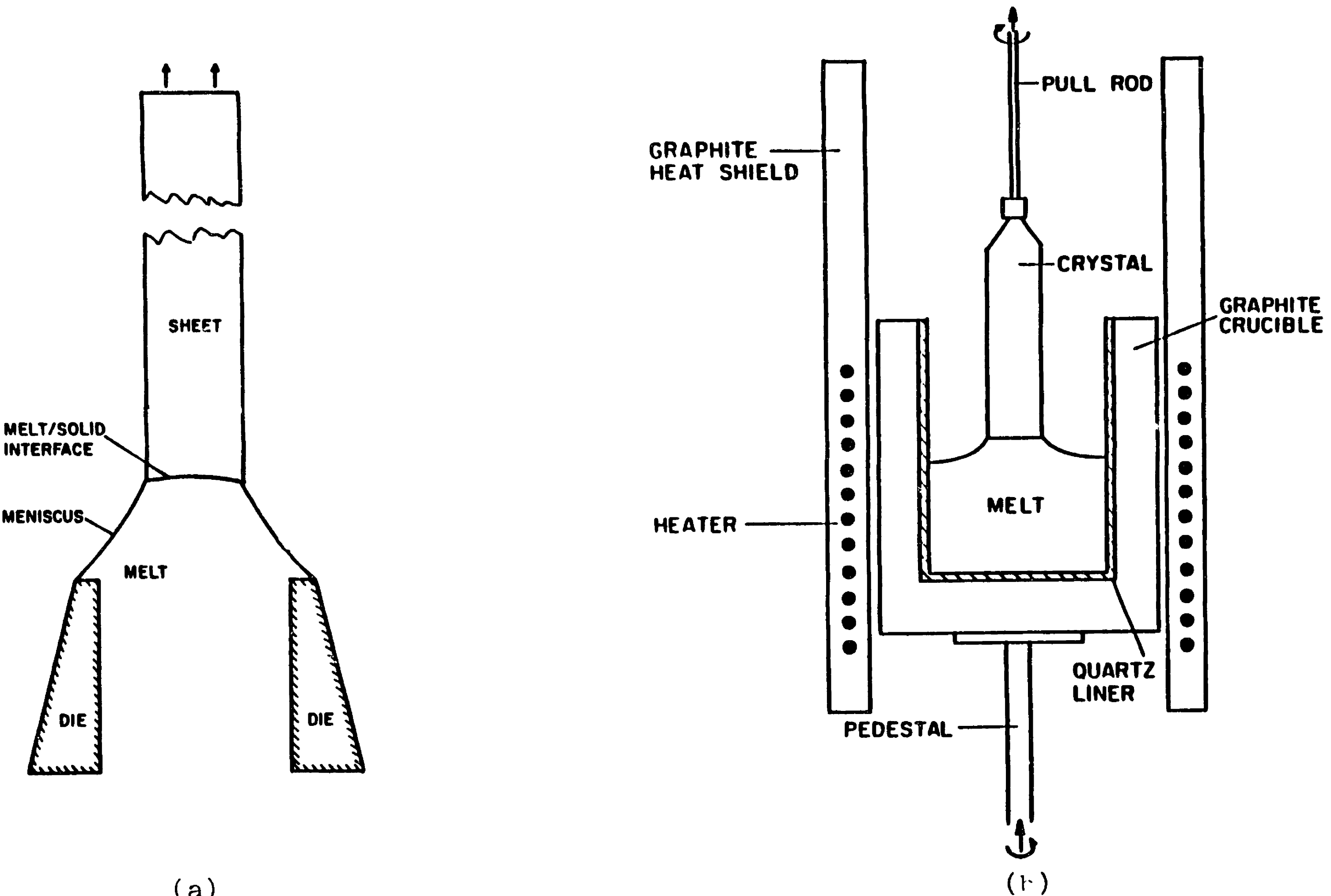

Fig. 1.5 Melt crystal growth. (a) Edge-defined film-fed growth. (b) Czochralski growth.

a heated zone. Surface tension acts against the force of gravity to form a stable molten zone. The polycrystalline rod enters the zone from one end while a single crystal is withdrawn from the other. A drawback of this method is the difficulty of maintaining a stable zone, especially when processing large-diameter rods. Various sheet growth methods produce thin sheets of polycrystalline silicon at speeds up to 5 cm/min for use as low-cost substrate for photovoltaic cells. A technique which has been used extensively for this application, Edge-Defined Film-Fed Growth (EFG), is shown in Fig. 1.5 and has been studied by a thermal-capillary analysis (Ettouney, 1983) similar to the one discussed here. Finally, the most common method of melt crystal growth for silicon is the Czochralski process. Here a cylindrical crystal or "boule" is pulled from a pool of melt which is contained in a crucible. Dislocation-free (EPD $< 200/cm^2$) silicon boules of diameters from 3"-6" or larger are obtained at moderate growth rates (1-10 cm/hr) using this method.

Liquid Encapsulated Czochralski growth (LEC), an important modification of the Czochralski process, is detailed in Fig. 1.6. In LEC growth, an inert substance (usually Boric Oxide, B_2O_3) is floated on the surface of the melt to prevent the escape of volatile components from the melt. This is important in the growth of III-V compounds, for example, gallium arsenide and indium phosphide, where the stoichiometric ratio of the elements must be precisely controlled in order to produce a high-quality crystal. The equilibrium vapor pressure of arsenic over molten GaAs is 0.9 atmosphere (Arthur, 1967; Richman, 1963; Boomgaard and Schol, 1957) and is approximately 20 atmospheres

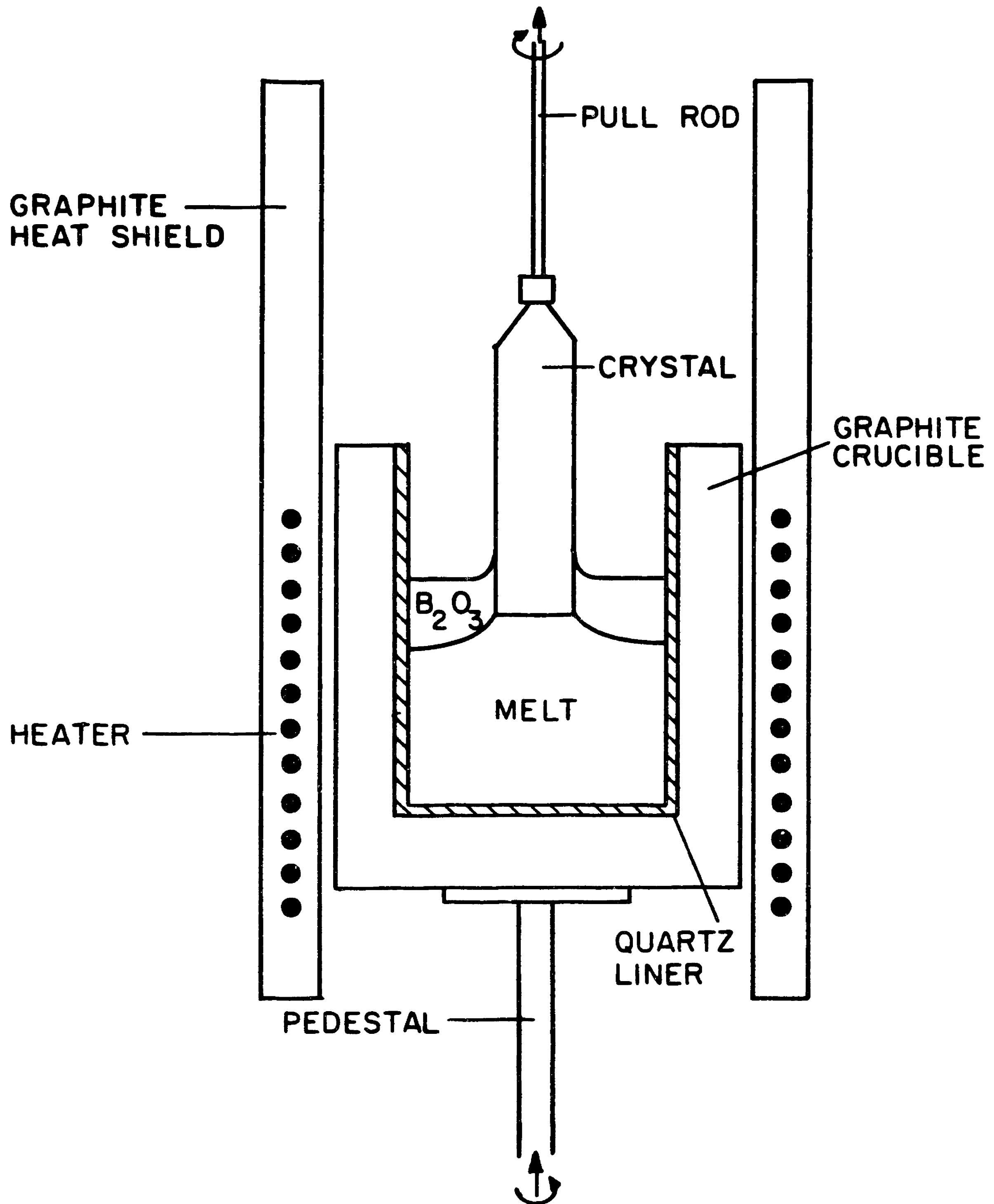

Fig. 1.6 Liquid Encapsulated Czochralski crystal growth.

for phosphorous vapor over molten InP (Richman, 1963; Boomgaard and Schol, 1957). An encapsulant layer over the contents of the crucible and a pressurized furnace vessel are necessary for the growth of these compound semiconductor crystals. We describe both the CZ and LEC processes in more detail in the following section.

1.3 The Czochralski Process

The CZ method is named after J. Czochralski (Czochralski, 1917) who developed it to measure the crystallization velocity of metals. Silicon and germanium crystals were first grown using this method by Teal, Little, and Buehler (Teal and Little, 1950; Teal and Buehler, 1952), and later Dash (1959) developed techniques to grow dislocation-free crystals. Today, Czochralski crystal growth is widely used to produce semiconductor crystals. Over 80 percent of silicon used in the electronics industry is grown by this method (Zulehner, 1983). The liquid encapsulated Czochralski process, a modification of the Czochralski process, is a promising means of production for III-V compounds such as gallium arsenide and indium phosphide (Metz et al., 1962; Foster, 1977).

The growth system for the CZ and LEC processes consists of a crucible supported by a pedestal which can be rotated and moved vertically during crystal growth. The crucible is surrounded by a graphite resistance heater or a radio-frequency coil with a graphite susceptor which acts as a heat source. A pull rod is located above the center of the crucible and also travels vertically, lowering the seed to the surface of the

melt at the start of the process and subsequently pulling the crystal from the melt. Heat shields are sometimes placed above the crucible in order to achieve the desired radiative heat transfer characteristics. The entire assembly is housed in a large temperature-controlled enclosure.

The procedure of growing a crystal by the Czochralski method starts by filling the crucible with high purity polycrystalline material and often a small quantity of an impurity or dopant, which alters the electronic properties of the grown crystal. The enclosure is filled with an inert atmosphere such as nitrogen or argon, and the crucible is heated to melt the substrate. Next a single-crystal, precisely-oriented seed crystal attached to the pull rod is lowered to the surface of the melt. After the seed and melt have reached thermal equilibrium, the seed is slowly withdrawn from the melt and a single crystal is pulled upward. A meniscus forms about the edge of the crystal by surface tension as the melt is pulled upward. The shape of this meniscus is determined by the action of surface tension against the force of gravity.

Usually, the crystal is grown through a "necking" operation during the startup of growth where a length of very small diameter crystal is solidified in an attempt to eliminate dislocations by forcing them to "grow out" to the surface of the crystal. After necking the crystal is grown to the desired diameter by reducing the power output of the heater, subsequently system parameters (usually growth rate and heater output) are adjusted to achieve constant-diameter growth. An active control mechanism is employed to keep the crystal diameter at the desired value. At the end of the run the crystal is withdrawn completely

from the melt and is slowly cooled. Often the crystal is pulled past a special configuration of heaters or coolers which subject the boule to a specified thermal history to minimize thermal stress and to anneal the material by keeping it at a high temperature for a long period of time. A typical process cycle time, from the initial cleaning and loading of a system with a 6.5 kg charge of material to the final 80 mm diameter silicon boule, is approximately 17 hours (Williams and Reusser, 1983).

The precise temperature gradient needed for uni-directional solidification of single-crystal solid is achieved by providing a cooler ambient above the melt. Maintaining uniform heat transfer conditions throughout the growth run is complicated by furnace imperfections and the unsteady, batchwise nature of the process caused by the decreasing depth of the melt. In an attempt to control the heat transfer in the system, the crystal and crucible are rotated to lessen any thermal asymmetry of the heater, the crucible is raised during growth to keep the melt/solid interface and meniscus in a specified region of the heater, and active control mechanisms are used to control the crystal radius.

The control of temperature gradients in the crystal is particularly crucial in the growth of gallium arsenide. Jordan, Caruso, and Von Neida (1980) found that the distribution of crystalline defects in LEC grown GaAs could be qualitatively explained by thermal stresses in the growing crystal; this effect is shown in Fig. 1.7. Furthermore, Nanishi et al. (1982) related the pattern of defect densities directly to the resultant quality of devices fabricated on a gallium arsenide

(a)

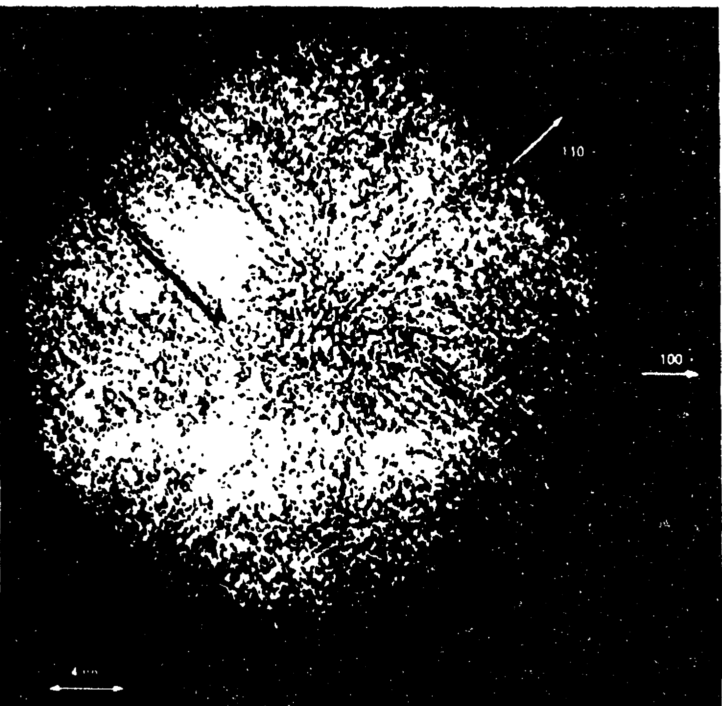

(b)

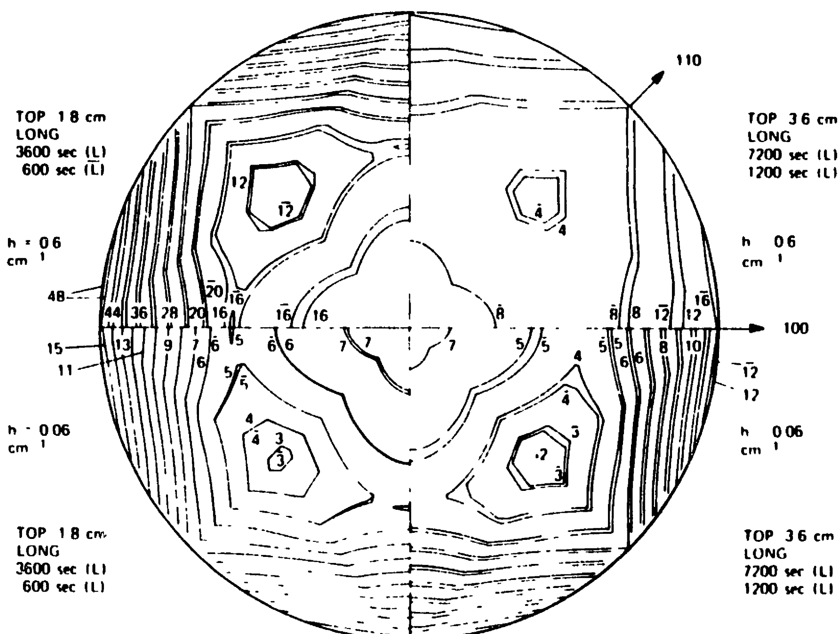

Fig. 1.7 (a) Experimental dislocation distribution in a gallium arsenide wafer. (b) Calculated thermal stress patterns. (Jordan et al., 1980).

wafer.

The batchwise nature of Czochralski and liquid encapsulated Czochralski growth coupled with the features of meniscus-controlled crystal growth for these processes have forced active control to produce crystal boules of uniform diameter. In an "uncontrolled" furnace, where process parameters such as heater output or pull rate are held constant through a growth run, the crystal radius changes as growth proceeds in response to the varying thermal environment caused by the dropping melt level (Robertson and Young, 1975). The evolution of crystal shape is coupled to the changing thermal environment and the response of the system to perturbations which tend to change the temperature field, meniscus shape, or crystal radius. Therefore, the dynamic "shape stability" of the crystal is an important issue in process control. Surek (1976) originally discussed shape stability as the evolution and stability of the crystal dimensions as a function of meniscus shape. In this work, we address the similar, but more comprehensive, issue of the "inherent" stability of the entire growth process.

Here, it is appropriate to define our concept of inherent stability for the CZ and LEC systems. In practice, CZ and LEC crystal growth methods are unstable since they are batch processes and change continuously in time. However, if we imagine a hypothetical steady-state process where the length of the crystal is far enough away from the melt so that length changes do not affect heat transfer (an infinitely long crystal) and a melt level which remains constant through the growth run, we can examine the stability of this operating state. If this idealized steady state is stable, then we claim that the real CZ and

LEC processes are "inherently" stable. For an inherently stable system, small deviations in the system, for example changes in crystal radius, would tend to self-correct. For an unstable system, perturbations would tend to amplify as time progresses.

The inherent stability of the system is an important factor in process control. A controller need only compensate for the variations in the heat transfer environment over time as the melt level drops and the crystal is pulled away from the melt for a process which is inherently stable. For an unstable system, the controller must counter the effects of perturbations to the system as well as account for batch-induced changes.

In practice, diameter control in CZ and LEC growth provides for higher crystal yields by reducing the cutting waste in the production of wafers of a specified diameter needed for subsequent processing and introduces some element of reproducibility in the growth process. This last feature is very important since there are so many processing parameters to be dealt with — furnace configuration, crucible and crystal rotation rates, pedestal lift rate, heater power, crystal pull rate, etc. Because of the large number of operating parameters, existing control algorithms are usually formulated empirically and solely for the control of crystal diameter (see Kim et al., 1983, for example). Further refinements for process optimization, for example, simultaneous control of diameter, temperature gradients, and melt/solid interface shape, are not easily found. Furthermore, generalizations needed for adapting existing CZ silicon control strategies to other systems, such as LEC growth of gallium arsenide in a low axial temperature

gradient, are difficult to apply and often fail (Carruthers, 1983; Jordan, 1985). A phenomenon which occurs in many low-gradient LEC GaAs systems is the development of oscillations in the crystal radius (Jordan et al., 1983; Elliot et al., 1984).

Strategies for diameter control utilize some technique for detecting changes in crystal shape and commonly vary heater power or pull rate to counter these changes. A review article by Hurle (1977) discusses these methods at length. There are four basic techniques used to detect diameter changes:

1) Optical reflection from the meniscus. This form of diameter control was first reported by Patzner, Dessauer, and Poponiak (1967) and involves monitoring the "bright ring" of light reflected by the meniscus and enhanced by the variation of emissivity between solid and liquid to detect incipient diameter changes. Lorenzini et al. (1974) have described the commercial importance of this method for the production of silicon boules.

2) Crystal imaging. This method involves direct measurement of crystal shape profiles by optical, infra-red, or X-ray systems. The first description of such a system was by Bachmann et al. (1970) in a system imaged by a TV camera. These techniques have not been used with widespread success since diameter changes can only be detected after a significant lag time.

3) Weighing the crystal or crucible. This technique is enjoying increased popularity due to its simplicity and wide range of applications, especially for LEC systems where the meniscus is covered and optical reflection techniques are not feasible

(see Jordan et al., 1983, for a description of diameter control for LEC GaAs growth). Levinson (1959) first envisioned the use of such a system in a patent filed in the United States. Bardsley et al. (1977a,b) describe the theory and implementation of a weighing system which relates the weight gain or derivative weight gain to the changes in meniscus shape and subsequent diameter changes.

4) The use of a shaping die. This method for shape control was pioneered by Stepanov (1959) and Gaule and Pastore (1961) for the growth of single crystal ribbons and is utilized in the EFG process for the high-speed growth of silicon sheet and sapphire ribbons. Although it is not widely used for shape control in the CZ and LEC processes, some success has been achieved for shaping crystal with a ring, termed a "coracle," which floats on the surface of the melt (Cole et al., 1976; Schmaker et al., 1976).

1.4 Previous Work

Even though the CZ method has been used since 1950 to grow semiconductor crystals, few efforts at modeling the process have been attempted. However, demands on increased substrate quality, especially for LEC gallium arsenide, have lead to a desire for a more complete understanding of Czochralski growth in hopes of more effectively using the process for producing better crystals. Reviews of previous models are presented below, and research concerning the stability and control of the CZ method follows in the next section.

1.4.1 Process Modeling

Many idealizations have been used to simplify the modeling of the Czochralski process because of the difficulty of accounting for the complicated fluid flows in the melt and the meniscus-controlled shaping of the crystal, a manifestation of the coupled effects of heat transfer and capillarity. These works are listed in Table 1.1 according to the major idealizations employed in each analysis and have ranged from simple analytical relationships between pull rate and crystal radius to system-oriented heat transfer models which considered crystal, melt, and the surrounding furnace. With the exception of the recent work by Crowley (1983), Derby et al. (1985), Derby and Brown (1986b,1986c,1986d), and Atherton et al. (1986) for systems characterized by conduction-dominated heat transfer in the melt, previous modeling efforts ignored all or some crucial part of the interplay between the geometry of the crystal growth system and heat transfer. This is especially apparent by the treatment of the crystal radius in these works as a system parameter. The crystal radius and the evolving crystal shape varies with heat transfer in the system and is an unknown; this feature results from the meniscus-controlled character of the CZ process and calls for a mathematical model which describes the process as a moving-boundary problem. Therefore, the correct approach to modeling this process requires the determination of the system geometry in addition to solving for heat transfer.

Billig (1955) first derived an approximate relationship between the crystal radius and the pull rate by solving a one-dimensional

Table 1.1 Classification of thermal models for CZ and LEC crystal growth

	1-dimensional fin approximation (fixed interface)	2-dimensional axisymmetric calculations featuring fixed interfaces	melt/solid interface	melt/solid, meniscus, and crystal radius
radius-pull rate relation	Billig (1955) Ciszek (1976) Kim et al. (1983)			
crystal only	Kuo and Wilcox (1972) Buckley-Golder and Humphreys (1979) Van der Hart and Uelhoff (1981) Rea (1981)	Brice (1968) Borodin et al. (1979) Jordan et al. (1980) Duseaux (1983)	Wilcox and Duty (1966) Ramachandran and Dudukovic (1985)	
melt only		Langlois and Shir (1977) Kobayashi (1978) Mihelcic et al. (1982) Crochet et al. (1983) Patera and Tangborn (1986)		
melt and crystal			Arizumi and Kobayashi (1969) Kobayashi and Arizumi (1970) Arizumi and Kobayashi (1972)	Crowley (1983) Derby et al.(1985) Srivastava et al. (1985)
system-oriented		Williams and Reusser (1983) Matsumoto et al. (1984) Wouters (1985)		Derby and Brown (1986b,c) Derby and Brown (1986d) Atherton et al. (1986)

approximation for heat transfer in the crystal with no heat transfer from the melt. Billig assumed that the temperature field in the crystal could be represented by averaging the radial temperature and solving the resultant one-dimensional axial heat conduction problem for a semi-infinite crystal held at the melting temperature at one end while experiencing convective cooling about its perimeter. By equating the total flux of the heat into the crystal at the melt/solid interface to the amount of latent heat released by solidification, Billig postulated that the radius of a steadily growing crystal should be inversely proportional to the square of the steady-state growth rate of the crystal. This relation has been used by others in predicting the dependence of crystal radius on pull rate, see for example the work of Ciszek (1976). An empirical relationship between radius and pull rate based on experimental data was presented by Kim et al. (1983) along with other control correlations for the Czochralski growth of silicon. The steady-state form of this relation differs from that of Billig in that it predicts that the radius should vary inversely with the pull rate to the first power. These radius-pull rate relationships are important in describing the behavior of CZ systems and are compared with our model calculations in later chapters.

Wilcox and Duty (1966) were the first to couple the calculation of heat transfer and melt/solid interface shape for a steadily growing CZ crystal. Their numerical approach solved for the temperature field and interface shape with the assumption that heat transfer between the crystal and melt could be represented by a heat transfer coefficient. This model could not be used predictively since the heat transfer

coefficient is an unknown function of position along the melt/solid interface and because the crystal radius is represented as a system parameter, not as an unknown. Many researchers have concentrated on the determination of the thermal field in the crystal alone with a fixed melt/solid interface. These studies were concerned with the determination of the temperature field and gradients in the crystal as a function of various parameters (Brice, 1968; Kuo and Wilcox, 1972; Van der Hart and Uelhoff, 1981; Rea, 1981; Ramachandran and Dudukovic, 1985) or with the thermal field and resultant distribution of thermal stress (Jordan et al., 1980; Buckley-Golder and Humphreys, 1979; Borodin et al., 1979; Duseaux, 1983). These results were still qualitative in nature since the coupling of heat transfer from the melt and external surroundings was not accounted for and the radius was again treated as a parameter. In addition, only Van der Hart and Uelhoff (1981), Rea (1981), and Ramachandran and Dudukovic (1985) accounted for detailed radiative transfer with the surroundings.

Arizumi and Kobayashi calculated heat transfer for both melt and crystal assuming a conduction-dominated temperature field in the melt (Arizumi and Kobayashi, 1969) and later extended their calculations to include aspects of fluid flow in the melt (Kobayashi and Arizumi, 1970a,b; Kobayashi, 1978) and detailed radiative heat transfer (Arizumi and Kobayashi, 1972). Bulk fluid flow calculations for Czochralski melts have been performed by many researchers (Kobayashi and Arizumi, 1970a,b; Kobayashi, 1978; Langlois and Shir, 1977; Mihelcic et al., 1982; Crochet et al., 1983). The early work of Kobayashi and Arizumi (1970a,b) was concerned mainly with the effects of crystal and crucible

rotation on steady-state fluid flow in the melt. Langlois and Shir (1977) presented transient flow calculations for system rotation and thermally-driven convection. Both Kobayashi and Langlois have published extensively concerning different aspects of their modeling efforts, see Kobayashi (1981) and Langlois (1981). More recent works by Mihelcic et al. (1982), Crochet et al. (1983), and Patera and Tangborn (1985) have extended these analyses with calculations for more intense free convective flows and parameters which more closely resemble real semiconductor melts. All of these studies have modeled the CZ melt as an axisymmetric two-dimensional cylindrical domain, neglecting the shape of the melt meniscus, curvature of the melt/solid interface, and the true three-dimensional nature of the domain. Although these studies have elucidated many features of the complex flow patterns possible in the melt, no studies have succeeded in calculating the flows in large-scale CZ systems where the flow is probably intensely chaotic and heat transfer is strongly influenced by convection (Hurle, 1983).

The models of Crowley (1983), Derby et al. (1985), and Srivastava et al. (1985) have attempted to capture the free-boundary aspects of the CZ system. Crowley's approach, though a major improvement over previous models with fixed or partially fixed geometries, only described heat transfer in a small region of the system near the growth interface and the holm region of the meniscus. Although the shapes of the interfaces and crystal radius were well represented, specific inputs from experimental measurements were required for thermal boundary conditions near the melt/solid interface, so that the model had limited

ability to predict the response of the system to a change in external parameters, such as a change in the crucible temperature. The work of Srivastava et al. (1985) extended earlier work of Ramachandran and Dudukovic (1985) by including the melt region and the meniscus. Their work treated the steady-state radius as a parameter and varied the pull rate in order to close a heat balance around the system so the effect of a varying radius could be implicitly accounted for. The work of Derby et al. (1985) attempted the simulation of LEC growth of gallium arsenide and is described in Chapter 4.

System-oriented modeling efforts for optimizing the design of particular growth systems which include the effects of furnace heat shields and temperature distributions were represented in the works of Williams and Reusser (1983) and Matsumoto et al. (1984). These studies were limited by assumptions of fixed interfaces and required experimentally measured thermal boundary conditions. Wouters (1985) developed techniques for calculating radiative fluxes in a model CZ furnace. The batchwise nature of CZ growth and the calculation of processing strategies are explained by Derby and Brown (1986b,c). Extension of these works to the fully dynamic simulation of CZ growth is presented in Chapter 5. Atherton, Derby, and Brown (1986) examine the role of radiative heat transfer in a prototype system.

1.4.2 Process Control and Stability

The CZ and LEC methods are batch processes, and the growth of uniform crystals depends on the ability to achieve reproducible quasi-steady growth conditions. An important issue in the control of the CZ process is the "inherent" stability of the system. Practical crystal growers agree that the diameter of the crystal will vary in the absence of active control, and many have concluded that the process is inherently unstable. However, this issue is obscured by the batchwise nature of the process where transients occur over the long time scale corresponding to the dropping of the melt level in the crucible and the concomitant changes in the heat transfer environment. In fact, there is experimental evidence that diameter changes are indeed only manifestations of the long-time scale thermal transients. Robertson and Young (1975) described an experiment where germanium crystals with fairly uniform diameter were grown in a CZ system without diameter control thus indicating the the process may have been stable. If the CZ process is inherently stable, processing strategies need only counter the transient effects of the batch process. However, if the system is unstable, the controller must actively control the system around a constant-diameter set point while simultaneously accounting for the batch effects.

The stability of the meniscus alone has been studied in the context of the Czochralski process by Mika and Uelhoff (1975) and more generally for rotationally symmetrical fluid bodies (as would form around a cylindrical crystal pulled from the melt) by Boucher and Kent (1977).

These works are of limited value in understanding the overall stability of the CZ process since the capillary stability of the meniscus has little to do with the dynamic evolution of the crystal radius. Surek (1976) was the first to identify the concept of shape stability for the growing crystal, and analyzed the response of the crystal diameter to a perturbation to the growth system which changed the height of the melt meniscus. Neglecting heat transfer and basing the analysis solely on the properties of the melt meniscus and the non-zero wetting angle at the melt/crystal/ambient tri-junction, he claimed that the Czochralski process was inherently unstable. Surek, Coriell, and Chalmers (1980) included a simplified heat transfer analysis by Steel and Hill (1975) in Surek's previous approach to the shape stability of crystals grown from the melt and found that this effect stabilized the CZ process for most cases. For example, they predicted that the Czochralski process would be unstable only for the growth of small crystals (for silicon, this occurred for diameter < 0.3 cm).

Crowley (1983) attempted to assess the stability of the Czochralski process with her moving-boundary heat transfer model of CZ growth discussed in the previous section. Starting from initial conditions which represented a constant-diameter crystal of a fixed length and a melt of given temperature, Crowley computed the time evolution of the system after a drop in the temperature prescribed at the melt surface. Since a new steady state was not found, Crowley concluded that the process was unstable. There are two other possible explanations for these results which were not addressed by Crowley. First, there was no assurance that a new steady state even existed for the new

melt temperature or that the solution was integrated for a long enough period of time to reach it. Second, it was likely that the crystal length used in the analysis was too short so that the length of the crystal affected heat transfer near the melt/solid interface. In this case, the movement of the top of the crystal would delay attaining any new quasi-steady state until the crystal had grown enough so that the top would not affect the overall heat transfer in the crystal.

We approach the stability and the dynamics of growth of the CZ process in Chapter 5 of this thesis. The stability of quasi-steady states is analyzed through a linear stability analysis of the thermal-capillary model of heat transfer, and the dynamics of CZ growth are obtained from a fully transient simulation.

1.5 Thesis Outline

The mechanisms of heat transfer and the coupled geometrical effects of the system interfaces in the CZ and LEC systems are discussed in Chapter 2 along with the basic assumptions and the resulting equations for the steady-state and transient thermal-capillary models. The finite-element method for solution of the governing equations for the steady and transient models is presented in Chapter 3. Within this framework we also formulate the method for the analysis of linear stability of the steady-state solutions.

In the remainder of the thesis we present calculations for prototype CZ silicon and LEC gallium arsenide systems. In Chapter 4, results of steady-state simulations are given and discussed. Aspects of stability

and system dynamics are presented in Chapter 5. Recommendations for further research along with the conclusions of this work follow in Chapter 6. Nomenclature, thermophysical property data, and a study on the transient simulation of a model solidification problem are included in the appendices.

Chapter 2. Thermal-Capillary Model of CZ and LEC Growth

In the following sections the physics of heat transfer in the Czochralski and liquid encapsulated Czochralski processes is discussed, and a mathematical approach for modeling these systems is formulated.

2.1 Heat Transfer in the CZ and LEC Systems

The CZ and LEC processes involve heat transfer in liquid and solid phases of differing thermophysical properties, a solidifying interface between the phases, menisci separating melt, encapsulant, and the surrounding ambient, and very high temperatures (the melting points of Si and GaAs are 1638 K and 1511 K, respectively). Conduction, convection, and radiation are all important mechanisms for heat transfer, as shown schematically in Fig. 2.1. The crucible is surrounded by a picket-fence resistance heater which heats the sides of the crucible primarily via radiation, and heat is conducted inward through the crucible wall to the melt. Heat also flows to the crucible's upper exposed surfaces and bottom surface where it is radiated and convected to the cooler ambient. An additional path for heat loss from the crucible bottom is through the supporting pedestal; often this pedestal is water-cooled.

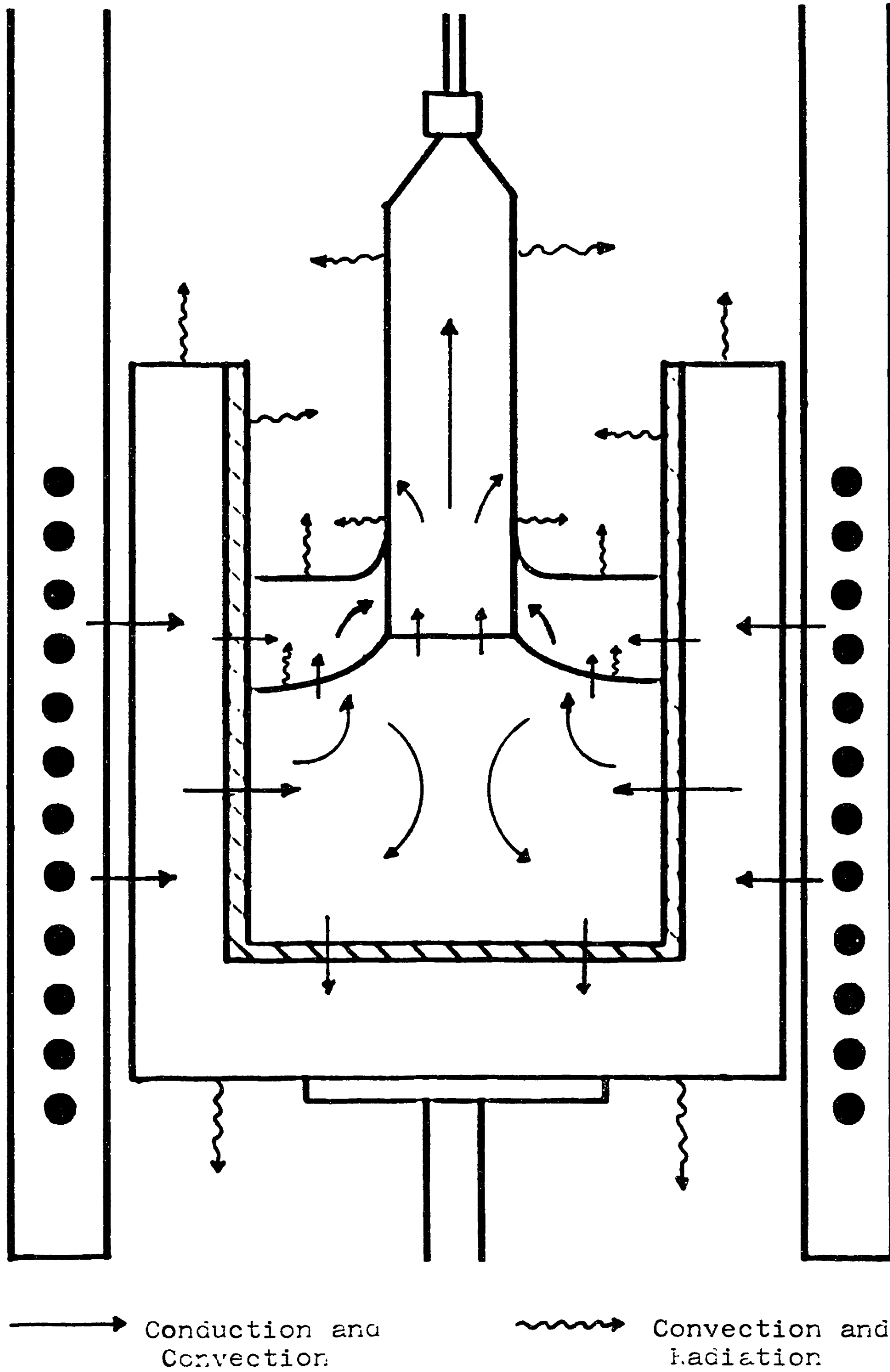

Fig. 2.1 Heat transfer mechanisms in an LEC system.

In the melt, heat is transported by conduction, convection, and possibly radiation through the bulk (Rosenberger, 1979). The velocity field in the melt is very complicated and is driven by a combination of the imposed crystal and crucible rotation, thermally-induced density gradients, and thermocapillary forces which arise from the variation of surface tension with temperature. Hurle (1983) discusses these aspects of flows in semiconductor melts.

The importance of convective heat transfer by fluid flows can be assessed by the comparing the ratio of heat transfer which occurs by convection to that which occurs by conduction. This ratio is expressed by the dimensionless Peclet number, which can be put into the form of the Reynolds number multiplied by the Prandtl number,

$$Pe = Re\ Pr \ , \qquad (2.1)$$

where $Re = LV/\nu$ and $Pr = \nu/\alpha$, with the quantities L = length, V = fluid velocity, ν = kinematic viscosity, and α = thermal diffusivity. In this context, the Reynolds number is a measure of the intensity of flow since it depends on a characteristic velocity, V, whereas the Prandtl number is a constant material property which depends only on the composition of the system. Convective heat transfer is assessed by the magnitude of the Peclet number for heat transfer. For most liquid metal and semiconductor melts, the Prandtl number is very small, $Pr \sim 10^{-2}$. Reported values of the Prandtl number for molten silicon, indium phosphide, and gallium arsenide are $2.\times10^{-2}$ (Schwabe, 1981), 1.5×10^{-2}, and 6.8×10^{-2} (Jordan, 1985), respectively. However, oxide melts have a much larger Prandtl number, typically $Pr \sim 1-10$, and heat transfer by convection is much more important in these systems

since, for the same intensity of flow, the Peclet number is much greater. Prandtl numbers for some oxide systems are Pr ≅ 25 for $Bi_{12}SiO_{20}$, Pr ≅ 1 for $Y_3Al_5O_{12}$, and Pr ≅ 0.4 for Al_2O_3 (Schwabe, 1981).

Forced convection in Czochralski systems occurs when the crucible and crystal are rotated. In practice, rotation tends to lessen the effects of furnace thermal asymmetry, and in addition, the resultant flows in the melt affect heat and mass transfer. Carruthers (1967) and Carruthers and Nassau (1968) were among the first to study through flow visualization in a simulated model system the velocity field in a Czochralski melt caused by crucible and crystal rotation. For the low Prandtl number semiconductor melts, crucible and crystal rotation rates are not high enough to significantly affect heat transfer. However, significant heat transfer effects from crucible and crystal rotation are observed for the higher Prandtl number oxide crystal growth systems. Experimental observations by Whiffin et al. (1976) for bismuth silicon oxide, and Takagi et al. (1976) and Cockayne et al. (1976) for garnet, pointed out dramatic changes in heat transfer as evidenced by sudden changes in crystal diameter or melt/crystal interface morphology ("interface flipping") as a function of crystal rotation. Carruthers (1976) demonstrated that these results could be explained by heat transfer changes caused by the transition of a fluid flow state dominated by buoyancy-induced free convection to one dominated by forced convection driven by crystal rotation.

Fluid flow caused by thermally-induced driving forces is much more complicated than that caused by crystal or crucible rotation. The most important driving force for natural convection in crystal

growth systems is caused by gravity acting upon density differences of liquid at differing temperatures (Carruthers, 1977; Langlois, 1981); however, Marangoni effects, flows driven by temperature-induced gradients of surface tension, can also be significant, especially in micro-gravity situations, such as those encountered in the processing of material in space, where the driving force for buoyancy-induced flow is reduced (Langlois, 1980; Schwabe, 1981; Lamprecht et al., 1983). Thermally-driven flows span the range from fully laminar to time-periodic to chaotic and finally to fully turbulent. In large-scale CZ systems, fully turbulent or intense chaotic flows are present and convection strongly influences heat transfer. The driving force for buoyancy-induced flow is much smaller in laboratory-scale systems; however, the fluid velocity field can still be either steady and laminar, time-dependent, or chaotic.

These different flow patterns have been experimentally observed by measuring the temperature in semiconductor melts of different configurations (Hurle and Jakeman, 1972; Kim, Witt, and Gatos, 1972; Muller and Neumann, 1983). The recorded temperature in these experiments was either constant in time, indicating steady laminar flow, fluctuating regularly, demonstrating time-periodic flows, or fluctuating in a random manner, indicating a chaotic flow in the melt. Additional insight into the nature of melt flows can be obtained by observing the compositional variations in crystals; the effect of fluid flow on melt composition near the crystal interface is incorporated into the growing crystal (Kim et al., 1972; Carruthers and Witt, 1975). Again, laminar, time-periodic, and chaotic flows are observed. Wargo

(1982) provides a complete discussion of convection and microscopic growth fluctuation effects on the resulting compositional makeup of Czochralski crystals.

The importance of convection to the overall heat transfer in the low Prandtl number semiconductor melts is probably quite small due to the low Peclet number for heat transfer for most flows. Even though the experimentally measured temperature fluctuations caused by convection in the melt cause microscopic melt back and regrowth of the melt/solid interface and lead to solutal banding in the crystal (Carruthers and Witt, 1975; Wargo, 1982), the temperature fluctuations are usually on the order of a few degrees (<10K) superimposed on a temperature gradient of 50-100 K/cm so that they are not significant on the macroscopic scale of several centimeters which is characteristic of the crystal radius. The intense laminar convection calculated by Langlois (1981) and Chang and Brown (1983b) and even the time-dependent weakly chaotic convection calculated by Crochet et al. (1983) and Mihelcic et al. (1982) for heat transfer in melts contained by small-scale crucibles does not lead to large changes in the temperature field from the results predicted for pure conduction in the melt. We approach the problem of modeling heat transfer in the melt by assuming that the system is conduction-dominated. This approach is valid as long as the Peclet number for heat transfer in the melt is small, a safe assumption for moderate flows and very small Prandtl numbers such as occur for small-scale semiconductor melts. We further discuss this conduction-dominated hypothesis later in this section and in Chapter 6.

We also argue that convective heat transfer in the encapsulant layer for LEC growth also has little effect on the axisymmetric temperature field of the system since the magnitude of the fluid velocity field is small and is composed primarily of flow in the azimuthal direction caused by crystal and crucible rotation. This is pointed out by experimental observation of small bubbles in the encapsulant which slowly rise vertically to the surface during the growth process (Elliot, 1984), thus indicating a nearly quiescent fluid. In this situation, the Peclet number for heat transfer should be quite small since the flow in the encapsulant is vanishingly small in the radial and axial directions. These facts concerning the importance of convection are used in justifying the conduction-dominated heat transfer model proposed below.

Heat leaves the melt by several paths. It is conducted out of the bottom of the crucible and into the crystal through the melt/solid interface. It is also radiated and convected away from the surface of the melt. In an LEC system, heat flows across the melt/encapsulant interface by both conduction and radiation into the boric oxide where it is either absorbed or radiated to the ambient above. Latent heat is released at the melt/solid interface by the phase change of melt into crystal. The latent heat and heat conducted from the melt flows into the crystal, is conducted upward and outward to the crystal surface, and is convected upward by the motion of the solid. Bulk radiative transfer can also occur in semiconductor crystals at high temperatures (Viskanta and Anderson, 1975; Kalejs et al., 1983).

Heat is exchanged at the surfaces of the melt, crystal, and encap-

sulant by radiation and convection. An order-of-magnitude analysis for CZ growth in an ambient at atmospheric pressure indicates that radiation is the dominant mode of heat transfer from system surfaces. This is not surprising since the temperatures of these systems are very high. An additional piece of supporting evidence is from experimental observations that different heat shield configurations alter the growth characteristics of a CZ puller (Wargo, 1983; Matsumoto et al., 1984). The radiative interactions among the system surfaces and the rest of the apparatus are complicated by the geometry of the CZ system. While a point at the top of the crystal views primarily the top or sides of the enclosure, points on the side of the crystal, the melt surface, and the exposed crucible wall see each other along with the rest of the furnace.

The encapsulant layer in the LEC system further complicates radiative transfer by acting as a participating medium through which radiation is transmitted. Growth conditions in LEC systems have been reported to be very sensitive to trace amounts of water in the boric oxide encapsulant (AuCoin et al., 1979; RASA Industries, 1981), and since water affects the absorption of radiation in the encapsulant, this indicates that radiation through the B_2O_3 layer is important to overall heat transfer.

Bulk radiative transport is important for semi-transparent materials which do not exhibit strong absorption of thermal radiation. This form of heat transport may be important for heat transport through some crystals and melts and is definitely important in the B_2O_3 encapsulant of LEC growth. Boric oxide is transparent in the visual wavelength

spectrum but begins to absorb radiation in the infrared region, thus affecting heat transfer through the encapsulant layer. This is demonstrated in Fig. 2.2 where the transmission spectrum of B_2O_3 is plotted with the spectral emissive power distribution from a black body at the melting point of gallium arsenide (1511 K). The boric oxide transmission spectrum was measured at room temperature for a 0.2 mm thick sample which contained approximately 220 ppm H_2O (RASA Industries, 1981). These conditions are quite different from those encountered in LEC growth where the B_2O_3 layer is usually centimeters thick, molten, and at high temperature, however these are the only data currently available. An absorption band for the O-H vibration of bound water in the B_2O_3 appears in the 2.7 μm to 3.0 μm region. This band varies in shape and position with the amount of H_2O present and accounts for the sensitivity of heat transfer in LEC growth to the composition of the encapsulant. Transmission drops rapidly for wavelengths above 3.5 μm.

The effect of the boric oxide layer on radiative heat transfer from the surface of the melt in LEC growth of gallium arsenide is seen by comparing the emissive power distribution in Fig. 2.2 to the B_2O_3 transmission spectrum, with the provisos that the use of this transmission spectrum for molten boric oxide is questionable and the real emissive power distribution of molten GaAs may differ significantly from the black body distribution. Approximately 25 per cent of the total emissive power for a black body at 1511 K is accounted for by radiation of 2 μm or less and is almost totally transmitted through the boric oxide. Over 40 per cent of the emissive power is distributed

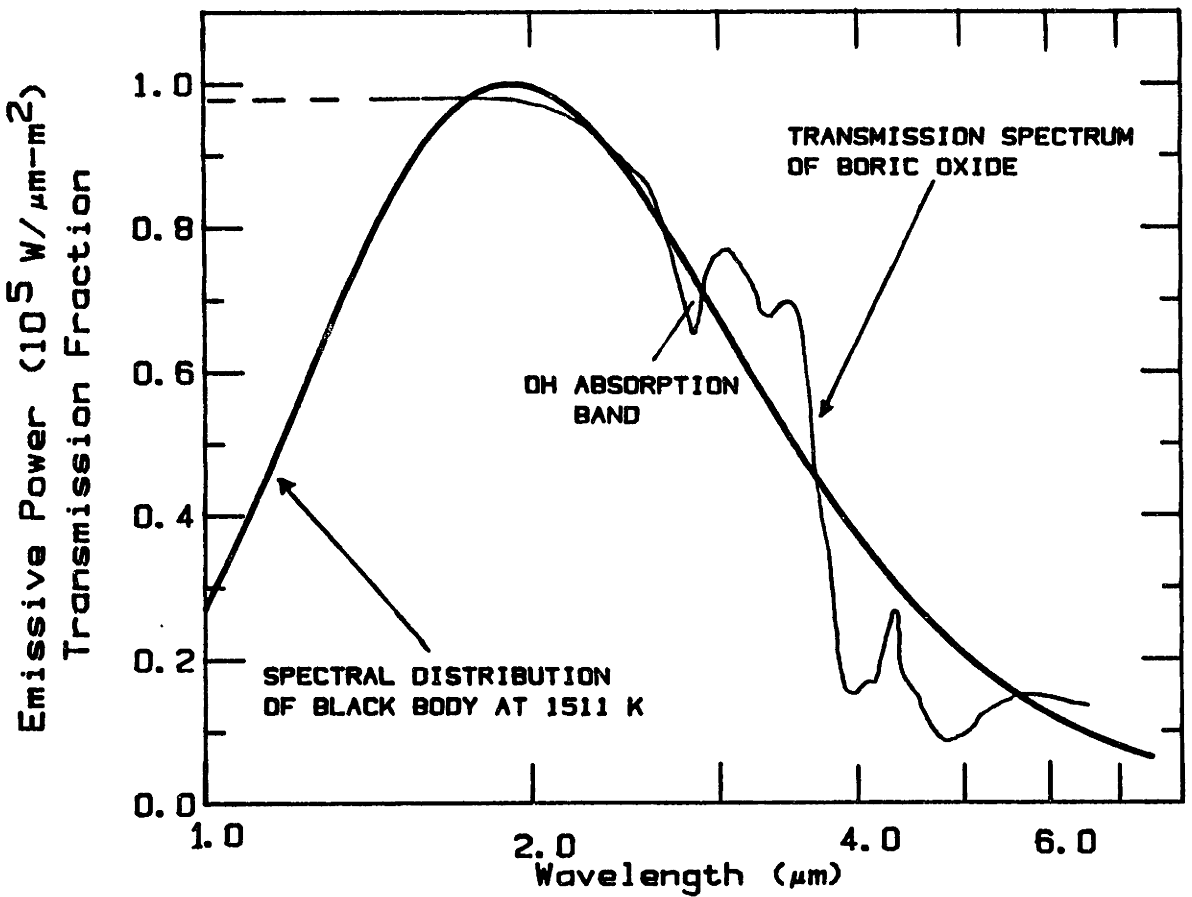

Fig. 2.2 Black body spectral emissive power distribution distribution at 1511 K superimposed on transmission spectrum of solid B_2O_3 (220 ppm H_2O) at room temperature (RASA Industries, 1981).

at wavelengths between 2 μm and 3.5 μm and most of this energy (70-80 per cent) is transmitted. However, the amount of water in the encapsulant significantly affects transmission in this range; boric oxide containing more water absorbs more energy. Radiation of wavelengths greater than 3.5 μm is almost completely absorbed and accounts for approximately 35 percent of total emissive power. Overall, from 50 to 60 per cent of the black body emissive power is transmitted through the B_2O_3 for the spectrum presented in Fig. 2.2.

The overall understanding of heat transfer in the CZ and LEC systems is not complete until the geometrical effects of the system interfaces are known. The shape of the physical domains of melt, solid, and encapsulant are determined by heat transfer and capillarity. The melt/solid interface falls along the melting point isotherm when the kinetics of solidification are very fast, as in most melt crystal growth systems, thereby coupling the shape of this interface and the resulting temperature field. Heat transfer is also strongly affected by the shape of the melt and encapsulant surfaces. These shapes are set by the capillary action of surface tension and gravity in the forming of a meniscus.

A complete accounting of the heat transfer mechanisms is beyond the developmental nature of this research but is not precluded by extensions to the work described here. The following assumptions are made in order to facilitate solution for the temperature field in this complex problem.

1) The temperature field is assumed to be axisymmetric. This allows for a two-dimensional model and is a reasonable approximation to the real system. In practice, the crystal and crucible are rotated at several rpm to improve the thermal symmetry of the system.

2) Heat transfer in the melt is dominated by conduction. Although not strictly correct, this assumption considerably simplifies the solution for heat transfer in the system. This assertion is accurate when convection levels are low such as in small-scale systems, low-gradient configurations, or magnetic CZ growth where strong magnetic fields are used to damp convection (Langlois, 1981; Hurle, 1983). In these situations, the Peclet number for heat transfer, as defined by eq. (2.1), is very small for low Prandtl number semiconductor liquids with low melt velocities.

3) Heat transfer in the crystal consists only of conduction and solid-body convection. This is correct for systems where bulk radiative transfer is not important. In addition, even in these systems with bulk radiative transfer, a temperature-dependent effective thermal conductivity can often account for this effect (Kalejs et al., 1983; Ettouney et al., 1984).

4) Heat transfer in the encapsulant layer of LEC growth is dominated by conduction. As discussed above, experimental observations indicate that flows in the encapsulant layer are quite small. However, this fact alone does not preclude heat transfer by convection since the Prandtl number for B_2O_3 is at least 1000; the Peclet number for heat transfer will be significant for all but vanishingly slow flows. This assumption must be considered a first attempt at modeling heat transfer in the LEC system.

5) Radiative heat transfer in the system is approximated by surface fluxes to an ambient temperature distribution. This is a first-order approximation to the real situation where all surfaces in the furnace participate in radiative exchange. In order to precisely account for the exchange of radiative energy among the system surfaces, the system must be treated as a radiation enclosure (see Wouters, 1985; Ramachandran and Dudukovic, 1985; Atherton et al., 1986). This issue will be discussed in more detail in the conclusions of this thesis.

6) The boric oxide layer in LEC growth will be considered either totally transparent or totally opaque to radiation. Reality probably lies between these two approximations, but in the absence of data on the radiative transmission of molten B_2O_3 near the melting point of the semiconductor, a more detailed treatment is not warranted. These limiting cases are justified as a first approximation.

We list below the assumptions used in determining the locations of the system interfaces. These assumptions coupled to those made above will allow the ensuing model development.

1) The kinetics of the melt/solid phase transformation are infinitely fast. This assumption is valid for the CZ process and most other melt growth systems since the time scale for the solidification reaction is much smaller than that for heat transfer. It also leads to the conclusion that the melt/solid interface must follow the shape of the melting point isotherm in the system.

2) The shape of the meniscus is unaffected by hydrodynamic forces. We assume that the dynamic viscous and pressure forces caused by fluid motion are small with respect to surface-tension forces. This permits the use of a static force balance to specify the shape of the meniscus and is an excellent assumption since the Capillary number is very small for these systems. For melt velocities in silicon from 1 to 10^3 cm/s, the corresponding Capillary numbers are Ca ~ 10^{-5} to 10^{-2}.

3) The wetting angle of melt to its own solid is a constant material property. This has been postulated by others through thermodynamic equilibrium arguments (Herring, 1951; Bardsley et al., 1974) and has been verified experimentally by Surek and Chalmers (1975) for the solidification of silicon over a very wide range of growth rates. The angle formed by the meniscus at the edge of the crystal is equal to this wetting angle for constant-diameter growth, and the departure of meniscus angle from the wetting angle determines the subsequent evolution of crystal shape (Bardsley et al., 1974; Crowley, 1983).

The validity of these assumptions will be addressed through the remainder of this thesis and in the final chapter. We will see, however, in the ensuing chapters that meaningful results are obtained within the framework of these assumptions.

2.2 Quasi-Steady-State Formulation

We model the steady-state growth of a cylindrical boule of crystal from a melt (covered with encapsulant for the LEC system) in a crucible of inner radius R_c. The crystal is pulled continuously from the melt at a rate V_p. We imagine a quasi-steady state process in which the melt depth in the crucible, and hence the volume of the melt, changes on a much smaller time scale than the thermal transients in the system. This condition holds for a CZ growth system when

$$\frac{\text{characteristic time for conductive heat transfer}}{\text{characteristic time for melt volume change}} = \frac{(R_c^2/\alpha^*)}{(R_c/V_p)} << 1 .$$

With the thermal diffusivity of molten silicon, $\alpha^*=0.26$ cm²/s, and typical values of crucible radius and pull rate of $R_c=5$ cm and $V_p=0.001$ cm/s,

$$\frac{(R_c^2/\alpha^*)}{(R_c/V_p)} = \frac{96 \text{ s}}{5000 \text{ s}} \sim 0.02 << 1 , \qquad (2.2)$$

and the quasi-steady state assumption is justified. Then it is valid to reconstruct the time history of a growth run from a sequence of steady-state calculations with decreased melt depths. Note that this method of growth simulation is only valid for a run where the crystal is maintained at a constant radius. The complete simulation of a growth run must be able to represent the dynamic crystal shape changes which are typical of meniscus-controlled growth processes and thus calls for fully transient calculations. We address these aspects of modeling the CZ and LEC systems in the following section.

Our prototype LEC system for the thermal-capillary model is show schematically in Fig. 2.3 with the notation needed to represent the physical domains of the crystal (D_s), melt (D_m), and encapsulant (D_e) and the crucible (D_c) and liner (D_ℓ). The time-dependent quantities denoted in Fig. 2.3 are set as constants or functions of position only for the quasi-steady-state model. Although the figure and following discussion refer to modeling the liquid encapsulated Czochralski process, the Czochralski system is represented in exactly the same manner with the exclusion of the encapsulant layer. Each of the domains is characterized by a set of thermophysical properties which can be temperature-dependent. In this model, we usually assume a constant set of properties for the system since the real properties which characterize the system are not well known. For modeling the CZ silicon process, we use a temperature-dependent thermal conductivity for the crystal as was done by Ettouney et al. (1984). Segments of the boundary have been labelled as ∂D_i where the value of i corresponds to the surfaces shown in Fig. 2.3. The positions of the system boundaries are represented as functions defined on a cylindrical coordinate system which is centered at the bottom of the melt. In dimensional terms, the quasi-steady value for the radius is denoted by $\tilde{R}$, the solidification front as $\tilde{H}_0(\tilde{r})$, and the melt and encapsulant menisci as $\tilde{H}_1(\tilde{r})$ and $\tilde{H}_2(\tilde{r})$, respectively. Other geometrical quantities needed to specify the system are the height of the crystal, $\tilde{Z}$, and the volumes of melt and encapsulant, $\tilde{V}_m$ and $\tilde{V}_e$.

We scale lengths with the radius of the crucible R_c, so that $R \equiv \tilde{R}/R_c$, $H_i \equiv \tilde{H}_i/R_c$, $Z \equiv \tilde{Z}/R_c$, $V_m \equiv \tilde{V}_m/R_c^3$, and $V_e \equiv \tilde{V}_e/R_c^3$. Temperature

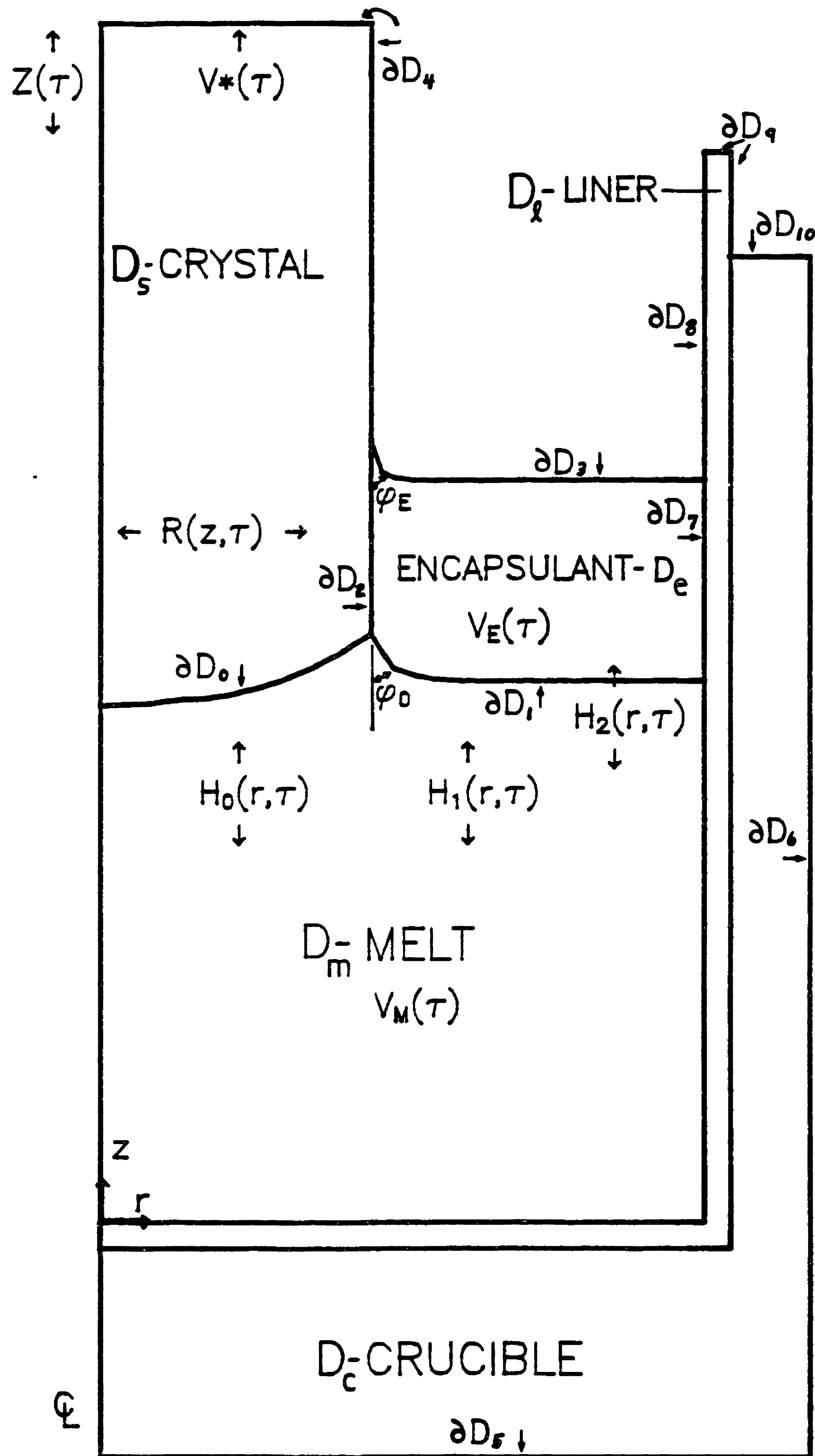

Fig. 2.3 Schematic diagram of thermal-capillary model.

is normalized with the equilibrium melting point of the semiconductor material, T_f, so that $\Theta(r,z) = T(r,z)/T_f$. All variables discussed below are given in dimensionless form unless explicitly stated otherwise. A complete list of variables and dimensionless groups is included in the Nomenclature section of Appendix A.

The equation set for the temperature field is listed in nondimensional form in eqs. (2.3-2.10). Heat transfer for an axisymmetric conduction-dominated system is described by the following equations,

$$\nabla\cdot(K_i(\Theta)\nabla\Theta) = 0 \text{ , for } i=m,e,\ell,c, \tag{2.3}$$

$$\nabla\cdot(K_s(\Theta)\nabla\Theta) - Pe_s(\mathbf{e}_z\cdot\nabla\Theta) = 0 \text{ , for the crystal,} \tag{2.4}$$

where $\nabla = \mathbf{e}_r(\partial/\partial r) + \mathbf{e}_z(\partial/\partial z)$ is the gradient operator in cylindrical coordinates and $\mathbf{e}_r$ and $\mathbf{e}_z$ are the unit vectors. $K_i(\Theta)$ is the appropriate temperature-dependent thermal conductivity for each region, and Pe_s is the Peclet number, a dimensionless form of the steady-state growth rate which is the same as the crystal pull rate. The thermophysical properties for the LEC gallium arsenide system and the CZ silicon system are given in Tables A.1 and A.2 in Appendix A.

The conditions on the boundaries between regions guarantee that temperature is continuous and that energy is conserved along each interface. At the melt/crystal interface (∂D_0), latent heat is released upon solidification and enters as an additional flux across the interface as follows,

$$K_m(\mathbf{n}\cdot\nabla\Theta)_m - K_s(\mathbf{n}\cdot\nabla\Theta)_s = Pe_s S(\mathbf{n}\cdot\mathbf{e}_z) \text{ ,} \tag{2.5}$$

where the Stefan number S is a measure of latent heat and $\mathbf{n}$ is the

outward pointing normal to the interface,

$$\mathbf{n} = \frac{\mathbf{e}_z - H_{0r}\mathbf{e}_r}{(1+H_{0r}^2)^{1/2}} , \tag{2.6}$$

where H_{0r} denotes the partial derivative $\partial H_0/\partial r$.

The surfaces of the regions exchange energy with the surroundings by convection and radiation, as represented by eq. (2.7) for all exposed surfaces (∂D_i, $i=1,...,10$). Detailed view factors for radiation are not included; instead, the effects of the system viewing surfaces at different temperatures is incorporated by an ambient temperature distribution $\Theta_a(r,z)$, and the fluxes are represented as,

$$-K_i(\mathbf{n}\cdot\nabla\Theta) = Bi_j\{\Theta - \Theta_a(r,z)\} + Ra_j\{\Theta^4 - \Theta_a^4(r,z)\} , \tag{2.7}$$

where the subscript i denotes the region and j denotes the specific interface. The non-dimensional quantities Bi_j and Ra_j are the Biot and Radiation numbers, relative measures of the importance of convective and radiative fluxes. The outward-pointing normal to the surface **n** is defined as follows:

$$\mathbf{n} = \begin{cases} \dfrac{\mathbf{e}_z - H_{jr}\mathbf{e}_r}{(1+H_{jr}^2)^{1/2}} & \text{for } j=1,3 \quad , \\ -\mathbf{e}_r \, , & \text{for } j=4,6,9 \, , \\ -\mathbf{e}_r \, , & \text{for } j=7,8 \quad , \\ \mathbf{e}_z \, , & \text{for } j=4,9,10, \\ -\mathbf{e}_z \, , & \text{for } j=5 \quad , \end{cases} \tag{2.8}$$

where $H_{jr} \equiv \partial H_j/\partial r$ and index j refers to the interfaces labeled in

Fig. 2.3. For the LEC process, the term for convective cooling by the gaseous ambient is not included for those surfaces which are covered by the encapsulant (∂D_j, j=1,2,7) and Bij=0. The heat flux at those surfaces consists only of conduction to the adjacent region and, for a radiatively transparent encapsulant, radiation from the surface through the encapsulant layer window. Calculations have been performed for encapsulant layers which are either totally transparent or opaque to radiation; these results are presented in Chapter 4.

For the first calculations of this steady-state model the crucible and liner regions were not included, and boundary conditions were imposed directly on the side and bottom of the melt. The melt adjacent to the crucible wall is set as a specified temperature, Θ_c,

$$\Theta(1,z) = \Theta_c \ . \tag{2.9}$$

For the bottom of the melt, the temperature was either set as above in eq. (2.9), or a flux boundary condition was specified according to eq. (2.7). Finally, the centerline of the system is specified as an axis of symmetry by

$$\mathbf{e}_r \cdot \nabla\Theta \Big|_{r=0} = 0 \ . \tag{2.10}$$

The shapes of the melt, encapsulant, and the size of the crystal are determined by solving the following equations simultaneously with the heat transfer problem described above. The melt/solid interface $z = H_0(r)$ follows the shape of the equilibrium melting point isotherm, as shown implicitly in the following condition,

$$\Theta(r,H_0(r)) = 1 \ . \tag{2.11}$$

This technique for locating the solidification front is known as the isotherm method and was originally developed by Ettouney and Brown, (1983). This approach is only valid for systems where crystal faceting does not occur and phase change kinetics are very fast; however, these conditions are satisfied in most CZ growth systems.

The locations of the melt and encapsulant menisci, $H_1(r)$ and $H_2(r)$, are governed by a force balance between surface tension and gravity given by the Young-Laplace equation of capillary statics:

$$2\mathcal{H}_i = Bo_i(H_i - \lambda_i) , \tag{2.12}$$

where Bo_i is the Bond number for the meniscus defined by H_i and is a measure of the relative importance of gravity to surface tension in setting the shape of the interface. The mean curvature of the surface is denoted by $\mathcal{H}_i$ and is defined for an axisymmetric surface by

$$2\mathcal{H}_i = \frac{\frac{\partial^2 H_i}{\partial r^2}}{\left[1+\left(\frac{\partial H_i}{\partial r}\right)^2\right]^{3/2}} + \frac{\frac{\partial H_i}{\partial r}}{r\left[1+\left(\frac{\partial H_i}{\partial r}\right)^2\right]^{1/2}} . \tag{2.13}$$

The variable λ_i on the right hand side of the Young-Laplace equation (2.12) corresponds to a datum pressure for each meniscus. These terms are unknown since no datum location exists along either surface where the mean curvature is precisely zero. Thus ambient pressure cannot be directly related to the pressures in the encapsulant and melt. These unknowns, λ_i, are then determined by specifying the volumes of the melt and encapsulant layer. For λ_1 this condition is

$$\int_0^R H_0(r)rdr + \int_R^1 H_1(r)rdr = V_m/2\pi \ , \qquad (2.14)$$

and for λ_2,

$$\int_R^1 (H_2(r)-H_1(r))rdr = V_e/2\pi \ . \qquad (2.15)$$

The technique of solving for the unknown datum pressures λ_i by specifying known volumes for regions enclosed by the menisci has been used before in other capillary problems (see Brown et al., 1980).

The boundary conditions for the Young-Laplace equation are specified by the following set of equations. The melt meniscus is connected to the edge of the growing crystal at the tri-junction between melt, solid, and the surrounding media (a gaseous ambient for CZ growth and encapsulant for LEC),

$$H_0(R) = H_1(R) \ . \qquad (2.16)$$

A small wetting angle $\tilde{\phi}_e$ is specified at the junction of encapsulant and crystal for $H_2(r)$ as,

$$\left.\frac{\partial H_2}{\partial r}\right|_{r=R} = -\cot \tilde{\phi}_e \ . \qquad (2.17)$$

Both menisci also wet the crucible wall at some angle, but because the heat transfer of the system is not significantly affected by the shapes of the menisci near the wall this angle is taken to be 90° in order to minimize the degree of numerical refinement necessary to resolve the meniscus in this region. These non-wetting edge conditions are given by

$$\left.\frac{\partial H_1}{\partial r}\right|_{r=1} = \left.\frac{\partial H_2}{\partial r}\right|_{r=1} = 0 \ . \qquad (2.18)$$

At the tri-junction of melt/solid/encapsulant (or melt/solid/ambient for the CZ system) the melt meniscus pins to the edge of the crystal and wets its own solid at a specified angle, $\tilde{\phi}_0$, during constant-diameter growth. This angle is related to the equilibrium wetting angle of a liquid in contact with its own solid and was first discussed by Herring (1951) for crystal sintering. Bardsley et al. (1974) applied similar reasoning to determine the meniscus shape in CZ growth, and Surek and Chalmers (1975) experimentally found that for silicon growth this angle was constant over a wide range of growth rates. Thus we specify that the joining liquid-crystal meniscus angle must take on the value of $\tilde{\phi}_0$ as a necessary condition for constant-diameter steady growth. We accomplish this by adjusting the crystal size so that

$$\left.\frac{\partial H_1}{\partial r}\right|_{r=R} = -\cot \tilde{\phi}_0 \ . \qquad (2.19)$$

This complete set of partial differential equations, boundary conditions, and constraints defines a nonlinear free-boundary problem for the temperature field in the melt, crystal, encapsulant, liner, and crucible and for the shapes of each region. The solution of a problem of this complexity is intractable using conventional analytical methods. We have developed a sophisticated numerical technique for the solution of the thermal-capillary model equations, and we present this approach in Chapter 3. Steady-state calculations for CZ silicon and LEC gallium arsenide growth are presented in Chapter 4.

2.3 Transient Formulation

In Section 2.2 we argued that a quasi-steady model for the Czochralski and liquid encapsulated Czochralski processes was valid since the characteristic time for heat transfer is much smaller than the time scale for melt volume changes, as demonstrated in eq. (2.2). Unanswered questions remain however about the stability of the steady-state solutions and the dynamics of crystal shape evolution in these meniscus-controlled growth systems. Both issues are crucial to the development of control strategies for the CZ and LEC systems. We present the formulation of our transient thermal-capillary model in this section. The discussion of process stability is deferred until Section 3.4 of Chapter 3 where the conditions for linear stability of the discretized equation set are put forth.

We follow the notation of the prototype system discussed in the previous section for the subsequent development of the equations for the dynamic model. The positions of the system boundaries are now taken to be time-dependent, and, in dimensional quantities, the crystal shape is denoted by a time- and position-dependent radius $\tilde{R}(\tilde{z},t)$, for $\tilde{H}_0(\tilde{R},t)\leq\tilde{z}\leq\tilde{Z}(t)$. The solidification front is given as $\tilde{H}_0(\tilde{r},t)$, and the melt and encapsulant menisci are represented as $\tilde{H}_1(\tilde{r},t)$ and $\tilde{H}_2(\tilde{r},t)$. The additional geometrical quantities are the height of the crystal, $Z(t)$, and the melt volume, $\tilde{V}_m(t)$, and the crystal is pulled from the melt at a rate of $V_p(t)$. A schematic diagram of the fully transient system is shown in Fig. 2.4.

As in the steady formulation, we choose a characteristic length

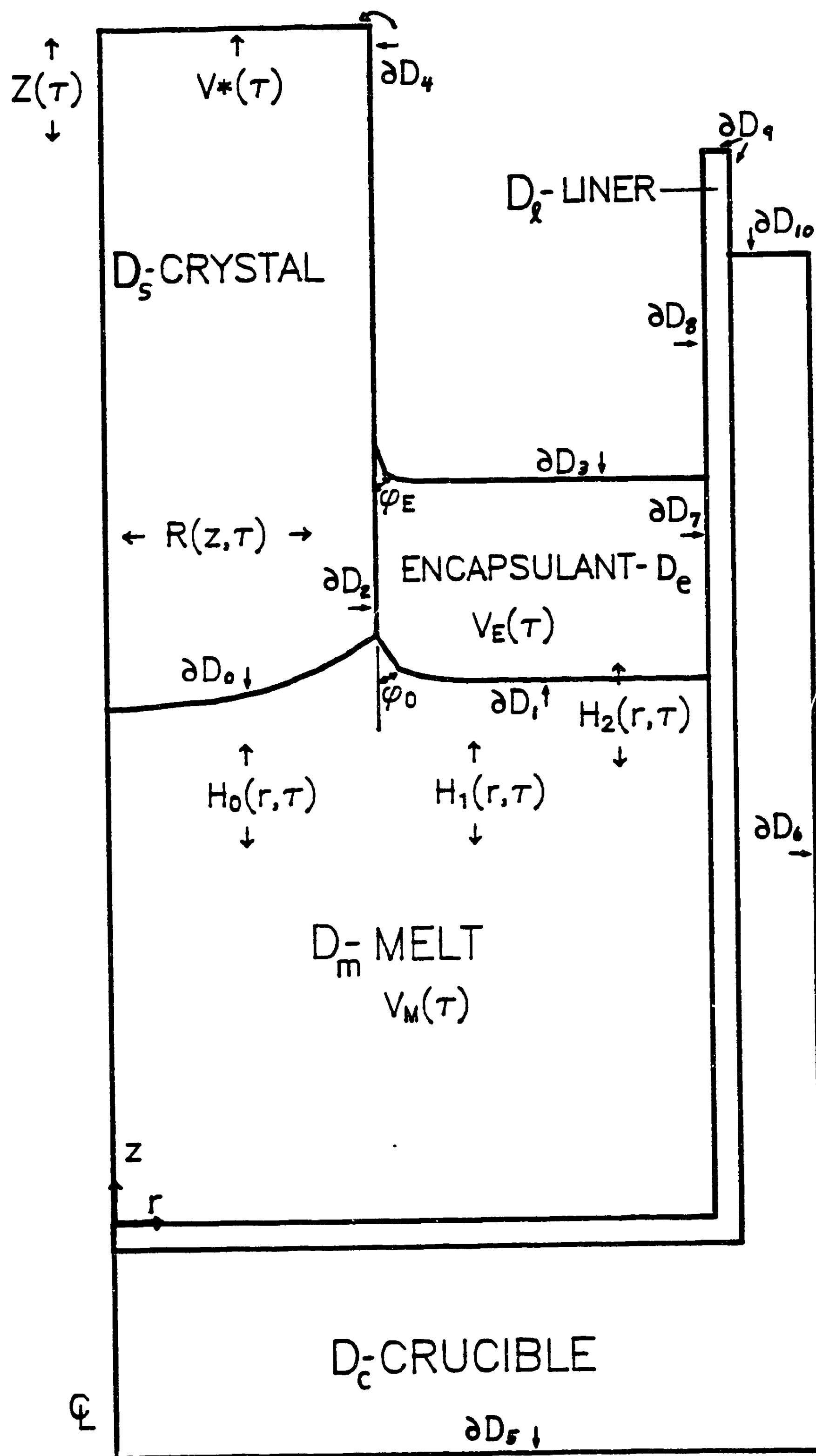

Fig. 2.4 Schematic diagram for fully transient thermal-capillary model.

which corresponds to the radius of the crucible, R_c, and the time constant is based on a characteristic velocity V_0 representative of a nominal pull rate. Thus we scale the dimensionless time as $\tau = V_0 t/R_c$, and the dimensionless pull rate is set as $V^*(\tau) = V_p(t)/V_0$. Temperatures in the system are normalized by the melting point of the semiconductor material, T_f, and $\Theta(r,z,\tau) = T(\tilde{r},\tilde{z},t)/T_f$. A complete list of variables and dimensionless groups is included in the Nomenclature section of Appendix A.

With the assumption that heat transfer is axisymmetric and is dominated by conduction in the melt and encapsulant, the energy balances become:

$$Pe_s\left[\frac{\partial\Theta}{\partial\tau} + V^*(\tau)\frac{\partial\Theta}{\partial z}\right] = \nabla\cdot(K_s(\Theta)\nabla\Theta) \text{ , for the crystal,} \quad (2.20)$$

$$Pe_i\frac{\partial\Theta}{\partial\tau} = \nabla\cdot(K_i(\Theta)\nabla\Theta) \text{ , for } i= m,e,\ell,c, \quad (2.21)$$

where Pe_i is the dimensionless Peclet number and K_i is a thermal conductivity ratio which can be a function of temperature. The Peclet number weights the time derivative of the energy balance according to the different characteristic heat transfer times in each phase. Note that in line with our assumption of conduction-dominated heat transfer in the melt and encapsulant, the second term of eq. (2.20), which represents convection caused by the solid-body motion of the pulled crystal, is not included in eq. (2.21), the corresponding energy balance for all other regions.

The temperature field described by eqs. (2.20-2.21) is continuous between different regions and fluxes are prescribed at all external

surfaces as in the steady-state formulation of eq. (2.7). The only difference in the form of these fluxes for transient case arises from the time-varying shape of the crystal. Now the outward-pointing normal to the radius (surface ∂D_4) is given by

$$\mathbf{n} = \frac{\mathbf{e}_r - R_z \mathbf{e}_z}{(1+R_z^2)^{1/2}} , \qquad (2.22)$$

where $R_z \equiv \partial R/\partial z$.

At the solidification front, heat is liberated by the crystallization phase change and is included as a flux term along the melt/solid interface. This condition for the transient equation set differs from eq. (2.5) for the steady formulation since time-dependent perturbations to the local solidification rate must be included. This effect is accounted for by the extra term involving $\partial H_0/\partial \tau$ on the right hand side of the new interface condition,

$$K_m(\mathbf{n}\cdot\nabla\Theta)_m - K_s(\mathbf{n}\cdot\nabla\Theta)_s = Pe_s S[V^*(\tau) - \frac{\partial H_0}{\partial \tau}](\mathbf{n}\cdot\mathbf{e}_z) . \qquad (2.23)$$

The dynamic radius of the crystal is represented as $R(z,\tau)$ and is specified by the kinematic equation,

$$\frac{\partial R}{\partial \tau} + V^*(\tau)\frac{\partial R}{\partial z} = 0 , \qquad (2.24)$$

so that the crystal shape is convected upward by the pull rate $V^*(\tau)$, which can be a time-dependent parameter. This specification of the radius can also be interpreted as setting the convected derivative of the crystal shape $DR/D\tau$ (see Bird et al., 1960) to zero so that the shape remains constant in a frame of reference moving along with

the crystal. The radius of the crystal emerging from the melt is specified by a dynamic condition which depends only upon the wetting angle formed by the meniscus and crystal,

$$\left.\frac{\partial R}{\partial \tau}\right|_{z=H_0(R,\tau)} = [V^*(\tau) - \left.\frac{\partial H_0}{\partial \tau}\right|_{r=R(H_0,\tau)}]\tan(\tilde{\phi} - \tilde{\phi}_0) \;, \qquad (2.25)$$

where $\tilde{\phi}$ is the dynamic angle of the meniscus contacting the crystal and $\tilde{\phi}_0$ is the equilibrium wetting angle for constant-diameter growth. Figure 2.5 shows the geometric details of the tri-junction and these angles. We can represent the contact angle in terms of the shape of the melt meniscus at the tri-junction as follows,

$$\mathbf{e}_r \cdot \mathbf{n}_1 = \cos \tilde{\phi} \;, \qquad (2.26)$$

$$\mathbf{e}_z \cdot \mathbf{n}_1 = \cos(90^\circ - \tilde{\phi}) = \sin \tilde{\phi} \;, \qquad (2.27)$$

where $\mathbf{n}_1$ is the unit normal vector to the melt meniscus and $\mathbf{e}_r$ and $\mathbf{e}_z$ are unit coordinate vectors in the r and z directions. We use the expression for the unit normal vector given in eq. (2.7) and divide eq. (2.26) by eq. (2.27) to obtain,

$$\frac{\partial H_1}{\partial r} = -\cot \tilde{\phi} \;. \qquad (2.28)$$

This relation is then used to put the tri-junction equation solely in terms of $R(z,\tau)$, $H_0(r,\tau)$, and $H_1(r,\tau)$. The tri-junction equation, eq. (2.25) above, is derived from the contact angle observations explained previously in Section 2.2 and application of the kinematic condition at the tri-phase point. This condition was first used by Crowley

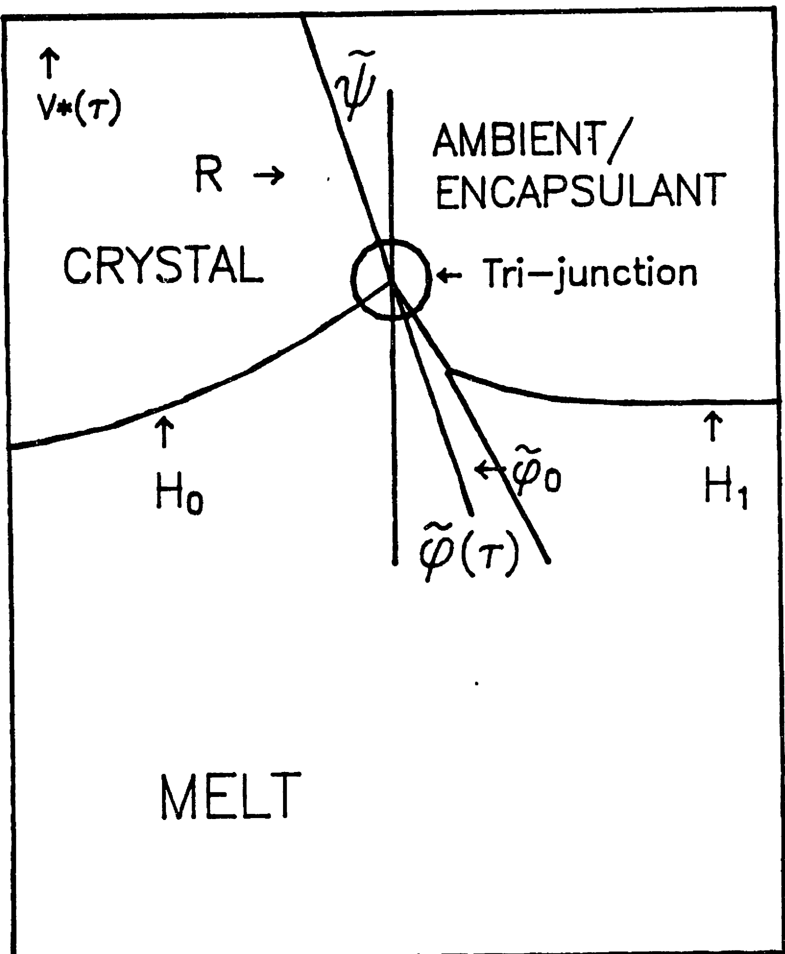

Crystal shape convected upwards,

$$\frac{\partial R}{\partial \tau} + V_*(\tau)\,\frac{\partial R}{\partial z} = 0$$

with condition at tri–junction,

$$\frac{\partial R}{\partial \tau} = V_{\text{tri-junction}} \tan \tilde{\psi}$$

$$= [V_*(\tau) - \partial H_0/\partial \tau]\, \tan(\tilde{\varphi}(\tau) - \tilde{\varphi}_0)$$

Fig. 2.5 Detail of tri-junction dynamics.

(1983) for describing the evolution of the radius in CZ crystal pulling. Note that in the case of $\tilde{\phi} = \tilde{\phi}_0$ the time derivative of the crystal radius is zero, and constant-diameter growth is achieved. We specified that this condition must hold in the distinguishing condition for crystal radius, eq. (2.19), of the steady-state model.

The melt/crystal interface and melt and encapsulant menisci are described by equilibrium relationships so that there are no explicit time derivatives in the governing equations. The dynamic equations which describe these interfaces are then identical to eqs. (2.11-2.12) of the steady-state model. In addition, the boundary conditions eqs. (2.16-2.18) remain the same. The only changes to the Young-Laplace equation are that the static head terms, $\lambda_i(\tau)$, are now time-dependent. The volume constraint for the melt takes on the same form as eq. (2.14) but now is time-dependent with $V_m(\tau)$. The volume constraint for the encapsulant is more complicated since the crystal is now a function of axial position and time and becomes,

$$\pi R^2(H_2(R,\tau),\tau) + 2\pi\int_{R(H_2(R,\tau),\tau)}^{1} H_2(r,\tau)r\,dr - \pi R^2(H_1(R,\tau),\tau) - 2\pi\int_{R(H_1(R,\tau),\tau)}^{1} H_1(r,\tau)r\,dr - \pi\int_{H_1(R(H_1,\tau),\tau)}^{H_2(R(H_2,\tau),\tau)} R^2(z,\tau)\,dz = V_e \quad (2.29)$$

Two more conditions are needed to completely specify the system; the rate of change of melt volume and the position of the top of the crystal must be specified. Note that these quantities were considered parameters for the steady-state model but now need to be included as variables since they change in time. The melt volume decreases

as melt passes through the material surface defined by the melt/crystal interface (∂D_0),

$$\frac{\partial V_m}{\partial \tau} = -2\pi \int_0^R \frac{\rho_s}{\rho_m} [V^*(\tau) - \frac{\partial H_0}{\partial \tau}] r dr \ . \qquad (2.30)$$

Finally, the crystal top position is given by the simple relation,

$$\frac{\partial Z}{\partial \tau} = V^*(\tau) \ , \qquad (2.31)$$

where the crystal top moves at the pull rate $V^*(\tau)$.

The initial solution for a transient run is obtained from the appropriate steady-state result from the model described in the previous section. This set of transient equations is quite challenging since it consists of partial differential equations which have no explicit time derivatives. These cases arise from the equilibrium isotherm condition for the melt/solid interface and the static capillary equations of the menisci. A numerical approach to the solution of these governing equations is employed, as described in Chapter 3, and details of transient simulation as well as stability calculations are contained in Chapter 5.

Chapter 3. Numerical Methods

The set of governing equations derived in Chapter 2 defines a nonlinear free-boundary problem (for the quasi-steady-state model) or moving-boundary problem (for the transient model), the complexity of which defies analytical solution and demands the use of numerical methods. The thermal-capillary model for crystal growth, with three unknown boundaries for the Czochralski system and four for the liquid encapsulated Czochralski system, taxes all previously developed solution techniques. In this chapter, we develop innovative numerical algorithms based on the finite element method which are used to accurately and efficiently solve this difficult problem.

We outline general concepts of the finite element method in Section 3.1 and follow with specific application to the quasi-steady-state and transient models in Sections 3.2 and 3.3, respectively. In these sections, we present the details of discretizing the equations put forth in Chapter 2 and outline the application of the powerful Newton-Raphson solution method. Building upon both models and Newton's method, in Section 3.4 we introduce the formulation of linear stability criteria which are used to determine the nature of quasi-steady solutions calculated for the CZ and LEC processes. The mathematical tools developed in this chapter enable the complete characterization of the model systems,

and the results from the models for CZ and LEC growth are presented and discussed in following chapters.

3.1 Finite Element Method

The finite element method was originally developed by structural engineers as a tool to solve the equations of elasticity and structural mechanics (Zienkiewicz, 1971). Since then it has been successfully applied to a great number of other problems, including the equations of transport for species, heat, and momentum (Gallagher et al., 1975; Finlayson, 1980). In addition to successes in the practical use of the finite element method, mathematical theory exists that explains the convergence of various versions of the method for classes of elliptic and parabolic problems defined on fixed domains (Strang and Fix, 1973).

The basic philosophy underlying the finite element method is to approximate the solution of partial differential equations, such as those posed in this work, with low-order polynomial interpolating functions which are defined in a piecewise manner over small portions of the domain. Since the interpolating functions are constructed on a simple geometrical element, the formulation, solution, and application of boundary conditions for the problem are relatively easy. The approximating power of the method increases with the number of unknowns and the degree of discretization. However, the difficulty of formulation is virtually independent of these gains in accuracy since increasing the degree of discretization merely requires that the same basic elemental formulation algorithm be repeated for a greater number of elements.

These aspects make the finite element method well-suited to programming on a computer.

The finite element method is a way of discretizing a mathematical continuum problem into simpler component parts. The discretized problem is readily solved, and thus the method enables one to solve problems whose complexity prohibits analytical solutions. The formulation and solution of a discretized continuum problem is briefly described here. Following the notation presented by Zienkiewicz (1971), we represent a set of differential equations satisfied by a function **u** as

$$\mathbf{A}(\mathbf{u}) = \mathbf{0} \,, \tag{3.1}$$

with boundary conditions

$$\mathrm{B}(\mathbf{u}) = \mathbf{0} \,. \tag{3.2}$$

The discretized solution is given in general terms as

$$\mathbf{u} \cong \hat{\mathbf{u}} = \sum N^i a_i = \mathbf{Na} \,, \tag{3.3}$$

where **u** represents the solution to the continuum problem, $\hat{\mathbf{u}}$ is the approximation to **u** in the discretized problem, **N** is a vector of chosen interpolating functions (usually polynomials), and **a** is the vector of unknown parameters which must be determined so as to minimize the error of the discrete solution $\hat{\mathbf{u}}$. The notation **Na** stands for the standard inner product in $\mathbb{R}^n$.

We seek to determine the unknown parameters **a** by solving the integral equation

$$\int \mathbf{v}\, \mathbf{A}(\hat{\mathbf{u}})\, dV + \int \mathbf{v}\, \mathrm{B}(\hat{\mathbf{u}})\, dS = \mathbf{0} \,, \tag{3.4}$$

where the integrals are performed over the physical volume and surfaces of the problem domain and **v** is a set of arbitrary weighting functions equal to the number of unknowns. If the integral equation (3.4) holds for all **v** then the differential equations and boundary conditions, eqs. (3.1) and (3.2), will also be satisfied (Zienkiewicz, 1971). The set of conditions used to determine the unknowns, eq. (3.4), are called residual equations, and this technique of approximating the continuum solution is the general method of weighted residuals as discussed at length by Finlayson (1972). For the work presented here, the weighting functions are chosen to be the interpolating functions, $v_i = N_i$, and is known as the Galerkin weighting method. For problems where natural variational principles exist, the Galerkin weighting method will give the same answer as the variational procedure; furthermore, in comparison with other weighted residuals methods, this answer will be the most accurate approximation by the chosen shape function basis set **N** and the parameters **a** to the continuum solution (Zienkiewicz,1971; Strang and Fix, 1973).

In the implementation of the finite element method, the physical domain of the problem is subdivided into elements which constitute a mesh over which piecewise interpolating polynomials are defined. The solution f(r) for a one-dimensional problem is then approximated as a sum of the interpolating functions $\{\Psi^i(r)\}$ as

$$f(r) = \sum_{i=1}^{N} \beta_i \, \Psi^i(r) \quad , \tag{3.5}$$

with N as the number of nodes used to define the mesh. In each element the basis functions are represented by elemental polynomials $\{\psi^i(\xi)\}$

expressed in the transformed coordinate ξ ,$-1\le\xi\le1$, as follows:

$$f(r) = \sum_{i=1}^{3} \beta_{(i)}\psi^{i}(\xi) , \qquad (3.6)$$

where $\{\beta_{(i)}\}$ are the unit element values of the global coefficients $\{\beta_i\}$ from eq. (3.5). There are three elemental nodes for the quadratic Lagrangian basis functions used in this work. The forms of these elemental one-dimensional quadratic basis functions are shown in Fig. 3.1. The values of the coefficients directly interpolate the value of the function f(r) at the nodes. This is seen from the shapes of the basis functions of Fig. 3.1 where the value of ψ^i is one at the ith node and zero at all others.

The isoparametric mapping used to transform the global sum of eq. (3.5) to its elemental components of eq. (3.6) is

$$r = \sum_{i=1}^{3} r_i\psi^{i}(\xi), \qquad (3.7)$$

where r is the coordinate of the global system and the set $\{r_i\}$ are the positions of the elemental nodes. All calculations are carried out in the coordinate system ξ of the unit element. This technique allows for the easy formulation of the problem into elemental segments. The global elements are systematically mapped into the unit element, elemental contributions to the problem are summed, and calculations proceed until all elements have been accounted for.

In a similar manner, a two-dimensional function f(r,z) is approximated as

$$f(r,z) = \sum_{i=1}^{N} \alpha_i\Phi^{i}(r,z) , \qquad (3.8)$$

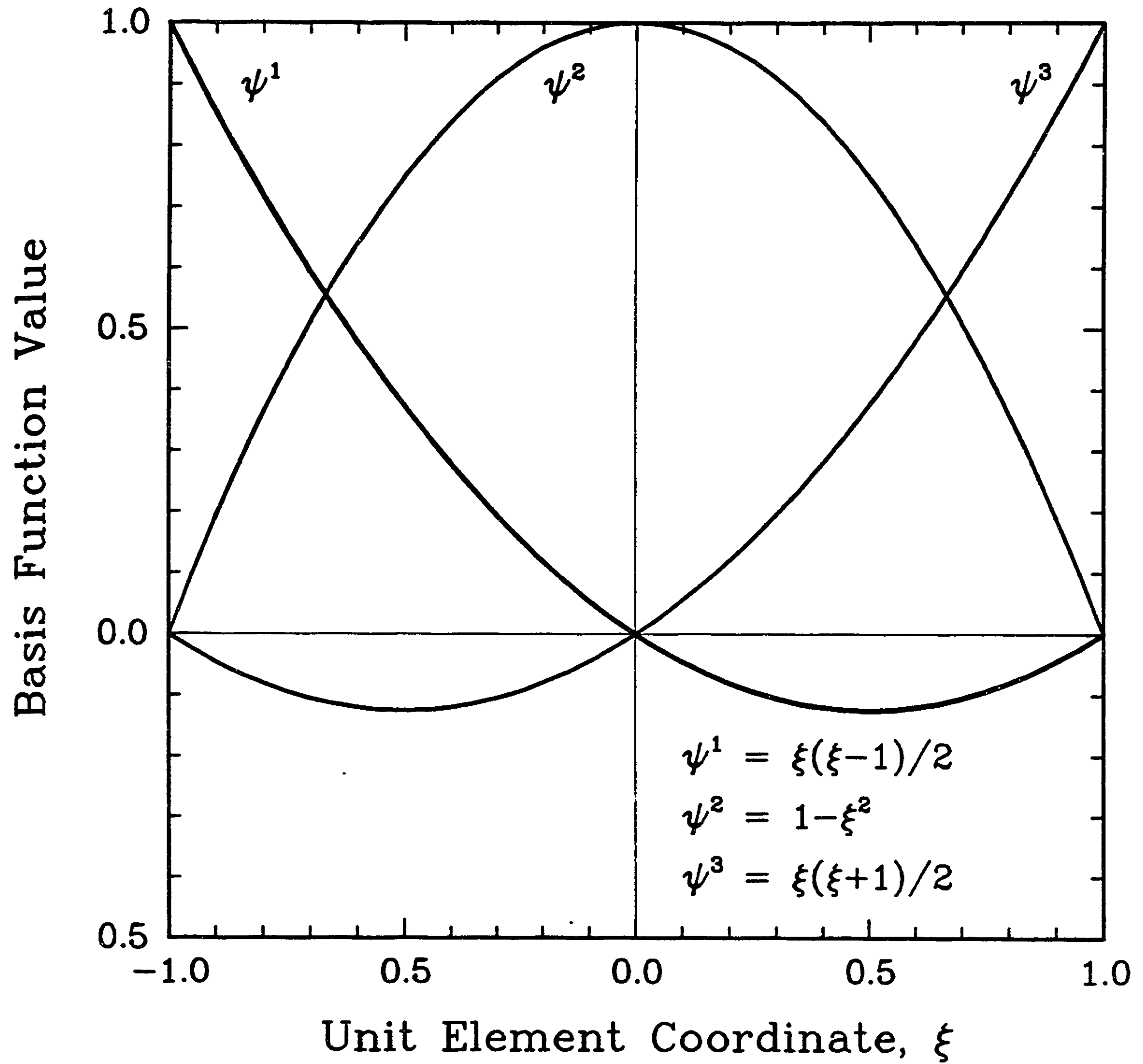

Fig. 3.1 Lagrangian quadratic basis functions in a unit element.

where $\{\alpha_i\}$ are the unknowns, $\{\phi^i(r,z)\}$ is the set of two-dimensional polynomial basis functions, and N is the total number of nodes defining the finite element mesh.

Within each element, the basis functions are mapped into a unit element defined in the coordinate system (ξ,η) where $(-1\leq\xi\leq1, -1\leq\eta\leq1)$ by an isoparametric transformation analogous to eq. (3.7). The elemental basis functions $\{\phi^i(\xi,\eta)\}$ used in this work are standard nine-constant biquadratic Lagrangian polynomials which are formed as the tensor products of the one-dimensional quadratic basis functions shown in Fig. 3.1. The functional forms of these basis functions are listed in Table 3.1. The function is interpolated within an element as

$$f(r,z) = \sum_{i=1}^{9} \alpha_{(i)}\phi^i(\xi,\eta) , \qquad (3.9)$$

where the $\{\alpha_{(i)}\}$ are the unit element values of the coefficients $\{\alpha_i\}$ associated with the nine-node element. The spatial coordinates of a point (ξ,η) are related to the cylindrical coordinate system (r,z) by the two-dimensional isoparametric transformation

$$r = \sum_{i=1}^{9} r_i\phi^i(\xi,\eta) , \qquad (3.10)$$

$$z = \sum_{i=1}^{9} z_i\phi^i(\xi,\eta) , \qquad (3.11)$$

where the set (r_i,z_i) are the locations of the nodes in the elements (Strang and Fix, 1973).

An important aspect of this two-dimensional biquadratic mapping is the increased ability over linear bases to approximate curved boun-

Table 3.1 Functional forms of Lagarangian biquadratic basis functions in unit element coordinate system.

2-dimensional basis function	Tensor product	Polynomial form
$\phi^1(\xi,\eta)$	$\psi^1(\xi)\psi^1(\eta)$	$\xi(\xi-1)\eta(\eta-1)/4$
$\phi^2(\xi,\eta)$	$\psi^2(\xi)\psi^1(\eta)$	$(1-\xi^2)\eta(\eta-1)/2$
$\phi^3(\xi,\eta)$	$\psi^3(\xi)\psi^1(\eta)$	$\xi(\xi+1)\eta(\eta-1)/4$
$\phi^4(\xi,\eta)$	$\psi^1(\xi)\psi^2(\eta)$	$\xi(\xi-1)(1-\eta^2)/2$
$\phi^5(\xi,\eta)$	$\psi^2(\xi)\psi^2(\eta)$	$(1-\xi^2)(1-\eta^2)$
$\phi^6(\xi,\eta)$	$\psi^3(\xi)\psi^2(\eta)$	$\xi(\xi+1)(1-\eta^2)/2$
$\phi^7(\xi,\eta)$	$\psi^1(\xi)\psi^3(\eta)$	$\xi(\xi-1)\eta(\eta+1)/4$
$\phi^8(\xi,\eta)$	$\psi^2(\xi)\psi^3(\eta)$	$(1-\xi^2)\eta(\eta+1)/2$
$\phi^9(\xi,\eta)$	$\psi^3(\xi)\psi^3(\eta)$	$\xi(\xi+1)\eta(\eta+1)/4$

daries. This is especially important for the solution of the thermal-capillary model since it is crucial to accurately approximate the locations of the free- and moving-boundaries and the conditions imposed along these boundaries. The edges of the quadrilateral elements are quadratic in shape, and the curved elements in the (r,z) coordinate system are mapped to a square element in the (ξ,η) coordinate system, as schematically shown in Figure 3.2. Another feature of this technique is that it locally maps the normal and tangential directions into the (ξ,η) coordinate system, thus leading to simple and accurate evaluation of boundary integrals; this is one of the advantages that the finite element method holds over finite difference methods. Finite element error analysis also establishes that the rate of convergence of the approximation by the discretized solution to the continuum solution is not reduced by the presence of boundary integrals (Strang and Fix, 1973). Again, this is especially important in the system of two-dimensional energy equations coupled with the one-dimensional interface shape equations in the thermal-capillary model.

3.2 Quasi-Steady-State Formulation

Much of the groundwork for the development of the solution technique presented in this section is contained in Ettouney (1983) and Chang (1982) for the finite element modeling of other solidification problems. Before we examine the details of the thermal-capillary model for CZ and LEC growth, a review of the modeling issues of these works is appropriate. Chang (1982) modeled the effects of free convection

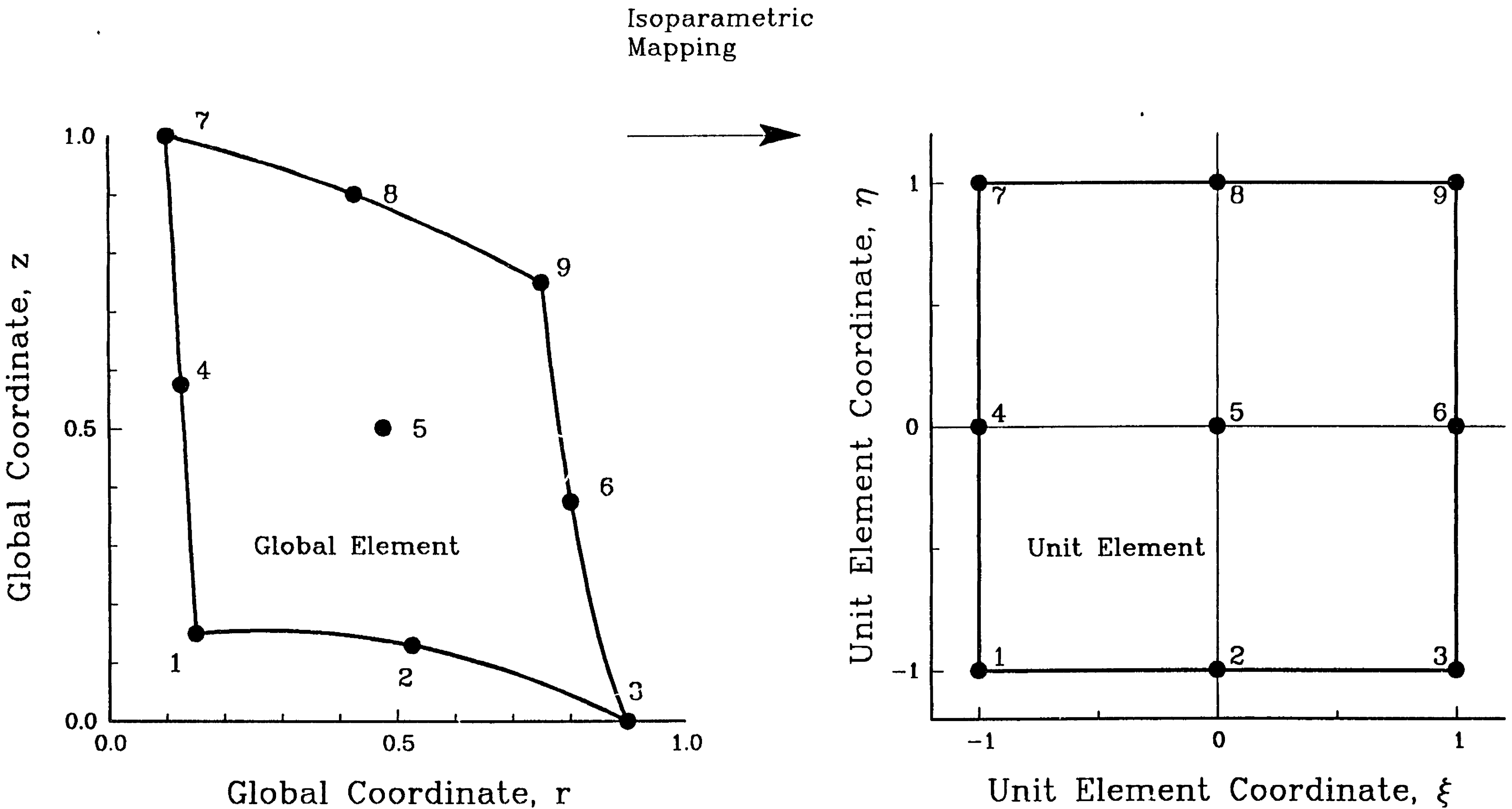

Fig. 3.2 Isoparametric mapping of a biquadratic element.

in the Bridgman-Stockbarger crystal growth system, and Ettouney (1983) examined similar transport phenomena in the edge-defined film-fed (EFG) crystal growth process.

The major issue faced by both researchers was how to accurately and efficiently locate the position of the melt/crystal interface in these solidification systems. Mathematically posed, this issue is how one distinguishes the unknown position of the free boundary while also solving for the field variables. The most desirable method was determined to be the Newton/Isotherm technique as put forth by Ettouney and Brown (1983). In this scheme, the melting-point isotherm is used to implicitly locate the position of the melt/crystal interface and the latent heat flux condition at the interface is specified as a boundary condition for the temperature field. This choice of shape distinguishing condition and field boundary condition was found to yield the most accurate results in a model solidification problem, a result confirmed later in a transient solidification problem by Lynch and Sullivan (1985).

Another innovation introduced by Ettouney and Brown (1983) was the iteration technique used to solve for the nonlinear free-boundary problem. While successively iterating between the temperature field calculations and the determination of interface position yielded a converged solution, a Newton-Raphson procedure which solved simultaneously for the interface and the temperature field proved much more efficient. The Jacobian matrix entries for the Newton-Raphson procedure were calculated analytically after the free boundary was mapped into a fixed domain by a coordinate transformation which was

a function of the interface position (as originally done in a one-dimensional solidification problem by Landau, 1950).

An additional complexity addressed in the work of Ettouney (1983) was the determination of the location of the melt meniscus in EFG growth. He handled this problem in a similar manner as for the solidification interface. By mapping the entire domain into a coordinate system where all free boundaries were immobilized and applying the Newton-Raphson method, he successfully solved for all interfaces and the temperature field simultaneously.

Chang (1982) took advantage of the local mapping features of the finite element method used with the isoparametric basis set and recast the Newton/Isotherm method for use in the original, untransformed coordinate system. In this method, a global mapping to immobilize the free boundary was not necessary; instead, the Jacobian entries needed for Newton's method were obtained directly from analytical differentiation of the discretized equation set. This technique was also used by Saito and Scriven (1981) in a study of a coating flow where the fluid surface was a free boundary. There are no differences in the results of these methods, the global boundary-immobilization mapping and the local elemental mapping combined with the Newton-Raphson procedure both yield accurate, efficient convergence for free-boundary problems.

The work presented here takes advantage of the local elemental mapping techniques put forth by Chang (1982) in a meniscus-defined solidification problem similar to the EFG system of Ettouney (1983), so we are in a position to benefit from both of these past works.

The details of implementation will be outlined below as we continue with the development of the finite element/Newton/Isotherm method applied to our thermal-capillary model for CZ and LEC growth.

3.2.1 Discretization by the Galerkin Finite Element Method

The regions of melt, crystal and encapsulant are divided into quadrilateral elements as shown in Fig. 3.3 for approximate locations of the three interfaces and the crystal radius. The finite element mesh is defined so that the unknown interfaces always fall along rows of nodes. The one-dimensional interface approximations define the edges of the biquadratic quadrilateral elements discussed above. In the iteration procedure used to solve the nonlinear equations which describe the field and boundary shape equations, the mesh deforms to follow the interfaces as the correct solution is approached. Following the classical finite element method, a continuous temperature field is defined over the regions of the system using biquadratic basis functions $\{\Phi^i(r,z)\}$ as follows:

$$\Theta(r,z) = \sum_{i=1}^{N_\theta} \alpha_i \Phi^i(r,z) \; , \tag{3.12}$$

where N_θ is the number of nodes in the two-dimensional mesh and the coefficients $\{\alpha_i\}$ are the interpolated temperatures of the nodes. These unknowns constitute a subset the entire solution vector since the interface positions must also be solved.

The energy balances in each phase are discretized by the Galerkin finite element method. In this technique the inner product is formed

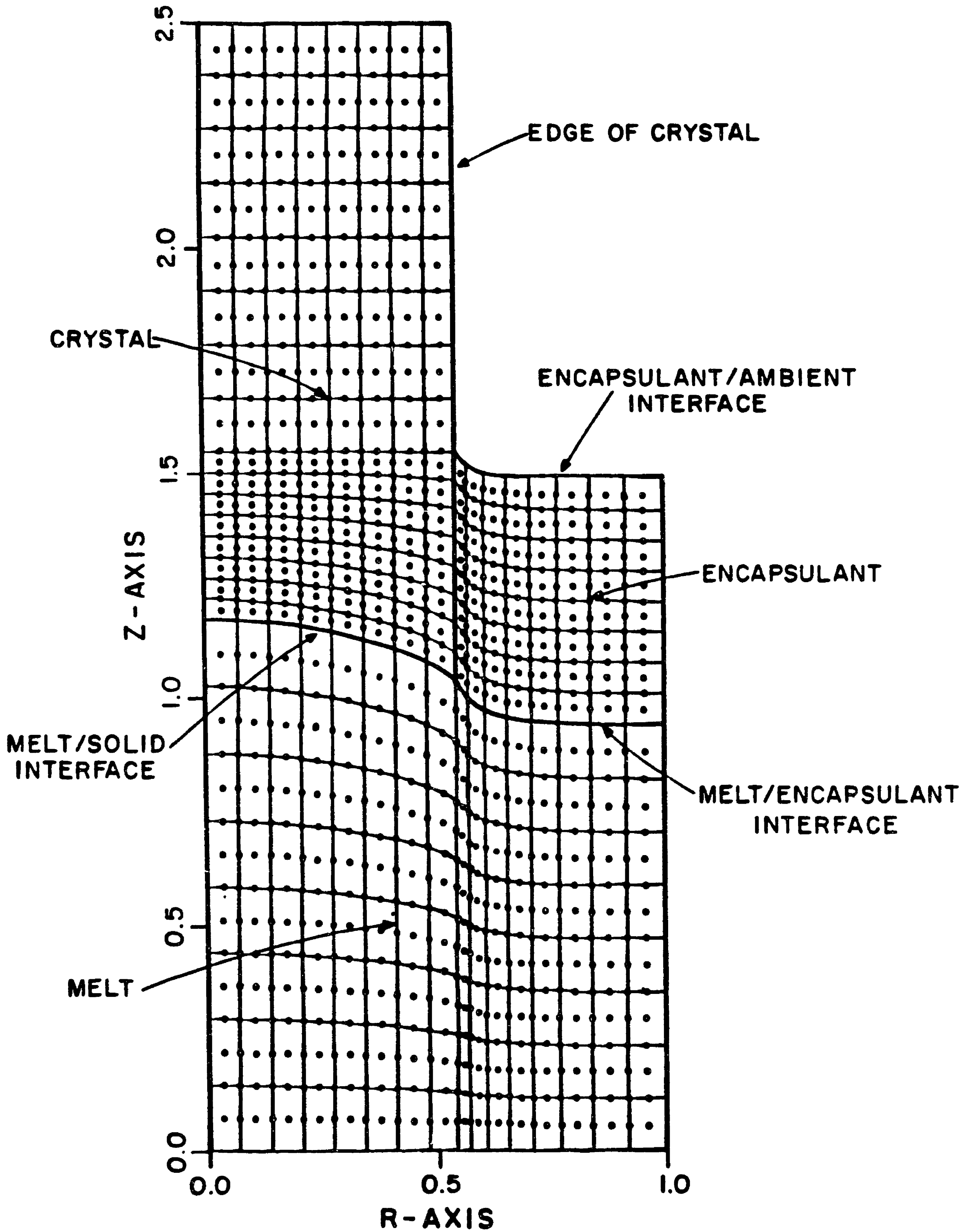

Fig. 3.3 Sample finite element mesh for converged solution.

by integrating the product of the differential equation and each finite element basis function over the physical domain, thus yielding the following set of N_θ equations,

$$\int_{D_k} \Phi^i\{\nabla\cdot(K_k(\Theta)\nabla\Theta)\}\,dV - \int_{D_s} \Phi^i\{Pe_s(e_z\cdot\nabla\Theta)\}\,dV = 0$$

$$\text{for } k=m,s,e,\ell,c\ , \quad i=1,N_\theta \quad . \tag{3.13}$$

We transform this equation by operating on the term involving second derivatives. We integrate by parts,

$$\int \Phi^i\{\nabla\cdot(K_k\nabla\Theta)\}\,dV = -\int \{\nabla\Phi^i\cdot(K_k\nabla\Theta)\}\,dV + \int \{\nabla\cdot(\Phi^i K_k\nabla\Theta)\}\,dV, \tag{3.14}$$

and then apply the divergence theorem to the last term on the right-hand side,

$$\int \Phi^i\{\nabla\cdot(K_k\nabla\Theta)\}\,dV = -\int \{\nabla\Phi^i\cdot(K_k\nabla\Theta)\}\,dV + \int \Phi^i K_k(\mathbf{n}\cdot\nabla\Theta)\,dS, \tag{3.15}$$

where the last term on the right-hand side is now a boundary integral with $\mathbf{n}$ denoting the outward-pointing normal to the surface. This technique transforms the differential equations into the weak form (Zienkiewicz, 1971; Strang and Fix, 1973) and allows for the use of a lower-order interpolating basis set by reducing the order of the original differential equations. In fact, the basis functions are required only to be continuous across elements and once-differentiable within an element; continuous first or second derivatives across elements

are not necessary.

We can now easily include the boundary conditions in the weighted residual equations by substituting the expressions for surface fluxes into the boundary integral in eq. (3.15) which arises from the application of the divergence theorem the last term of eq. (3.14). Substituting the result of eq. (3.15) with the boundary conditions into the original integral equation (3.13), we obtain a set of integral equations in terms of the coefficients for temperature and interface shape. These equations are

$$-\int_{D_k} K_k \nabla\Phi^i \cdot \nabla\Theta \, dV - \int_{D_s} Pe\Phi^i \frac{\partial\Theta}{\partial z} \, dV + \int_{\partial D_0} PeS\Phi^i (\mathbf{n}_0 \cdot \mathbf{e}_z) \, dS$$

$$-\sum_j \int_{\partial D_j} [Bi_j \Phi^i (\Theta - \Theta_a) + Ra_j \Phi^i (\Theta^4 - \Theta_a^4)] \, dS = 0,$$

$$\text{for } k = m,s,e,\ell,c \, , \quad j = 1,\dots 10 \, , \quad i = 1,\dots N_\theta \, , \qquad (3.16)$$

where the subscript k denotes the domain, j specifies the domain surface as laid out in Chapter 2, Fig. 2.3, and i represents the temperature unknown number. This equation set is nonlinear because of the term Θ^4 in the radiation condition and because of the implicit dependence of the basis functions and the Galerkin integrals on the interface shapes. This set of N_θ integral equations is assembled element by element and evaluated using numerical nine-point Gaussian quadrature for volume integrals and three-point Gaussian quadrature for the surface integrals.

Three-point Gaussian quadrature in the one-dimensional line integral guarantees exact evaluation for polynomial functions of fifth degree or lower (Dahlquist and Bjorck, 1974). Similarly, nine-point quadrature for the area integrals will give exact answers for fifth degree or lower polynomials defined in either coordinate direction. Since we use quadratic and biquadratic basis functions (second degree polynomials along coordinate axes), we are assured that there is no error in evaluating the integrals numerically. This evaluation procedure is greatly simplified by the piecewise nature of the basis functions $\{\Phi^i\}$. Since each function is nonzero only over a patch of elements spanning a small portion of the entire domain, only a few elemental contributions need be calculated for each equation. This feature, characteristic of finite element and finite difference approximation methods, is also known as compact support.

For some of the earlier simulations, the regions of liner and crucible were not included, and the melt temperature adjacent to the crucible wall was prescribed. In these cases the coefficients $\{\alpha_i\}$ for the nodes along the inner crucible wall were set at a specified value,

$$\alpha_i = \Theta_c \text{ , for i=wall nodes.} \tag{3.17}$$

These are essential boundary conditions (Zienkiewicz, 1971; Strang and Fix, 1973), and the values $\{\alpha_i\}_{wall}$ are not determined by the Galerkin weighting procedure described above; they are simply set to interpolate the prescribed boundary values. For the Lagrangian basis functions used in this work, the essential boundary condition

is interpolated by setting the values of the nodes which fall along the boundary to the prescribed values.

In a similar manner, we represent the shapes of the interfaces with one-dimensional quadratic Lagrangian basis functions (Finlayson, 1980) as,

$$H_0(r) = \sum_{i=1}^{N_0} \beta_{0_i} \Psi^i(r) , \tag{3.18}$$

$$H_1(r) = \sum_{i=1}^{N_1} \beta_{1_i} \Psi^i(r) , \tag{3.19}$$

$$H_2(r) = \sum_{i=1}^{N_2} \beta_{2_i} \Psi^i(r) , \tag{3.20}$$

where N_0, N_1, and N_2 are the number of nodes defining interfaces H_0, H_1, and H_2, the coefficients $\{(\beta_0, \beta_1, \beta_2)_i\}$ denote the nodal values of the interfaces, and $\{\Psi^i(r)\}$ is the set of one-dimensional basis functions. We have assumed in this representation that the shapes of the interfaces can be described as functions of r only. This assumption is valid as long as the interfaces are single valued in r and the slope of the interfaces, dH_i/dr, is not infinite.

This assumption is generally valid for the Czochralski system; the axial temperature gradient induced by a hot melt below and a cool ambient above promotes a horizontally-oriented melt/crystal interface shape, and the action of gravity on the surface of the melt coupled with a non-zero equilibrium growth angle for the melt meniscus and a non-zero wetting angle for the encapsulant meniscus also ensure single-valued melt/ambient and encapsulant/ambient interfaces. A breakdown of this representation is possible if there are large axial

variations in the radius of the crystal and the meniscus is forced to pin to a severely outward-sloping crystal surface, as happens, for example, when the crystal is melting inward at a fast rate during growth. However, this event rarely occurs in practice, and if modeling this situation proves necessary or desirable, it could be treated by a polar coordinate transformation similar to that employed by Saito and Scriven (1981).

The melt/crystal and meniscus interface shapes are determined from the Galerkin integrals formed from the isotherm condition and the Young-Laplace equations, respectively. In addition, the Young-Laplace equations incorporate the pinning condition of the melt to the crystal and the wetting angle conditions for the slope of the meniscus at the crucible wall and at the crystal side for the encapsulant meniscus. The Galerkin equations for the melt/solid interface H_0 are

$$\int_0^R \Psi^i[\theta(r,H_0(r))-1]\, r dr = 0, \qquad (3.21)$$

where $i=1,N_0$. The Young-Laplace equation for the melt meniscus H_1 is expressed in the weak form with the pinning condition serving as an essential boundary condition as

$$-\int_R^1 \left\{\frac{\frac{\partial\Psi^i}{\partial r}\frac{\partial H_1}{\partial r}}{[1+(\frac{\partial H_1}{\partial r})^2]^{1/2}} + Bo_1\Psi^i(H_1+\lambda_1)\right\} r dr = 0, \qquad (3.22)$$

for $i=1,N_1$. The equation for the encapsulant/ambient meniscus for

H_2 is similarly put into the weak form with the wetting condition at the crystal:

$$-\int_R^1 \left\{ \frac{\frac{\partial \Psi^i}{\partial r} \frac{\partial H_2}{\partial r}}{[1+(\frac{\partial H_2}{\partial r})^2]^{1/2}} + Bo_2 \Psi^i (H_2 + \lambda_2) \right\} r dr$$

$$+ \frac{\Psi^i R \cot \tilde{\phi}_e}{[1+\cot^2 \tilde{\phi}_e]^{1/2}} = 0. \qquad (3.23)$$

The volume constraints,

$$\int_0^R H_0(r) r dr + \int_R^1 H_1(r) r dr = V_m/2\pi \ , \qquad (3.24)$$

$$\int_R^1 (H_2(r) - H_1(r)) r dr = V_e/2\pi \ , \qquad (3.25)$$

and the condition for the equilibrium growth angle,

$$\left. \frac{\partial H_2}{\partial r} \right|_{r=R} = -\cot \tilde{\phi}_e \ . \qquad (3.26)$$

form the remaining residual conditions. The volume constraints are used to determine the reference pressure differences $\{\lambda_i\}$ in the Young-Laplace equations, and the equilibrium growth angle condition serves to set the crystal radius. These points were discussed at length in the derivation of the governing equations in Chapter 2.

3.2.2 Iterative Solution with the Newton-Raphson Method

The complete set of the nonlinear algebraic residual equations is represented in vector notation as a function $\mathbf{F}$,

$$\mathbf{F}(\mathbf{y}) = \mathbf{F}(\boldsymbol{\alpha},\boldsymbol{\beta},R,\boldsymbol{\lambda}) = \mathbf{0}, \tag{3.27}$$

where the entire vector of unknowns is $\mathbf{y}^T = (\boldsymbol{\alpha}^T,\boldsymbol{\beta}^T,R,\boldsymbol{\lambda}^T)$ = (temperature unknowns, interface unknowns, crystal radius, reference pressures), with the superscript T denoting the transpose of the vector. In this form the coupling between the temperature field and the shapes of the phases is obvious, as is the extreme difficulty with convergence that one would expect with any iterative method for the solution which tries to satisfy the equations successively. Here is where we apply the knowledge gained from the work of Ettouney (1983) and Chang (1982). Newton's method has proven its prior utility in these free-boundary problems and is the most rational choice for use here. We therefore iterate simultaneously for the entire solution vector $\mathbf{y}$ with the Newton-Raphson method.

Since this method is iterative, we choose an initial guess for the temperature field and interface shapes, $\mathbf{y}^{(0)}$, and update this guess until a converged solution is obtained. We measure the degree of convergence by monitoring the norm of the residuals vector $\mathbf{F}(\mathbf{y})$, and a converged solution is usually taken to be one where this norm is zero within the constraints of machine accuracy. At each iteration, the solution vector is updated according to the formula

$$\mathbf{y}^{(k+1)} = \mathbf{y}^{(k)} + \mathbf{J}^{-1}\mathbf{F}(\mathbf{y}^{(k)}) \ , \tag{3.28}$$

where $\mathbf{y}^{(k+1)}$ is the new solution vector, $\mathbf{y}^{(k)}$ is the approximation to the solution vector from the previous iteration, and J^{-1} is the inverse of the Jacobian matrix. The Jacobian matrix J has components $J_{ij}=\partial F_i/\partial y_j$ which represent the sensitivity of the residuals vector to perturbations in the solution vector and are obtained by analytical differentiation of the residual equations. The structure of the dependence of the residual equations on the temperature and interface unknowns gives J the "arrow" structure shown schematically in Fig. 3.4.

The most difficult Jacobian entries to determine are those which represent the sensitivity of the temperature field to changes in the positions of the interfaces. These entries are contained in the column vectors which make up the right-hand side of the Jacobian matrix, as pictured in Fig. 3.4. We choose to calculate these entries by the method put forth by Chang (1982); below, we present the practical differences between this elemental method and the global mapping method pioneered by Ettouney (1983).

We represent the residual equations of the Galerkin finite element problem in general terms as

$$\int_{D(\text{interfaces})} \boldsymbol{\Phi}^T \mathbf{A}(\hat{\mathbf{u}})\, dV = \mathbf{0} \;, \tag{3.29}$$

where $\boldsymbol{\Phi}$ is the set of basis functions, $\mathbf{A}(\hat{\mathbf{u}})$ is the discretized differential equation set, and the volume integral is taken over the entire physical domain D whose shape is given by the locations of the system interfaces. In the global mapping technique used by Ettouney (1983), we transform the original differential equation set into a domain where the boundaries

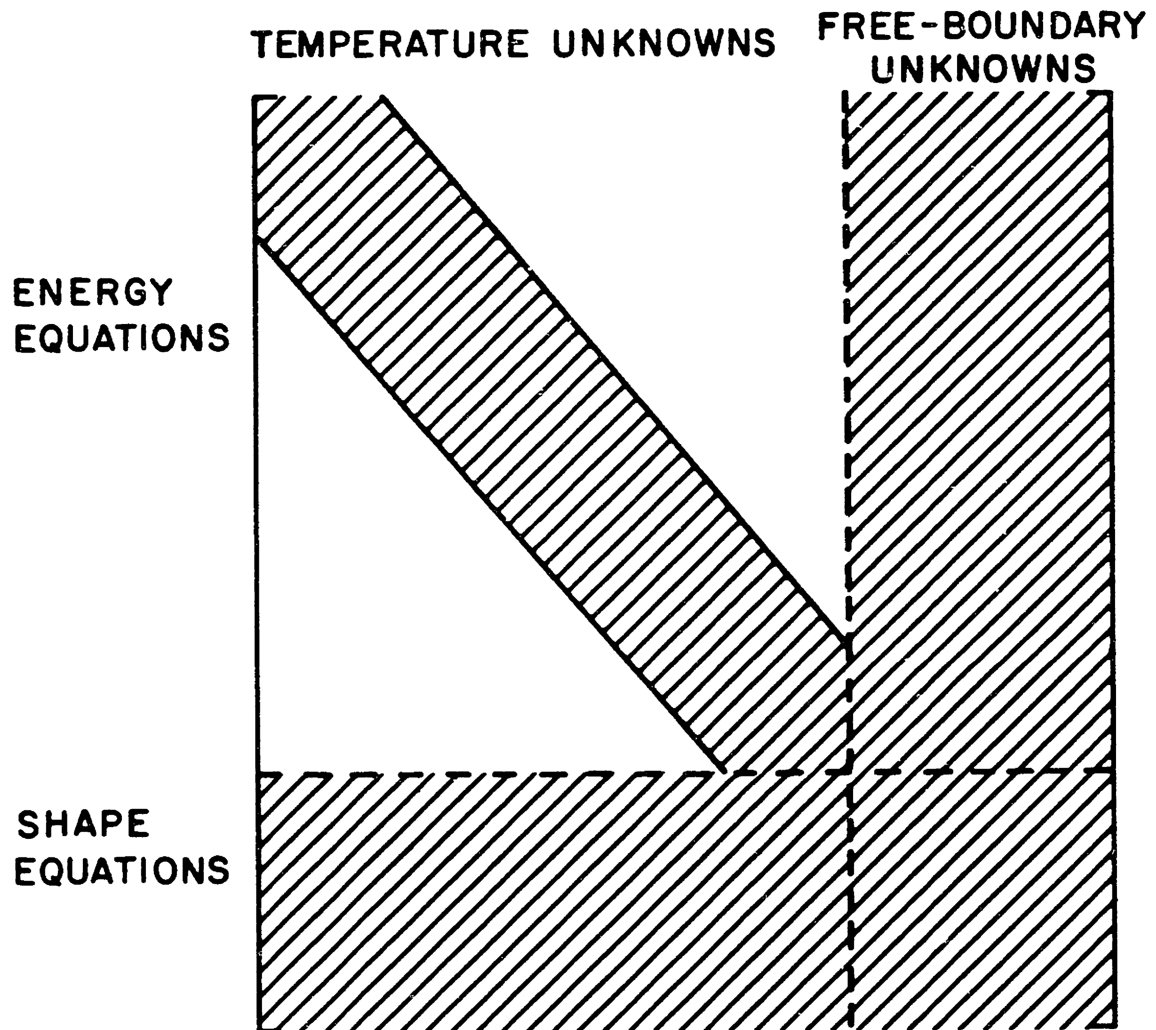

Fig. 3.4 Characteristic "arrow" structure of Jacobian matrix for a free-boundary problem.

are immobilized. The original residual equations then take the following form,

$$\int_{\tilde{D}_{fixed}} \Phi^T \tilde{A}(\hat{u})\, d\tilde{V} = 0 \,, \tag{3.30}$$

where $\tilde{A}(\hat{u})$ is the set of transformed differential equations in the new domain $\tilde{D}_{fixed}$. The implicit dependence of the original integral equation (3.29) on the shape of the domain now manifests itself in explicit form in the transformed differential equation set over the fixed domain. The Jacobian entries for the sensitivity of the solution with respect to interface position are determined in closed form by differentiation of the new equation set $\tilde{A}(\hat{u})$.

In the method used here, the sensitivity of the residual equations to the locations of the interfaces accounts for the effects on the basis functions of displacing the finite element mesh and are computed by the isoparametric mapping technique suggested by Chang (1983). This technique is also detailed in the work of Saito and Scriven (1981) and Chang and Brown (1983a). We represent the concept of this method as follows. In the actual implementation of the finite element method, the Galerkin discretized equations are integrated over each element as

$$\int_{D(interfaces)} \Phi^T A(\hat{u})\, dV = \sum_{e=1}^{N} \int_{D_e} \Phi^T A(\hat{u})\, dV_e = 0 \,, \tag{3.31}$$

where the index e represents element number and D_e is the volume enclosed by element e.

We still have the problem that the elemental integrals depend implicitly on the shape of the interfaces; however, this difficulty is overcome by the next step of the finite element method. We evaluate each elemental integral by mapping it into the fixed (ξ,η) coordinate system,

$$\int_{D_e} \boldsymbol{\phi}^T \mathbf{A}(\hat{\mathbf{u}}(r,z))\, dV_e = \int_{\tilde{D}_{e,fixed}} \boldsymbol{\phi}^T \mathbf{A}(\hat{\mathbf{u}}(\xi,\eta))\,|J_e|\, d\tilde{V}_e = \mathbf{0}\ , \qquad (3.32)$$

where $\boldsymbol{\phi}$ are the basis functions on the unit element and J_e is the transformation Jacobian which describes how the shape of the original volume integral is translated into the unit element. The transformation Jacobian is calculated directly from the isoparametric mapping and is given for the one-dimensional case as

$$J_e = \frac{\partial r}{\partial \xi}\ , \quad \text{(one-dimensional)}, \qquad (3.33)$$

and for the two-dimensional case,

$$J_e = \frac{\partial r}{\partial \xi}\frac{\partial z}{\partial \eta} - \frac{\partial r}{\partial \eta}\frac{\partial z}{\partial \xi}\ , \quad \text{(two-dimensional)}. \qquad (3.34)$$

The original (r,z) coordinates are related to the transformed coordinates (ξ,η) by the mapping equations (3.7), (3.10) and (3.11). In addition, the dependence of the basis functions on the element shape is explicitly given by these mappings.

The dependence of the integrals on interface shape is contained solely in the transformation Jacobian J_e, and the derivatives of J_e with respect to interface position are evaluated in closed form, since the relationships between the spacing of the nodes (r_i,z_i) and the

interface shapes and crystal radius are given in the generation of the mesh. The nodes of the finite element mesh are specified, according to their location, as fractions of interface position. For example, an element positioned in the melt under the crystal has nodes which are located radially as a function of the quasi-steady crystal radius, $r_i = \text{fraction}_{r,i} * R$, and axially as a function of the melt/solid interface, $z_i = \text{fraction}_{z,i} * H_0(r_i)$.

In practice the Newton-Raphson iteration scheme, eq. (3.28), is recast as a set of equations in which a correction vector $\boldsymbol{\delta}$ is computed by solution of the matrix problem

$$\mathbf{J}(\mathbf{y}^{(k)})\ \boldsymbol{\delta}^{(k+1)} = -\mathbf{F}(\mathbf{y}^{(k)}) \ , \tag{3.35}$$

and the solution vector $\mathbf{y}$ is updated to the (k+1) iterate as

$$\mathbf{y}^{(k+1)} = \mathbf{y}^{(k)} + \boldsymbol{\delta}^{(k+1)} \ . \tag{3.36}$$

We solve the equation set (3.35) by Gaussian elimination using a computer code for banded matrices with the arrow structure (Thomas and Brown, 1986; Thomas, 1987). Figure 3.5 demonstrates the convergence rate of the Newton iteration for a typical calculation based on the mesh shown in Fig. 3.3.

The rate of convergence demonstrated in Fig. 3.5 is quite dramatic; the norm of the residual decreases by orders of magnitude in successive iterations. We can quantify the rate of convergence of a sequence $\mathbf{y}^0, \mathbf{y}^1, \mathbf{y}^2, \ldots$ which converges to $\mathbf{y}$ by setting $\varepsilon_n = \|\mathbf{y}^n - \mathbf{y}\|$. If for $C \neq 0$,

$$\lim_{n \to \infty} \frac{\varepsilon_{n+1}}{\varepsilon_n^{\,p}} = C \ , \tag{3.37}$$

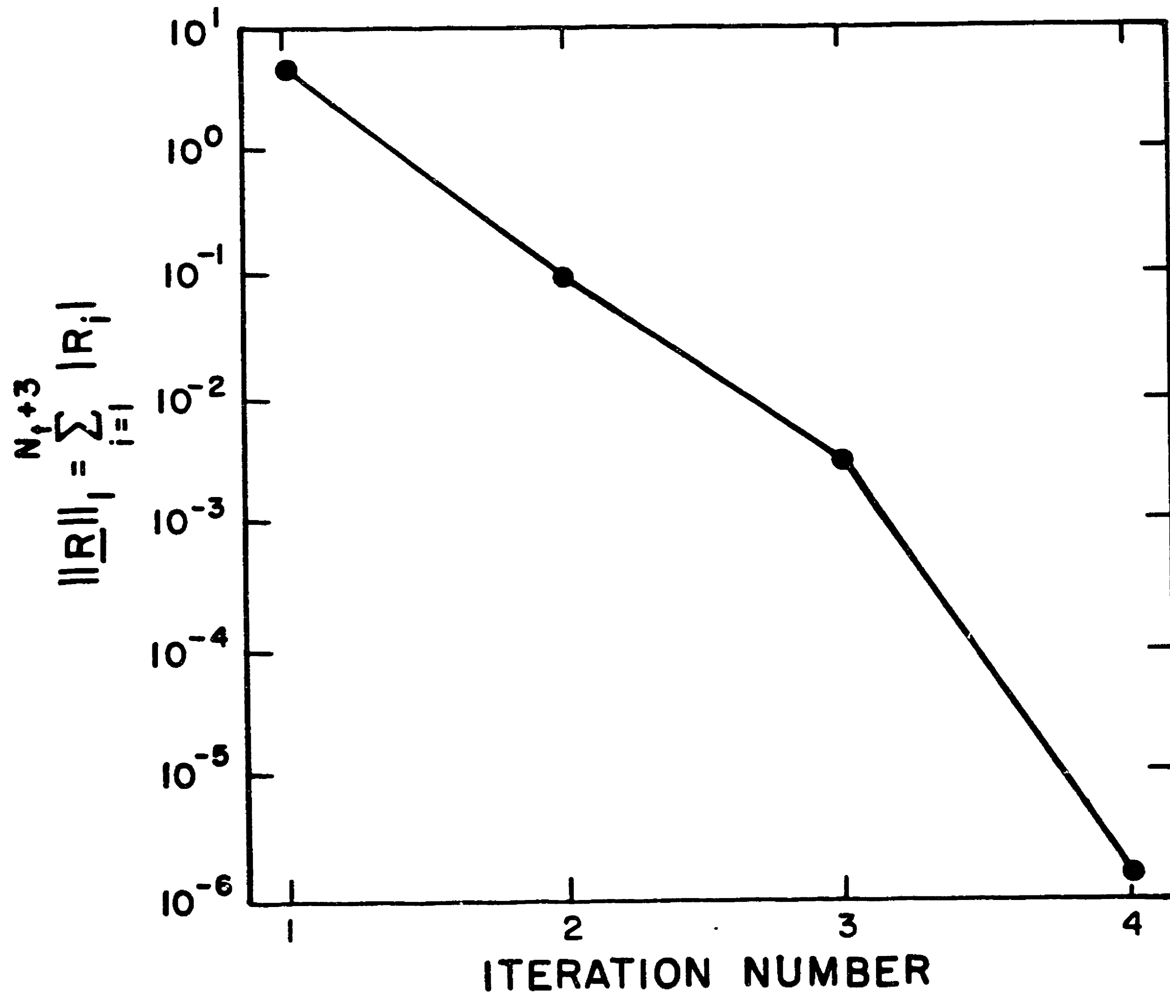

Fig. 3.5 Convergence for a typical calculation using the finite-element/ Newton method for the solution of the quasi-steady-state thermal-capillary model.

then p is the order of convergence of the sequence and C is the asymptotic error constant. Newton's method will produce quadratic convergence (p=2) to the solution of any set of equations, provided that the solution estimate is in the neighborhood of a root of the equation set (Dahlquist and Bjorck, 1974). The convergence demonstrated in Fig. 3.5 is quadratic as the estimated solution approaches the true solution (note that $\log\|\mathbf{F}\|$ plotted as a function of iteration number clearly shows that the residual is decreasing as $\|\mathbf{F}\|^2$ per iteration as $\|\mathbf{F}\|$ approaches zero) and is typical of other calculations in this work.

3.3 Transient Formulation

We describe below the solution method for the transient thermal-capillary model derived in Chapter 2. Although a Galerkin finite element method similar to that employed in the solution of the quasi-steady-state model is used, additional complications for the transient formulation are explained. The spatial discretization of the transient equations is presented in Section 3.3.1. The method for time-integration of the resulting set of ordinary differential/algebraic equations is discussed in Section 3.3.2.

3.3.1 Spatial Discretization

We discretize the spatial domain into a finite element mesh which follows the evolving shapes of the boundaries. The procedure is identical to that described previously for the quasi-steady-state problem except that in this formulation the mesh evolves in time. A continuous temperature field is approximated by standard nine-node biquadratic Lagrangian interpolating functions as

$$\Theta(r,z,\tau) = \sum_{j=1}^{N_\theta} \alpha(\tau)_j \Phi^j(r(\tau),z(\tau)) \ , \qquad (3.38)$$

where N_θ is the total number of nodes in the finite element mesh, $\alpha(\tau)_j$ is the time-dependent temperature of node j, and Φj is the interpolating polynomial associated with that node. Note that the functions $\{\Phi j\}$ are implicitly functions of time since they are defined by the finite element mesh which changes in time to track the moving boundaries.

The Galerkin weighted residuals are derived from the transient heat transfer equations of Chapter 2. We separate the individual terms and obtain

$$\int_{D_k} \Phi^i\{Pe_k \frac{\partial\Theta}{\partial\tau}\} \, dV - \int_{D_k} \Phi^i\{\nabla\cdot(K_k(\theta)\nabla\Theta)\} \, dV + \int_{D_s} \Phi^i\{Pe_s V^*(\tau)(e_z\cdot\nabla\Theta)\} \, dV = 0$$

$$\text{for } k=m,s,e,\ell,c \ , \quad i=1,N_\theta \ . \qquad (3.39)$$

The two terms following the temperature time derivative are the same

as those in the quasi-steady-state equations. The factor $V^*(\tau)$ appears in the last term so that a time-dependent pull rate can be easily included. This formulation was chosen since often the pull rate is varied through a growth run as a diameter-control parameter. The pull rate and the Peclet numbers Pe_k are based on a scaling velocity chosen to represent a typical pull rate, as discussed previously in the scaling of the transient equations in Chapter 2. As in the quasi-steady-state formulation, the second term of eq. (3.39) is integrated by parts and put into the weak form with the boundary conditions along each surface included.

The resulting integral equations for the temperature field are given below with the time-derivative terms on the left-hand side of the equation,

$$\int_{D_k} \Phi^i \{Pe_k \frac{\partial \Theta}{\partial \tau}\} \, dV + \int_{\partial D_o} \Phi^i Pe_s S \frac{\partial H_o}{\partial \tau} (\mathbf{n}_o \cdot \mathbf{e}_z) \, dS =$$

$$-\int_{D_k} K_k \nabla\Phi^i \cdot \nabla\Theta \, dV - \int_{D_s} Pe_s \Phi^i \frac{\partial \Theta}{\partial z} \, dV + \int_{\partial D_o} Pe_s S V^*(\tau) \Phi^i (\mathbf{n}_o \cdot \mathbf{e}_z) \, dS$$

$$-\sum_j \int_{\partial D_j} [Bi_j \Phi^i (\Theta - \Theta_a) + Ra_j \Phi^i (\Theta^4 - \Theta_a^4)] \, dS,$$

$$\text{for } k = m,s,e,\ell,c \;, \quad j = 1,\ldots 10 \;, \quad i = 1,\ldots N_\theta \;, \qquad (3.40)$$

where k denotes the domain, j represents the domain surfaces identified previously in Chapter 2, Fig. 2.4, and the temperature unknowns are indexed with i. The second term on the left-hand side of the equation

is the time-dependent latent heat contribution at the melt/crystal interface caused by departure of the crystal growth velocity from the pull rate. In the quasi-steady model the growth rate was identical to the pull rate, but now the interface growth velocity is given by $[V^*(\tau)-\partial H_0/\partial\tau]\mathbf{e}_z$ with pull rate as $V^*(\tau)\mathbf{e}_z$.

We use the notation from the quasi-steady-state formulation and write the resulting equation set as

$$\int_{D_k} \Phi^i Pe_k \frac{\partial\Theta}{\partial\tau}\, dV + \int_{\partial D_0} \Phi^i Pe_s S \frac{\partial H_0}{\partial\tau} (\mathbf{n}_0 \cdot \mathbf{e}_z)\, dS = F_i(\mathbf{y}) \,, \qquad (3.41)$$

where k represents each region, the unknowns are numbered $i=1,N_\theta$, F_i is the ith component of the quasi-steady-state residual equation, and $\mathbf{y}$ is the complete vector of temperature and interface unknowns.

We substitute the finite element approximation for the temperature field, eq. (3.38), into the above equation, and the time dependent term within the leading volume integral on the left-hand side becomes

$$\frac{\partial\Theta}{\partial\tau} = \frac{\partial}{\partial\tau}\Big(\sum_{j=1}^{N_\theta} \alpha_j \Phi^j\Big) = \sum_{j=1}^{N_\theta} \Big(\frac{\partial\alpha_j}{\partial\tau} \Phi^j + \alpha_j \frac{\partial\Phi^j}{\partial\tau}\Big) \,. \qquad (3.42)$$

The last term on the right-hand side of the above equation can be further reduced by applying the chain rule of differentiation,

$$\frac{\partial\Phi^j}{\partial\tau} = \sum_{n=1}^{N_\theta} \Big(\nabla_n \Phi^j \cdot \frac{\partial \mathbf{X}_n}{\partial\tau}\Big) \,, \qquad (3.43)$$

where $\nabla_n \equiv (\partial/\partial r_n)\mathbf{e}_r + (\partial/\partial z_n)\mathbf{e}_z$ is the gradient with respect to the nodal coordinates (r_n,z_n) while holding (r,z) constant and $\mathbf{X}_n$ are the coordinates of node n $(r_n(\tau),z_n(\tau))$. Lynch (1982) has shown that

the term $\nabla_n\Phi^j$ is related to the fixed coordinate frame by the following relation for an isoparametric mapping,

$$\nabla_n \Phi^j = -\Phi^n \nabla \Phi^j \ , \tag{3.44}$$

where on the right hand side of the equation $\nabla = (\partial/\partial r)\mathbf{e}_r + (\partial/\partial z)\mathbf{e}_z$ is the gradient operator with respect to the fixed coordinate frame (r,z). Finally, we write

$$\frac{\partial \Phi^j}{\partial \tau} = - \sum_{n=1}^{N_\theta} \Phi^n \frac{\partial \mathbf{X}_n}{\partial \tau} \cdot \nabla \Phi^j = -\mathbf{V}^e \cdot \nabla \Phi^j \ , \tag{3.45}$$

where $\mathbf{V}^e$ is an "elemental" velocity which is a function of the interface velocities and describes how each element deforms in time with respect to the fixed coordinate system.

We now return to the temperature time derivative term with this relation and obtain after substituting from eq. (3.45),

$$\frac{\partial \Theta}{\partial \tau} = \sum_{j=1}^{N_\theta} [\Phi^j \frac{\partial \alpha_j}{\partial \tau} - \mathbf{V}^e \cdot (\alpha_j \nabla \Phi^j)] = \sum_{j=1}^{N_\theta} [\Phi^j \frac{\partial \alpha_j}{\partial \tau}] - \mathbf{V}^e \cdot \nabla \Theta \ , \tag{3.46}$$

The change to the temperature time-derivative term caused by the moving mesh is now easily seen as a convective elemental velocity correction. This correction is directly related to the velocities of the moving interfaces since the node spacing is a specified function of interface location. This point will be addressed below in the discussion of the mass matrix. We rewrite the dynamic equation of energy conservation, eq. (3.41), as

$$\int_{D_k} \Phi^i Pe_k \{ \sum_{j=1}^{N_\theta} [\Phi^j \frac{\partial \alpha_j}{\partial \tau}] - \mathbf{v}^e \cdot \nabla \Theta \} \, dV + \int_{\partial D_0} \Phi^i Pe_s S \frac{\partial H_0}{\partial \tau} (\mathbf{n}_0 \cdot \mathbf{e}_z) \, dS$$

$$= F_i(\mathbf{y}) \;, \qquad (3.47)$$

where k denotes region and $i=1,N_\theta$.

In a fashion analogous to the approximation of the temperature field, the shapes of the interfaces are approximated by one-dimensional quadratic functions as follows:

$$H_0(r,\tau) = \sum_{i=1}^{N_0} \beta_0(\tau)_i \Psi^i(r(\tau)) \;, \qquad (3.48)$$

$$H_1(r,\tau) = \sum_{i=1}^{N_1} \beta_1(\tau)_i \Psi^i(r(\tau)) \;, \qquad (3.49)$$

$$H_2(r,\tau) = \sum_{i=1}^{N_2} \beta_2(\tau)_i \Psi^i(r(\tau)) \;, \qquad (3.50)$$

$$R(z,\tau) = \sum_{i=1}^{N_3} \beta_3(\tau)_i \Psi^i(z(\tau)) \;, \qquad (3.51)$$

where N_0,N_1, and N_2 are the number of nodes defining interfaces H_0,H_1, and H_2, and N_3 is the number of nodes defining the radius. Note that in contrast to the quasi-steady-state formulation where the radius is specified by one value corresponding to constant-diameter growth, the transient problem includes a dynamic radius which can change as a function of z. Again $\{(\beta_0,\beta_1,\beta_2,\beta_3)_i\}$ are the time-dependent nodal function values and $\{\Psi i\}$ are are implicitly time-dependent interpolating functions.

These approximations are used in a Galerkin integral weighting formulation for the melt/solid interface and melt and encapsulant

menisci which yield the same residual equations as in the quasi-steady equation set; see eqs. (3.21-3.23). For these equations, there is no explicit time derivative since the distinguishing conditions for both cases are equilibrium relationships. This feature results in a system of differential/algebraic equations (DAE's) when linked with the temperature field equations, eq. (3.47). Implementing the latent heat flux at the melt/solid interface as a boundary condition for the temperature field equations and distinguishing the isotherm as a means for locating the interface is known as the Isotherm method. This was first used by Ettouney and Brown (1983) for steady solidification problems and more recently by Lynch and Sullivan (1985) for transient phase change problems.

The kinematic condition which describes the dynamic radius is a pure advection equation; the crystal shape is literally pulled past the fixed coordinate z. The solution of this hyperbolic equation is not well approximated by Galerkin methods. We therefore adopt a Streamline Upwind/Petrov-Galerkin scheme fashioned after the work of Brooks and Hughes (1982). This scheme is able to damp the spurious oscillations observed in the solution of convection-dominated problems obtained by the Galerkin weighted residual formulation, but it suffers from a slight loss of accuracy for approximating the solution. Johnson et al. (1984) examined approximating error for the Streamline Upwind/Petrov-Galerkin method and derived that, for these methods,

$$\|error\| \leq Ch^{k+1/2} , \qquad (3.52)$$

where C is a constant greater than zero, k is the order of the polynomial

approximating functions, and h is a measure of the element size. For elliptic and parabolic problems solved by the conventional Galerkin finite element method,

$$\|error\| \leq Ch^{k+1} , \tag{3.53}$$

and there is greater solution accuracy than that obtained by the upwinded methods. Quadratic approximating functions are used in the work presented here, and k=2 for the error criteria above.

The Streamline Upwind/Petrov-Galerkin weighted residual formulation for the radius equation is as follows,

$$\int_{H_0}^{Z} \{\Psi^i + p\frac{\partial \Psi^i}{\partial z}\}\{\frac{\partial R}{\partial \tau} + V^*(\tau)\frac{\partial R}{\partial z}\}\, dz = 0 , \tag{3.54}$$

where p is a scaling factor to account for the spacing of the mesh. We choose the value of p for this problem based on suggestions in Hughes and Tezduyar (1984),

$$p = \frac{2}{\sqrt{15}} \left|\frac{\partial z}{\partial \xi}\right| . \tag{3.55}$$

This form of p was shown by Raymond and Garder (1976) to minimize phase error for a one-dimensional, pure advection model problem.

Following the procedure discussed above for correcting the time-derivative of the temperature equations for the moving mesh, we arrive at the transient equations for the discretized kinematic radius condition,

$$\int_{H_0}^{Z} \{\Psi^i + p\frac{\partial \Psi^i}{\partial z}\}\{\sum_{j=1}^{N_3} [\Psi^j \frac{\partial \beta_{3j}}{\partial \tau}] - V^e \frac{\partial R}{\partial z}\} \, dz = F_i(\mathbf{y}) \, , \tag{3.56}$$

where,

$$F_i(\mathbf{y}) = - \int_{H_0}^{Z} \{\Psi^i + p\frac{\partial \Psi^i}{\partial z}\} \, V^*(\tau) \, \frac{\partial R}{\partial z} \, dz \, , \tag{3.57}$$

and V^e is the elemental velocity caused by the stretching of the one-dimensional elements in the z direction. The value of the radius emerging from the melt is given directly by the kinematic condition applied to the tri-junction,

$$\left.\frac{\partial R}{\partial \tau}\right|_{z=H_0(R,\tau)} = [V^*(\tau) - \left.\frac{\partial H_0}{\partial \tau}\right|_{r=R(H_0,\tau)}]\tan(\tilde{\phi} - \tilde{\phi}_0) \, , \tag{3.58}$$

where $\tilde{\phi}$ is the dynamic angle of the meniscus contacting the crystal, $\tilde{\phi}_0$ is the equilibrium wetting angle for constant-diameter growth, and $V^*(\tau)$ is the crystal pull rate. This condition is applied as a time-dependent essential boundary condition for the radius shape equation (3.56).

The transient equation set is made complete by augmenting the equations presented above with the algebraic constraints for the pressure terms λ of the meniscus equations derived in Chapter 2. For λ_1 this condition is

$$\int_{0}^{R(H_0(R,\tau),\tau)} H_0(r) r dr + \int_{R(H_1(R,\tau),\tau)}^{1} H_1(r) r dr = V_m(\tau)/2\pi \, , \tag{3.59}$$

and for λ_2,

$$\pi R^2(H_2(R,\tau),\tau) + 2\pi\int_{R(H_2(R,\tau),\tau)}^{1} H_2(r,\tau)rdr - \pi R^2(H_1(R,\tau),\tau)$$

$$- 2\pi\int_{R(H_1(R,\tau),\tau)}^{1} H_1(r,\tau)rdr - \pi\int_{H_1(R(H_1,\tau),\tau)}^{H_2(R(H_2,\tau),\tau)} R^2(z,\tau)dz = V_e \ . \tag{3.60}$$

The ordinary differential equations (also derived in Chapter 2) for the rate of melt volume change and the position of the top of the crystal are, respectively,

$$\frac{\partial V_m}{\partial \tau} = -2\pi\int_{0}^{R(H_0(R,\tau),\tau)} \frac{\rho_s}{\rho_m} [V^*(\tau) - \frac{\partial H_0}{\partial \tau}]rdr \ , \tag{3.61}$$

and

$$\frac{\partial Z}{\partial \tau} = V^*(\tau) \ . \tag{3.62}$$

The four equations above do not involve spatial derivatives and so do not need to be discretized by the finite element method.

Finally, all the transient equations are assembled into a set of generalized differential equations, which is represented in vector form as

$$\mathbf{M}(\mathbf{y}) \frac{\partial \mathbf{y}}{\partial \tau} = \mathbf{F}(\mathbf{y}) \ , \tag{3.63}$$

where $\mathbf{M}$ is termed the mass matrix. The structure of the mass matrix

is similar to that of the quasi-steady-state Jacobian in that it consists of a banded portion augmented with columns. Unlike the Jacobian, however, the mass matrix is singular since there are no explicit time-derivatives for the melt/solid interface and the menisci. This is easily seen by examining the structure of the mass matrix, where complete rows of zero elements cause **M** to be singular, as shown below,

$$\mathbf{M} = \begin{bmatrix} \mathbf{M}_1 & \mathbf{M}_2 \\ & \\ \mathbf{0} & \mathbf{0} \\ \mathbf{0} & \mathbf{M}_3 \end{bmatrix} , \tag{3.64}$$

where the unknowns vector is ordered $\mathbf{y}^T=(\boldsymbol{\alpha}^T,\boldsymbol{\beta}_0{}^T,\boldsymbol{\beta}_1{}^T,\boldsymbol{\beta}_2{}^T,\boldsymbol{\beta}_3{}^T,\boldsymbol{\lambda}^T,V_m,Z)$. For this ordering of unknowns the mass matrix consists of $\mathbf{M}_1$, a real $N_\theta x N_\theta$ matrix which is banded, $\mathbf{M}_2$, a real $N_\theta x(N_0+N_1+N_2+N_3+4)$ rectangular matrix, and $\mathbf{M}_3$, a real $(N_3+4)x(N_3+4)$ square matrix which has nonzero components from the crystal shape equations but is is also singular from the absence of explicit time derivatives in the volume constraints, eqs. (3.59) and (3.60). Individual components of the $\mathbf{M}_1$ matrix are given by

$$M_{1_{ij}} = \int_{D_k} Pe_k \Phi^i \Phi^j \, dV , \tag{3.65}$$

where k denotes region and $i,j=1,N_\theta$. Similarly, the block diagonal components of $\mathbf{M}_3$ are

$$M_{3_{ij}} = \int_{H_0}^{Z} \Psi^i \Psi^j \, dV \ , \tag{3.66}$$

where i,j denote radius unknowns. These block diagonal components are the standard terms arising from a Galerkin finite element discretization. The remaining mass matrix contributions, the $\mathbf{M_2}$ matrix and the non-diagonal components of $\mathbf{M_3}$, account for the convective motion of the mesh. These terms multiply the time derivatives of the interfaces. In addition, the time-dependent melt/crystal growth rate perturbations to the latent heat flux condition, the second term of eq. (3.41), and the melt volume rate of change, eq. (3.61), are included as mass matrix terms which multiply the time derivatives of the melt/solid interface unknowns.

3.3.2 Temporal Discretization

The complete set of transient equations takes the form of the vector equation (3.63), repeated here

$$\mathbf{M}(\mathbf{y}) \frac{\partial \mathbf{y}}{\partial \tau} = \mathbf{F}(\mathbf{y}) \ , \tag{3.67}$$

where $\mathbf{y}$ represents the set of all unknowns, the nonlinear vector function $\mathbf{F}(\mathbf{y})$ is the Galerkin finite element discretization of the quasi-steady-state equations, and $\mathbf{M}(\mathbf{y})$ is the mass matrix. As discussed in the previous section, $\mathbf{M}$ is singular; therefore, explicit integration schemes are not feasible, as discussed at length by Ungar and Brown (1985). Systems of this type are known as differential/algebraic equations (DAE's) and are particularly difficult to solve numerically since

they are infinitely stiff —— no time scale exists for the algebraic equations (see Gear, 1971b and Petzold, 1982). Additional motivation for using fully implicit integration methods is given in the work of Derby and Brown (1986a) where implicit integration methods yielded an order of magnitude increase in efficiency over comparable explicit techniques for a model solidification problem (Bourret et al., 1985) which was numerically stiff. This work is presented in its entirety in Appendix B.

A fully implicit trapezoid rule with second-order accuracy in time (also known as a second-order Adams-Moulton method) is employed to solve eq. (3.67). Since previous time information is needed for this second order method, we start with two implicit backward Euler time steps,

$$\mathbf{M}(\mathbf{y}_{n+1})[\mathbf{y}_{n+1} - \mathbf{y}_n] - \Delta\tau_n \, \mathbf{F}(\mathbf{y}_{n+1}) = 0 \;, \tag{3.68}$$

where the subscripts n and n+1 refer to quantities at the nth and $n+1^{st}$ time step; for the first two time steps n=0,1. The initial condition, $\mathbf{y}_0$, is a steady solution obtained from the quasi-steady-state model, and the first time steps $\Delta\tau_n$ are taken to be very small in order to minimize the error at the start of the integration.

The trapezoid method is used for the ensuing time steps:

$$\mathbf{M}(\mathbf{y}_{n+1})[\mathbf{y}_{n+1} - \mathbf{y}_n - \frac{\Delta\tau_n}{2}\left(\frac{\partial \mathbf{y}}{\partial \tau}\right)_n] - \frac{\Delta\tau_n}{2}\,\mathbf{F}(\mathbf{y}_{n+1}) = 0 \;, \tag{3.69}$$

where $(\partial \mathbf{y}/\partial \tau)_n$ is calculated for the first trapezoid step (n=2) with a first-order backward difference formula as

$$(\frac{\partial \mathbf{y}}{\partial \tau})_n = \frac{1}{\Delta\tau_{n-1}} (\mathbf{y}_n - \mathbf{y}_{n-1}) \ . \qquad (3.70)$$

Subsequently (for time steps n≥3) this time derivative is obtained from a consistent second-order backward difference formula,

$$(\frac{\partial \mathbf{y}}{\partial \tau})_n = \frac{2}{\Delta\tau_{n-1}} (\mathbf{y}_n - \mathbf{y}_{n-1}) - (\frac{\partial \mathbf{y}}{\partial \tau})_{n-1} \ . \qquad (3.71)$$

We solve the implicit equation set for stepping in time iteratively by a quasi-Newton method similar to that used for solution of the quasi-steady-state equations. At each time step, a correction vector $\boldsymbol{\delta}$ is used to update the guess for the solution $\mathbf{y}_{n+1}$ as

$$\mathbf{y}_{n+1}^{(k+1)} = \mathbf{y}_{n+1}^{(k)} + \boldsymbol{\delta}^{(k+1)} \ , \qquad (3.72)$$

where tne superscripts denote iteration number. The initial guess for $\mathbf{y}_{n+1}$ is obtained from a second-order Adams-Bashforth predictor based on the previous two time steps; the form of this predictor is given as eq. (3.76) and is discussed below. The correction vector $\boldsymbol{\delta}^{(k+1)}$ is determined for the backward Euler method from the matrix problem

$$\mathbf{J}\ \boldsymbol{\delta}^{(k+1)} = -\mathbf{M}(\mathbf{y}_{n+1}^{(k)})[\mathbf{y}_{n+1}^{(k)} - \mathbf{y}_n] + \Delta\tau_n\ \mathbf{F}(\mathbf{y}_{n+1}^{(k)}) \ , \qquad (3.73)$$

and for the trapezoid rule,

$$\mathbf{J}\ \boldsymbol{\delta}^{(k+1)} = -\mathbf{M}(\mathbf{y}_{n+1}^{(k)})[\mathbf{y}_{n+1}^{(k)} - \mathbf{y}_n - \frac{\Delta\tau_n}{2} (\frac{\partial \mathbf{y}}{\partial \tau})_n] + \frac{\Delta\tau_n}{2}\ \mathbf{F}(\mathbf{y}_{n+1}^{(k)}) . \qquad (3.74)$$

The form of the matrix $\mathbf{J}$ is

$$\mathbf{J} = \left(\mathbf{M} + \frac{\partial \mathbf{M}}{\partial \mathbf{y}}\ \mathbf{y} + \frac{\Delta\tau_n}{a} \frac{\partial \mathbf{F}}{\partial \mathbf{y}} \right) \bigg|_{\mathbf{y}=\mathbf{y}_{n+1}^{p}} \ , \qquad (3.75)$$

where in the last term on the right-hand side of the equation, a=1 for the backward Euler method and a=2 for the trapezoid rule. The first term on the left-hand side, $\mathbf{M} = \{M_{ij}\}$, is the mass matrix, and the second term, $(\partial\mathbf{M}/\partial\mathbf{y})\mathbf{y} = \mathbf{A}$ with $\{A_{ij}\} = \sum_k (\partial M_{ik}/\partial y_j) y_k$ for k=1,N, is the derivative of the components of the mass matrix with respect to all unknowns (a third rank tensor) multiplied by the unknowns vector. The third term, $\partial\mathbf{F}/\partial\mathbf{y} = \mathbf{B}$ with $\{B_{ij}\} = \partial F_i/\partial y_j$, is the sensitivity matrix for **F**, which is also the Jacobian for the quasi-steady-state residual equations; see Section 3.2.2 of the quasi-steady-state analysis.

The Jacobian for the transient equation set is evaluated at the predictor value of $\mathbf{y}^p_{n+1}$ as given by the explicit second-order Adams-bashforth formula,

$$\mathbf{y}^p_{n+1} = \mathbf{y}_n + \frac{\Delta\tau_n}{2}\left[\left(2 + \frac{\Delta\tau_n}{\Delta\tau_{n-1}}\right)\left(\frac{\partial\mathbf{y}}{\partial\tau}\right)_n - \frac{\Delta\tau_n}{\Delta\tau_{n-1}}\left(\frac{\partial\mathbf{y}}{\partial\tau}\right)_{n-1}\right] , \qquad (3.76)$$

where the second-order backward difference formula eq. (3.71) is used to determine $(\partial\mathbf{y}/\partial\tau)_n$ and $(\partial\mathbf{y}/\partial\tau)_{n-1}$. The matrix **J** is only updated when the procedure has failed to converge in four iterations; thus the same **J** may be carried along for several time steps. Additional time savings are realized by performing a single decomposition of the Jacobian into an **LU** form (Dahlquist and Bjorck, 1974) and using only a back substitution to solve for the time integration correction vector, eqs. (3.73) and (3.74), on subsequent iterations. This is accomplished with a routine which uses Gaussian elimination while taking advantage of the "arrow" structure of the matrix (Thomas and Brown, 1986; Thomas, 1987). The number of operations and, hence, the computation time saved by this strategy over a full Newton iteration

scheme is significant since the decomposition of the Jacobian into **LU** form is ~ np^2 operations (where p is the width of the banded portion of the matrix) while a back-substitution consists of only ~ 2np operations. The modified-Newton iteration procedure attempts to perform as few **LU** decompositions as possible and thus realize savings in computational effort.

The strategies for varying the step size $\Delta\tau_n$ are based on local error estimation. Truncation error in the trapezoid rule time expansion is proportional to the lowest order neglected term, i.e. the third order term in the expansion, $\partial^3\mathbf{y}/\partial\tau^3$. This term is calculated by combining the second-order forward and backward time series expansions and solving for the third order term. The neglected term of highest order in the trapezoid rule is

$$\Delta\mathbf{y} = \frac{\Delta\tau_n^3}{12}\frac{\partial^3\mathbf{y}}{\partial\tau^3} = \frac{\mathbf{y}_{n+1} - \mathbf{y}^p_{n+1}}{3(1 + \frac{\Delta\tau_{n-1}}{\Delta\tau_n})} , \tag{3.77}$$

where the predictor of eq. (3.76) is used. Following the suggestion of Ungar and Brown (1985), the first-order backward difference formula of eq. (3.70) is used in calculating the predictor $\mathbf{y}^p$ for this time step size selection scheme. The estimate of local truncation error is used to project a step size for the next step which will result in local error proportional to a parameter, here represented as ε

$$\Delta\tau_{n+1} = \Delta\tau_n \left(\frac{\varepsilon}{\|\Delta\mathbf{y}\|}\right)^{1/3} , \tag{3.78}$$

where $\|\Delta\mathbf{y}\|$ is the L_2-Euclidean norm of the vector error term $\Delta\mathbf{y}$ normalized by the absolute value of the maximum component of **y** as

$$\|\Delta \mathbf{y}\| = \frac{\{ \sum_{i=1}^{N} \Delta y_i^2 / N \}^{1/2}}{\max_i |y_i|} , \tag{3.79}$$

where N is the total number of unknowns and Δy_i is calculated with eq. (3.68) above. We accept the new step size $\Delta\tau_{n+1}$ if it is greater than the old step size $\Delta\tau_n$ or if it is less than $0.8\Delta\tau_n$. If $\Delta\tau_{n+1}$ is greater than $0.8\Delta\tau_n$ and less than $\Delta\tau_n$ the step size is not changed. This strategy is summarized below:

$$\text{if } \left\{ \begin{array}{c} \Delta\tau_{n+1} > \Delta\tau_n \\ \text{or} \\ \Delta\tau_{n+1} < 0.8\Delta\tau \end{array} \right\} , \text{ Accept new step size } \Delta\tau_{n+1} , \tag{3.80}$$

$$\text{if } 0.8\Delta\tau_n \;\Phi\; \Delta\tau_{n+1} \;\Phi\; \Delta\tau_n , \text{ Keep current step size } \Delta\tau_n . \tag{3.81}$$

The error criterion ε was chosen typically as 10^{-4} so that the error at each time step was proportional to 0.01 per cent.

Details of the fully implicit method and the heuristic guidelines for choosing step size, eqs. (3.80) and (3.81), are found in the paper by Gresho et al. (1980). General discussions of numerical time-integration methods are included in texts by Gear (1971a) and Finlayson (1980).

3.4 Linear Stability Formulation

From the previous section, it is clear that the dynamic simulation of CZ growth requires much more computational effort than quasi-steady-state calculations. It is desirable then to obtain as much information as possible about the Czochralski growth system from quasi-steady-

state simulations. This is facilitated by examining the stability of quasi-steady solutions to small perturbations in a linear stability analysis. As will be shown below, this analysis requires much less computational effort than the full dynamic simulation and only slightly more than quasi-steady-state calculations. Furthermore, information about the time constants for a stable system returning to its stationary state or an unstable system leaving that state are made available through such a study, even though the full nonlinear dynamics can only be assessed through a complete transient simulation.

The derivations of the previous section for the fully transient discretized equation set describing CZ and LEC growth are easily extended to the analysis of the linear stability of the steady-state equations. However, the foundation for the ensuing analysis lies with the Newton-Raphson method first developed for the quasi-steady model. The arrow Jacobian contains a wealth of information about the nature of the solution at a steady-state and, in addition to its role in the Newton/Isotherm iteration scheme, also is essential in describing the dynamic behavior of the steady solution.

The conditions for linear stability are derived by considering the initial response of a disturbed solution $\mathbf{y}_0$ of the steady-state problem (for more in-depth discussions of stability, see Denn, 1975 and Iooss and Joseph, 1980). We perturb this solution by a small disturbance $\delta\mathbf{x}$, where δ is a constant and $\|\delta\mathbf{x}\| << 1$,

$$\mathbf{y} = \mathbf{y}_0 + \delta\mathbf{x} \,, \tag{3.82}$$

This quantity is substituted into the set of differential/algebraic equations which describe the nonlinear dynamic problem,

$$\mathbf{M}(\mathbf{y}_0+\delta\mathbf{x})\ [\frac{\partial \mathbf{y}_0}{\partial\tau} + \delta\ \frac{\partial \mathbf{x}}{\partial\tau}] = \mathbf{F}(\mathbf{y}_0+\delta\mathbf{x})\ . \tag{3.83}$$

Now we expand each term in a Taylor series about the steady-state solution $\mathbf{y}_0$,

$$[\mathbf{M}(\mathbf{y}_0) + \delta\frac{\partial \mathbf{M}}{\partial \mathbf{y}}\mathbf{x} + O(\|\delta\mathbf{x}\|^2)][\frac{\partial \mathbf{y}_0}{\partial\tau} + \delta\frac{\partial \mathbf{x}}{\partial\tau}] = \mathbf{F}(\mathbf{y}_0) + \delta\frac{\partial \mathbf{F}}{\partial \mathbf{y}}\mathbf{x} + O(\|\delta\mathbf{x}\|^2). \tag{3.84}$$

We know that $\mathbf{y}_0$ is a steady-state solution, so $\partial\mathbf{y}_0/\partial\tau$ and $\mathbf{F}(\mathbf{y}_0)$ are identically zero. Since $\delta\mathbf{x}$ is arbitrarily small, we discard all higher-order terms, divide the equation set by δ, and obtain the following linearized condition,

$$\mathbf{M}(\mathbf{y}_0)\frac{\partial \mathbf{x}}{\partial\tau} = \mathbf{J}(\mathbf{y}_0)\mathbf{x}\ , \tag{3.85}$$

where both the mass matrix $\mathbf{M}$ and the steady-state Jacobian $\partial\mathbf{F}/\partial\mathbf{y} = \mathbf{J}$ are evaluated at the steady solution $\mathbf{y}_0$.

Solutions to this equation are in the form of

$$\mathbf{x}(\tau) = \sum_{i=1}^{N} \hat{\mathbf{x}}_{0_i} e^{\sigma^i \tau}, \tag{3.86}$$

where the vectors $\{\hat{\mathbf{x}}_{0i}\}$ consist of components of the eigenvectors $\{\hat{\mathbf{x}}_i\}$ which are present in the initial solution $\mathbf{x}(\tau=0) = \mathbf{x}_0$, with $\sum_i \hat{\mathbf{x}}_{0i} = \mathbf{x}_0$, and $\{\sigma^i\}$ are the eigenvalues of the generalized eigenvalue problem

$$\sigma\mathbf{M}(\mathbf{y}_0)\hat{\mathbf{x}} = \mathbf{J}(\mathbf{y}_0)\hat{\mathbf{x}} \tag{3.87}$$

which results from eq. (3.85) above. If the real part of all of the eigenvalues $\{\sigma^i\}$ are less than zero, the steady-state solution $\mathbf{y}_0$ is locally stable. However, if one or more eigenvalues has a positive real part, the solution is unstable to small disturbances.

Although the stability of the operating state can be determined by calculating the eigenvalues of eq. (3.87), this procedure is not practical for the large matrices which result from our finite element discretization. The computational effort involved for calculations of this type is large since an iterative solution technique requiring several matrix transformations is required. For this generalized eigenvalue problem with nonsymmetric matrices and singular **M**, application of the **QZ** algorithm (Moler and Stewart, 1973) would require ~ $6n^3$ operations to reduce **J** to upper Hessenberg form while simultaneously reducing **M** to triangular form and then ~ $13n^2$ operations for the **QR** shifts (Francis, 1961-62; Peters and Wilkinson, 1970) needed to calculate the eigenvalues. In addition, the memory requirements needed for the storage of the several large matrices involved and working area needed are prohibitive.

Another complication which must be addressed in the determination of system stability by the generalized eigenvalue problem is the required form of a physically allowable disturbance. In the real system, physical disturbances which change the shape of previously solidified crystal are not realizable. However, the generalized eigenvalue problem, eq. (3.87), will allow any disturbance to the system unless constraints are also invoked in terms of orthogonal projections of the eigenvectors. The proper choice of constraints and their implementation for this problem are not trivial. The allowed disturbances to the steady-state solution are arbitrary as long as initial perturbations in the crystal shape $R(z,\tau)$ above the tri-junction are not be imposed. This is easily accomplished in the time-integration of eq. (3.85) by setting the

appropriate components of the initial disturbance vector $\mathbf{x}_0$ to zero.

In light of the difficulties laid out above for stability analysis through extensive eigenvalue calculations, a random initial guess $\mathbf{x}_0$ is generated, the appropriate components of the initial disturbance vector are set to zero according to the limitations discussed above, and the equation set, eq. (3.85), is integrated in time using the techniques put forth in the previous section. If the vector $\mathbf{x}$ dies away to zero the solution is stable, otherwise the excited unstable mode should grow exponentially and $\mathbf{x}$ will diverge. The rate of decay or growth of the disturbance can be determined by monitoring the norm of the disturbance $\|\mathbf{x}\|$ with time.

It is essential that the time-integration algorithm is stable for a definitive statement to be made about the real behavior of the linear stability equation. Our choice of method insures this since the fully implicit trapezoid rule is always stable (Gear, 1971a and Gresho et al., 1980). The computational savings in the solution of this problem over the solution of the full dynamic problem, eq. (3.67), and the generalized eigenvalue problem, eq. (3.87), are a result of the simple linear, constant coefficient form of eq. (3.85). Once the initial matrices $\mathbf{M}$ and $\mathbf{J}$ are formed and the Jacobian matrix for the time integration is decomposed into **LU** form (~ np^2 operations, where p is the width of the banded portion of the matrix), a single back-substitution (~ 2np operations) at each time step is all that is needed to solve the fully implicit time-stepping equations, as long as the step size is not changed. In practice, we start with a fairly small time step and quickly increase it to a limiting value

at which point calculations proceed very rapidly.

An important distinction must be made when discussing the stability of the real CZ process. We can only rigorously discuss the stability of true steady-state solutions, a prospect which is unrealizable for batch processes. However, we can postulate whether the quasi-steady CZ process is "inherently" unstable by examining the stability of a prototype system like the model proposed in the quasi-steady-state formulation. We achieve this prototype from the fully dynamic model by ensuring that the melt volume does not change and that the top of the crystal is far enough away so that heat transfer in the system is unaffected by its position. In our calculations, this is attained by setting the density of solid to zero in eq. (3.61) so that the rate of change of melt volume is zero and by using a long crystal while modifying eq. (3.61) so that $dZ/d\tau=0$ and the crystal top is stationary. Fixing the position of the top of the crystal insures that a true steady-state is achieved even if the length of the crystal is not quite long enough to qualify as infinite. These conditions correspond to the hypothetical continuous processing of a CZ system where the level of the melt remains constant and the crystal is infinitely long and produces a true steady-state solution whose stability can be unambiguously determined.

If this prototype steady-state, continuous-processing system is stable, we expect that the true quasi-steady CZ system is inherently stable. In this case, control strategies need only counter the batchwise nature of the real process. If however conditions exist where the continuous-processing system is unstable, a controller for the real

process would be expected to control the inherent instability of the system around a specified set point while simultaneously correcting for the transient nature of the batch process. Obviously, from a processing viewpoint, it is crucial to know which of these two situations exist. In addition, information about the time constants in the system are of great interest. The dynamic response of the crystal radius to operating parameter changes will define the limits of the controller.

We discuss the stability and overall dynamic nature of the CZ process in Chapter 5 where model calculations for Czochralski growth of silicon are presented.

Chapter 4. Quasi-Steady-State Results

Results from the finite element thermal-capillary model discussed in Chapters 2 and 3 for quasi-steady simulation of the CZ and LEC crystal growth processes are presented in this chapter. In Section 4.1, calculations are presented for a model liquid encapsulated Czochralski GaAs system with an encapsulant layer which is transparent to radiation. We extend the calculations to include the simulation of small-scale CZ growth of silicon and LEC growth of gallium arsenide with a radiatively transparent and opaque encapsulant layer in Section 4.2. The importance of the shape of the meniscus and the geometry of the tri-junction of melt/solid/ambient for modeling the process are shown, and the effects of the encapsulant in LEC on overall heat transfer are discussed. We also examine the effects of melt volume and crucible position relative to the heater on the crystal radius and the shape of the melt/solid interface.

The quasi-steady heat transfer model used in Section 4.2 is augmented with constraints for constant crystal radius and melt/solid interface deflection in Section 4.3 for the demonstration of processing strategy calculations. Combinations of growth rate, crucible temperature, and bottom-heater temperature are tested as processing parameters for satisfying the constrained thermal-capillary problem over a range

of melt volumes corresponding to the sequence occurring during the batchwise CZ growth of a small-diameter silicon crystal. The applicability of each control strategy is judged by the range of existence of solution, in terms of melt volume, and by the values of the axial and radial temperature gradients in the crystal. Applications of calculations of this type are discussed within the context of stability and control.

4.1 Initial Results for LEC Gallium Arsenide Growth

In this section we present results for the first calculations of the quasi-steady thermal-capillary model for Liquid Encapsulated Czochralski growth of GaAs. We compute temperature fields and geometries of meniscus shapes and crystal radii in Section 4.1.1; the sensitivity of the solution for a reference case growth system is examined by changing operating parameters, and insight to the physics of heat transfer and capillarity is obtained. Section 4.1.2 follows with a short discussion of the calculations.

4.1.1 Calculations

Calculations were carried out for a prototype of a small-scale GaAs experimental system with a crucible of 5 cm inner radius which was assumed to be isothermal at 1.1 times the melting point temperature of GaAs; a schematic diagram of this system is given in Fig. 4.1. The thermophysical properties used in the analysis are given in Table 4.1 (also in Appendix A), and a complete set of geometrical and operating

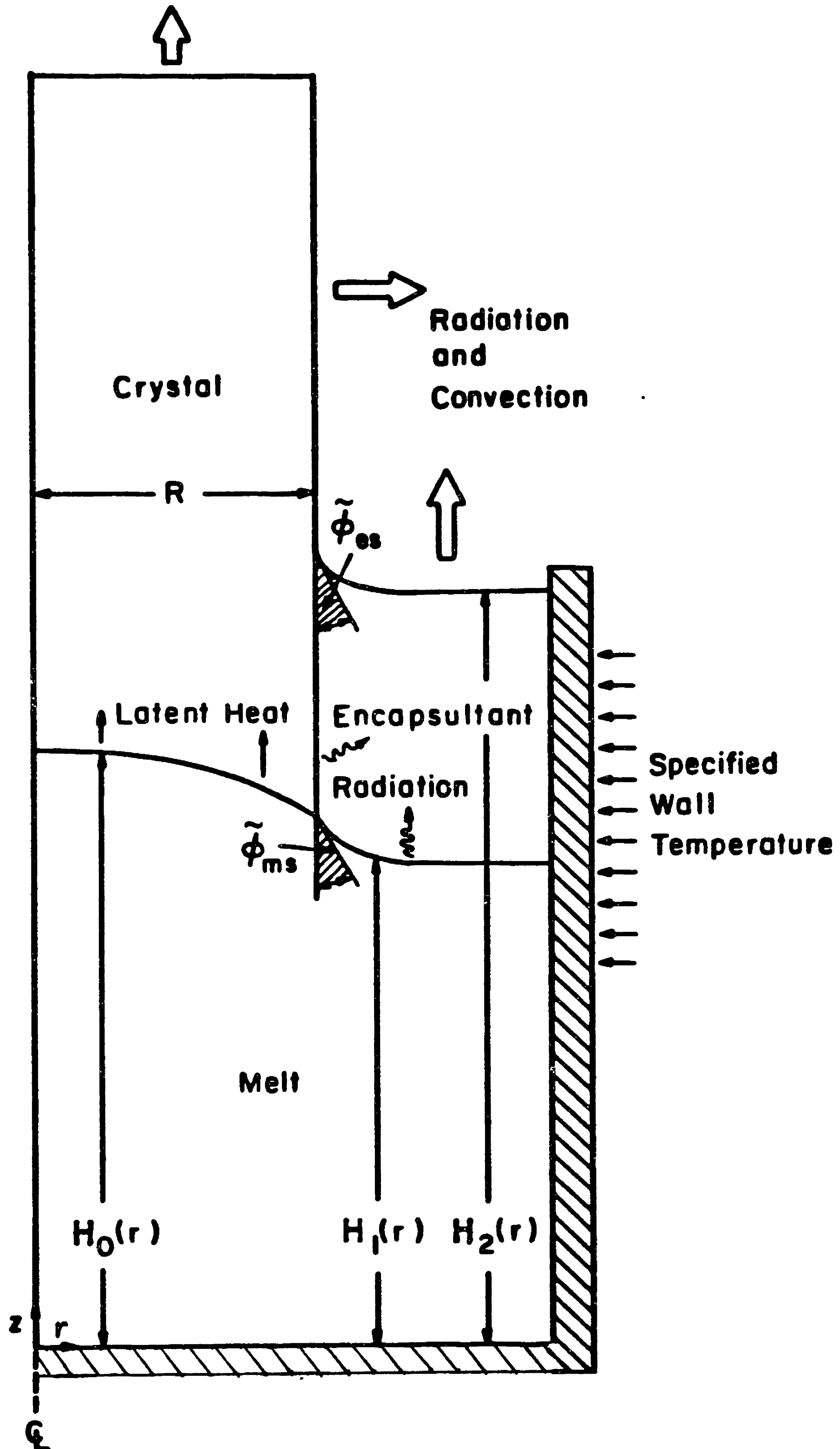

Fig. 4.1 Schematic diagram of prototype LEC system for calculations of Section 4.1.

Table 4.1 Material properties and physical constants for LEC gallium arsenide calculations of Section 4.1.

Property	Value
Equilibrium wetting angles:	
Melt/crystal/encapsulant (ϕ_{ms})	15°
Melt/crucible/encapsulant (ϕ_{mc})	0°
Encapsulant/crystal/ambient (ϕ_{es})	5°
Encapsulant/crucible/ambient (ϕ_{ec})	0°
Densities:	
Melt (ρ_m)	5.71 g/cm^3
Crystal (ρ_s)	5.17 g/cm^3
Encapsulant (ρ_e)	1.51 g/cm^3
Ambient (ρ_a)	0. g/cm^3
Melt/encapsulant difference ($\Delta\rho_1$)	4.20 g/cm^3
Encapsulant/ambient difference ($\Delta\rho_2$)	1.51 g/cm^3
Gravitational constant (g)	981 cm/sec^2
Heat capacity of crystal (C_{ps})	0.424 J/gK
Heat of fusion (ΔH_f)	25.1 kcal/g-mol
Melting Temperature (T_f)	1511 K
Newtonian heat transfer coefficients:	
Melt/encapsulant interface (h_1)	0. W/cm^{2}K
Encapsulant/ambient interface (h_2)	7x10^{-4} W/cm^{2}K
Crystal/encapsulant interface (h_3)	0. W/cm^{2}K
Crystal/ambient interface (h_4)	7x10^{-4} W/cm^{2}K
Radiative emissivities:	
Melt/encapsulant interface (ε_1)	0.55
Encapsulant/ambient interface (ε_2)	0.55
Crystal/encapsulant interface (ε_3)	0.55
Crystal/ambient interface (ε_4)	0.55
Surface tensions:	
Melt/encapsulant interface (σ_1)	700 dyne/cm
Encapsulant/ambient interface (σ_2)	100 dyne/cm
Stefan-Boltzmann Constant (σ^*)	5.67x10^{-12} W/cm^{2}K^4
Thermal conductivities:	
Melt (k_m)	0.14 W/cmK
Crystal (k_s)	0.07 W/cmK
Encapsulant (k_e)	0.02 W/cmK

parameters listed in Tables 4.2 and 4.3 for the reference case of the parametric sensitivity studies discussed subsequently.

Calculations were performed with the 320 element mesh spaning regions of melt, solid, and encapsulant shown in Fig. 4.2. We solved the equation set by Gaussian elimination using a computer code for banded matrices with the arrow structure. For this discretization of 320 elements, a maximum of 16 in the radial direction and 24 in the axial dimension, the equation set had 1415 unknowns and each iteration required 110 cpu seconds on the Cray 1 computer at Bell Laboratories. We discuss significant improvements in the computational efficiency of the program in ensuing sections with the use of an improved arrow matrix solver (Thomas and Brown, 1986; Thomas, 1987).

Isotherms and interfaces computed for the base case are shown in Fig. 4.3; for this plot and all others of this section, the isotherm spacing is set at 23K (which corresponds with a spacing $\Delta\Theta=0.015$ in the dimensionless temperature field). Here the crystal radius filled almost half the radius of the crucible and the melt/crystal interface was convex into the crystal. The elevation of the melt "shoulder" or holm was approximately 0.45 cm above the mean level of the melt and the deflection stretched less than 1 cm away from the crystal surface. In the region of the three-phase contact at the edge of the crystal, the isotherms in all three phases were very curved, radically different from the nearly constant radial temperature fields necessary for a one-dimensional heat transfer model to be appropriate. Radiation through the encapsulant is an important heat transfer mechanism. The radiative flux through the B_2O_3 acts as a heat sink along the

Table 4.2 Dimensionless groups for LEC gallium arsenide calculations of Section 4.1.

Group	Definition	Base Case Value
Biot Numbers	$Bi_j \equiv \frac{h_j R_c}{k_s}$	j=1,3, 0.0 j=2,4, 0.05
Bond Numbers	$Bo_i \equiv \frac{g R_c^2 \Delta\rho_i}{\sigma_i}$	i=1, 150.0 i=2, 370.0
Peclet Number	$Pe \equiv \frac{V_p R_c \rho_s C_{ps}}{k_s}$	0.1
Radiation Numbers	$Ra_i \equiv \frac{\sigma^* \varepsilon_i R_c T_f^3}{k_s}$	all i, 0.8
Stefan Number	$S \equiv \frac{\Delta H_f}{C_{ps} T_f}$	1.0
Thermal Conductivity Ratios:		
Melt/Solid	$K_1 \equiv \frac{k_m}{k_s}$	2.0
Encapsulant/Solid	$K_2 \equiv \frac{k_e}{k_s}$	0.5
Menisci reference pressures (unknowns in Young-Laplace equation)	$\lambda_i \equiv \frac{p_i^o}{\Delta\rho_i g R_c}$	---

Table 4.3 Operating parameters for LEC gallium arsenide calculations of Section 4.1.

Parameter	Base Case Value Dimensional	Dimensionless
Radius of crucible (R_c)	5.0 cm	1.0
Volume of melt (V_m)	392.7 cm^3	3.14
Nominal depth	5.0 cm	1.0
Volume of encapsulant (V_e)	147.5 cm^3	1.18
Nominal thickness	2.5 cm	0.5
Crystal pull rate (V_p,Pe)	2.3 cm/hr	0.1
Crucible wall temperature (T_c,Θ_c)	1660 K	1.1
Ambient temperature (T_a,Θ_a)	1280 K	0.85

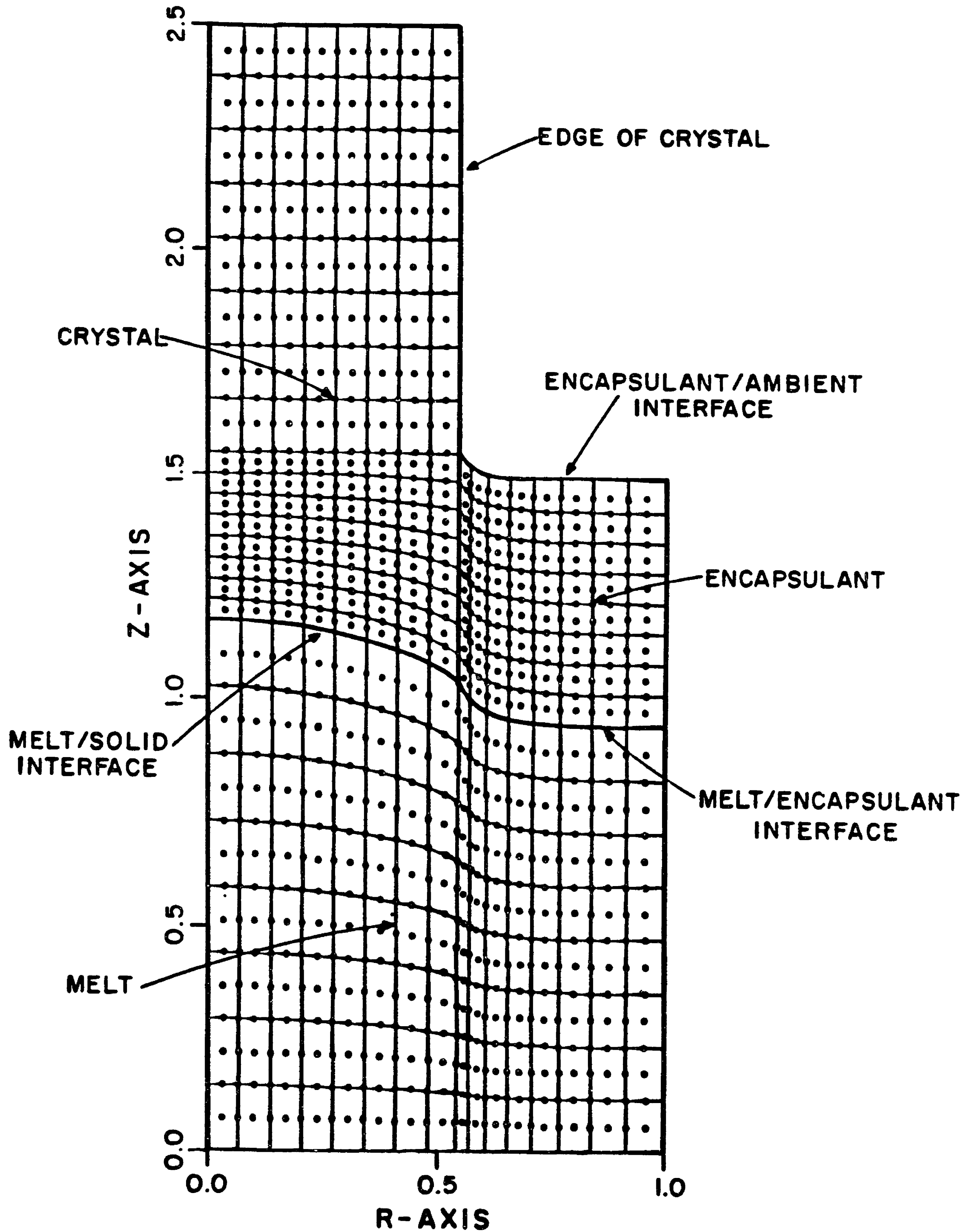

Fig. 4.2 Sample finite element mesh used for LEC gallium arsenide calculations of Section 4.1. Mesh contains 320 elements and 1361 nodes. There are a total of 1415 unknowns for this system.

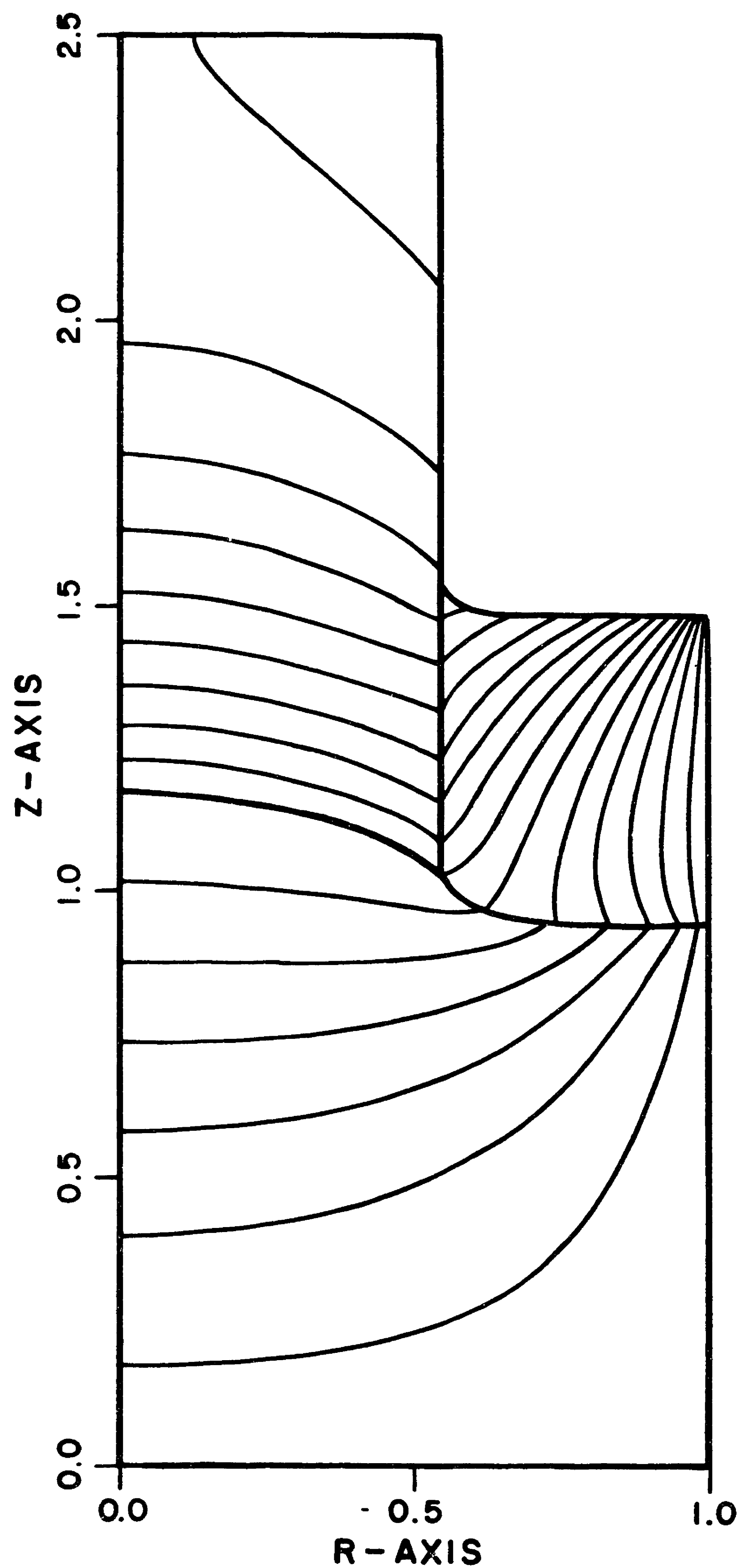

Fig. 4.3 Isotherms and interface shapes for reference case (parameters listed in Tables 4.2 and 4.3). The finite element mesh used in this calculation is shown in Fig. 4.2. Isotherms for all plots of Section 4.1 are incremented by 23K ($\Delta\Theta = 1.5 \times 10^{-2}$).

submerged interfaces and is noted by the change in sign of the temperature gradient across the melt/encapsulant and crystal/encapsulant boundaries.

The accuracy of the finite element calculations was estimated by repeating the calculation of the base case for several finite element meshes smaller than the one pictured in Fig. 4.2. These results are given in Table 4.4 and show the reliablity of finite element approximations constructed with even coarser element discretizations. For example, the crystal radius predicted using a mesh of only 80 elements (391 unknowns) gave a prediction for the steady-state radius that differed only 2 percent from the result for the 320 element mesh.

The sensitivity of the heat transfer model to various operating and thermophysical input data was determined by varying parameters about the base case shown in Fig. 4.3. These results are discussed in the following sections for variations of several important parameters.

4.1.1.1 Pull Rate

Increasing the pull rate increased the amount of heat liberated per unit area of the melt/solid interface and caused it to become more concave with respect to the crystal. The rearrangement of the temperature field necessary to accommodate the extra latent heat drove the melt/solid interface higher. The need to dissipate the greater amount of latent heat coupled with the geometrical effects of surface tension forming the melt/encapsulant interface then decreased the radius of the crystal. Results for varying the pull rate between 2.3 cm/hr (the base case of Pe=0.1) and 18.7 cm/hr (Pe=0.8) are shown

Table 4.4 Results of Mesh Refinement

	Mesh Size I	Mesh Size II	Mesh Size III
	80 elements 391 unknowns	180 elements 823 unknowns	320 elements 1415 unknowns
Crystal Radius, R	0.5575 (0.0222)*	0.5486 (0.0059)	0.5457
Melt/Solid Interface			
Centerline Height, $H_0(0)$	1.1809 (0.0073)	1.1745 (0.0018)	1.1724
Deflection, $H_0(0)-H_0(R)$	0.1450 (0.0454)	0.1402 (0.0108)	0.1387
Melt/B_2O_3 Meniscus			
Height at Crystal, $H_1(R)$	1.0359 (0.0021)	1.0343 (0.0006)	1.0337
Deflection, $H_1(R)-H_1(1)$	0.0989 (0.0928)	0.0925 (0.0221)	0.0905
Axial Temperature Gradient at Melt/Solid Interface			
Centerline, $-(\frac{\partial\theta}{\partial z})_m$	0.0928 (0.0153)	0.0919 (0.0055)	0.0914
Edge of Crystal, $-(\frac{\partial\theta}{\partial z})_m$	0.205 (0.0955)	0.212 (0.0230)	0.217
Crystal Temperature at Top of B_2O_3			
Centerline, $\Theta(0,H_2(R))$	0.9231 (0.0018)	0.9218 (0.0004)	0.9214
Edge, $\Theta(R,H_2(R))$	0.8977 (0.0012)	0.8969 (0.0003)	0.8966
CPU time, secs. on CRAY 1	10	---	109.8

* Numbers in parentheses are relative differences between results for smaller meshes and mesh III, computed as $|(I)-(III)|/(III)$.

in Fig. 4.4 as plots of the isotherms in the melt, crystal and encapsulant. The configurations of the finite-element mesh for these different pull rates are shown in Fig. 4.5. Figure 4.6 demonstrates the convergence rate typical of the Newton iteration scheme for the cases shown in Fig. 4.5. Each iteration was started with the reference case solution of Pe=0.1, and the last iterations achieved quadratic convergence as expected for Newton's method.

The axial temperature profiles along the centerline (r=0) and the crystal edge (r=R) are presented in Fig. 4.7. Increasing the pull rate was expected to increase the temperature gradient in the crystal and decrease the temperature gradient in the melt at the solidification front. As seen in Fig. 4.7, these trends were evident at the crystal center but not at the edge. Radiative and conductive heat transfer to the surroundings was intense enough to counterbalance the local increase in heat flux caused by the higher pull rates through a rearrangement of the temperature field, crystal size, and meniscus shape. At the pull rate of 2.3 cm/hr the gradient in the crystal at the centerline is -85.5 K/cm, a value which is reasonable for the growth of GaAs. Although the interfacial temperature gradient measured from the melt decreased with increasing pull rate, it did not reach zero, even at the highest growth rate. For Pe=0.8, the dimensional temperature gradient was -2.4 K/cm in the melt.

Over the range of pull rates 2.3-18.7 cm/hr, the crystal radius decreased from 2.73 cm to 1.70 cm. The proposed relation between the steady-state crystal radius and pull rate for Czochralski growth derived by Billig (1955) predicted that the crystal radius was proportional

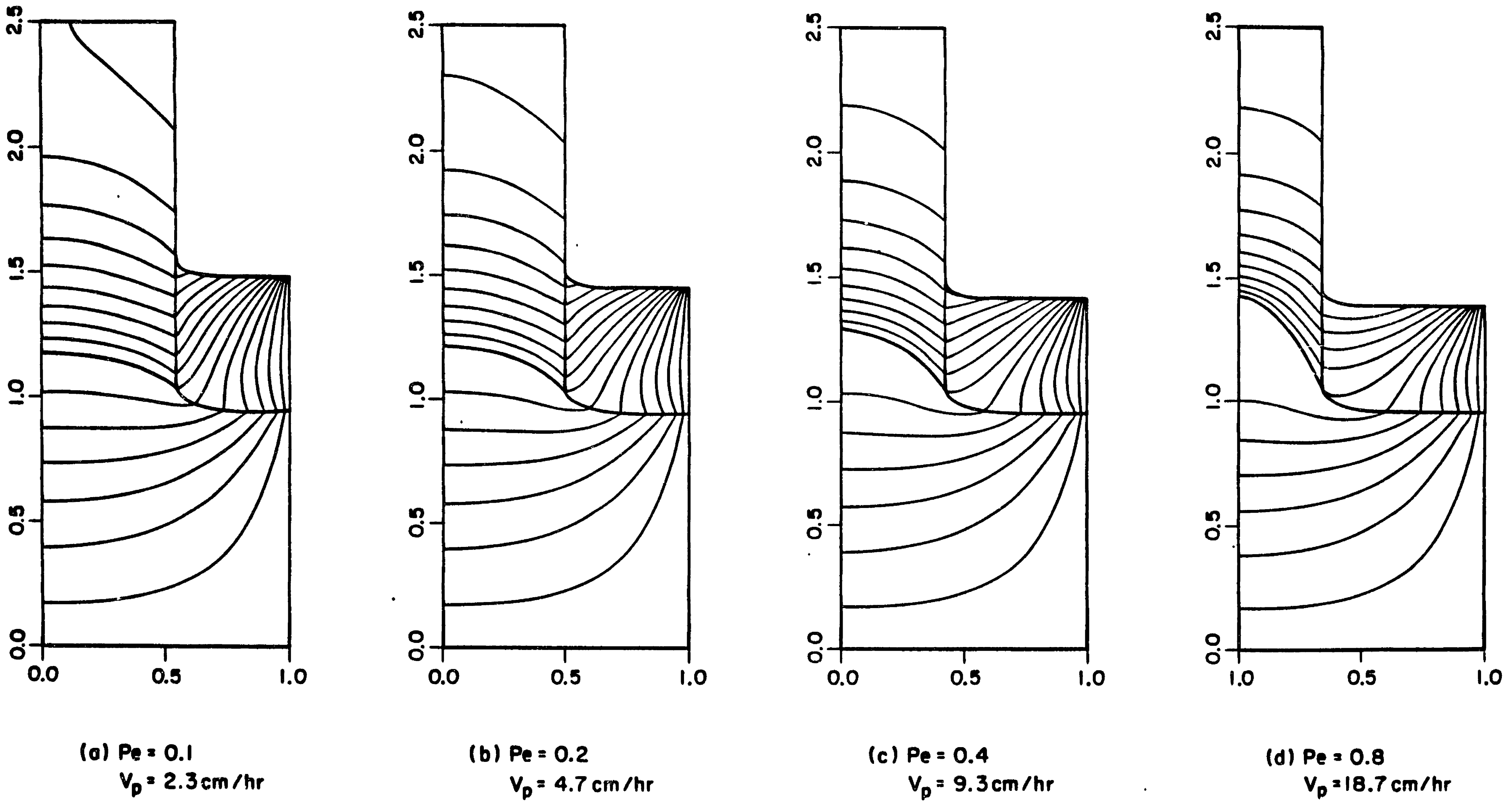

Fig. 4.4 Changes in isotherms and interface shapes with increasing pull rate. All other parameters are held fixed at those listed in Tables 4.2 and 4.3.

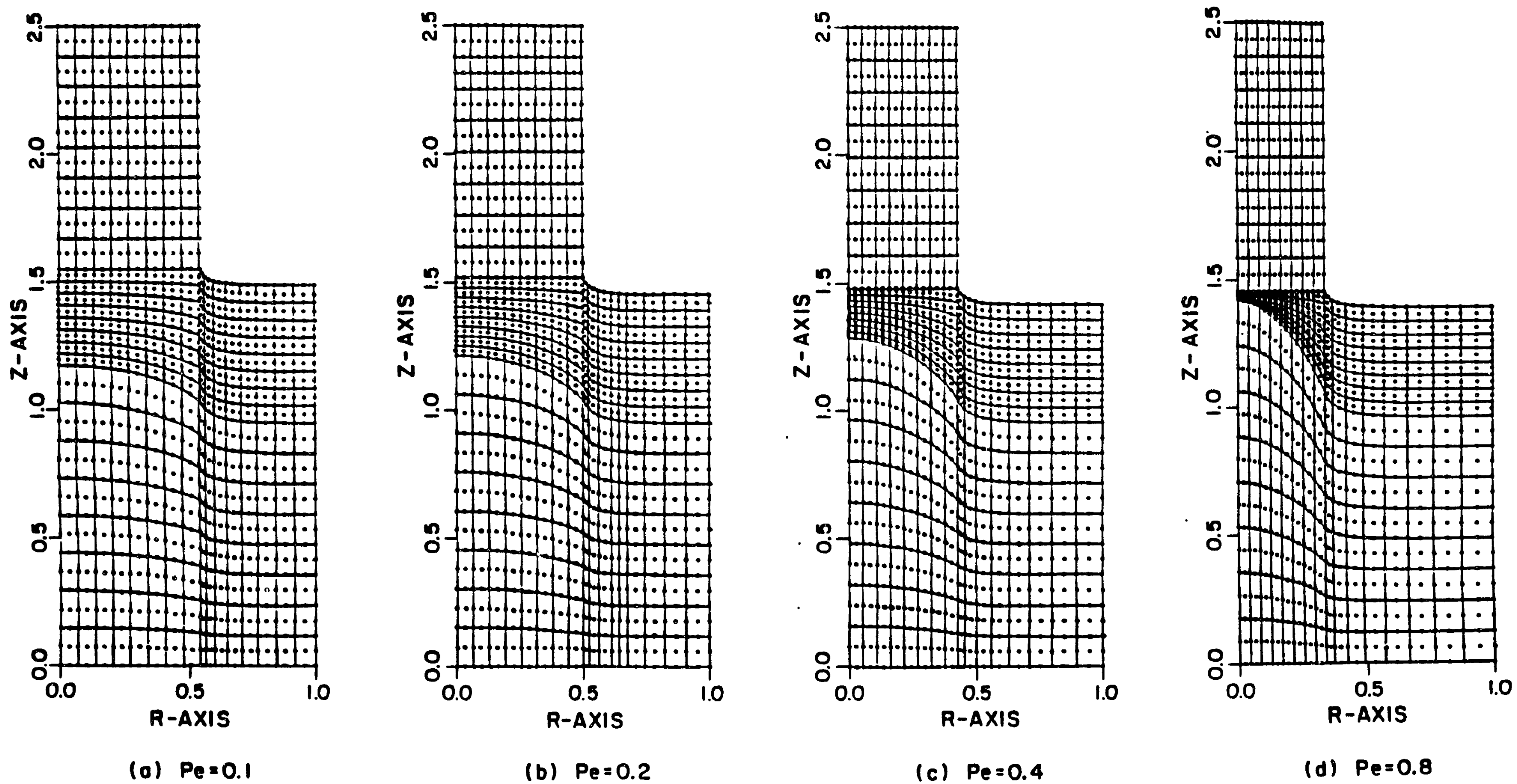

Fig. 4.5 Finite element meshes for the isotherms and interface shapes shown in Fig. 4.4.

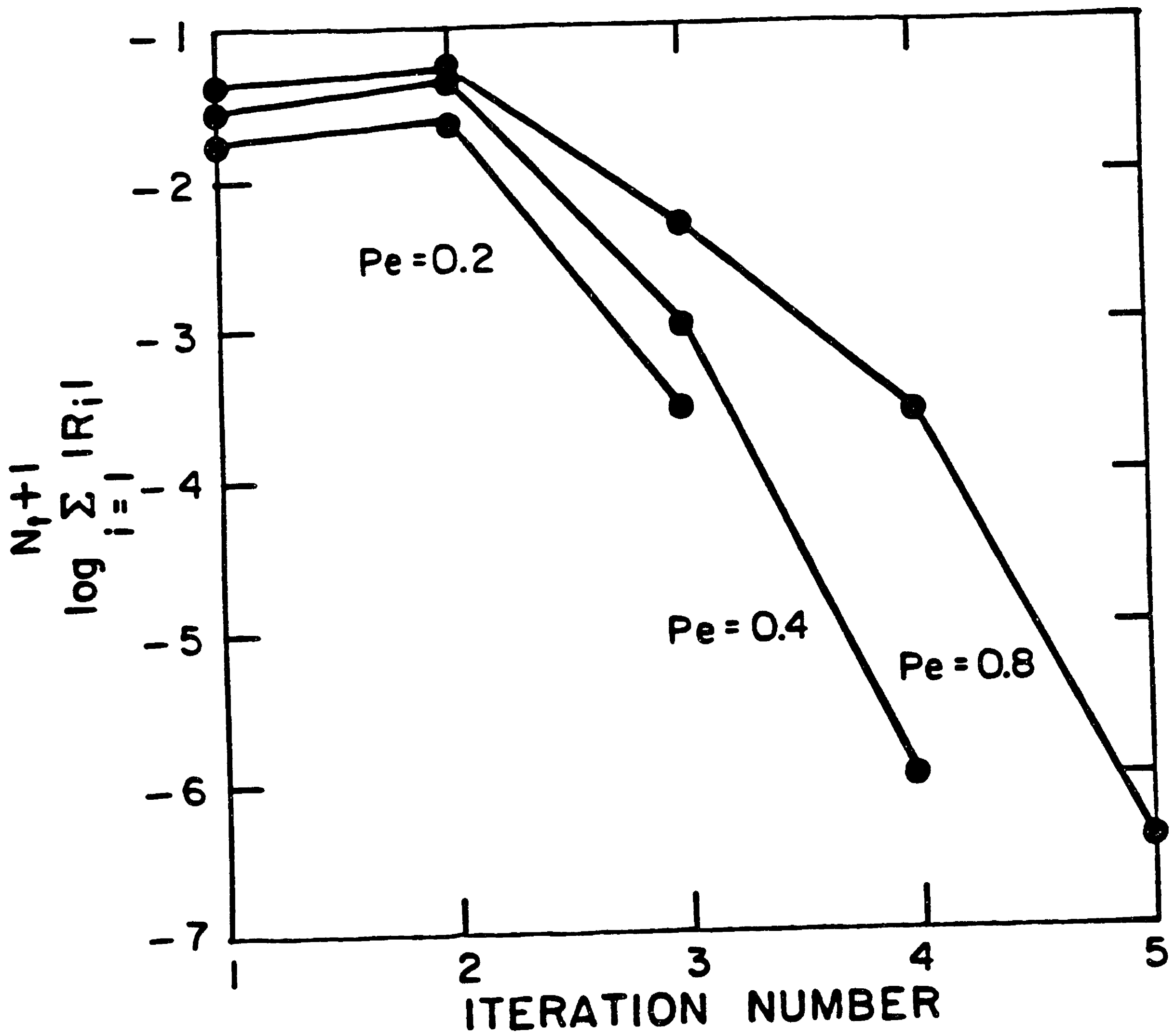

Fig. 4.6 Convergence of finite element solution with Newton iterations for calculations shown in Fig. 4.4.

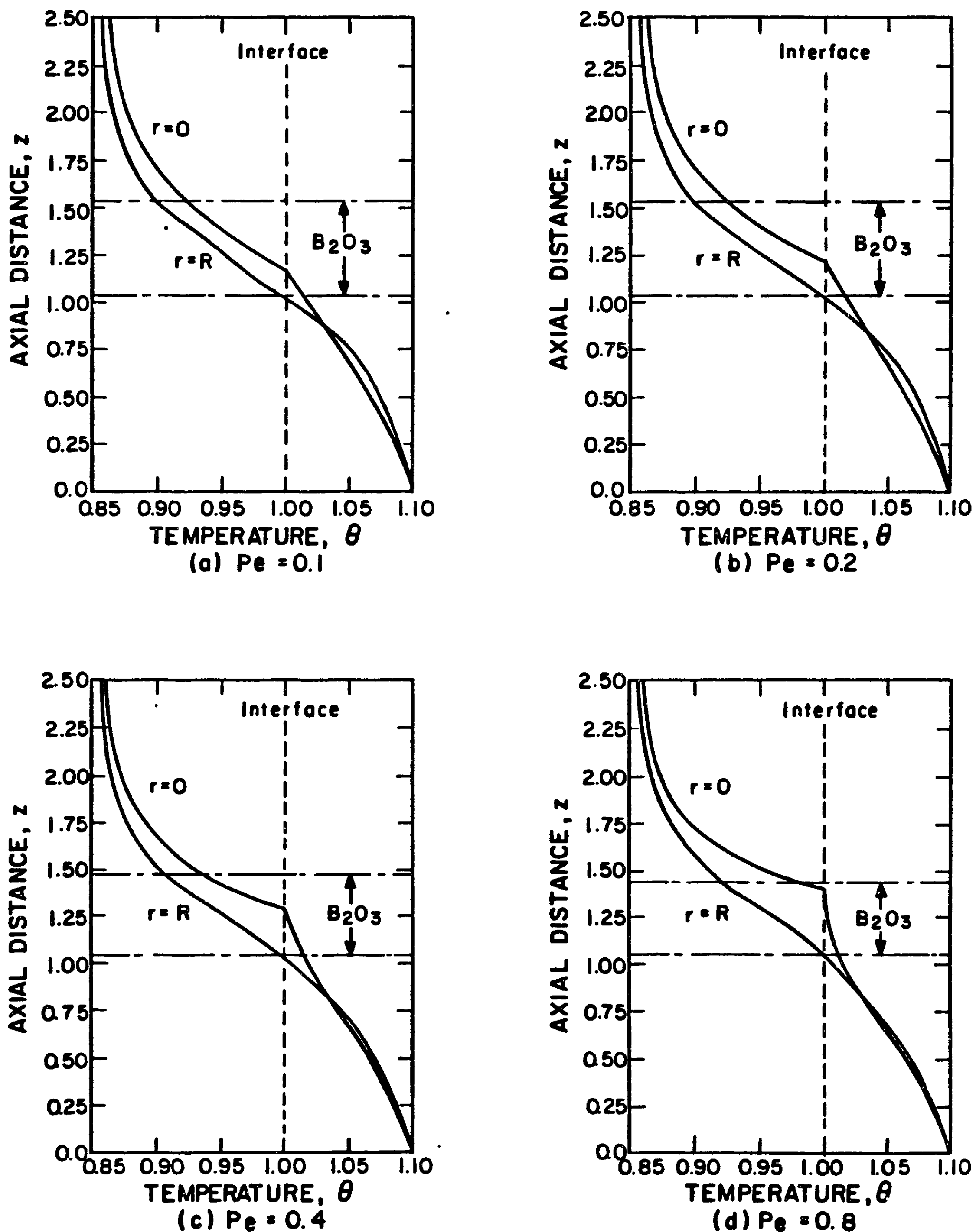

Fig. 4.7 Variation of axial temperature profiles along centerline ($r = 0$) and at the crystal radius ($r = R$) for pull rates of Fig. 4.4.

to the inverse square of the pull rate, or in dimensionless form, $R \sim Pe^{-2}$. Fitting this form to the results of the calculations of this section leads to the equation

$$R = 0.0776/Pe^2. \tag{4.1}$$

Kim et al. (1983) have suggested that the radius and pull rate of a Czochralski crystal be correlated as $R = A/(Pe+B)$ where A and B are empirical constants set by the heat transfer in the furnace. Fitting the data for Pe=0.1 and 0.2 to determine A and B yields

$$R = 0.568/(Pe + 0.941). \tag{4.2}$$

Both of these results are plotted along with the finite element results in Fig. 4.8 for the entire range of growth rates. The agreement with the correlation of Kim et al. is excellent (the correlation coefficient was 1.0000), whereas the derivation of Billig poorly describes the finite-element results (correlation coefficient of 0.68). This is not surprising, because Billig's assumptions of a thermally supercooled melt next to the interface and a one-dimensional crystal temperature fields in this region were not met by the results of the two-dimensional thermal-capillary model used here. The melt/solid interface height, crystal radius, and axial melt temperature gradients at the centerline of the solidification front are summarized in Table 4.5 for the growth rate calculations of this section.

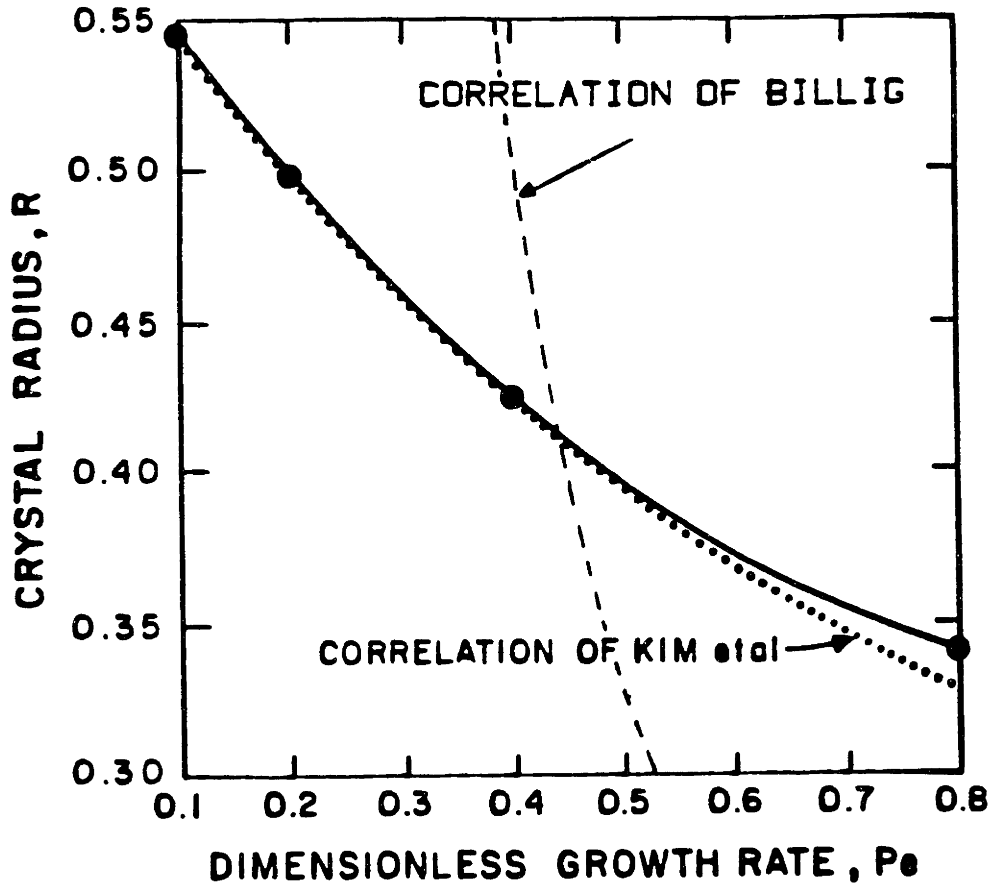

Fig. 4.8 Variation of crystal radius as a function of pull rate. All other parameters were held fixed at reference values. The dashed curves represent the relations of Billig (1955), eq. (4.1), and Kim et al. (1983), eq. (4.2).

Table 4.5 Results for Calculations with Varying Crystal Pull Rate.

Pull Rate (cm/hr)	Peclet Number Pe	Melt-Solid Interface Height		Crystal Radius		Temperature Gradient at $H_o(0)$	
		$H_o(0)$	$\tilde{H}_o(0)$ (cm)	R	$\tilde{R}$ (cm)	$\left.\frac{d\theta_m}{dz}\right\|_{H_o(0)}$	$\left.\frac{d\tilde{T}_m}{d\tilde{z}}\right\|_{\tilde{H}_o(0)}$ (Kcm^{-1})
2.33	0.1	1.1724	5.86	0.5457	2.73	-9.14×10^{-2}	-27.6
4.67	0.2	1.2141	6.07	0.4987	2.49	-7.25×10^{-2}	-21.9
9.33	0.4	1.2874	6.44	0.4240	2.12	-4.10×10^{-2}	-12.4
18.66	0.8	1.4220	7.11	0.3403	1.70	-7.87×10^{-3}	-2.4

4.1.1.2 Encapsulant Volume

The effect of encapsulant geometry changes on the temperature field and the crystal radius was complicated by the volume interaction of the depth of the B_2O_3 with the size of the crystal. The variation of this depth for the same volume of B_2O_3 and different growth rates is seen in Fig. 4.4. The depth of the layer measured at the crucible wall varied from 2.7 to 2.1 cm as the pull rate was changed from 2.3 to 18.7 cm/hr.

Calculations were carried out for differing volumes of encapsulant with all other operating parameters held fixed at the values for the base case; the isotherms and interfaces for these calculations are shown in Fig. 4.9. The calculations for V_e=0 were for a system without the encapsulant layer and with radiation and convection directly from the now melt/gas meniscus to the ambient. As expected, increasing the amount of the low-conductivity encapsulant inhibited heat transfer from the melt and crystal and resulted in small crystals for a given pull rate (2.3 cm/hr). Several features of these calculations were much less obvious.

The melt/crystal interface was more concave for the calculations with deeper encapsulant. Increasing the depth of the B_2O_3 caused a greater portion of heat transfer from the melt to occur by conduction through the crystal. Consequently, the temperature field was more two-dimensional near the tri-junction of melt, crystal, and encapsulant; however, the temperature gradient at the melt/crystal interface changed little with increasing the depth of the encapsulant.

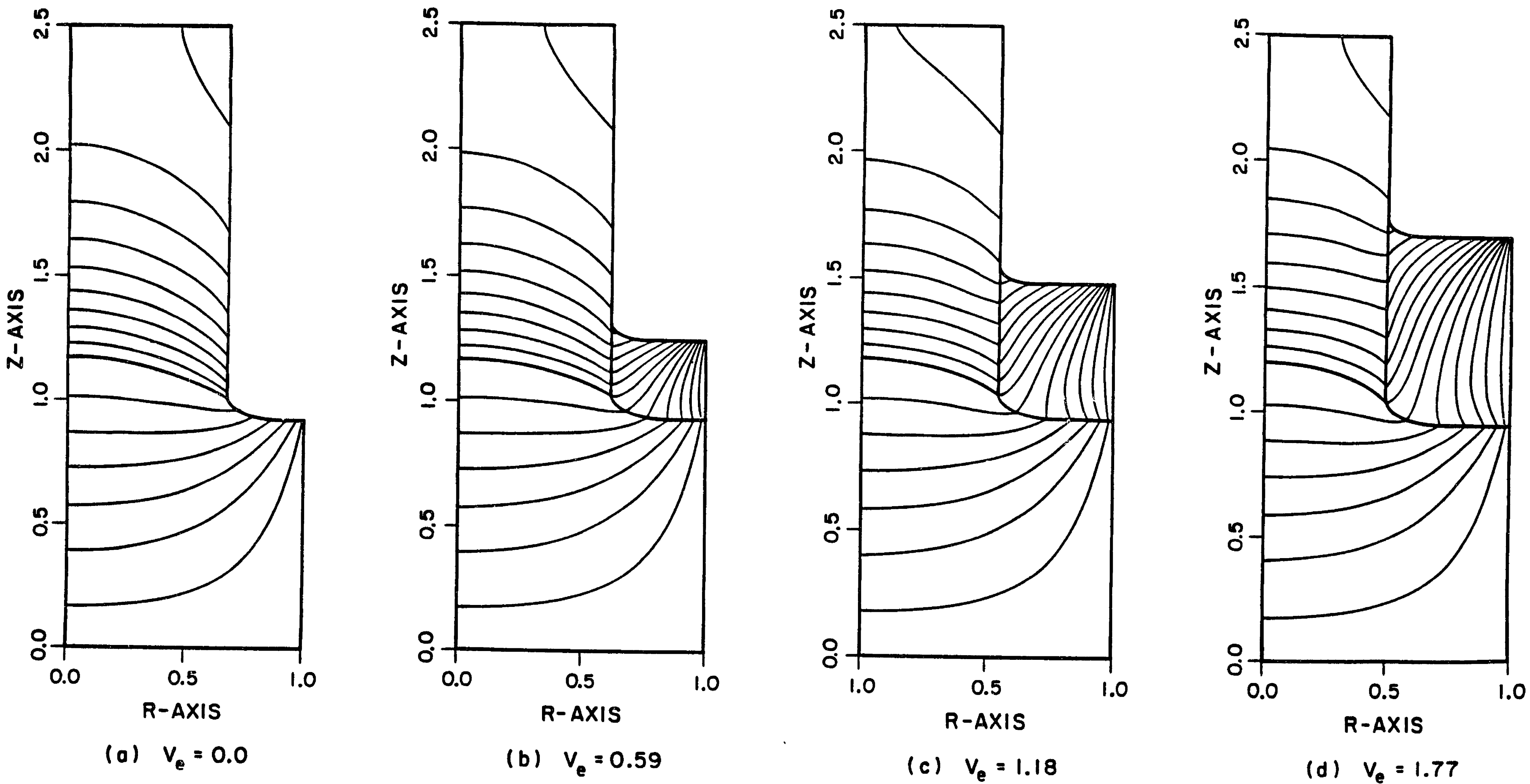

Fig. 4.9 Changes in isotherms and interface shapes with the volume of the encapsulant layer. All other parameters are held fixed at the values listed in Tables 4.1 and 4.2.

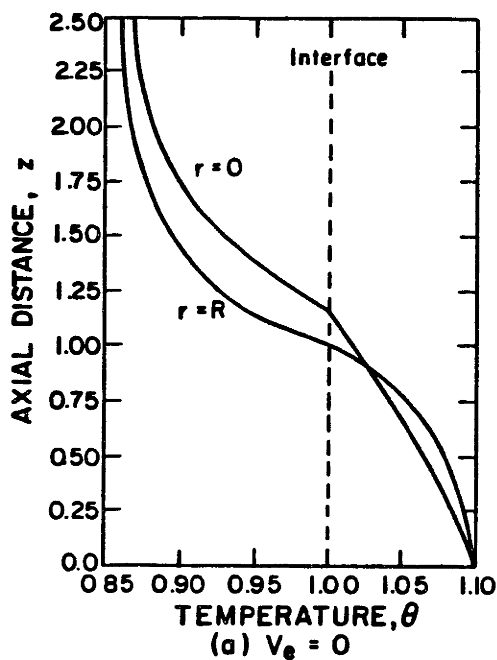

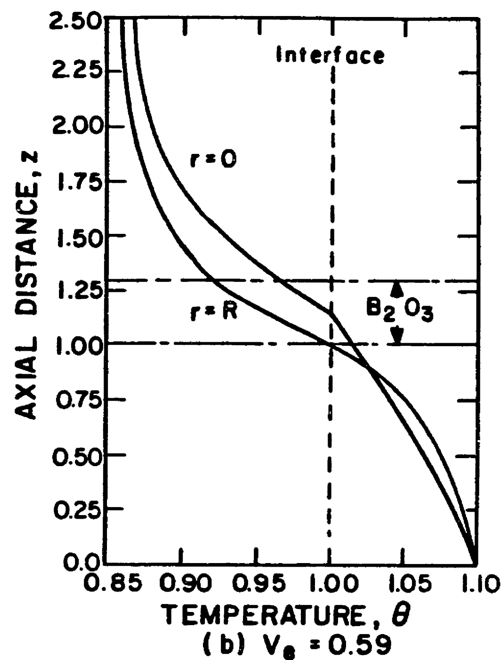

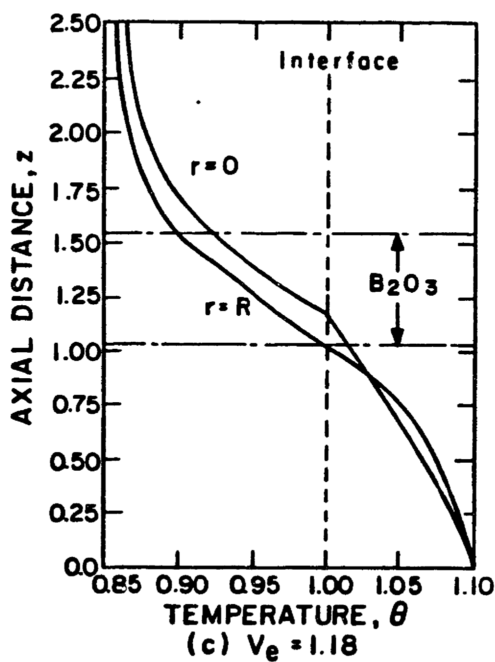

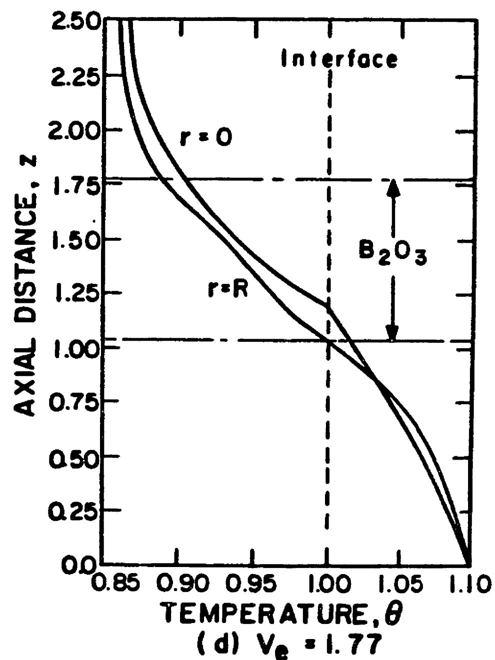

Fig. 4.10 Variation of axial temperature profiles along centerline ($r = 0$) and crystal radius ($r = R$) with increasing depth of the encapsulant.

Table 4.6 Variations of melt/crystal interface deflection, crystal radius, and interfacial temperature gradient with the depth of the encapsulant layer.

V_E	Thickness of B_2O_3 At Edge of Crucible		Melt-Solid Interface Height		Crystal Radius		Temperature Gradient at $H_o(0)$	
	$[H_2(1)-H_1(1)]$	$[\tilde{H}_2(R_c)-\tilde{H}_1(R_c)]$ (cm)	$H_o(0)$	$\tilde{h}_o(0)$ (cm)	R	$\tilde{R}$ (cm)	$\left.\frac{d\theta_m}{dz}\right\|_{H_o(0)}$	$\left.\frac{d\tilde{T}_m}{d\tilde{z}}\right\|_{\tilde{H}_o(0)}$
0	0	0	1.166	5.83	0.663	3.31	-9.05×10^{-2}	-27.4
0.589	0.315	1.57	1.162	5.81	0.626	3.13	-9.22×10^{-2}	-27.9
1.178	0.539	2.70	1.172	5.86	0.546	2.73	-9.14×10^{-2}	-27.6
1.767	0.755	3.77	1.194	5.97	0.500	2.50	-8.18×10^{-2}	-24.7

The axial temperature profiles along the centerline and the perimeter of the crystal are shown in Fig. 4.10 for the base case and three different depths of B_2O_3. The decrease of the absolute interface deflection caused by increasing the amount of encapsulant is recognized here as a decrease in the radial temperature difference between the center and periphery of the crystal. In each case, the maximum axial temperature gradient occurred at the melt/solid interface. The relative defection of the melt/solid interface measured as $[H_0(0) - H_0(R)]$ increased with increasing depth. Variations of melt/crystal interface deflection, crystal radius, and interfacial axial temperature gradient in the melt at the centerline are given in Table 4.6.

4.1.1.3 Heat Transfer Boundary Conditions

The sensitivity of the predictions for crystal shape and temperature field to changes in the heat loss at the surfaces of the system by radiation and gaseous convection was determined by a sequence of calculations with varying values of ambient temperature Θ_a, Biot number (for heat transfer to the ambient), and the emissivities along the various surfaces. Each of these computations is described below.

The isotherms and interface shapes computed for an increased ambient temperature of Θ_a=0.9 (T_a =1360 K) is shown in Fig. 4.11. This 7 percent increase in the black body temperature of the surroundings decreased radiative and convective heat transfer enough to lower the crystal radius to 1.81 cm from 2.73 cm. The decreases in the radiative heat transfer from the melt/B_2O_3 and crystal/B_2O_3 surfaces was quali-

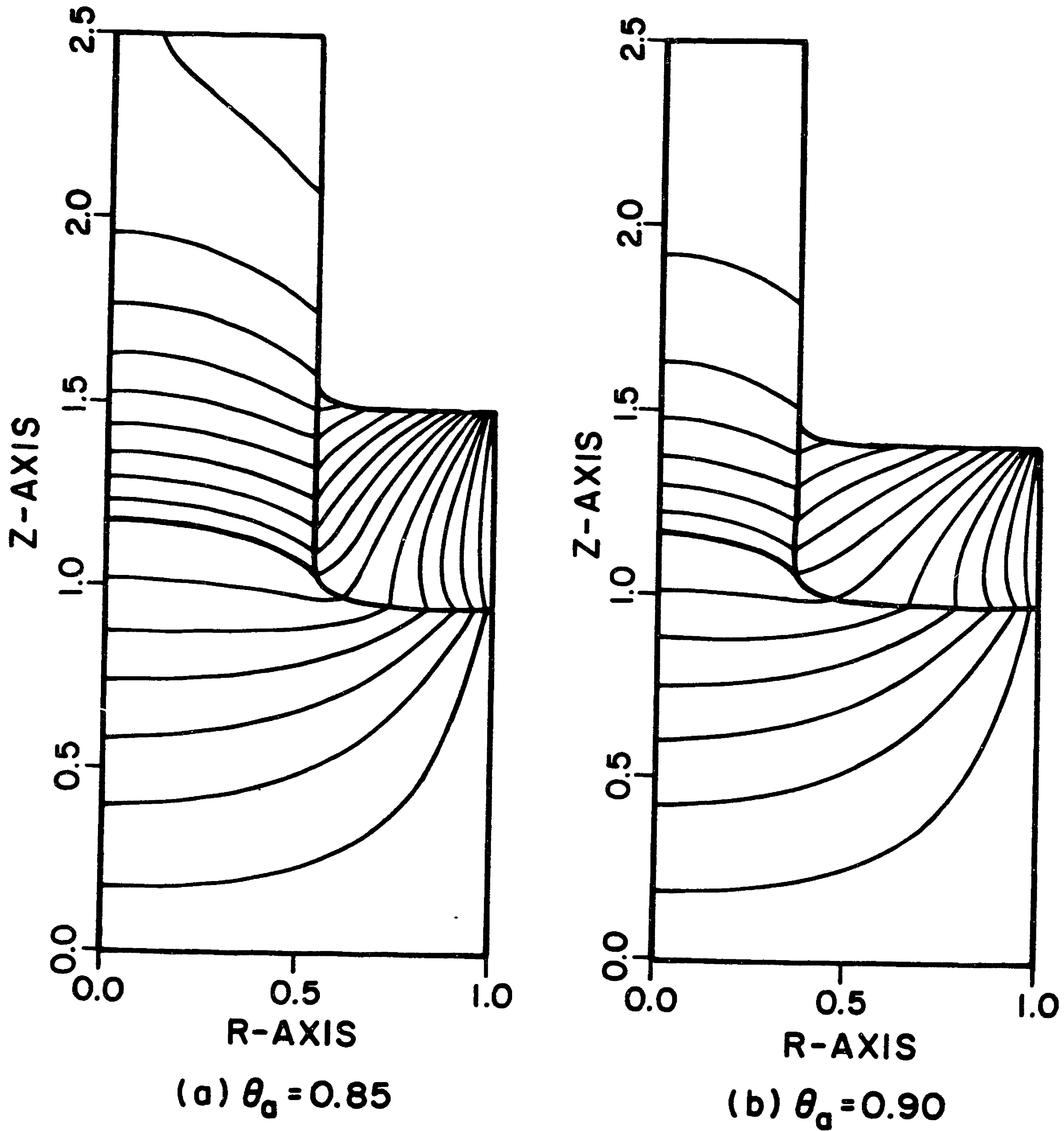

Fig. 4.11 Changes in isotherms and interface shapes with increase in ambient temperature. All other parameters are held fixed at those of reference case.

tatively noticed by the decrease in the magnitudes of the jumps in normal temperature gradient along these boundaries.

The strong sensitivity of the steady-state radius to ambient temperature motivated further investigation of the importance of the individual components of the interfacial heat fluxes. The effect of a factor of five increase in the Biot number along the boundaries with the gas is shown in Fig. 4.12, for Bi=0.01 and all other parameters fixed at the values for the base case. The crystal radius changed less than 0.1 percent, thus demonstrating the relatively minor role that convective cooling plays in the overall heat transfer in the system.

The importance of the description of radiation both through the encapsulant and to the environment was verified by the sensitivity of the results to changes in the emissivities along the surfaces. Isotherms and interface shapes are shown in Fig. 4.13 for two different sets of Radiation numbers. The first corresponded to a factor of two decrease in ε along all radiating boundaries (Ra_i=0.4), whereas the second was performed with lower emissivities on only the surfaces with the encapsulant, i.e. $Ra_{1,3}$=0.4 and $Ra_{2,4}$=0.8. Halving the radiative flux along all the surfaces drastically decreased the radius of the crystal to 0.61 cm (see Fig. 4.13b), flattened the melt/crystal interface, and increased the temperature gradient next to the solidification front. The added resistance to radiation along both menisci inhibited radiation through the B_2O_3 to the extent that the temperature gradients on either side of the boundaries with the encapsulant had the same sign.

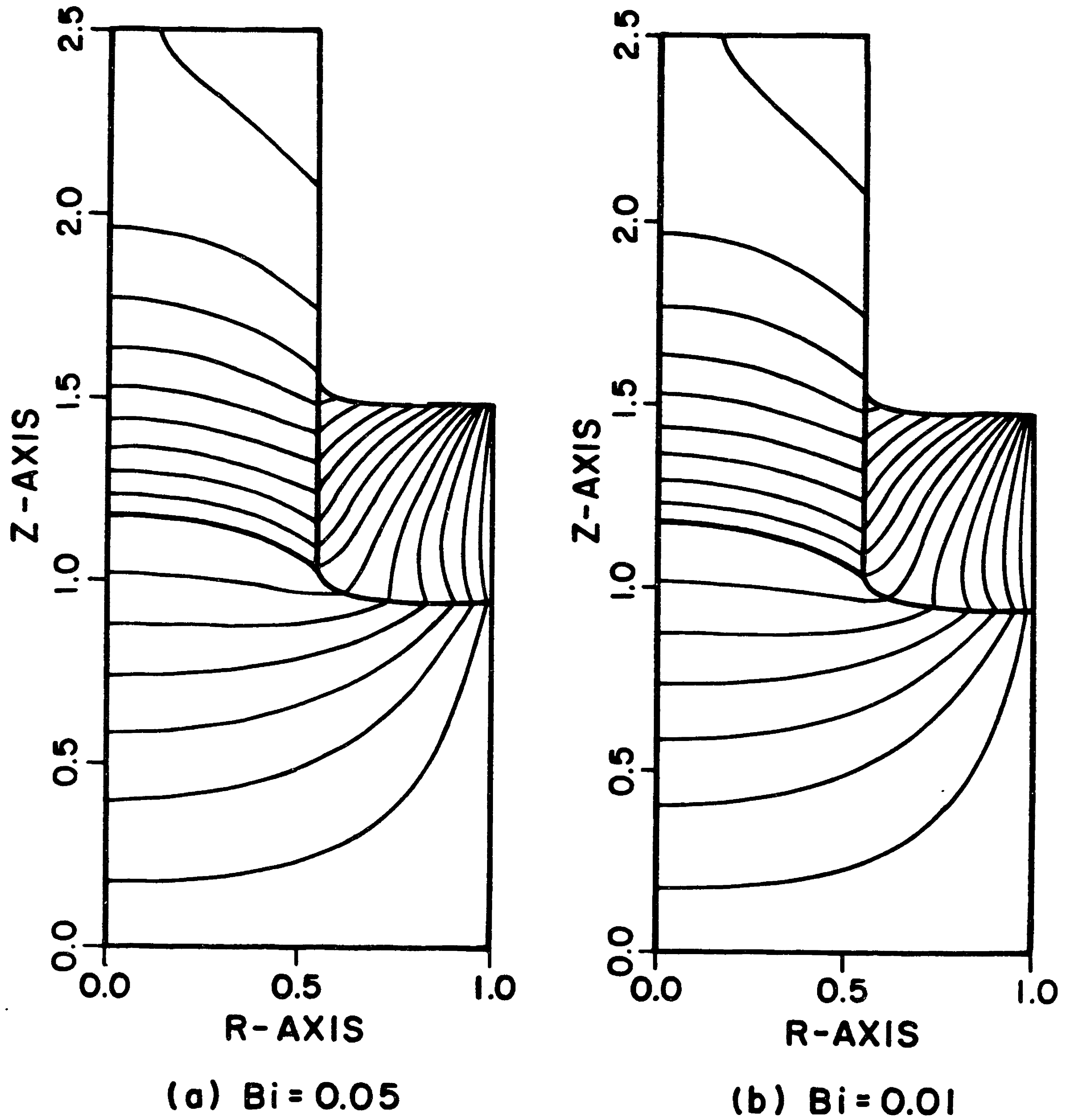

Fig. 4.12 Variation of isotherms and interface shapes with decrease of convective heat transfer coefficient (Biot number). All other parameters are held fixed at the values listed in Tables 4.1 and 4.2.

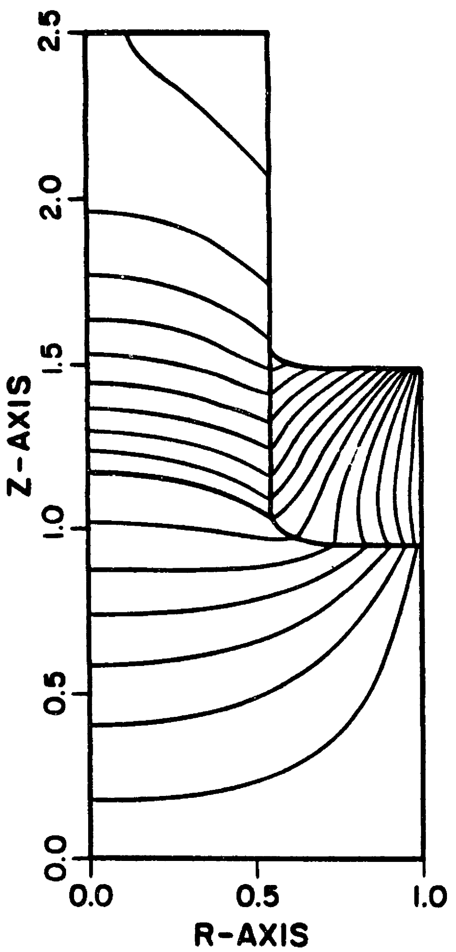

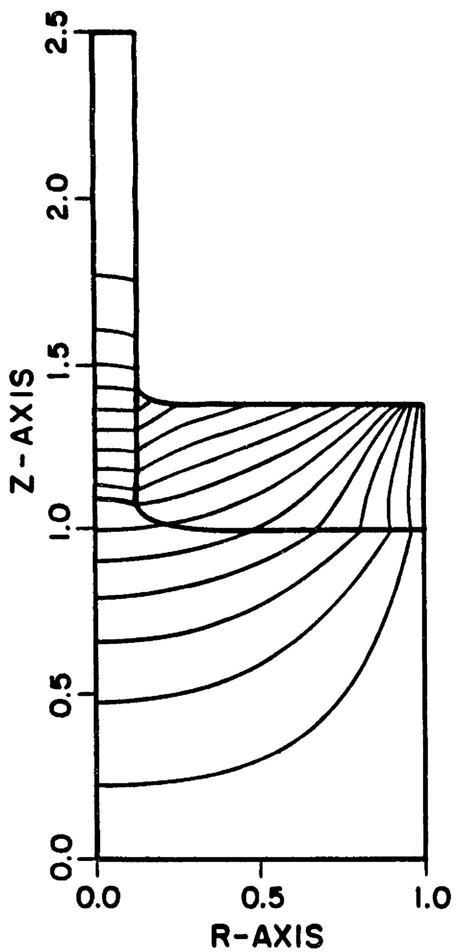

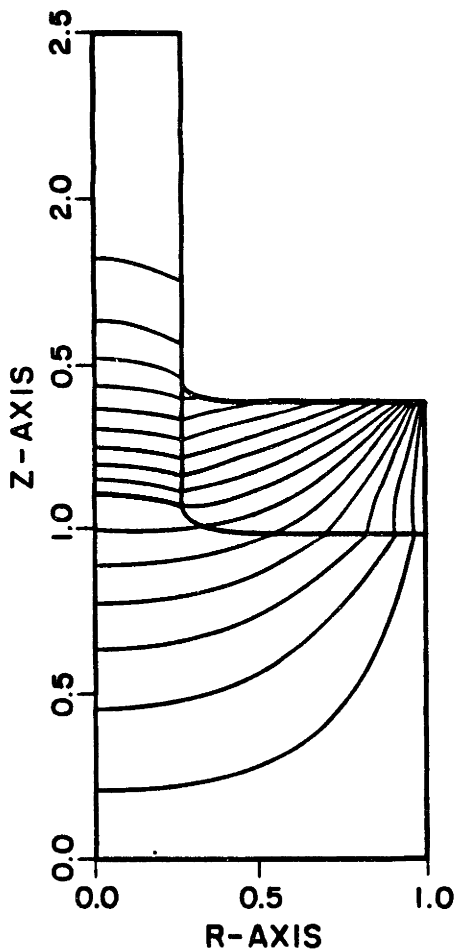

Fig. 4.13 Changes in isotherms and interface shapes with a decrease in surface emissivities (Radiation numbers). (a) Reference case, $Ra_i = 0.8$. (b) All $Ra_i = 0.4$. (c) $Ra_{1,3} = 0.4$ and $Ra_{2,4} = 0.8$. All other parameters are held fixed at those of reference case.

Specifying the emissivity along interfaces covered by the B_2O_3 to be lower than along surfaces bordering the ambient lowered the influence of radiation but did not eliminate it, as is seen by examining the temperature gradients along the internal surfaces in Fig. 4.13c. Here the crystal radius was decreased to 1.29 cm as compared to 2.73 cm for the base case. The interface shape was flattened and the axial temperature gradient was increased. The largest value of the gradient along the center of the crystal still appeared at the solidification interface; however, the gradient was more uniform near the melt/crystal surface than in the base case. This calculation also showed that most of the heat leaving the system is from the region near the melt/ crystal/encapsulant tri-junction; indeed, the accurate assessment of heat transfer and geometry of this region is crucial to modeling this system, as will be further demonstrated in the results of Section 4.2.

4.1.2 Discussion

The two-dimensional model for liquid encapsulated Czochralski growth presented here was the first to give simultaneous predictions of steady-state crystal shape and temperature field in this system (Derby et al., 1985). The accuracy of the calculations depend on the accuracy of the heat transfer model used in each phase and across phase boundaries and on the reliability of the thermophysical properties used in the model. These calculations for the prototype of a small-scale growth system predict reasonable dependence of the crystal radius on growth rate, but tend to allow higher growth rates and lower axial

temperature gradients than seen in practice. Muller et al. (1983) have recently measured temperature gradients in a InP crystal growing in a LEC system. They report temperature gradients near 80 K/cm at the interface and higher gradients as the crystal is pulled through the B_2O_3. The melt/crystal interface was convex to the crystal in all the experiments reported in the work of Muller et al. (1983). In our calculations, the crystal axial temperature gradient at the interface was determined to be -85.5 K/cm, a surprisingly similar value; however, the maximum axial temperature gradient occurred at the solidification front and the interface was concave. The qualitative discrepancies between our results and these experiments may be linked to the method used by Muller et al. (1983) for measuring axial temperature profiles. In their experiment, the thermocouple was moved upward through the melt and incorporated into the growing crystal during seeding at the initial stages of growth. Enough crystal had not been grown so that the assumption of a uniform radius protruding from the encapsulant was not satisfied. Under these conditions, heat transfer to the ambient changes continuously with time, so that the experiments can only be simulated using a transient analysis which accounts for the variations of the radius with time.

Also, the heat transfer through the crucible sides and bottom also plays an important role in setting the magnitude and curvature of the radial temperature gradients and interface shape in the LEC system. Heat losses through the usually unheated bottom of the crucible cause the temperature at the center of the crucible to be lower than at the sides and can result in convex interfaces and the formation

of solid on the bottom of the crucible. Radiation from the wall of the bare crucible also increases the temperature along the edge of the boule and makes the interface more convex. Further, the radiative character of the encapsulant can radically affect heat transfer from the surface of the melt and can force heat loss to follow a conduction path predominantly through the crystal, thereby resulting in a convex interface. All of these effects may be responsible for the differences between the experimental results of these researchers and our calculations. We address these issues in a more detailed manner in the following sections.

The simple model used for radiation through the B_2O_3 and to the surroundings is a major approximation to reality in our modeling of LEC growth. The limited calculations on the sensitivity to the parameters in the radiation model suggest that small changes in the ambient temperature and in the emissivities can make large differences in the crystal radius and in the temperature distribution in the crystal. A more complete model of radiation along these surfaces is probably needed before computations can be compared quantitatively with experiments. Several improvements can be easily built into the framework of the finite-element/Newton method. First, view factors and ambient temperature profiles more appropriate for the Czochralski geometry can be incorporated into the expressions for the surface fluxes, as first done by Rea (1981) and Van der Hart and Uelhoff (1981) in one-dimensional heat transfer analyses of conventional Czochralski growth and later by Ramachandran and Dudukovic (1985), Wouters (1985), and Atherton et al. (1986) for two-dimensional simulations. This complication will

couple together all temperatures along the radiating surfaces and hence partially destroy the banded structure of the portion of the Jacobian matrix based on temperature sensitivity by creating full columns and rows in the matrix for all entries corresponding to nodes along the radiating surfaces, possibly making other quasi-Newton iteration schemes attractive (see Atherton et al., 1986).

A more serious limitation of any modeling of LEC growth may be the lack of information on radiation through the B_2O_3. The assumption of total transparency of this molten glass is undoubtedly poor especially when even a small amount of water is present in the encapsulant layer (AuCoin et al., 1979; RASA Industries, 1981). More complex heat transfer models that account for absorption in the B_2O_3 and for reflected radiation are probably not justified without a better experimental data on the radiation properties of B_2O_3. We examine the limiting cases of a totally transparent and a totally opaque encapsulant layer in the calculations of the following sections.

Even with the simple radiation model the complete calculation of steady operating states for a LEC system is a powerful tool for understanding the interactions of various heat transfer mechanisms and capillarity. Moreover, the numerical method laid out in Chapter 3 is the basis for studies of stability of the entire growth process, for the determination of transfer functions for control algorithms and for complete simulation of transients in the process. Each of these extensions is made feasible because of the use of the Newton iteration scheme. The Jacobian matrix used at each step in this iterative procedure is needed in computer-aided algorithms for the calculation

of parametric sensitivity and stability (Brown et al., 1980; Yamaguchi et al., 1984) and in fully-implicit methods for time integration of the dynamic problem (Derby and Brown, 1986a,d; Ungar and Brown, 1985).

4.2 CZ Silicon and LEC Gallium Arsenide Growth

We extend the work presented in the previous section to include the analysis of Czochralski silicon growth and compare this system with additional calculations for Liquid Encapsulated Czochralski growth of gallium arsenide. In Section 4.2.1, we discuss the CZ Si case and concentrate on the effects of the meniscus shape and the coupled effects of melt volume and radiation from the crucible wall on the overall heat transfer. We continue in Section 4.2.2 with a study of LEC GaAs with an encapsulant which is either totally transparent or opaque to radiation. We also compare a hypothetical CZ GaAs system with the prototype CZ Si simulation of Section 4.2.1. A discussion of these calculations follows in Section 4.2.3.

In the following set of calculations, the crucible temperature is prescribed on the side wall, and heat loss through the bottom of the crucible is approximated by a heat flux from the bottom of the melt. A schematic diagram of this modeling system is presented in Fig. 4.14 for the LEC configuration. A representative finite-element mesh composed of 94 elements for the LEC system is shown in Fig. 4.15. There were a total of 461 equations for the mesh shown in Fig. 4.15; calculations performed on a Data General MV4000 minicomputer took approximately 4 CPU minutes per Newton iteration and converged quadra-

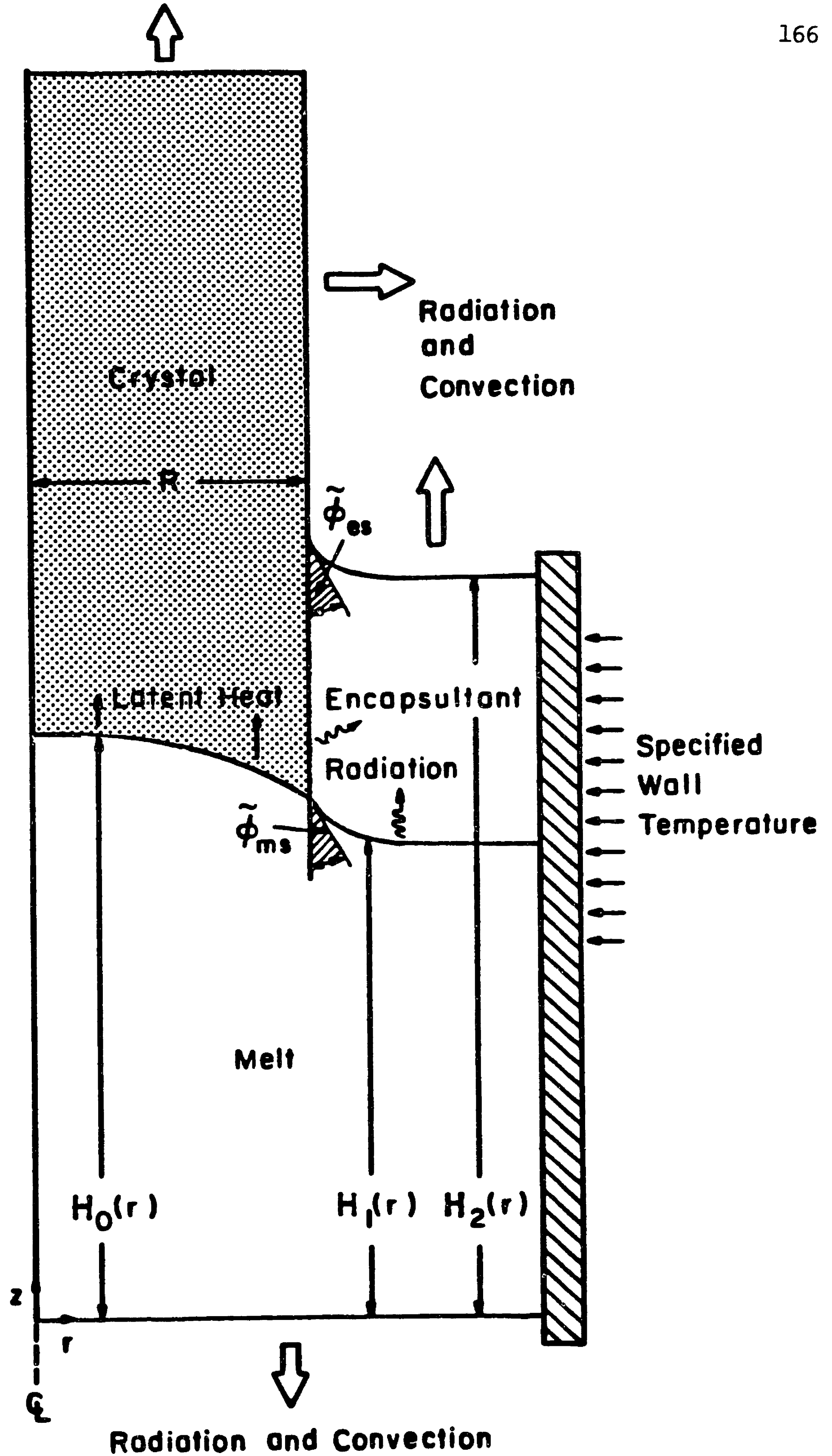

Fig. 4.14 Schematic diagram of prototype LEC system for calculations of Section 4.2.

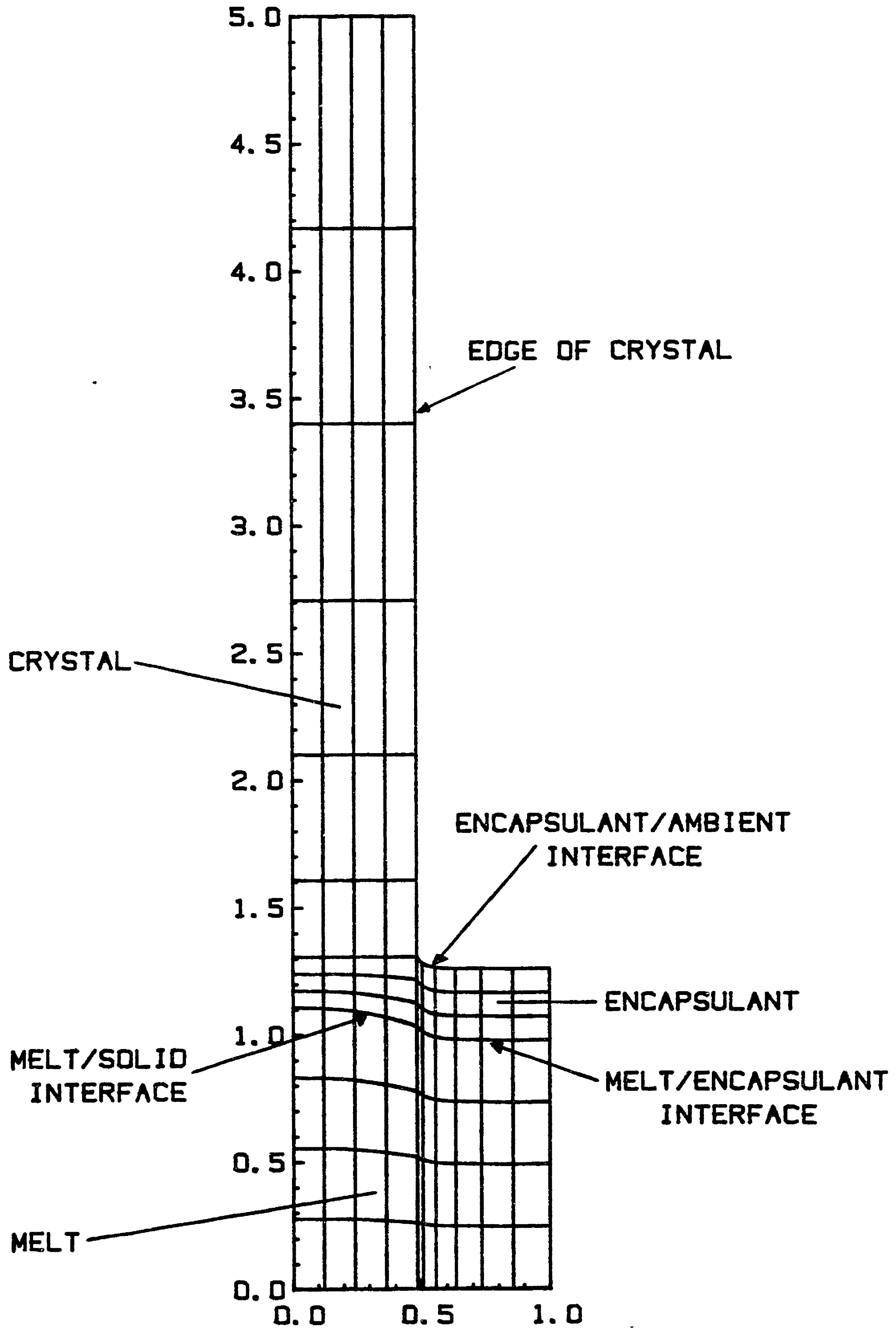

Fig. 4.15 Sample finite element mesh used for LEC gallium arsenide calculations of Section 4.2. Mesh contains 94 elements for a total of 461 unknowns.

tically in 4 or 5 iterations. Scaling this computational time to Cray-1 time produces an estimated 1-2 CPU seconds per iteration. This order-of-magnitude increase in computational efficiency over the calculations of the previous section is attributed to general program streamlining and the use of an efficient Gaussian elimination routine for arrow matrices in the Newton iteration scheme (Thomas and Brown, 1986; Thomas, 1987). The numerical error involved with this mesh size was shown in the previous section to be less than three percent in terms of crystal size, melt/solid interface shape and temperature gradient, well within the error of the estimated thermophysical properties of the silicon and gallium arsenide systems.

4.2.1 Calculations for CZ Growth of Silicon

The thermophysical properties used to model silicon crystal growth are listed in Table 4.7 and in Appendix A. All values, except the thermal conductivity of the solid silicon were assumed to be independent of changes in temperature. The conductivity k_s was assumed to vary as

$$k_s(T) = k_s(T_f)(T_f \; / \; T) \; , \qquad (4.3)$$

where T_f is the melting temperature of silicon (Bell, 1971). The dimensionless groups used in the modeling of a CZ system with a 7 cm radius crucible are listed in Table 4.8. Heat loss from the bottom of the melt through the crucible is modeled by a heat flux condition with the same Biot and radiation number used on other exposed surfaces,

Table 4.7 Thermophysical properties and parameters for Si and GaAs calculations of Section 4.2.

Property	Si	GaAs
<u>Melt</u>		
Density, ρ_m (g/cm^3)	2.42	5.71
Emissivity, ε	0.64	0.55
Specific heat, Cp_m (J/gK)	1.00	0.42
Thermal conductivity, k_m (W/cmK)	0.64	0.14
<u>Crystal</u>		
Density, ρ_s (g/cm^3)	2.30	5.17
Emissivity, ε	0.64	0.55
Specific heat, Cp_s (J/gK)	1.00	0.42
Thermal conductivity, k_s (W/cmK)	0.22(1683K/T)	0.07
<u>Interfaces</u>		
Equilibrium growth angle, $\tilde{\phi}_{ms}$ (°)	11	15
Heat of fusion, ΔH_f, (J/g)	1800	726
Melting temperature, T_f (K)	1683	1511
Meniscus surface tension, σ_m (dyn/cm)	720	700
<u>Parameters</u>		
Crucible radius, R_c (cm)	7.	7.
Heat transfer coefficient, h_j (W/cm^2K)	$7x10^{-4}$	$7x10^{-4}$
Pull rate, V_p (cm/hr)	5.	1.

Property	B_2O_3
<u>Encapsulant</u>	
Density, ρ_e (g/cm^3)	1.51
Emissivity, ε	0. or 1.[1]
Thermal conductivity, k_e (W/cmK)	0.02
<u>Interface</u>	
Meniscus surface tension, σ_e (dyn/cm)	100
Wetting angle, $\tilde{\phi}_{es}$ (°)	5

[1] For transparent or opaque encapsulant, respectively.

Table 4.8 Dimensionless groups used in reference cases for Si and GaAs calculations of Section 4.2.

Dimensionless group	Si	GaAs
Ambient temperature		
far above crucible, θ_a^∞	0.75	0.85
below crucible, $\theta_{a,b}$	0.85	0.95
Biot number, Bi	0.03	0.1
Bond number, Bo		
melt meniscus	160.	290.
encapsulant meniscus	-	725.
Crucible temperature, θ_c	1.1	1.1 or 1.05[1]
Heater Position, z_h		
uniform ambient	0.00	0.00
shallow crucible	0.75	1.00
deep crucible	1.00	-
Peclet number, Pe	0.1	0.06
Radiation number, Ra		
crystal, melt surfaces	0.55	1.0
encapsulant surface	-	0. or 1.8[1]
Stefan number, S	1.1	1.1
Thermal conductivity ratios		
solid, $K_s(\theta)$	$1./\theta$	1.
melt, $K_m(\theta)$	2.9	2.1
encapsulant, $K_e(\theta)$	-	0.26
Volume of melt, V_m	3.1416	3.1416
Volume of encapsulant, V_e	-	0.6732

[1] For transparent or opaque encapsulant, respectively.

as depicted in Fig. 4.14, but with the higher ambient temperature listed in Table 4.8. This representation of the bottom heat loss is only approximate but gives an adequate representation of the importance of this path for conduction from the melt. We actually include the crucible and liner in heat transfer calculations in the work presented in Chapter 5.

Two types of ambient temperature profiles were used in these calculations. In the meniscus shape calculations reported in Section 4.2.1.1, the ambient temperature above the surface of the melt was taken to be uniform at 1262K ($\Theta_a = \Theta_a^\infty = 0.75$) and below the bottom of the crucible was 1426K ($\Theta_a = \Theta_{a,b} = 0.85$). A more realistic configuration is shown in Fig. 4.16 along with the shapes of the melt and crystal and the thermal field predicted by our analysis. Here the ambient temperature distribution was written as an analytical function of position from the bottom of the crucible (z = 0) as

$$\Theta_a(z) = \Theta_c + \frac{1}{2}(\Theta_a^\infty - \Theta_c)(\tanh(10\,[z-z_h]) + 1)\ , \qquad (4.4)$$

where Θ_c is the crucible wall temperature ($\Theta_c = 1.1$) and Θ_a^∞ is the ambient temperature far above the crucible and heater; $\Theta_a^\infty = 0.75$ for all CZ silicon calculations. The extent of hot crucible wall and heater exposed to the crystal is modeled by varying the length z_h in this profile. The same ambient profile eq. (4.4) was used in the calculations of the effect of decreasing melt volume reported in Section 4.2.1.2.

The isotherms shown in Fig. 4.16 are spaced at 30K increments

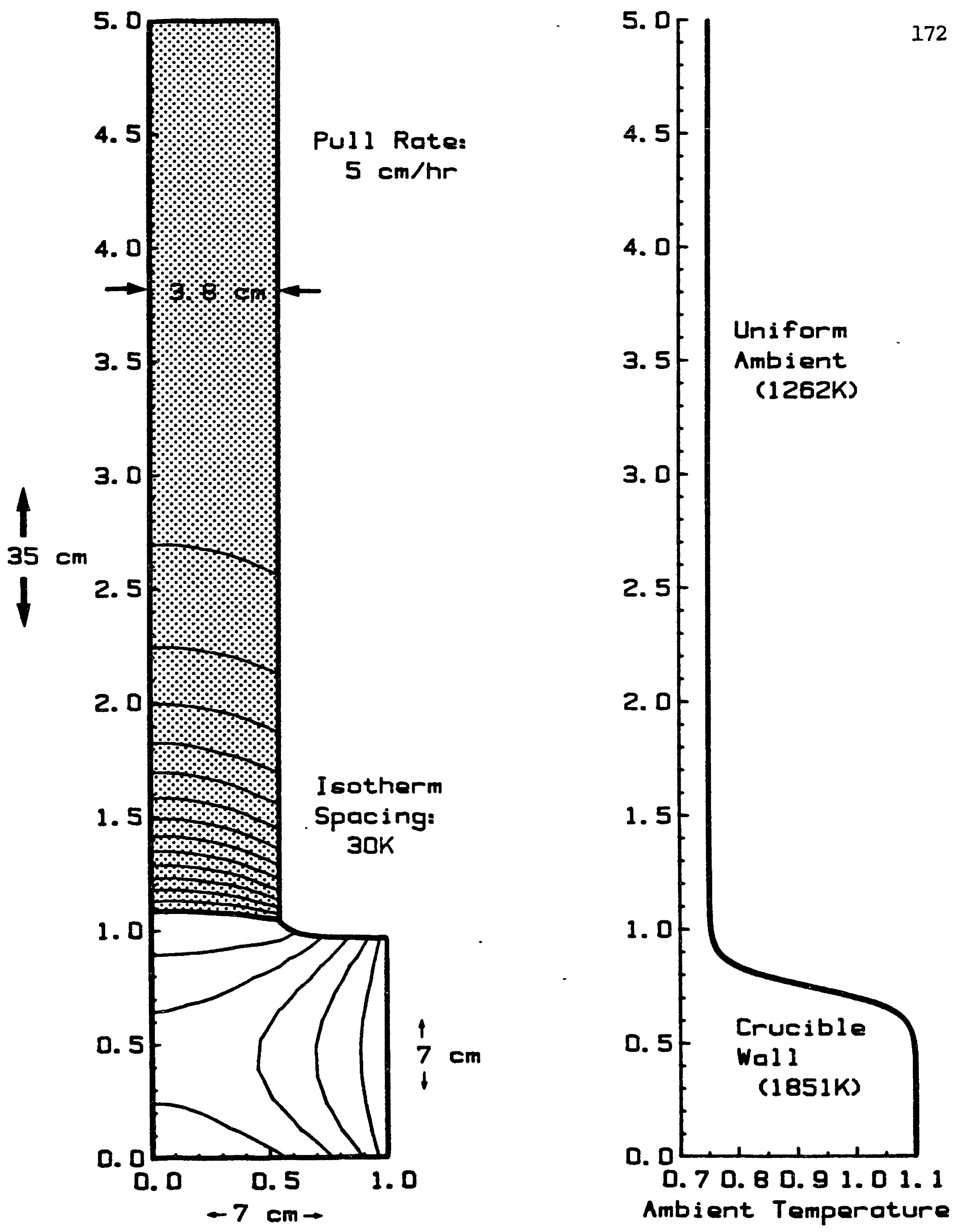

Fig. 4.16 Interface shapes and isotherms for reference configuration for CZ growth of silicon and ambient temperature profile used in calculation. Isotherms are spaced in 30K intervals around the melt/crystal interface. Shaded regions denote solid.

about the melting point which marks the shape of the melt/crystal interface. (This isotherm spacing of 30K is used for all plots in this and the remaining sections of this chapter). For the reference-case silicon calculation, the melt/solid interface was concave into the crystal. Heat conducted into the melt from the crucible wall and moved both upward to the surface of the melt and crystal and downward out of the bottom of the crucible. The crystal radius was 3.8 cm for this set of parameters.

4.2.1.1 Meniscus Shape

Calculations are presented in Fig. 4.17 for equilibrium growth angles at the three-phase contact curve varying from the reported 11° value for silicon (Surek and Chalmers, 1975) to 45° and 90°. The crystal radius decreased and the shape of the solidification interface changed from concave into the crystal to convex into the melt as the angle increased. The calculations with $\tilde{\phi}_{ms} = 90°$ corresponded to the assumption used by most previous investigators of a flat melt surface joining the crystal at right angles. This simplification obviously leads to erroneous results; ignoring the details of the region near the junction of the crystal and the meniscus can radically change the heat transfer in the system. Accurate modeling of heat flow in this region necessitated inclusion of the melt meniscus and the proper equilibrium angle.

The sensitivity of the system to small changes in the meniscus angle was quite small. When the angle was changed to 12°, the crystal

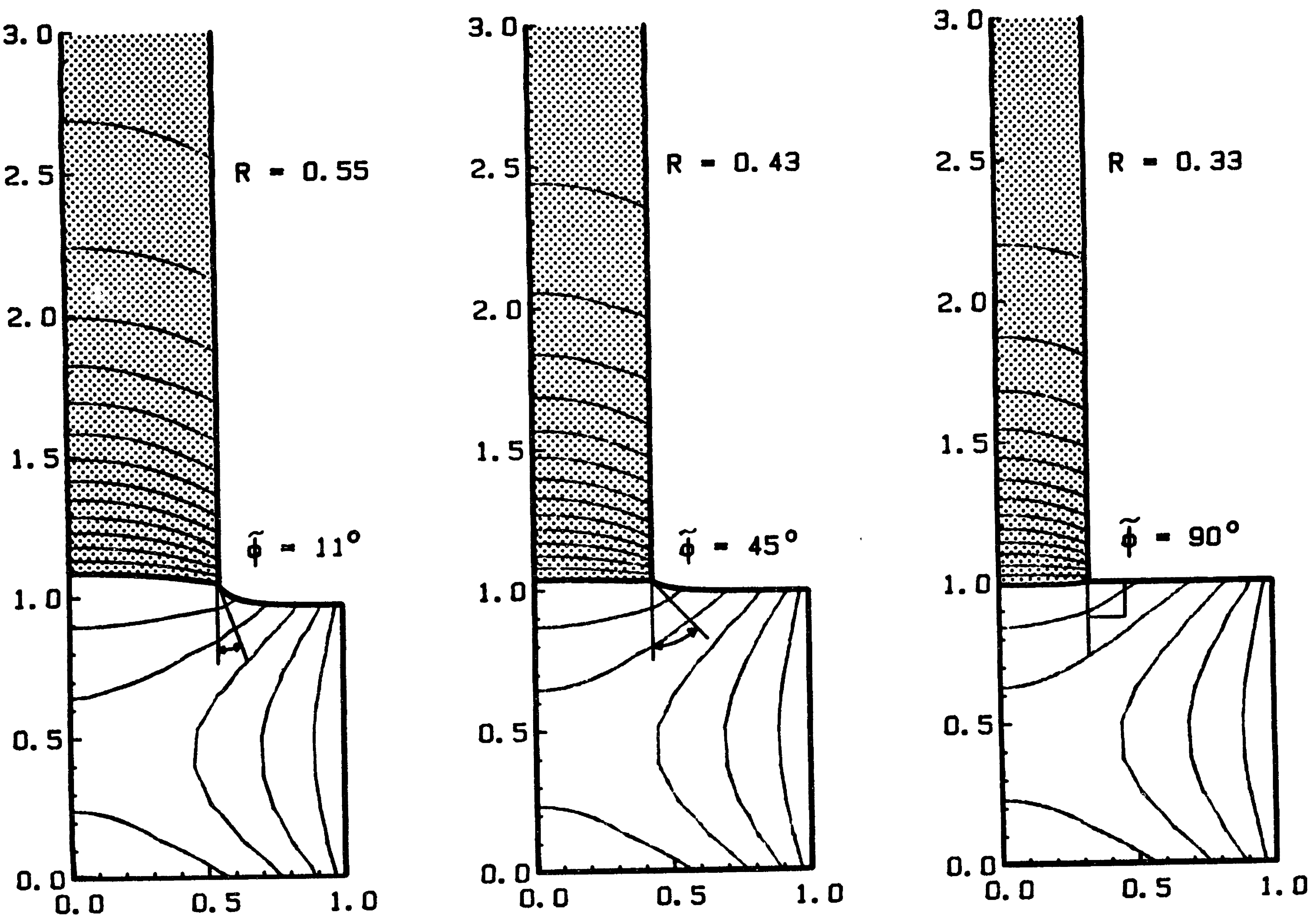

Fig. 4.17 Variation of isotherms and interface shapes resulting from changes in equilibrium growth angle $\tilde{\phi}_{ms}$. All other parameters are held fixed at the values listed in Table 4.8.

radius decreased by 0.97 percent. Similarly, setting the growth angle to 10° caused the steady-state radius to increase by just 1.03 percent.

4.2.1.2 Melt Volume and Crucible Wall

Simulating the change in the heat transfer and geometry of the melt that occur during the CZ process by examining the effect of decreasing the level of the melt had several interesting effects on the results of the thermal-capillary model. First, the amount of heat entering the melt from the crucible sides was decreased because the surface area in contact with the wall decreased. Also, the heat loss out of the bottom of the crucible became increasingly important in the shallower melt. Second, exposing the hot crucible wall as the melt level dropped allowed for radiative heat transfer from the crucible directly to the growing crystal. These two effects were examined separately through calculations with different ambient temperature profiles.

Calculations for a range of melt volumes and the uniform ambient described above are shown in Fig. 4.18 and demonstrate exclusively the effect of the changing aspect ratio of the melt of the growth process. The radius of the crystal increased as the level of the melt dropped because the amount of heat entering the melt from the sidewall decreased while heat from the crystal surface continued to be lost to the uniformly cool ambient. The effect of heat loss through the bottom of the crucible was manifested in the change of the shape of the solidification interface from concave to sigmoidal with decreasing

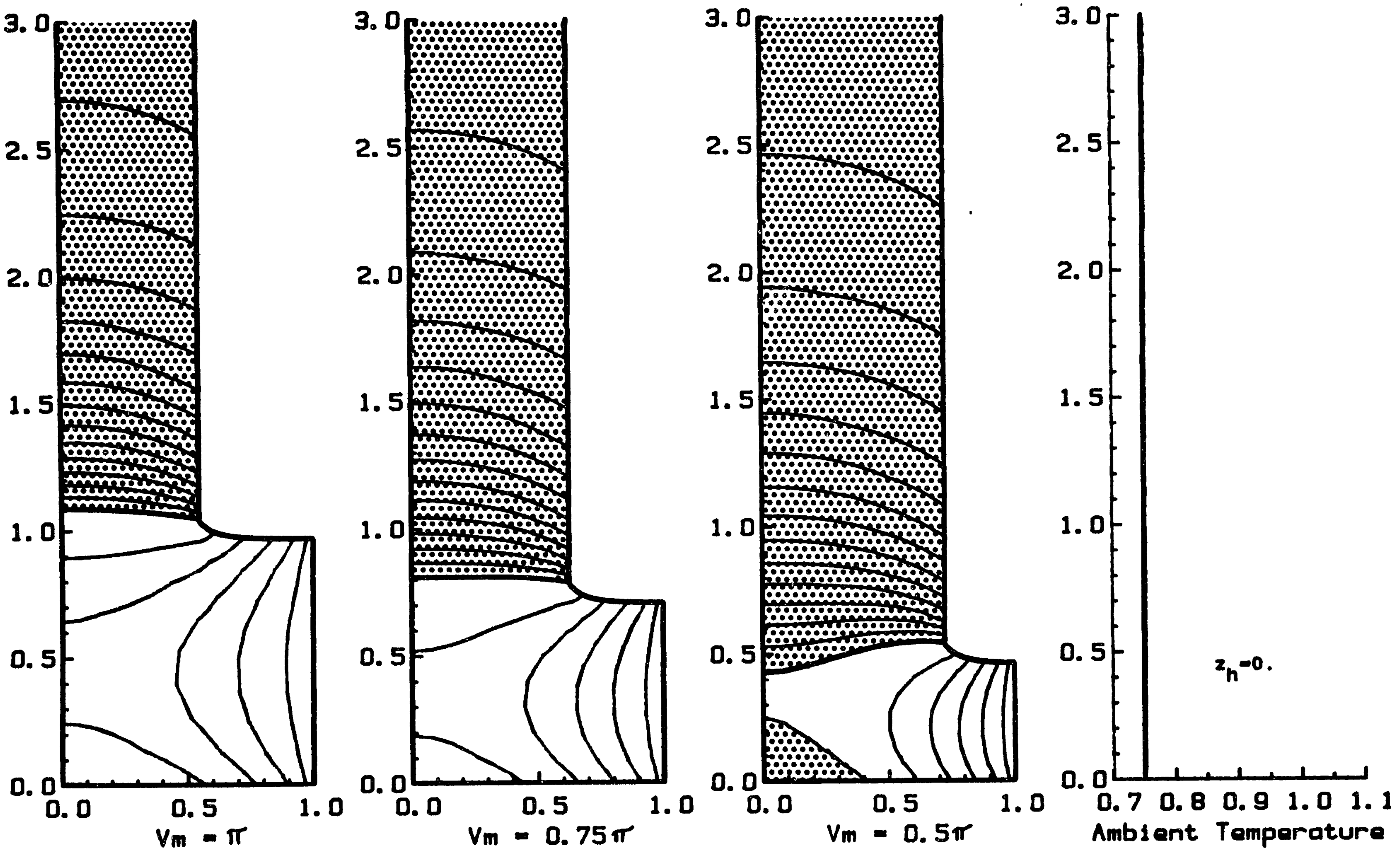

Fig. 4.18 Changes in isotherms and interface shapes with decreasing melt volume for CZ growth of Si using a uniform ambient temperature profile. All other parameters are held fixed at those of reference case.

volume. This transition is similar to the interface flipping in the Czochralski growth of oxide crystals (Takagi et al., 1976; Cockayne et al., 1976; Carruthers, 1976), where the effect has been attributed to changes in the pattern of convective motion with the shape of the melt and rotation of the crystal. However, the interface flipping in our calculations was due entirely to geometrically induced changes in conductive heat transfer.

As the level of the melt was dropped to $V_m = 0.5\pi$ a portion of the melt at the bottom of the crystal became thermally undercooled (the shaded region in Fig. 4.18) and was representative of a lump of solid silicon. For low melt volumes this solid grew large enough to touch the growing melt/crystal interface and lead to the "crystal bumping" experienced in practice.

The effect of exposing the hot crucible wall to the growing crystal was examined by calculations with the ambient temperature profile, eq. (4.4), for shallow ($z_h = 0.75$) and deep ($z_h = 1.0$) crucible-heater configurations. The isotherms and system shapes predicted for these profiles are shown in Figs. 4.19 and 4.20 for the same melt volumes used with the uniform ambient. The added radiative heat transfer to the crystal from the exposed wall can cause the crystal radius to decrease as the melt level was dropped for either crucible configuration. This effect occurred for a lower melt volume for the shallow crucible (Fig. 4.19) than for the deep crucible (Fig. 4.20). Interface flipping to an almost convex shape in the shallow geometry was caused by heat loss through the bottom of the crucible and radiative heat input into the crystal just above the solidification interface, as

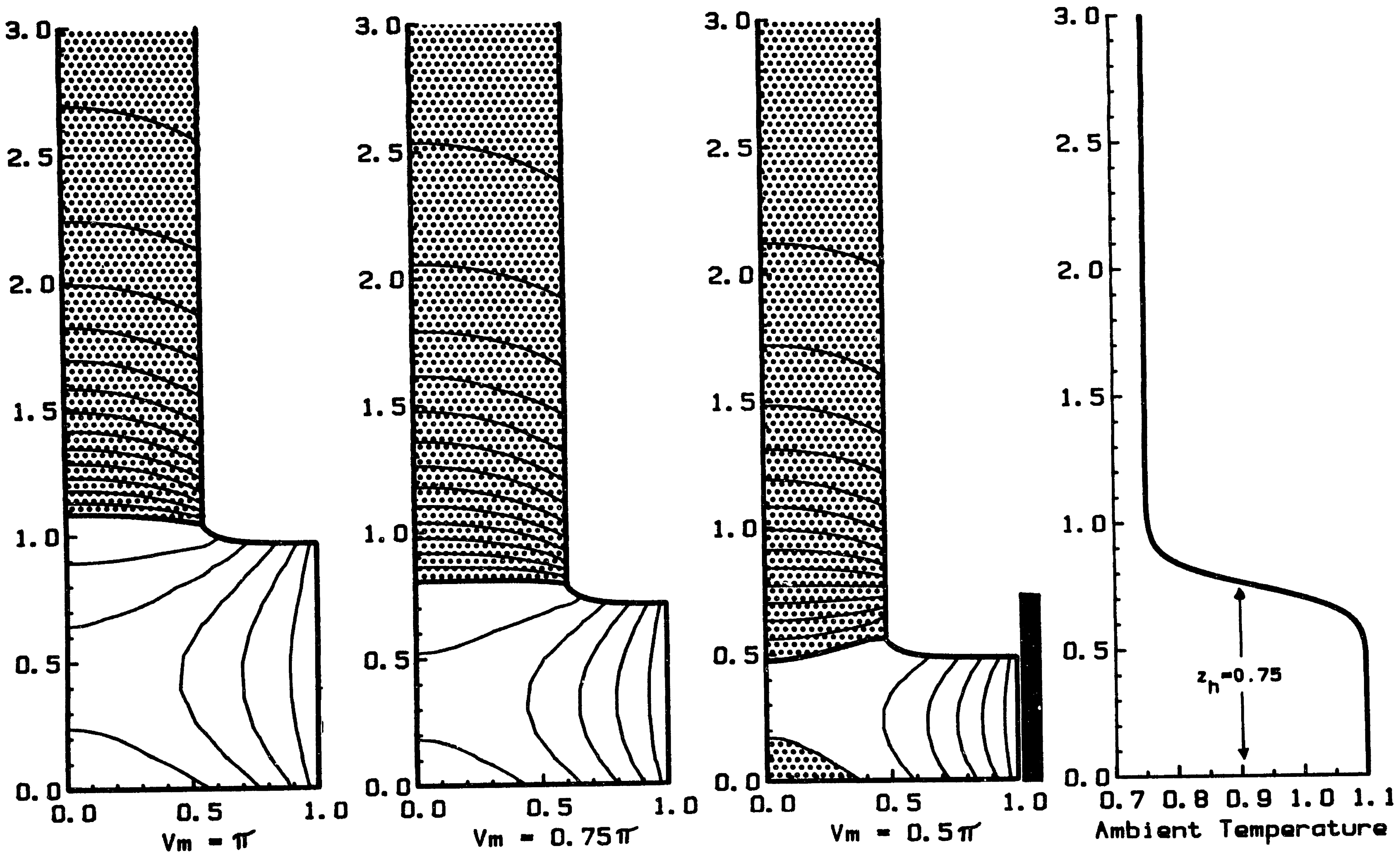

Fig. 4.19 Changes in isotherms and interface shapes with decreasing melt volume for CZ growth of Si using the ambient temperature profile for the shallow crucible (z_h = 0.75). All other parameters are held fixed at those of reference case.

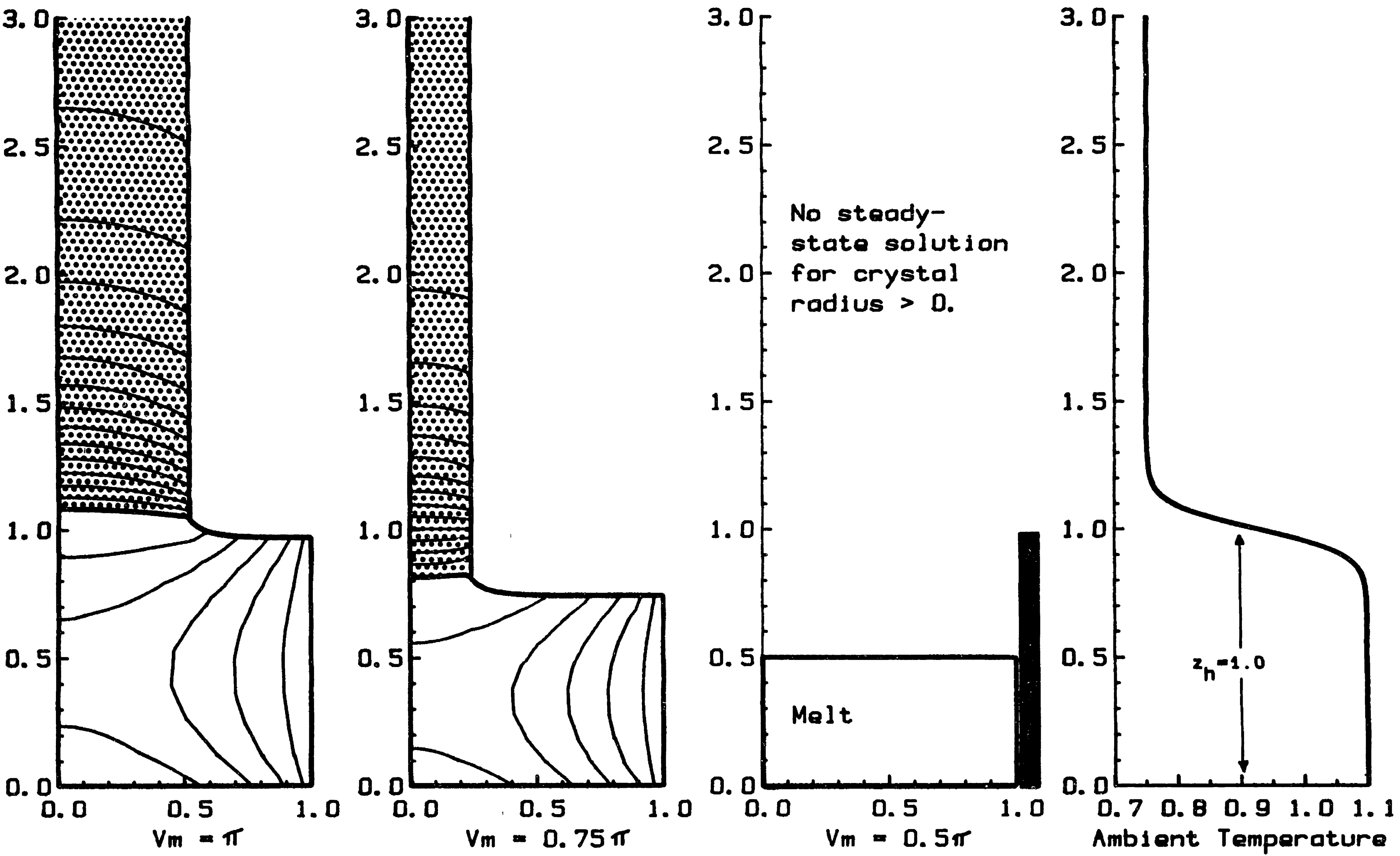

Fig. 4.20 Changes in isotherms and interface shapes with decreasing melt volume for CZ growth of Si using the ambient temperature profile for the deep crucible ($z_h = 1.0$). All other parameters are held fixed at those of reference case.

seen from the isotherms in Fig. 4.19. Heat input into the crystal by radiation became so overpowering for the deeper crucible configuration shown in Fig. 4.20 that a non-zero crystal radius did not exist for the melt volume $V_m = 0.5\pi$.

The axial temperature profiles along the centerline and the surface of the crystal are plotted in Fig. 4.21 for the shallow ·ucible and the three melt volumes shown in Fig. 4.19. The direction of heat flow between the ambient and the crystal is indicated by the difference between the temperatures along the crystal surface and the ambient. The convexity of the melt/solid interface for the lowest melt volume is clearly seen from the reversed position of the crystal edge and centerline axial temperature profiles with respect to the two previous melt volumes. The temperature gradients in the crystal at the centerline of the melt/solid interface ranged between -91 K/cm for $V_m = \pi$ to -51 K/cm for $V_m = 0.5\pi$, very realistic values for small-scale silicon growth. The temperature increase in the melt along the axis above the melting point was only 69K (4.08 percent above the melting temperature) for the dimensionless melt volume of $V_m = \pi$. Although the temperature difference is small, this region cannot be interpreted as a well-mixed core of uniform temperature such as would arise from intense convective mixing. This nearly-isothermal core is caused by the high thermal conductivity of the melt coupled with the turning nature of heat flow beneath the crystal. Heat enters the melt core from the sides and exits via paths upward and downward, thereby resulting in a flattened saddle-shaped temperature field there.

The changes in radius for decreasing melt volume and varying

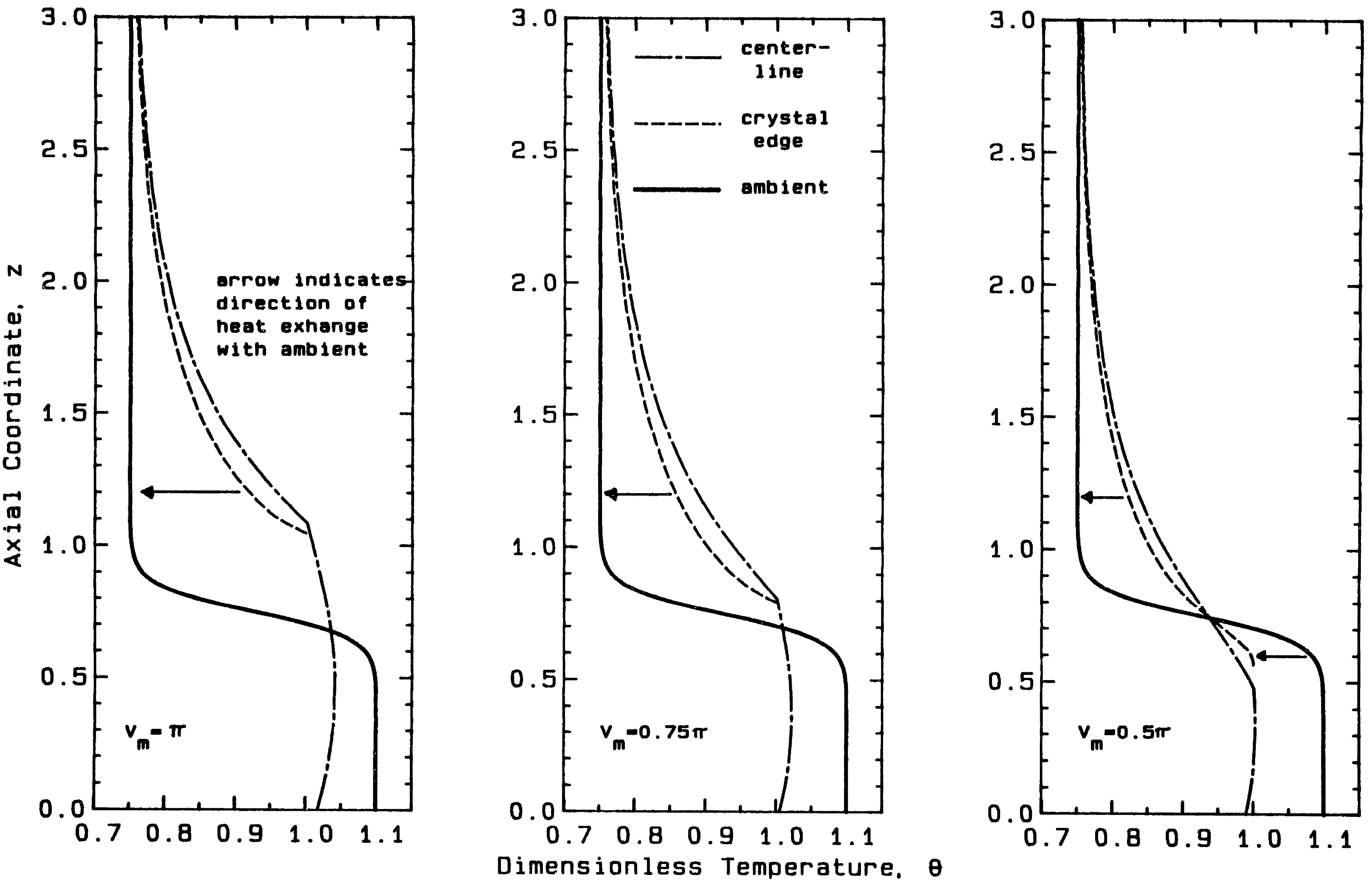

Fig. 4.21 Variation of axial temperature profiles along the centerline ($r = 0$) and at the crystal radius ($r = R$) for the three melt volumes of Fig. 4.19 (CZ growth of Si using the ambient temperature profile for the shallow crucible).

heater position are summarized in Fig. 4.22 and demonstrate the sensitivity of the response of the steady-state crystal radius to the thermal ambient viewed by the crystal with all other parameters held constant as the melt volume decreases. For the uniform ambient, the crystal radius increased steadily with decreasing melt volume. When an ambient temperature distribution was introduced, the increasing effect of radiation from the exposed wall caused the radius either to go through a maximum with decreasing melt volume or to decrease monotonically, depending on the depth of the crucible. This effect is most dramatic for the deep crucible where no steady-state growth was possible after a minimum volume was reached.

Varying the ambient temperature distribution by changing z_h simulated the common practice of changing the location of the crucible within the furnace as the melt level dropped so as to maintain the same temperature gradient throughout the process. The calculations summarized in Fig. 4.22 indicate that the pedestal location can be an effective control parameter for setting crystal radius.

Unfortunately, the melt/solid interface shape varied as a function of the aspect ratio of the melt and the pedestal location, so that control schemes based solely on crystal radius will lead to fluctuations in this shape. For example, changing the ambient temperature profile or pedestal location to the keep the radius constant at $R = 0.5$ with decreasing melt volume (see the plot on the right in Fig. 4.22) resulted in a deflection of the melt/solid interface shape, $\Delta = H_o(0) - H_o(R)$, that varied from $\Delta = -0.03$ (concave into the crystal) for $V_m = \pi$ to $\Delta = +0.10$ (convex to the crystal) at $V_m = 0.5\pi$. Clearly, other parameters,

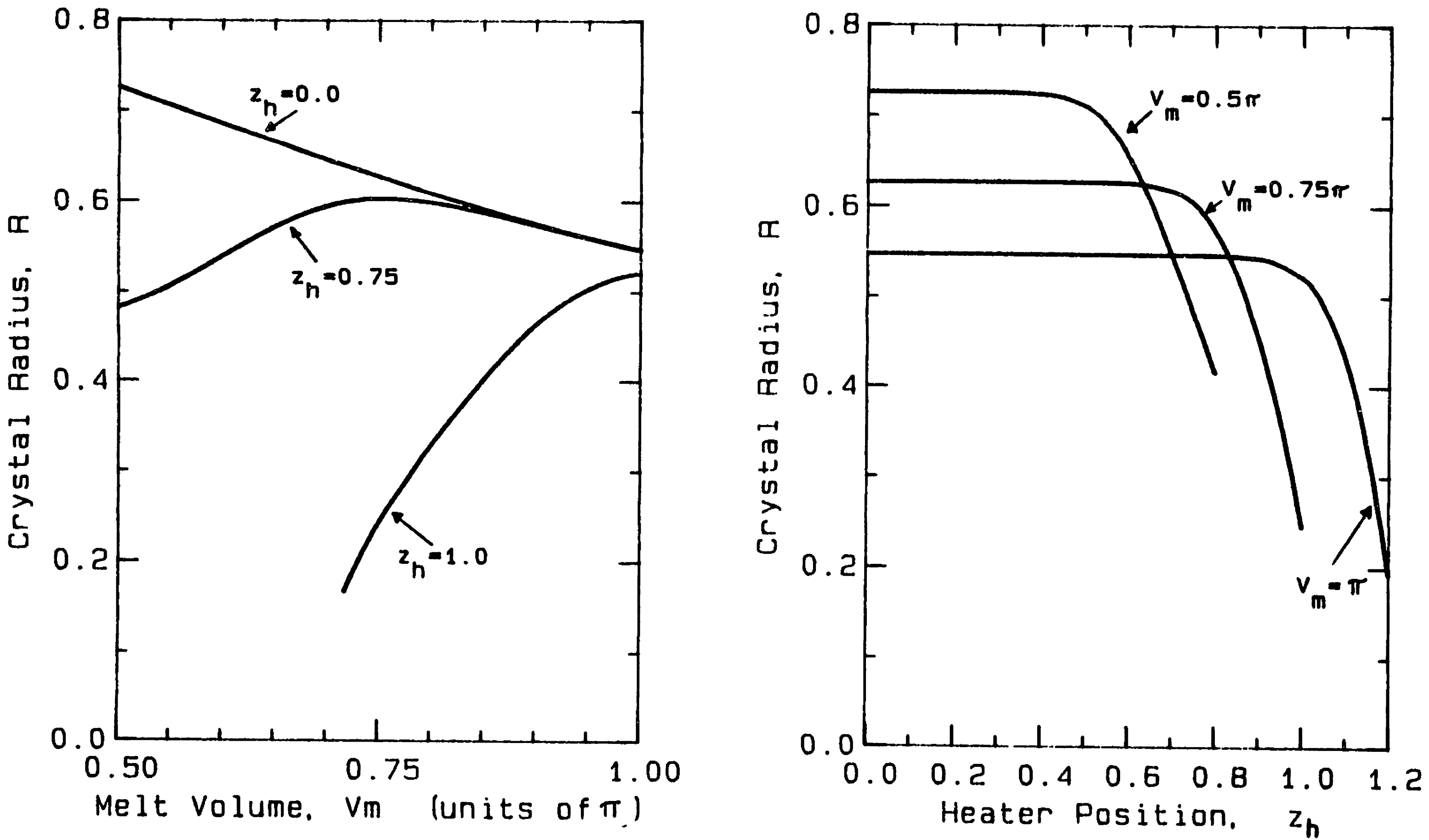

Fig. 4.22 Variation of crystal radius as a function of melt volume and as a function of heater position (the location of the top of the hot crucible in the ambient temperature distribution, z_h).

such as heater temperature or pull rate, must be prescribed if melt/solid interface morphology is to be effectively held constant. The possibility of using a bottom heater along with various processing strategies for this task is explored in Section 4.3 of this chapter.

4.2.2 Calculations for LEC Growth of Gallium Arsenide

The thermophysical parameters and dimensionless groups appropriate for the small-scale LEC system simulated here are listed in Appendix A and in Tables 4.7 and 4.8. The thermophysical properties for the Si and the GaAs system are similar and, except for the presence of the encapsulant layer in the latter, lead to similar heat transfer results. This point was emphasized by the calculations shown in Fig. 4.23 for the Si and GaAs parameter values, but without the encapsulant in the GaAs system. The lower thermal conductivities in the GaAs system lead to greater Biot and Radiation numbers, which caused larger radial temperature gradients in the GaAs crystal and greater curvature of the solidification interface. The heat flux at the surface of the melt and crystal also was greater for GaAs so that the ambient temperatures required to sustain steady growth was not as low as those required for the growth of Si. The greater density of GaAs lead to a smaller characteristic length (larger Bond number) for the curvature of the meniscus in this system.

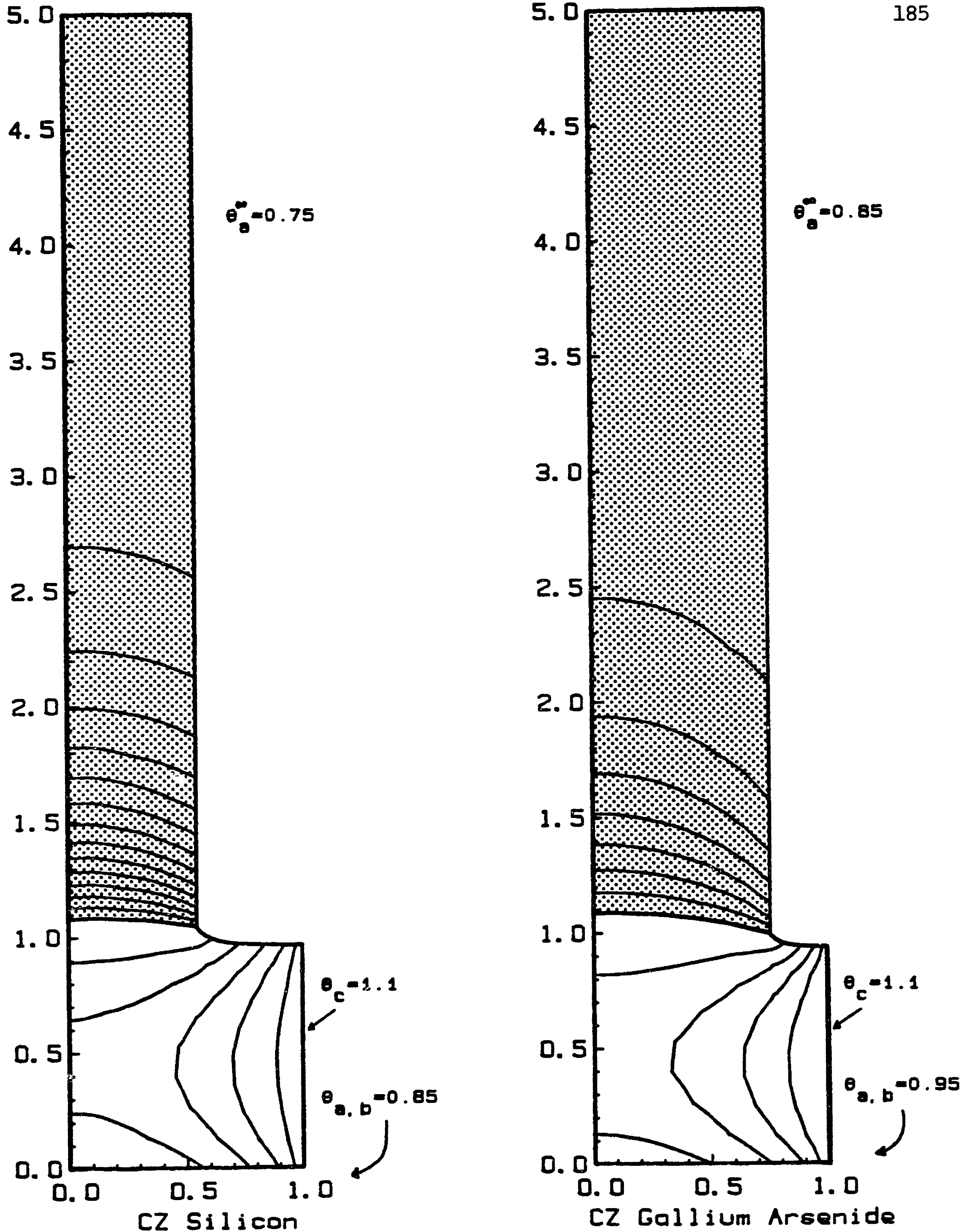

Fig. 4.23 Interface shapes and isotherms for reference configuration of CZ growth of silicon and hypothetical CZ growth of gallium arsenide, both with uniform ambient temperature profiles. Differences in ambient temperatures are indicated in the figure.

4.2.2.1 Radiative Character of Encapsulant

The effect of adding an encapsulant layer to the model for LEC growth is examined in Fig. 4.24 for two widely differing cases of heat transfer in the encapsulant. The calculation in the center had an encapsulant layer which was totally transparent to radiation; the result on the right had a totally opaque layer. The effect on the dimensionless parameters which describe heat transfer from the system surfaces are denoted in Fig. 4.24 for each case by showing the differing Radiation and Biot numbers for the surfaces. For the transparent encapsulant, the submerged surfaces of GaAs crystal and melt were cooled by radiation and conduction through the encapsulant. The encapsulant/ambient meniscus released heat only by convection to the gaseous ambient since the radiative emissivity for the surface of this transparent medium was assumed to be zero. The opaque encapsulant calculation required heat transfer solely by conduction across the submerged melt and crystal surfaces; both the Biot and Radiation numbers were set to zero along these surfaces. In contrast to the transparent encapsulant, the emissivity of the opaque encapsulant meniscus was set to unity, and the encapsulant/ambient surface was cooled by both radiation and convection to the ambient.

The interaction effect of radiation with the B_2O_3 caused pronounced effects on the overall heat transfer when the encapsulant was opaque, but was little changed from the CZ case when the layer was taken to be transparent. In the transparent case, the radius and the axial and radial gradients in the crystal were slightly reduced with the

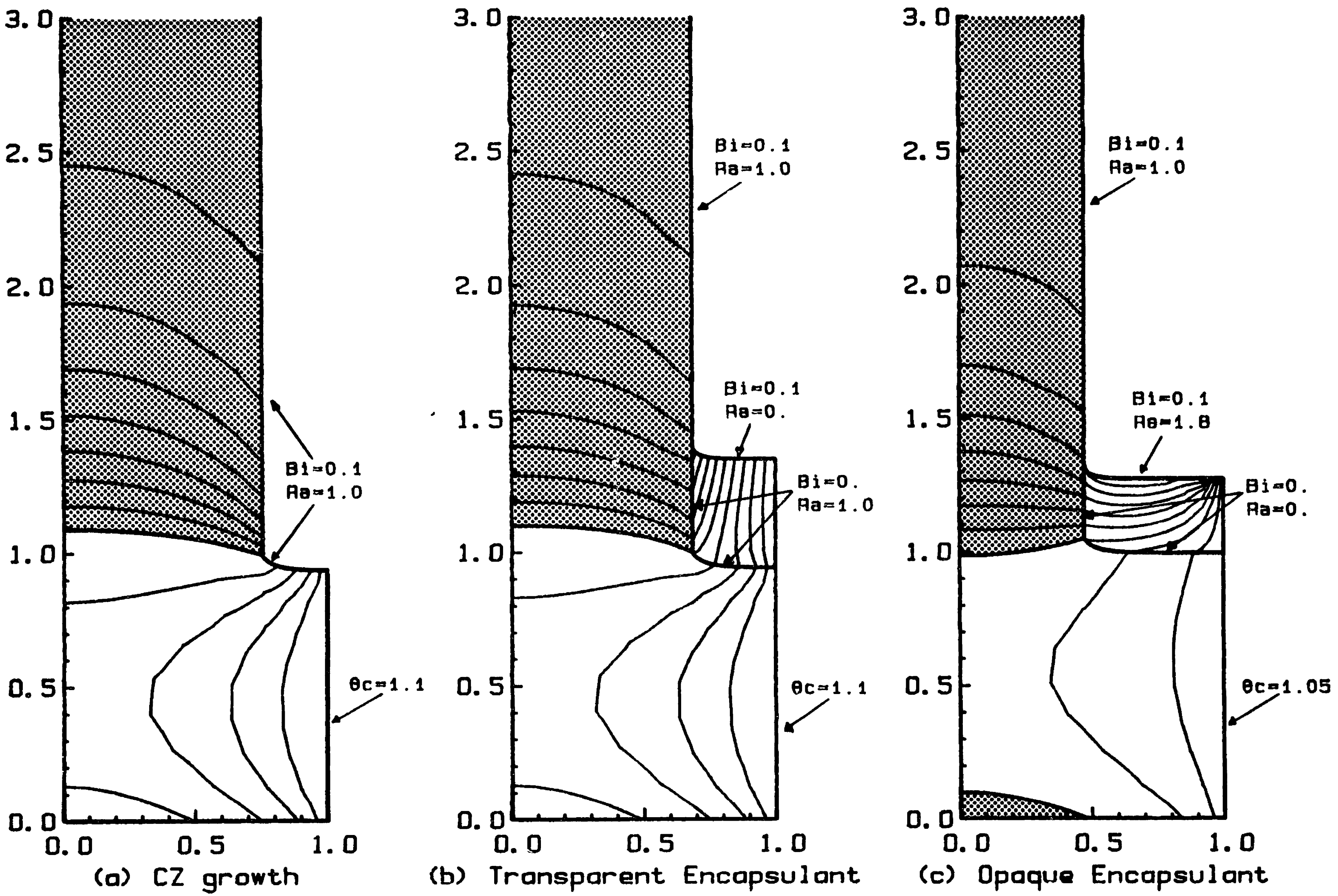

Fig. 4.24 Variation in isotherms and interface shapes for changing radiative character of the encapsulant layer for LEC growth of GaAs using the uniform ambient temperature profile. All other parameters are held fixed at those listed in Table 4.8. (a) Hypothetical CZ growth (no encapsulant). (b) LEC with transparent encapsulant. (c) LEC with opaque encapsulant.

addition of the encapsulant because of the small amount of heat conducted into the crystal from the encapsulant layer. The enormous changes in heat transfer in the opaque case were due to the effective barrier to heat flow from the covered surfaces that resulted from the very small thermal conductivity of the layer relative to that of the melt and crystal. The isotherms were nearly vertical for the transparent case and nearly horizontal for the opaque layer. While heat was flowing radially inward from the crucible wall to the crystal for the transparent encapsulant, the flux of heat through the opaque layer was primarily vertical from the surface of the melt to the ambient. The reduction of heat flux from the melt and crystal was so severe that the crucible wall temperature had to be decreased from $\Theta_c = 1.1$ for the CZ and transparent encapsulant calculations to $\Theta_c = 1.05$ for the opaque encapsulant in order to obtain a non-zero steady-state crystal radius. The melt/solid interface shape changed from concave into the crystal for a transparent layer to fully convex into the melt for an opaque one. The insulating character of the encapsulant encouraged heat to exit upward through the crystal via conduction rather than from the surface of the melt.

4.2.2.2 Pull Rate

The effect of changing the pull rate is shown in Figs. 4.25 and 4.26 for the LEC growth of GaAs with a transparent and opaque encapsulant layer, respectively. The behavior of both systems was complicated by the geometrical effects of the changing depth of the encapsulant

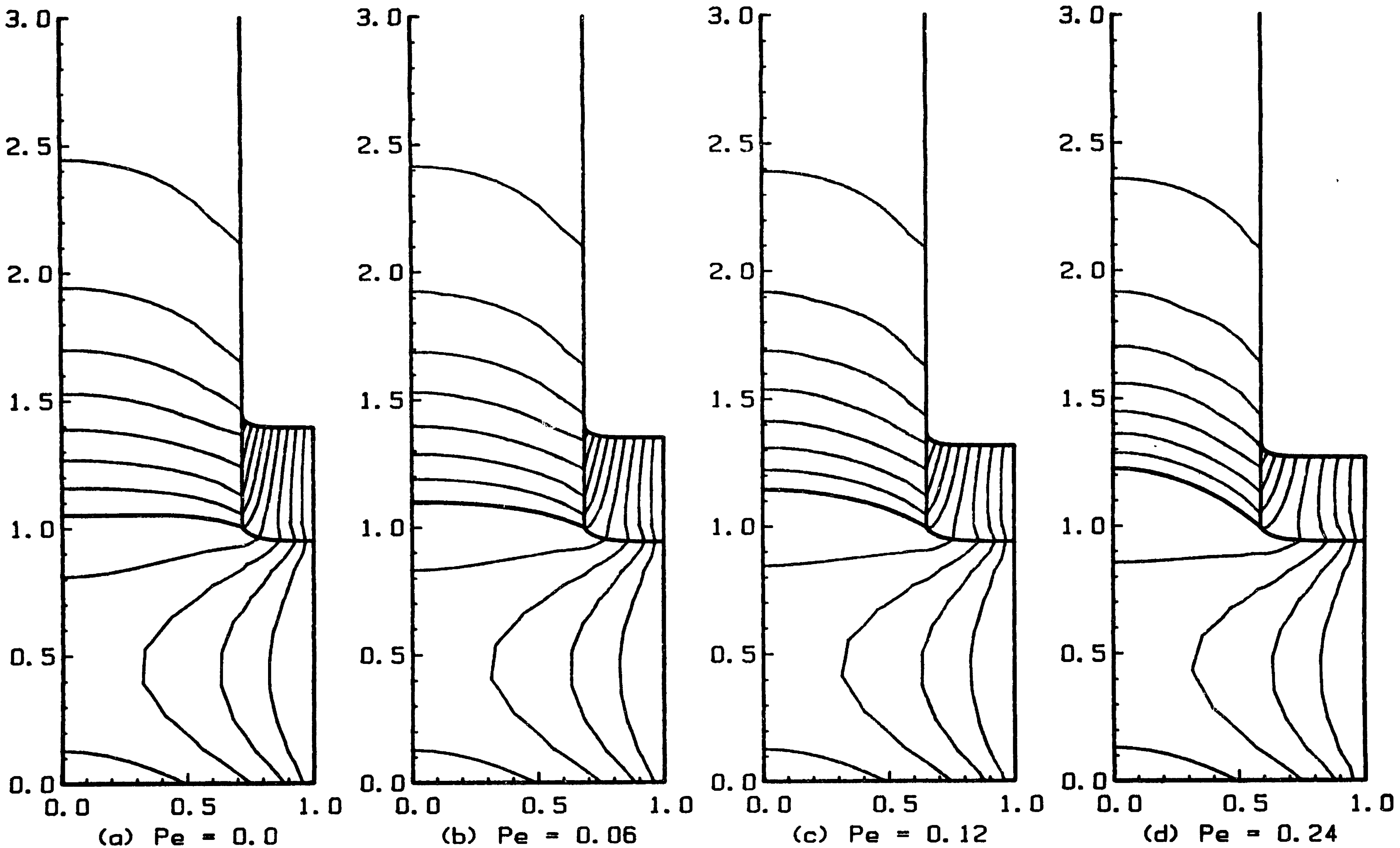

Fig. 4.25 Changes in isotherms and interface shapes with pull rate for LEC growth of GaAs with a uniform ambient temperature profile. The encapsulant layer is taken to be perfectly transparent, and all other parameters are held fixed at those listed in Table 4.8.

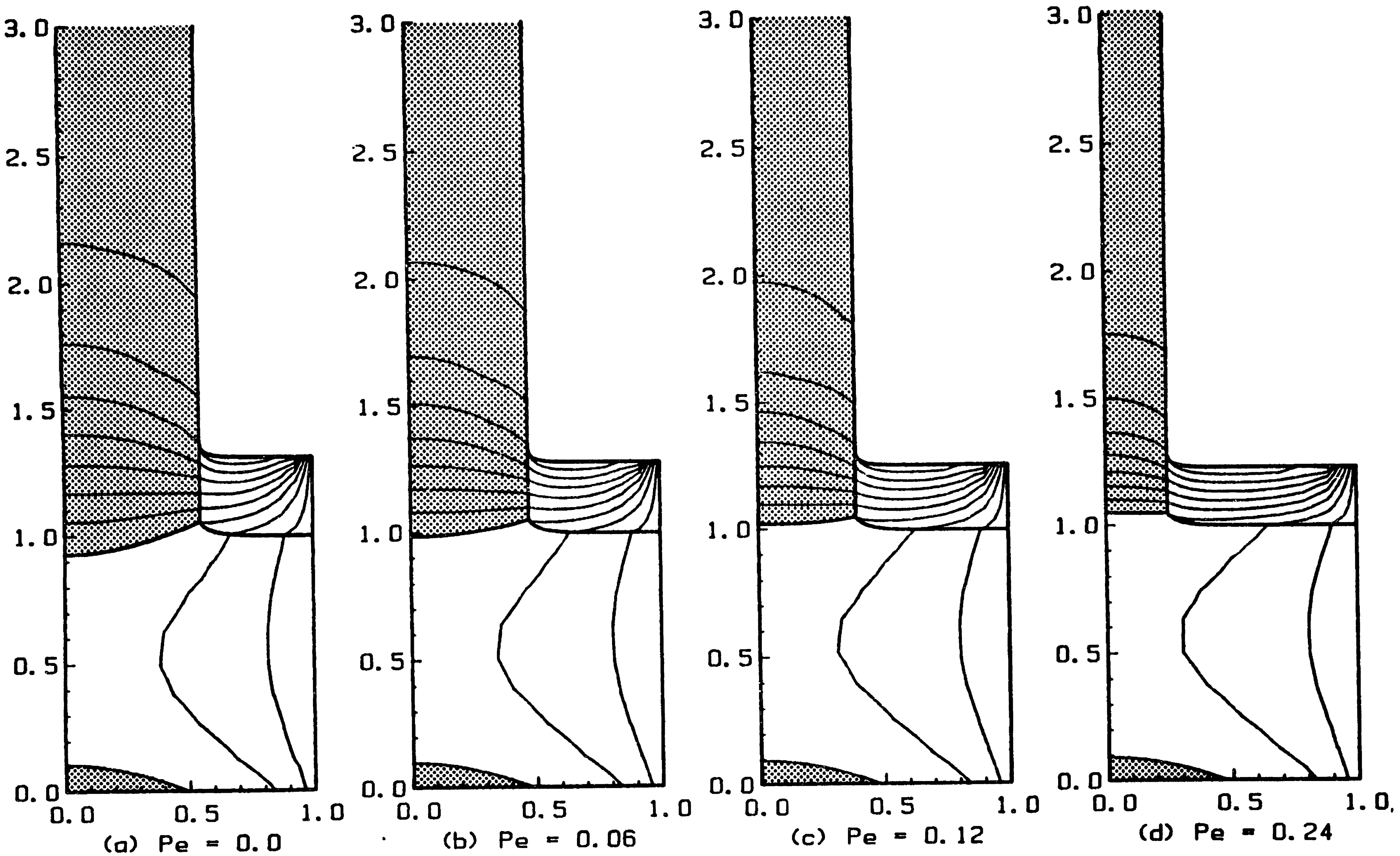

Fig. 4.26 Variations in isotherms and interface shapes with pull rate for LEC growth of GaAs with a uniform ambient temperature profile. The encapsulant layer is taken to be completely opaque, and all other parameters are held fixed at those listed in Table 4.8.

with crystal size. An increase in the pull rate caused a decrease in the steady-state crystal radius and made the melt/solid interface increasingly more convex into the crystal for the transparent case. This effect was less pronounced for the opaque encapsulant where the interface became nearly flat for Pe = 0.12. For Pe = 0.24, the solidification front was very slightly convex in the center of the crystal and concave at the edge.

These interactions are compared in Fig. 4.27 as a plot of radius as a function of pull rate for all the results of CZ and LEC growth of a material with thermophysical properties corresponding to GaAs. The proposed relation for the interaction of pull rate and crystal radius of Kim et al. (1983) is also shown in Fig. 4.27. As in the calculations of Section 4.1 and in calculations by Derby et al. (1985) for LEC GaAs growth and by Kalejs et al. (1983) for EFG growth of Si, the Billig (1955) relation did not well describe the behavior of the system nearly as well as the Kim et al. (1983) correlation and is not shown on the plot. The geometrical interactions of the encapsulant layer and crystal size strongly affected the heat transfer in the system. The response of the crystal radius for an opaque encapsulant departed significantly from the results of the CZ and transparent LEC calculations.

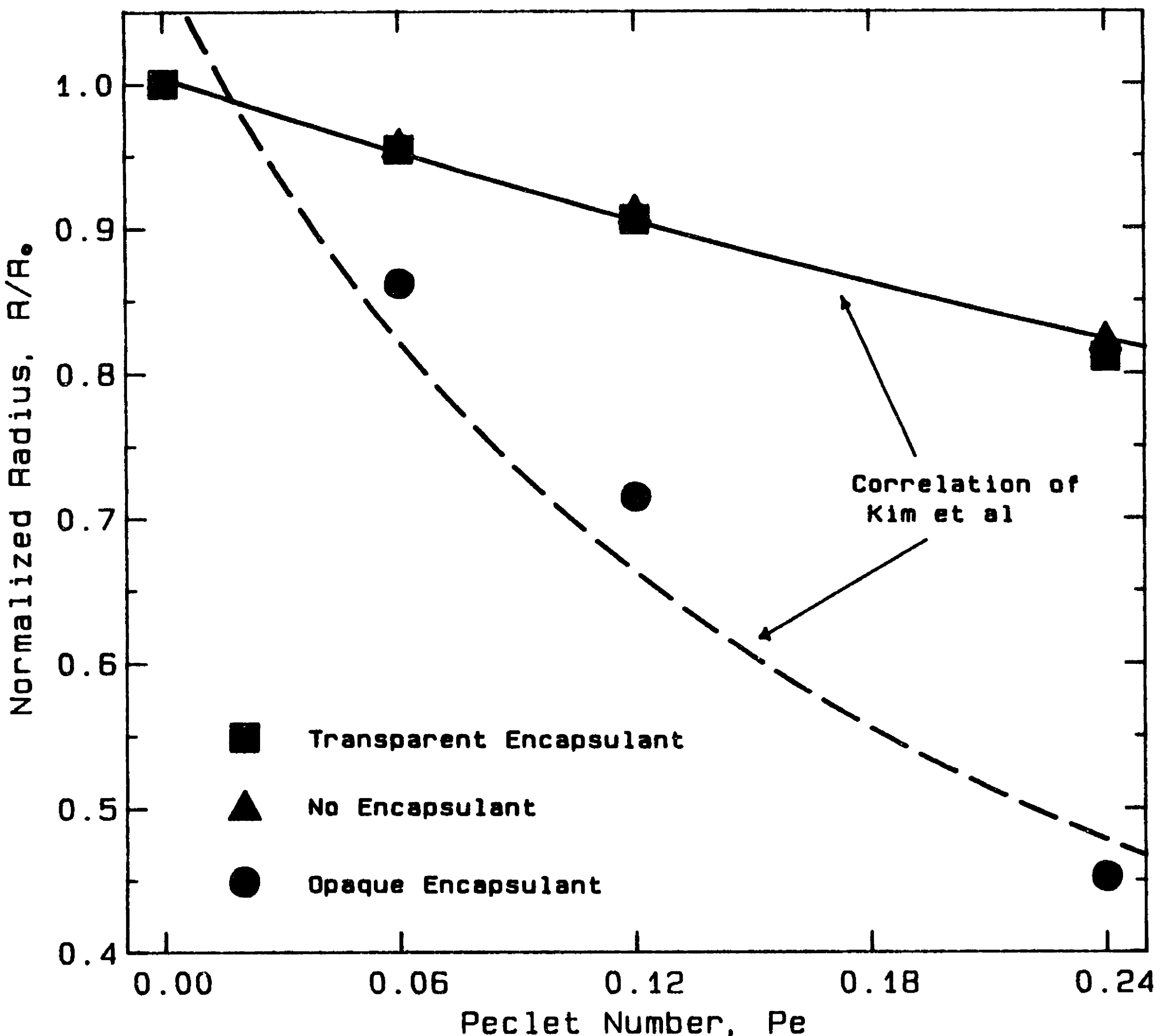

Fig. 4.27 Normalized crystal radius (radius divided by value obtained for zero pull rate, Pe = 0.) plotted as a function of pull rate for LEC growth of GaAs with a uniform ambient with all other parameters held fixed at reference values listed in Table 4.8. Data points are shown for cases of no encapsulant, transparent encapsulant, and opaque encapsulant. The solid and dashed curves represent the best fits to the correlation of Kim et al. (1983).

4.2.2.3 Encapsulant Volume

The effect of varying the volume of encapsulant is examined in Figs. 4.28 and 4.29 for transparent and opaque encapsulant layers. Results for the transparent layer are presented in Fig. 4.28 for encapsulant volumes greater and less than the reference value used for the calculations shown in Fig. 4.24. Effects of changes in encapsulant volume were almost insignificant; however, the axial temperature gradient in the crystal decreased slightly with increasing encapsulant depth.

Calculations for the same changes in the volume of an opaque encapsulant layer are shown in Fig. 4.29. The height of the encapsulant/ambient interface above the surface of the melt strongly affected heat transfer for the entire system. For a smaller encapsulant volume, heat lost from the melt and crystal was more easily accommodated and the radius of the crystal increased. However, this trend was reversed as the encapsulant volume and the insulating effect of its low-conductivity encapsulant was increased. Then, heat transfer from the submerged surfaces was inhibited and the crystal radius decreases significantly.

4.2.2.4 Melt Volume

A simulated sequence of growth configurations with decreasing melt volume and an ambient temperature distribution in the form of eq. (4.4) with $\Theta_a^o = 0.85$ and $z_h = 1.0$ is presented in Fig. 4.30 for LEC growth of gallium arsenide with an opaque encapsulant layer. The results were similar to the calculations for CZ silicon growth

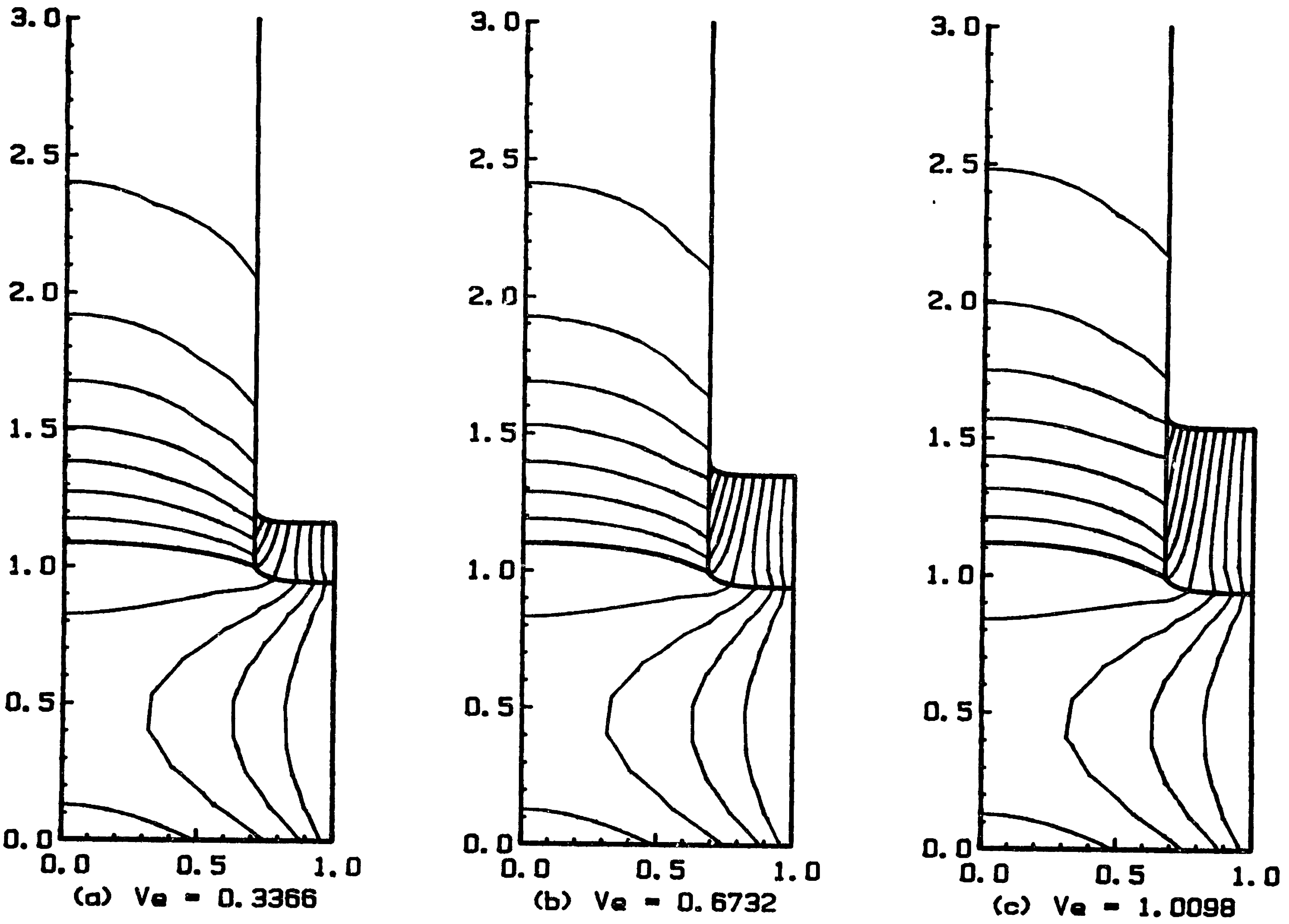

Fig. 4.28 Changes in isotherms and interface shapes with encapsulant volume for LEC growth of GaAs with a uniform ambient temperature profile. The encapsulant layer is taken to be perfectly transparent, and all other parameters are held fixed at those listed in Table 4.8.

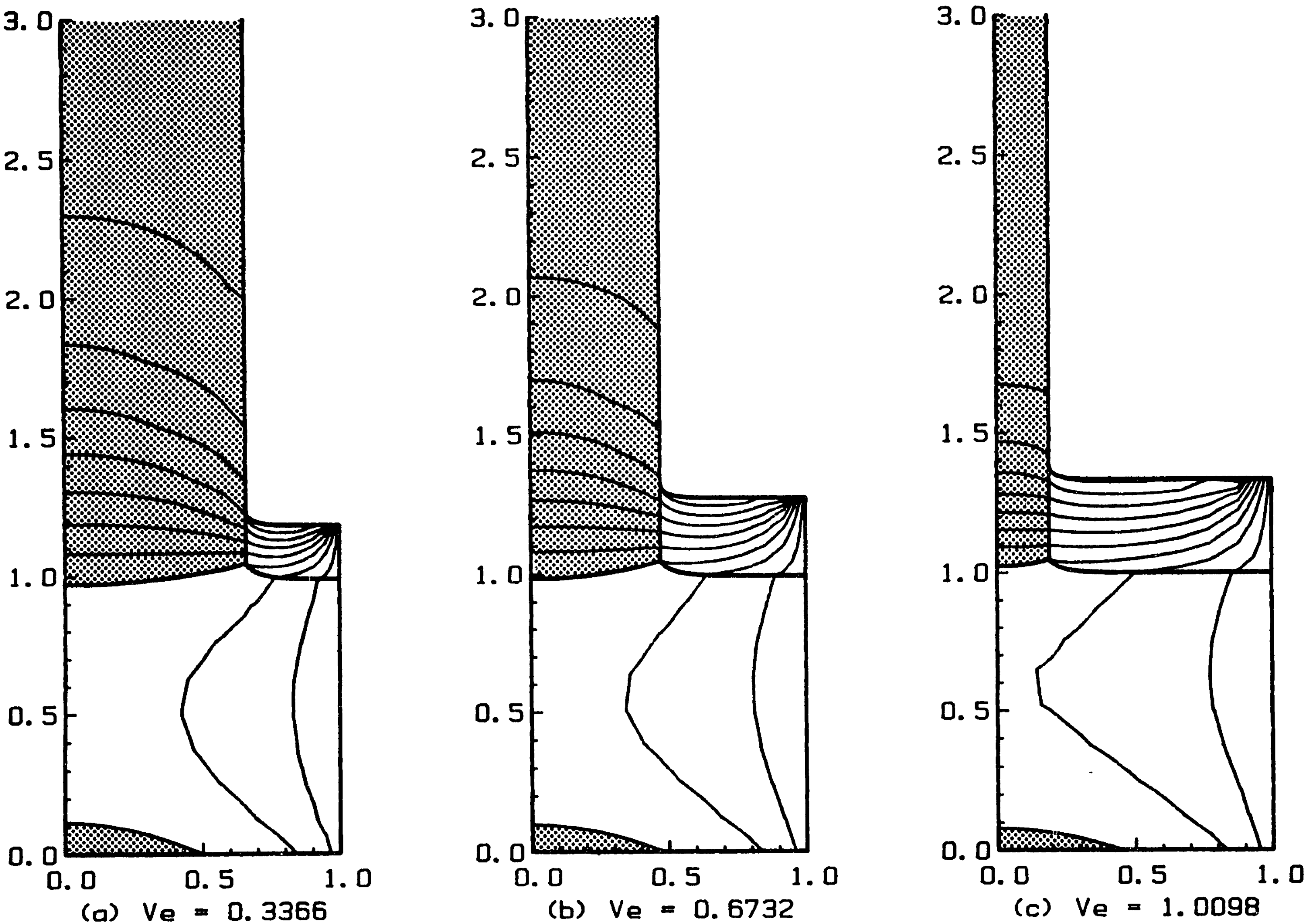

Fig. 4.29 Variations in isotherms and interface shapes with encapsulant volume for LEC growth of GaAs with a uniform ambient temperature profile. The encapsulant layer is taken to be completely opaque, and all other parameters are held fixed at those listed in Table 4.8.

shown in Fig. 4.19; the major difference caused by the dropping melt volume was that only the edge of the crystal above the encapsulant layer viewed the ambient temperature distribution. The crystal radius initially increased and then remained almost constant from $V_m = 0.75\pi$ to $V_m = 0.6\pi$ where heat began to flow into the crystal, as seen by the deflection of the isotherms in the region of the crystal immediately above the encapsulant layer. The interface shape was always convex into the melt and deflected more as the melt depth decreased. The extent of the undercooling in the melt at the bottom of the crucible increased as the melt dropped. Reducing the volume of the melt from the $V_m = 0.6\pi$ case resulted in an overlapping of the undercooled region and the melt/crystal interface.

4.2.3 Discussion

For the first time, predictions of the thermal field, crystal radius, melt meniscus and melt/solid interface locations as functions of external parameters are possible for the CZ and LEC systems by efficiently solving the entire thermal-capillary model. The predictions of the response of the crystal radius to input parameters like pull rate and ambient temperature depend on accurately describing the free-boundaries in this heat transfer problem and are not available from less sophisticated models. One of the major benefits of this modeling effort is the ability to isolate system responses to specific changes in growth parameters, thus yielding fundamental understanding of the interactions of heat transfer and interfacial phenomena. This information

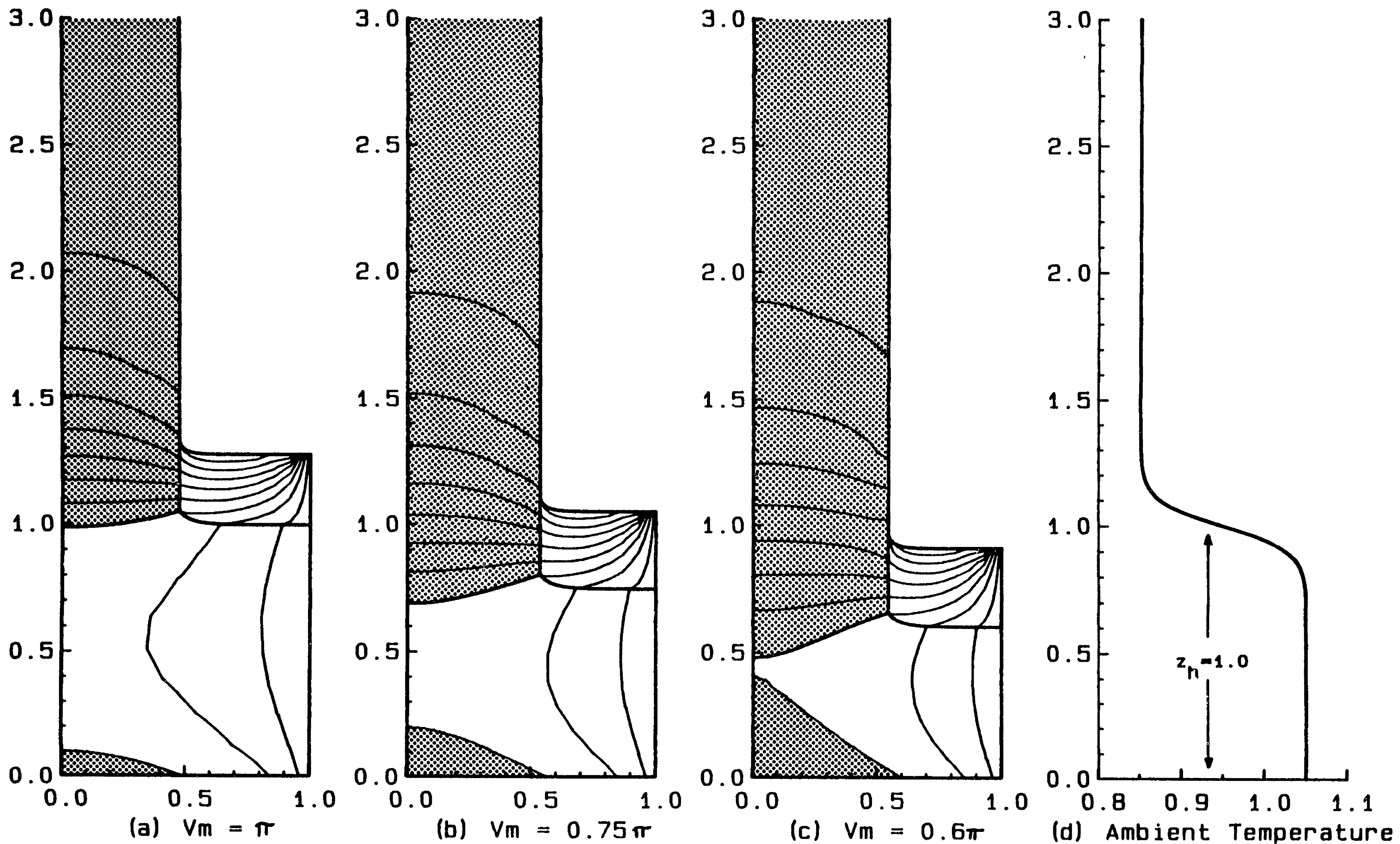

Fig. 4.30 Changes in isotherms and interface shapes with decreasing melt volume for LEC growth of GaAs using the ambient temperature profile for the deep crucible ($z_h = 1.0$). The encapsulant layer is taken to be completely opaque, and all other parameters are held fixed at those of reference case.

provides valuable insight into the effectiveness of design parameters, to the sensitivity of the results to specific thermophysical properties, and to the suitability of proposed strategies for process control. Examples of each of these applications have been discussed here.

For example, the comparison of results for LEC growth with transparent and opaque encapsulants points directly to the importance of the details of B_2O_3 radiation absorption in setting the precise sensitivity of crystal radius to parameters like pull rate and encapsulant volume. LEC growth with a transparent encapsulant was very much like ordinary CZ growth (see Fig. 4.24) in its response to changes in system parameters; introducing an opaque B_2O_3 layer more significantly insulated the melt and resulted in a dramatic increase in the sensitivity of the radius to pull rate. This point suggested at least one reason why LEC growth of GaAs is more difficult than CZ growth of silicon.

The calculations presented in Section 4.2.2 also explain the dependence of crystal radius on melt depth and melt/solid interface shape observed in the LEC InP experiments of Muller et al. (1983). Assuming the B_2O_3 is an opaque encapsulant leads to prediction of the convex interface shape and the decrease in crystal radius with melt volume reported by these researchers. These effects are only modeled when the exposure of the crystal protruding from the encapsulant to the hot surrounding crucible wall is included.

While the calculations reported here surely can aid design efforts for equipment and control strategies, they are probably too inaccurate to be used in on-line control algorithms. The details of the thermal field involving heat transfer in the crucible, the efficiency of radiative

exchange between various elements in the furnace, and the convection in the melt must be accounted for if a quantitative analysis, such as has been reported for the EFG system (Kalejs et al., 1983), is to be accomplished. We discuss these factors in more detail in Chapter 6 of this thesis.

4.3 Processing Strategies

Changes in the diameter of a growing Czochralski crystal are caused by disturbances to the thermal field in the melt or crystal and can occur over widely differing time scales. For example, short-term fluctuations in heat transfer in the melt and gaseous ambient are caused by chaotic or turbulent convection in the melt and gas and can lead to microscopic dopant striations in the crystal. Long-term transients arise from continuous changes in the thermal environment which take place as the melt level drops during growth, an artifact of the batchwise nature of the CZ process. The control of crystal diameter with respect to short-term disturbances depends on containing the transient response of the system to such perturbations, and the long-term changes in thermal environment are countered by appropriate adjustments in process parameters, a programmed crucible lift rate or crystal pull rate are examples of process parameters which are continuously changed during growth. In practice, automatic diameter control performs both of these functions by adjusting process variables. The effect of the two time scales on the response of a process or control variable is illustrated in Fig. 4.31.

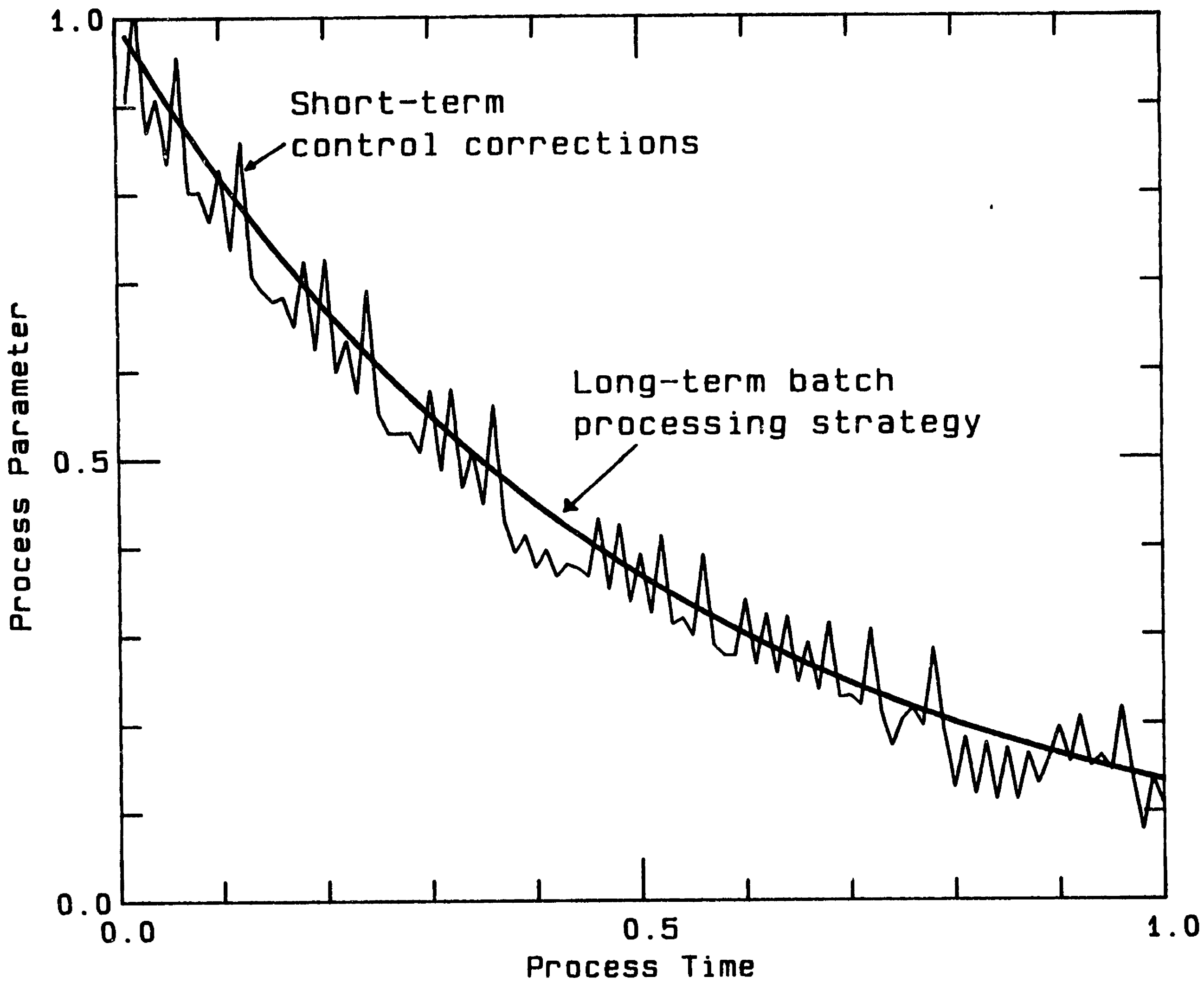

Fig. 4.31 Variation of a process parameter (or control variable), such as pull rate used to maintain constant crystal diameter, throughout a growth run to different time scale fluctuations in CZ process.

We focus on developing processing strategies for CZ growth of crystals with constant radius and melt/solid interface shape with respect to the slow time-scale transients introduced by the batch CZ process. We do this by studying the response of a complete thermal-capillary model for Czochralski growth to the lowering of the melt volume. The thermal-capillary model used here and the finite-element technique developed for its solution have been described previously. We build on the steady-state model by adding constraints for control of crystal radius and melt/crystal interface deflection.

The strategies are calculated by augmenting the algebraic equation set which results from the numerical approximation of the model with extra equations representing the selected constraints of constant crystal radius and melt/solid interface deflection. The constraints are satisfied by determining specific process variables, such as heater temperature and pull rate, as part of the solution of the thermal-capillary problem. The augmented equation set is solved systematically using the same Isotherm/Newton finite-element iteration formulation used for analysis of the unconstrained system. The technique is general in that any combination of constraints and process variables can be implemented simultaneously; various choices for process constraints and control variables are listed in Table 4.9.

We have chosen the crystal radius to be constant because this is the primary constraint in use today and because constant-diameter crystals are important for minimizing the cutting waste of the boules as they are prepared for subsequent circuit fabrication. The shape of the melt/crystal interface during growth is related to the crystalline

Table 4.9 Process constraints and variables for Czochralski growth.

Process Constraints	Process Variables
Constant Crystal Diameter	Pull Rate
Specified Interface Shape	Power Input - Crucible Temperature
Specified Thermal Gradients	Crucible Lift Rate
	Bottom Heater Temperature

quality through both the radial and axial temperature in the crystal adjacent to the interface and through the induced direction for motion of defects that form upon solidification. Interface shapes that are slightly concave with respect to the solid are preferred because dislocations migrate towards the surface of the crystal (Carruthers and Witt, 1975; Lorenzini et al., 1974). The constraint of constant interface deflection used here is a first attempt at setting interface morphology for optimized crystal quality. Analysis of this constraint through mathematical modeling is particularly useful because of the present inability for on-line measurement of either the melt/crystal interface shape or the temperature field near the interface. Modeling supplies the only correlation between interface morphology and these measurements of crystalline quality during the growth process.

The idea of controlling features of CZ growth other than crystal diameter is not new. Mil'vidskii and Golovin (1961) proposed that pull rate modulation be used to maintain a constant interface shape throughout growth while ignoring the diameter changes. More recently, Watanabe et al. (1984) have attempted to control the interface shape of LEC gallium arsenide by the use of a bottom heater. A predictive model which accurately assessed the heat transfer in the system could be used to develop strategies for the control of diameter <u>and</u> other features of the crystal.

An important issue for calculations of this type is the "inherent" stability of the Czochralski process. Stability is set by the interaction of heat transfer and capillarity and is determined by the response of the system to small disturbances, either mechanical or thermal

in nature. If the CZ process is inherently stable, diameter changes which occur during a growth run are only manifestations of the changing thermal environment, and the actions needed to control the process can be meaningfully addressed by assessing the quasi-steady heat transfer in a CZ system parameterized by decreasing melt volumes. The steady-state thermal-capillary model discussed in previous sections is well-suited for this task, and the modifications needed for process control calculations are described below. In addition to the control of crystal diameter, other factors which affect crystal quality, such as interface shape and thermal stress in the crystal, are accessible to control through model simulation. We discuss the issue of stability at length in Chapter 5, where we show that the Czochralski process is stable for a wide range of operating conditions and an approach such as that described above is justified.

The limitations on the ranges of validity of the results presented below are coupled to the assumptions made in the conduction-dominated thermal-capillary model. This model is limited to the growth of small-diameter crystals so that convection in the melt does not overpower conduction, or to systems with high enough applied magnetic fields that conduction is again dominant. The formulation of the strategies described here and the arguments about the multiple time scales for control of CZ growth carry over to larger-scale systems.

4.3.1 Methodology

The thermal-capillary model and numerical methods are outlined in Chapters 2 and 3, and here we describe the modifications necessary to calculate operating strategies. The discretized version of the pseudo-steady thermal-capillary model is represented in its simplest form as a vector of N nonlinear equations

$$\mathbf{F}(\mathbf{y};\mathbf{p}) = \mathbf{0} , \qquad (4.5)$$

where $\{y_i\}$ are the N-dimensional set of unknowns needed to approximate the temperature field, the shapes of the melt/crystal and melt/gas interfaces, and the radius of the crystal. The M-dimensional vector $\mathbf{p}$ contains the process parameters that describe the thermal environment of the crucible and the configuration of the melt. The N-dimensional vector function $\{F_i\}$ represents the set of nonlinear equations which result from the finite-element analysis of the governing equations. In the quasi-steady model the dimensionless melt volume V_m appears as an element of the vector $\mathbf{p}$ which parametrically describes the progress of the batchwise growth. We focus on the response of the system to variations in this parameter.

A full Newton-Raphson method is used to iteratively solve the nonlinear equation set (4.5) for the unknowns by successively computing approximations to the solution vector $\mathbf{y}^{(k)}$ by solving the linear problem

$$\mathbf{J}(\mathbf{y}^{(k)})\ \boldsymbol{\delta}^{(k+1)} = -\mathbf{F}(\mathbf{y}^{(k)}) , \qquad (4.6)$$

where $J_{ij} = \partial F_i/\partial y_j$ is the Jacobian sensitivity matrix and $\{\delta_i\}$ are corrections to the previous solution iterate so that

$$\mathbf{y}^{(k+1)} = \mathbf{y}^{(k)} + \boldsymbol{\delta}^{(k+1)}, \tag{4.7}$$

where the superscripts represent the iteration number.

In this framework we can specify additional equations which represent process constraints along with additional degrees of freedom, the process variables or parameters, for satisfying these conditions. We identify several possible process constraints and process variables in Table 4.9. For the calculations which follow, we have chosen to specify two process constraints, namely that the crystal radius and melt/solid interface deflection remain constant through a growth run. These specifications are represented by the following equations:

$$R - R_{set} = 0 , \tag{4.8}$$

$$H_o(R) - H_o(0) - \Delta_{set} = 0 . \tag{4.9}$$

where $H_o(R)$ and $H_o(0)$ are the heights of the melt/crystal interface above the bottom of the crucible measured at the edge of the crystal ($r=R$) and the centerline axis ($r=0$), respectively, and R_{set} and Δ_{set} are set-point values for the radius and interface deflection. We have chosen three different sets of process variables for which calculations are performed, all combinations of pull rate, crucible wall temperature, and bottom ambient temperature, and we denote $\tilde{\mathbf{p}}$ as the 2-dimension vector of parameters which are chosen as unknowns to satisfy the two extra constraints of above. Equations (4.8) and (4.9) are used to augment the original equation set, and the specified process variables are added to the original unknowns vector so that eq. (4.5) now becomes the (N+2)-dimensional set

$$\mathbf{F}^{aug}\ (\hat{\mathbf{y}};\hat{\mathbf{p}}) = \mathbf{0}\ , \qquad (4.10)$$

where $\hat{\mathbf{y}}$ is the new (N+2)-dimensional solution vector and $\hat{\mathbf{p}}$ is the reduced (M-2)-dimensional set of process parameters (note that $\hat{\mathbf{y}}$ = {$\mathbf{y}$ (Union) $\tilde{\mathbf{p}}$} and {$\hat{\mathbf{p}}$ (Union) $\tilde{\mathbf{p}}$} = $\mathbf{p}$). $\mathbf{F}^{aug}$ is the new vector function of dimension N+2. The solution technique follows as before with a fully implicit Newton-Raphson method:

$$\mathbf{J}^{aug}(\hat{\mathbf{y}};\hat{\mathbf{p}})\ \hat{\boldsymbol{\delta}} = -\mathbf{F}^{aug}\ (\hat{\mathbf{y}};\hat{\mathbf{p}})\ , \qquad (4.11)$$

where $\{\hat{\delta}_i\}$ is now of higher (N+2) dimension, and the augmented Jacobian $\mathbf{J}^{aug}$ is represented as

$$\mathbf{J}^{aug} = \frac{\partial \mathbf{F}^{aug}}{\partial \hat{\mathbf{y}}} = \frac{\partial \mathbf{F}^{aug}}{\partial \mathbf{y};\tilde{\mathbf{p}}} = \left[\begin{array}{c|c} \mathbf{J} & \dfrac{\partial \mathbf{F}}{\partial \tilde{\mathbf{p}}} \\ \hline \dfrac{\partial \mathbf{C}}{\partial \mathbf{y}} & \dfrac{\partial \mathbf{C}}{\partial \tilde{\mathbf{p}}} \end{array}\right] , \qquad (4.12)$$

where $\mathbf{J}$ is the original Jacobian NxN matrix for the unconstrained set of equations and $\partial\mathbf{F}/\partial\tilde{\mathbf{p}}$ is an Nx2 column vector which represents the partial derivatives of the original vector residuals function $\mathbf{F}$ with respect to the parameters chosen as the extra unknowns in the augmented problem, $\tilde{\mathbf{p}}$. The added constraints of equations (4.8) and (4.9) are denoted as $\{C_i\}$ so that $\partial\mathbf{C}/\partial\mathbf{y}$ is a 2xN row matrix of the partial derivatives of the constraint equations with respect to the original set of unknowns and $\partial\mathbf{C}/\partial\tilde{\mathbf{p}}$ is a 2x2 matrix of partial derivatives of the constraints with respect to the distinguished processing parameters. For our choices of constraints and parameters, the individual components of $\partial\mathbf{C}/\partial\tilde{\mathbf{p}}$ are zero. All of the components of the augmented

Jacobian are computed analytically. In this iteration scheme, quadratic convergence is achieved for all unknowns, and computation times are not significantly different from those reported for the previous calculations of Section 4.2.1.

4.3.2 Calculations

All of the following cases represent prototype CZ silicon calculations performed under the same conditions of the previous section with no crucible lift (the ambient temperature profile remains fixed with respect to the crucible). Calculations which represent a growth sequence of lowering melt volume without any augmented constraints are shown in Fig. 4.32 where the crystal radius and interface deflection are plotted as functions of melt volume for both ambient temperature profiles of the uniform ambient and shallow crucible (an ambient temperature profile generated by eq. (4.4) of Section 4.2 with $\Theta_a^\infty = 0.75$ and $z_h = 0.75$). In each simulated growth run, the crystal was pulled at a steady rate of 5 cm/hr (a dimensionless pull rate of Pe=0.1).

For the uniform ambient, the lowering melt level caused less heat to be transferred into the melt and thus lead to monotonic increase of the crystal radius as the melt volume decreases. When radiative heating from the exposed crucible wall is added in the shallow crucible, the radius first increases then decreases with decreasing V_m, as also shown by calculations in Section 4.2.1. For both ambient temperature profiles, the interface deflection uniformly increases and the interface evolves from an initial concave shape into the crystal ($\Delta<0$) to an

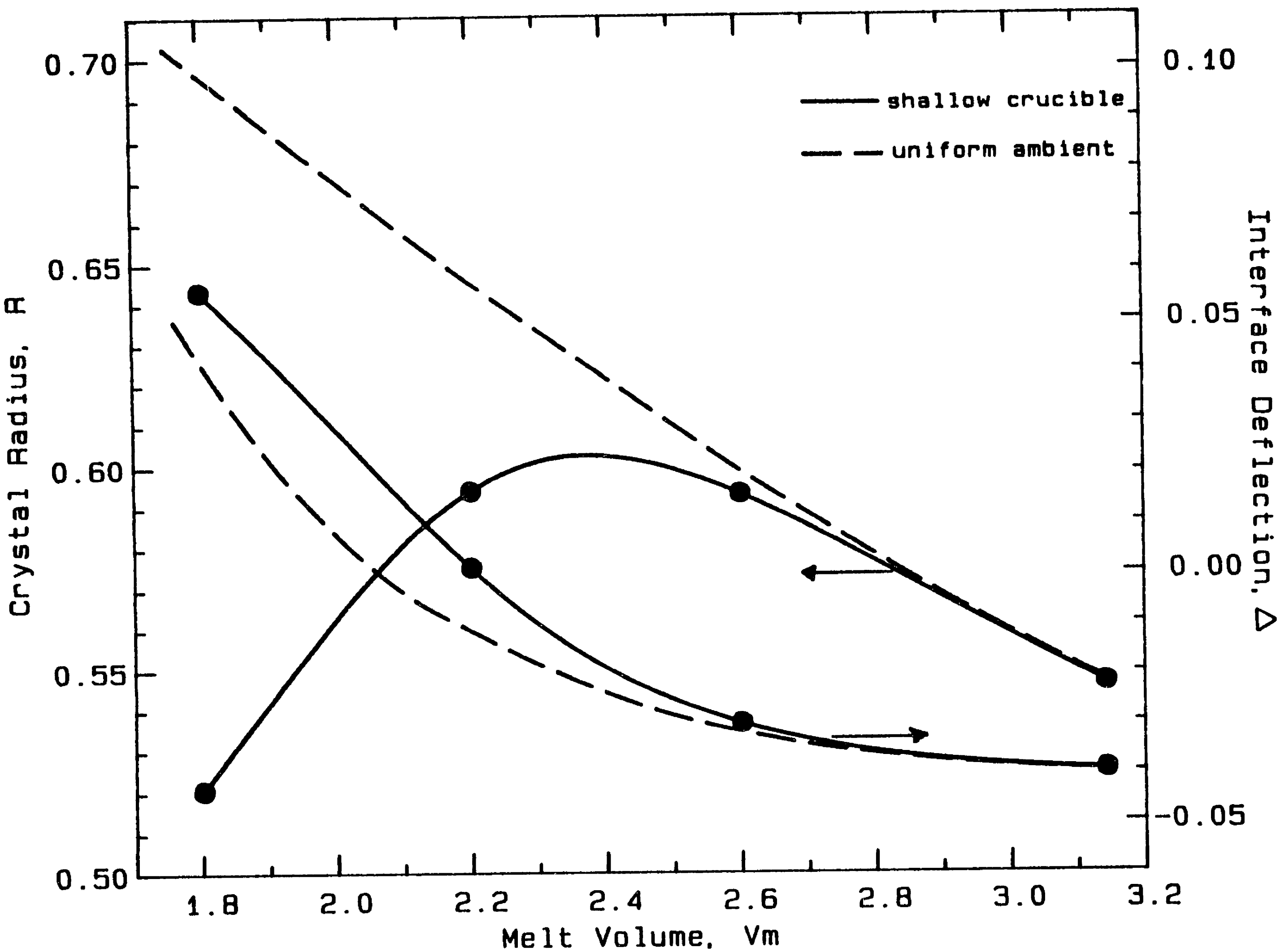

Fig. 4.32 Crystal radius and melt/crystal interface deflection for CZ silicon growth as a function of melt volume. All other parameters held constant. Results are presented for both the shallow crucible and uniform ambient temperature distributions.

increasingly convex shape into the melt (Δ>0). The shallow crucible configuration was chosen as a basis for the ensuing control calculations since it more realistically represents a CZ growth run. Temperature fields and interface shapes predicted for the shallow crucible run are shown in Fig. 4.33a-d for the sample points denoted by the solid circles of Fig. 4.32. These cases, representing various stages of the growth sequence, are used as a reference for comparing the following different processing strategies for fixing the crystal diameter and interface deflection.

4.3.2.1 Diameter

The values of pull rate and interface deflection shown in Fig. 4.34 are obtained when automatic diameter control is achieved by distinguishing the pull rate as the control variable and by augmenting the steady-state equation set with eq. (4.8) for R_{set}=0.5 (a 3.5 cm radius crystal in a crucible of 7 cm). The resulting pull rate behavior mimics the radius - melt volume curves of Fig. 4.32, initially increasing then falling for lower melt volumes. This behavior is understood by comparing the results of Figs. 4.32 and 4.34. For both the uniform ambient temperature profile and the system corresponding to a shallow crucible, the pull rate for controlled growth adjusts either upward or downward so that more or less latent heat is generated at the melt/solid interface to compensate for radius changes in the uncontrolled system. The interface deflection for the shallow crucible configuration is a function of latent heat generation and the proximity of the crucible bottom

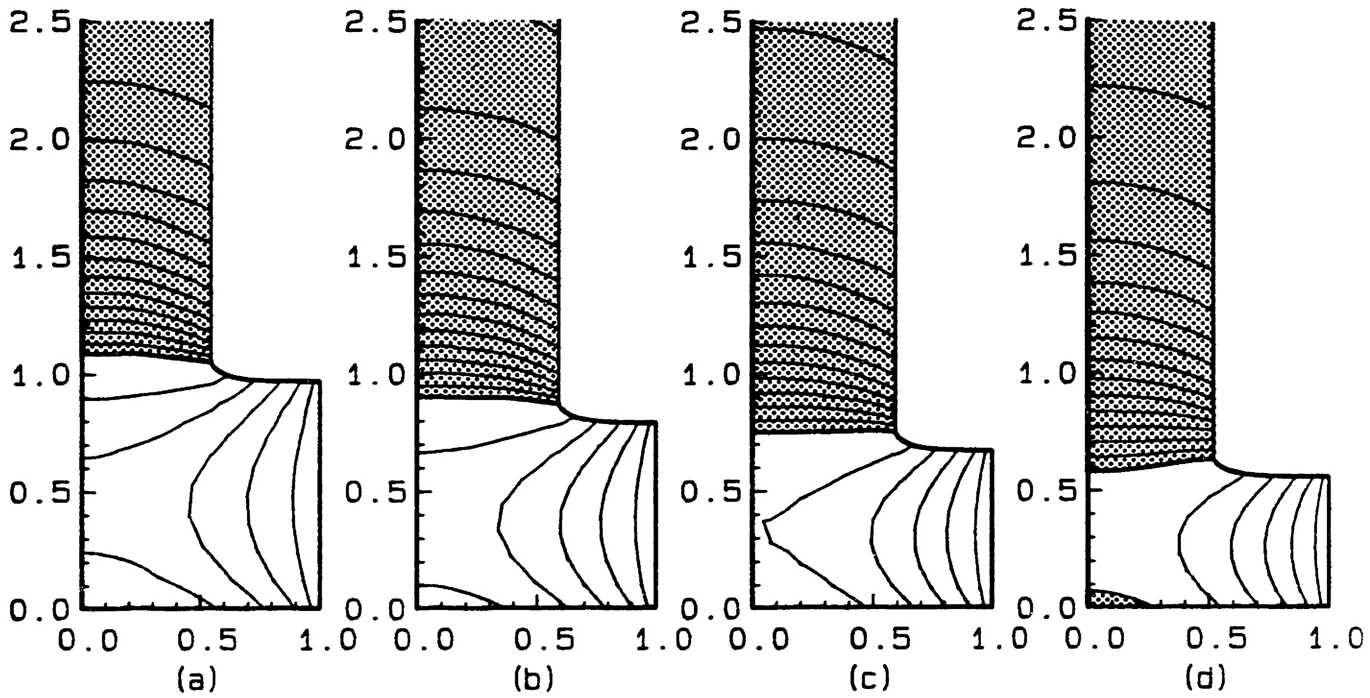

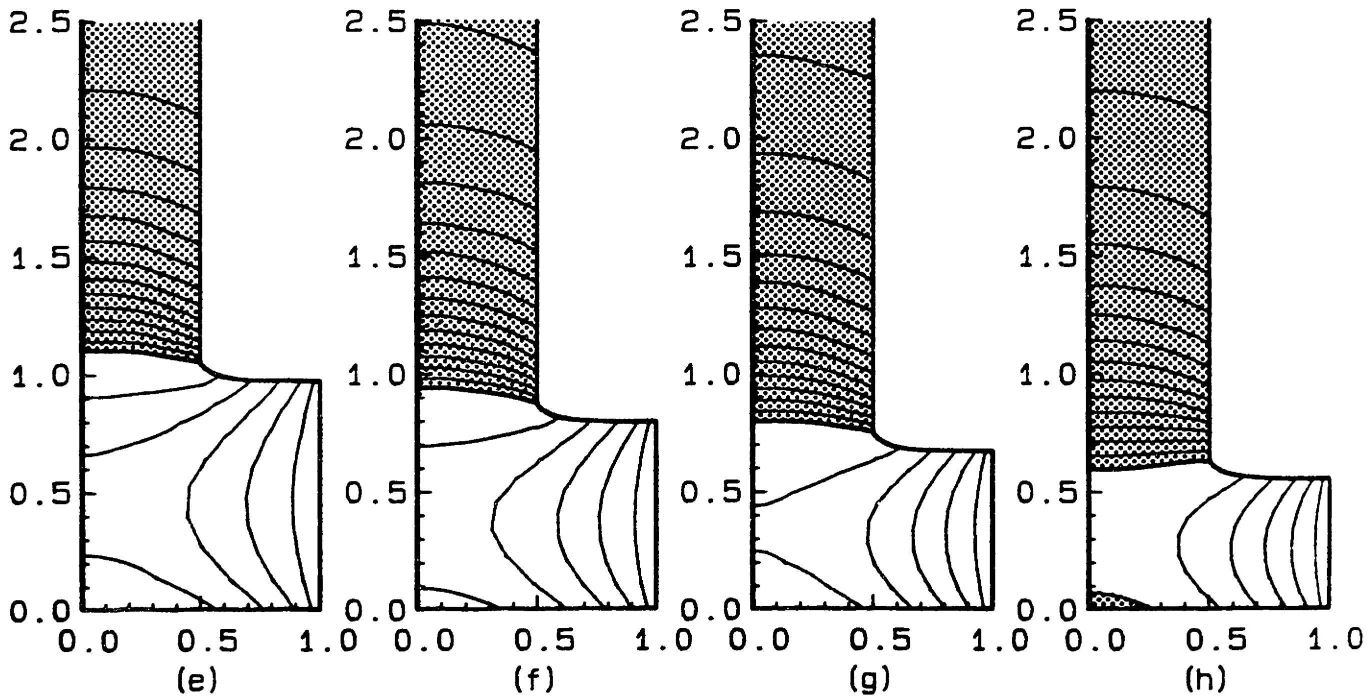

V_m=3.1416 V_m=2.6 V_m=2.2 V_m=1.8

Fig. 4.33 Isotherms and interface shapes for cases of Figs. 4.32 and 4.34 for melt volumes of V_m = 3.1416, 2.6, 2.2, and 1.8. (a-d) No control. (e-h) Pull rate used to control diameter. Isotherms are spaced in 30K intervals around the melt/crystal interface, and shaded regions denote solid silicon.

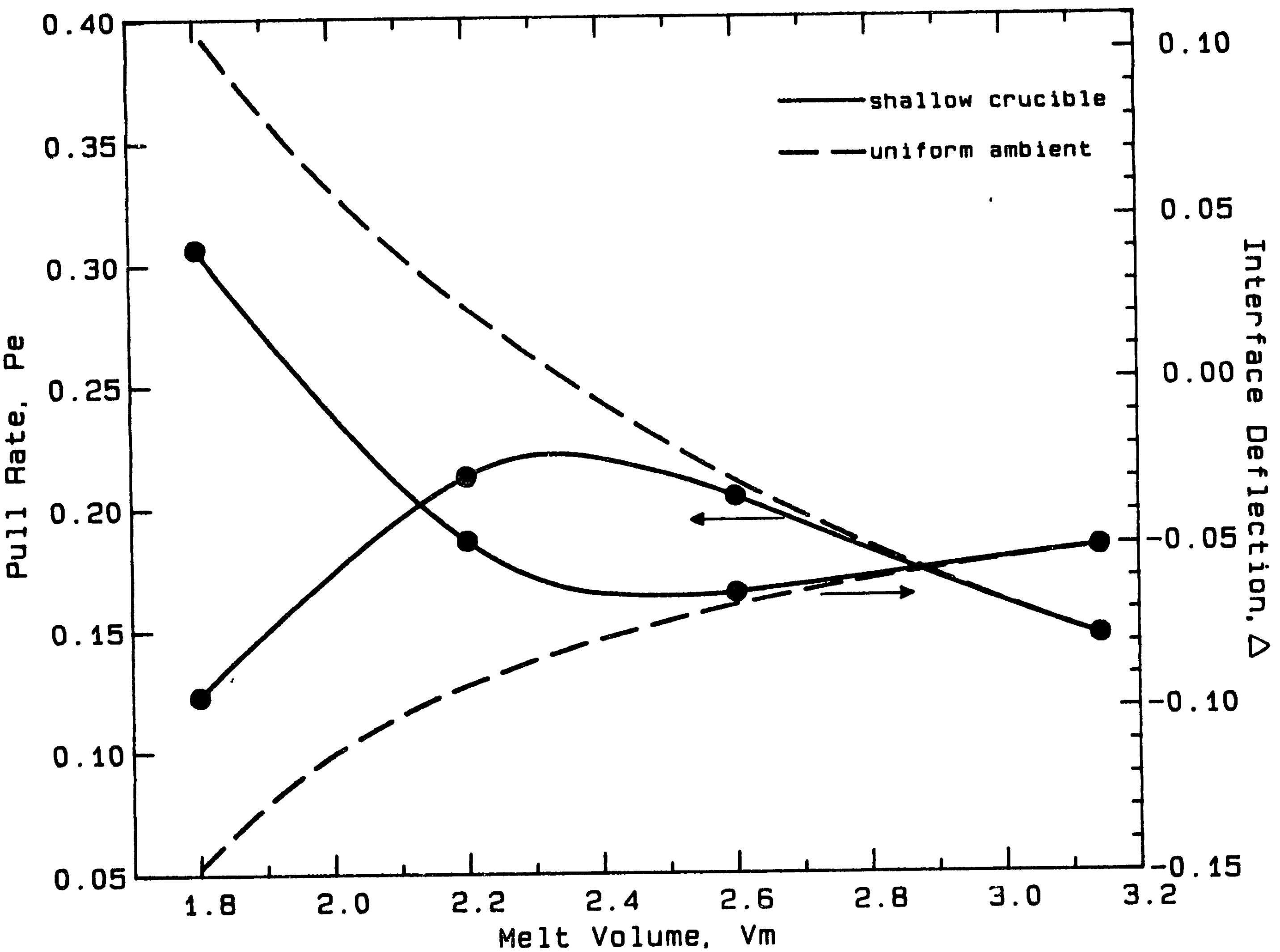

Fig. 4.34 Pull rate and interface deflection for CZ silicon growth as a function of melt volume when pull rate is designated as a control parameter to set crystal radius at R = 0.5 (R:Pe). Results are presented for both the shallow crucible and uniform ambient temperature distributions.

and varies from concave to convex even though the diameter is constant. For the uniform ambient, the interface deflection steadily decreases as the pull rate is ramped up; here latent heat generation dominates the effect of the crucible geometry in determining the interface deflection.

The results for the shallow crucible runs denoted by the solid circles of Fig. 4.34 for constant-diameter growth are plotted in Fig. 4.33e-h. In both the uncontrolled and constant-diameter sequences, a small region of the melt at the bottom of the crucible becomes thermally supercooled with decreasing melt volume, as was seen in the results of the Section 4.2.1.

4.3.2.2 Diameter and Interface Deflection

Three strategies were assessed for the control of diameter and interface deflection in the next series of calculations. Combinations of pull rate, bottom heater temperature, and crucible wall temperature are used to maintain the radius at R=0.5 and the interface deflection the same as the case of Fig. 4.33e, $\Delta=-0.0509$ (a deflection in real terms of -0.36 cm). The results for each of these strategies are described below according to which parameters are used to satisfy the two constraints.

Strategies Based on Pull Rate and Bottom Heater Temperature (R,Δ:$Pe,\Theta_{a,b}$)

Figure 4.35 represents the sequence of pull rates Pe and bottom heater temperatures $\Theta_{a,b}$ (the process variables) needed to keep the radius R and interface deflection Δ constant (the process constraints). The changes in pull rate and bottom heater temperature are shown as functions of melt volume. For these calculations, the control strategy could not maintain the desired constraints below a melt volume of $V_m \approx 2.2$ for the shallow crucible configuration. However, these conditions could be met down to very small melt volumes with calculations for the uniform ambient. We show the isotherms and geometries for this growth series in Fig. 4.36.

The inability of reaching low V_m operating states for the shallow crucible is understood by comparison of the uniform ambient and shallow crucible cases, as shown in Fig. 4.35. The control variable response for the uniform ambient is well-behaved and monotonic, like the corresponding behavior of the radius and interface deflection in the uncontrolled case of Fig. 4.32. However, as the melt level drops beyond V_m=2.4 for the shallow crucible configuration, the radius of the uncontrolled calculations of Fig. 4.32 begins to decrease while at the same time the interface deflection continues to increase. In this situation the process variable strategies shown in Fig. 4.35 oppose each other: as the bottom ambient temperature cools to counteract the tendency for the crystal radius to decrease, the pull rate responds by increasing to maintain a constant interface deflection. Increasing the pull rate alone would tend to decrease the crystal radius in opposition

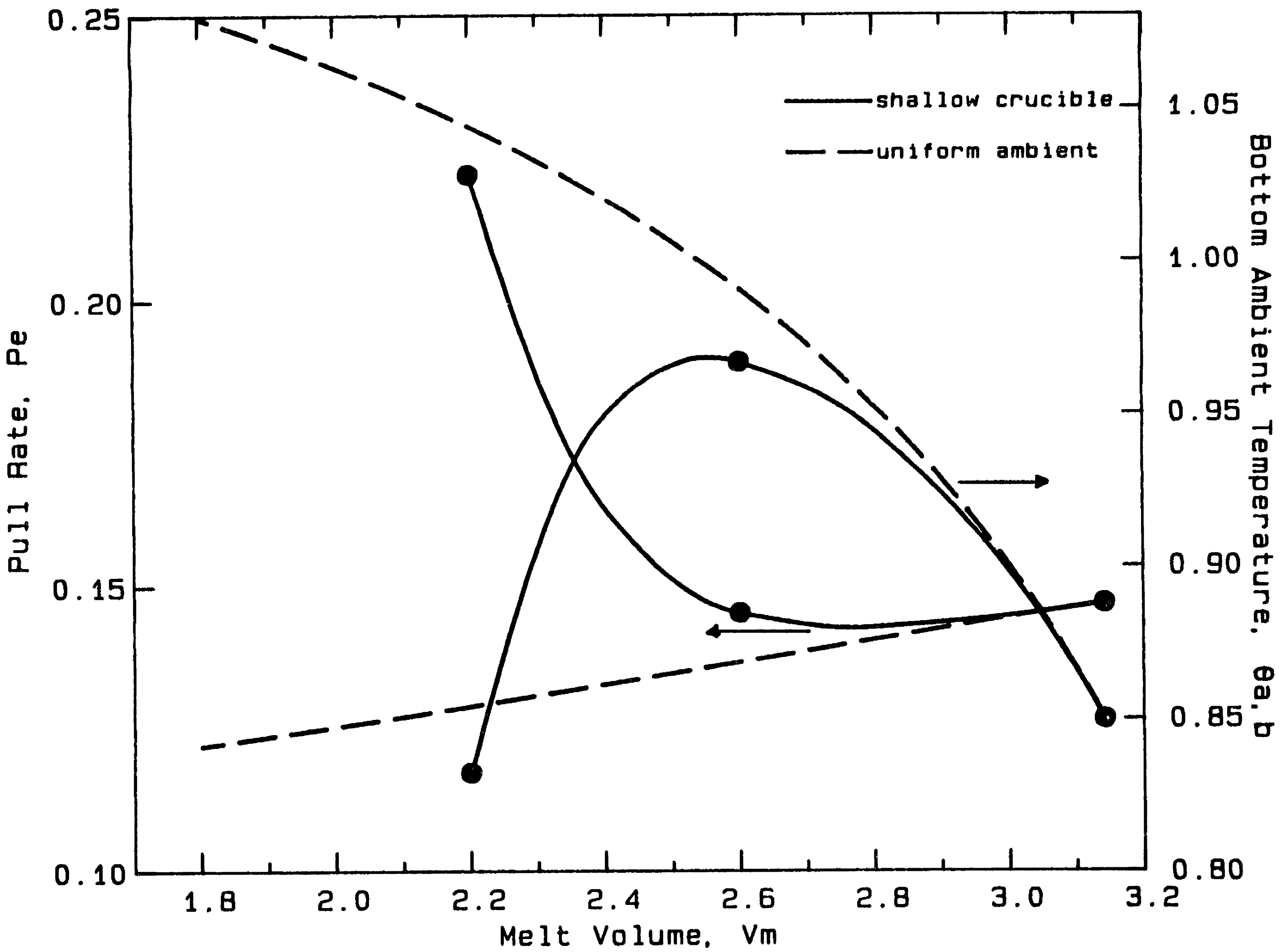

Fig. 4.35 Pull rate and bottom ambient temperature control of CZ silicon growth as a function of melt volume; control parameters act to set crystal radius at R = 0.5 and melt/crystal interface deflection at $\Delta = -0.0509$ $(R,\Delta:Pe,\Theta_{a,b})$. Results are presented for the shallow crucible temperature distribution.

Control Variables:

Pe

$\theta_{a,b}$

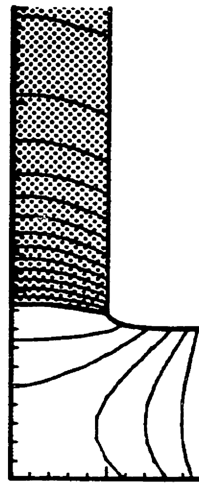

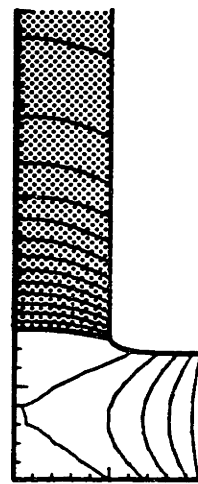

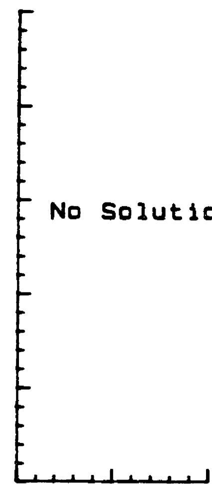

(b) (c) (d)

Initial Case

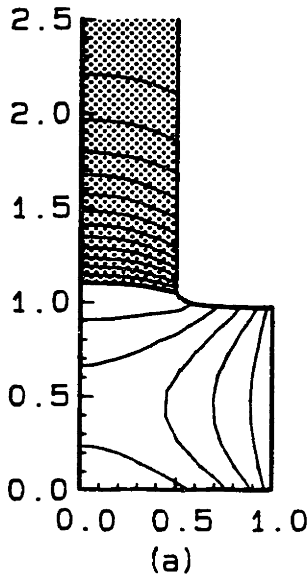

(a)

Pe

θ_c

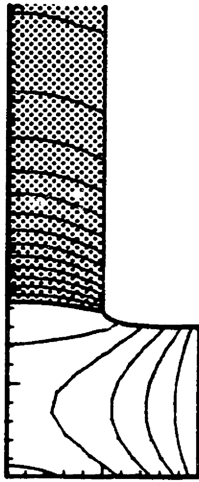

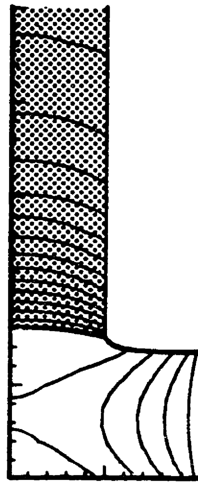

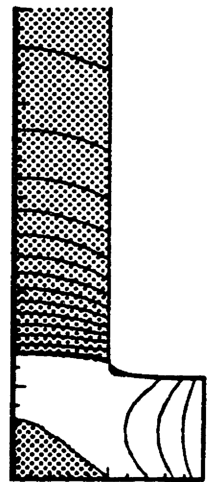

(e) (f) (g)

V_m=3.1416

$\theta_{a,b}$

θ_c

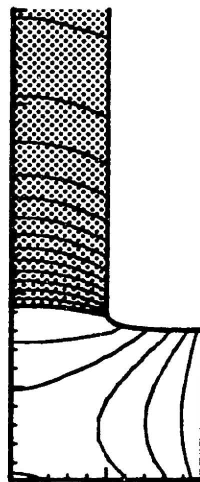

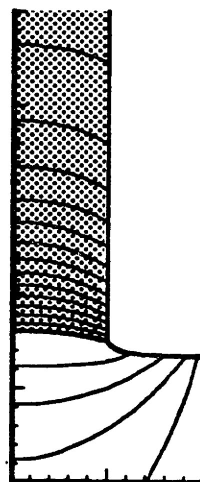

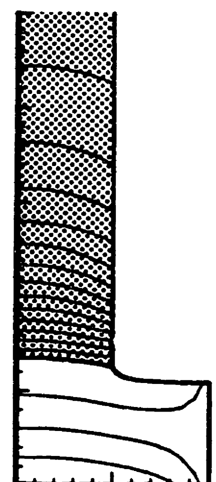

(h) (i) (j)

V_m=2.6 V_m=2.2 V_m=1.8

Fig. 4.36 Isotherms and interface shapes for different processing strategies of Figs. 4.35, 4.37, and 4.38 for melt volumes of V_m = 3.1416, 2.6, 2.2, and 1.8. (a) Initial case. (b-d) $(R,\Delta:Pe,\Theta_{a,b})$. (e-g) $(R,\Delta:Pe,\Theta_c)$. (h-j) $(R,\Delta:\Theta_{a,b},\Theta c)$.

to the desired outcome. It would not be surprising if the limit of melt volume for this control strategy represents a mathematical turning point in the solution to the augmented steady-state problem. We have not pursued this point in these calculations, but limit point phenomena are discussed more fully in the stability calculations of Chapter 5.

Strategies Based on Pull Rate and Crucible Wall Temperature ($R,\Delta:Pe,\Theta_c$)

A traditional control strategy for CZ growth varies the pull rate Pe and crucible wall temperature, represented here by the specified temperature Θ_c, for diameter control. We use these two parameters to set both crystal radius and interface deflection, and the results of these calculations are shown in Fig. 4.37. This strategy is successful throughout the run, and fairly low melt volumes were attainable. Initially, only slight changes in wall temperature were needed to keep the diameter constant while the pull rate modulated the shape of the melt/solid interface. When the hot crucible wall became exposed for melt volumes $V_m<2.3$, a sharp decrease in the wall temperature was needed to maintain constant diameter while the pull rate increased to prevent the melt/solid interface from becoming more convex. The lowest melt volume accessible by this strategy was set by the growth of a region of solid silicon on the bottom of the crucible; at $V_m = 1.6$, the pulled crystal "bumped" with the solid at the bottom of the melt, and growth could not be maintained. Sample isotherms and geometries for this growth sequence are shown in Fig. 4.36.

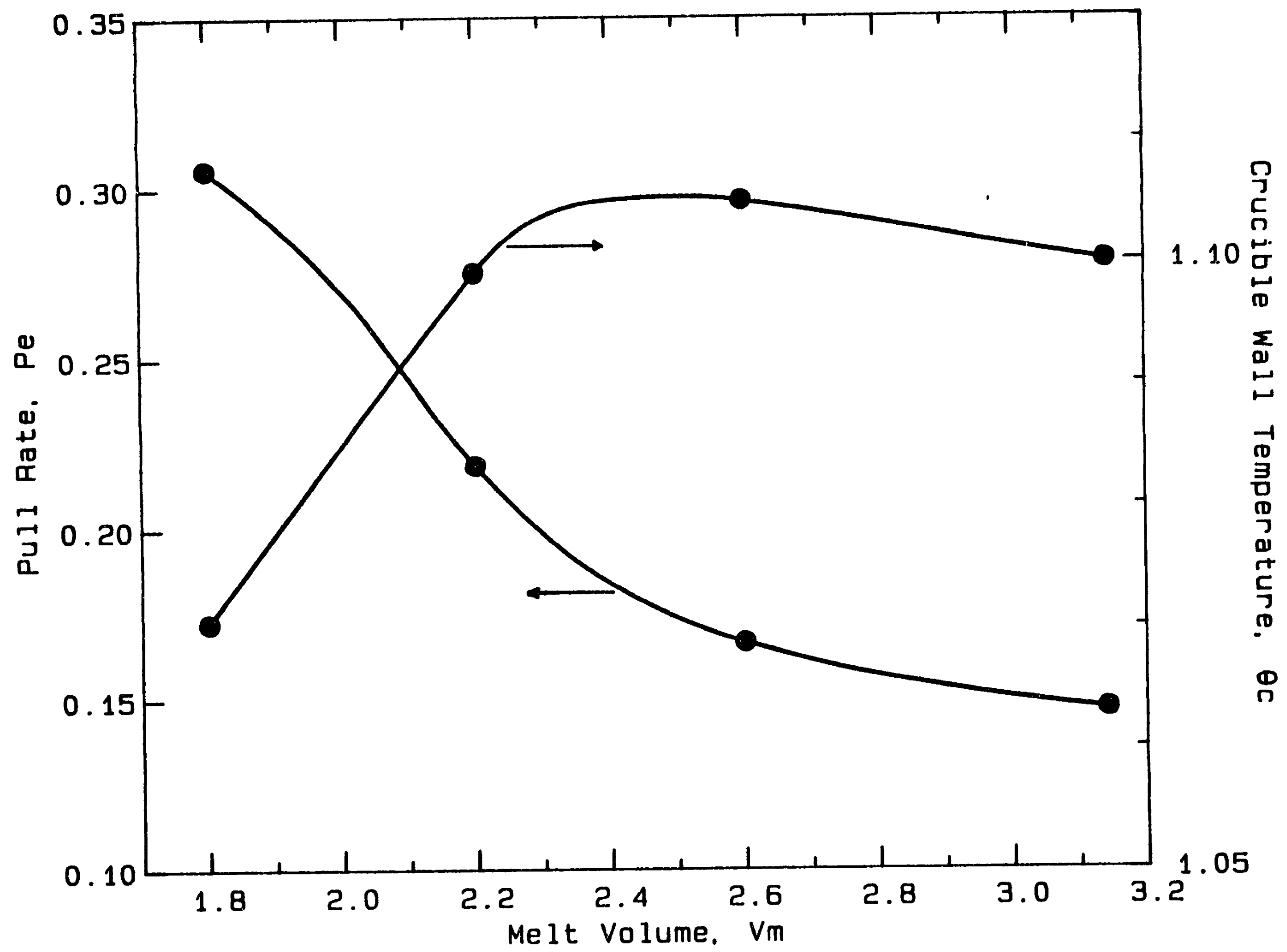

Fig. 4.37 Pull rate and crucible wall temperature control of CZ silicon growth as a function of melt volume ($R,\Delta:Pe,\theta_c$). Radius and interface deflection held constant at values of $R = 0.5$ and $\Delta = -0.0509$. Results are presented for the shallow crucible temperature distribution.

Strategies Based on Bottom and Crucible Heater Temperatures
$(R, \Delta : \Theta_{a,b}, \Theta_c)$

The final strategy is represented in Fig. 4.38 where the bottom ambient temperature and crucible wall temperature are plotted in relation to melt volume. This strategy was also successful in maintaining constant R and Δ for a large range of melt volumes. It seemed that the bottom ambient temperature kept the interface deflection in check by setting amount the upward heat flux through the melt to the melt/solid interface, and the crucible wall temperature maintained a constant diameter by controlling the total amount of heat entering the melt. As shown in Fig. 4.36, the isotherms for low melt volumes for this processing strategy are almost horizontal under the crystal, indicative of approximately one-dimensional heat transfer up to the solidification interface. No region of undercooled melt formed at the bottom of the melt, even at extremely low melt volumes.

4.3.3 Discussion

Temperature gradients evaluated at the melt/solid interface and in the crystal are listed in Table 4.10 for each of the processing strategy cases. The axial and radial temperature gradients predicted in the crystal were very similar for any set of parameters that maintained both radius and interface deflection constant. This is not a surprising result since the temperature field, at least at the melt/solid interface, had to be similar in all three cases if the interface deflection were to remain the same. The axial temperature gradient at the solidification

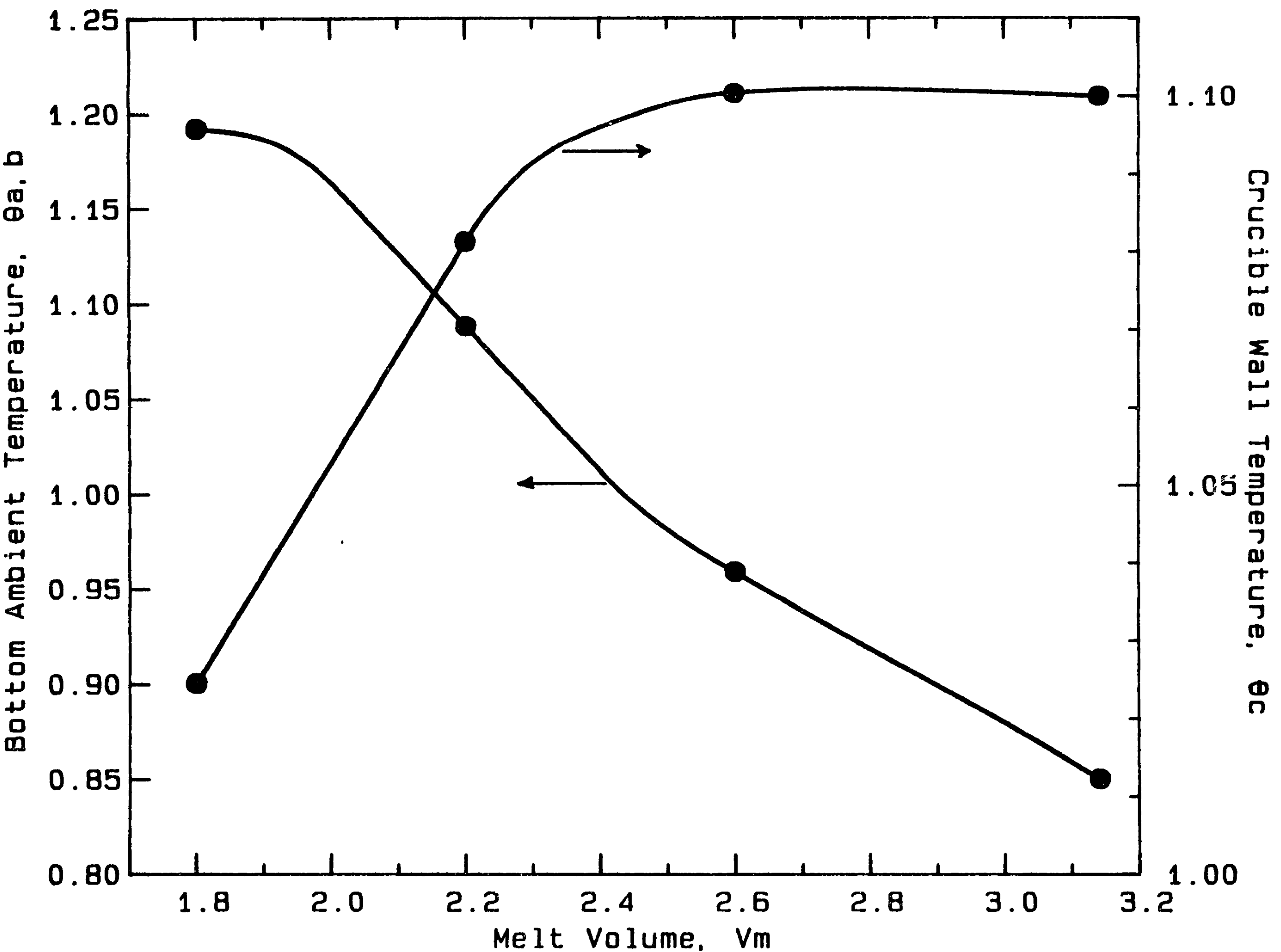

Fig. 4.38 Bottom ambient and crucible wall temperature control of CZ silicon growth as a function of melt volume $(R,\Delta:\Theta_{a,b},\Theta_c)$. Radius and interface deflection held constant at values of $R = 0.5$ and $\Delta = -0.0509$. Results are presented for the shallow crucible temperature distribution.

Table 4.10 Temperature gradients for calculations without control and with the four control algorithms presented in Section 4.3.

Melt Volume and Control Strategy (Bracketed number refers to isotherm Figure)	$\partial T/\partial \tilde{z}$ at centerline and melt/solid interface	$\partial T/\partial \tilde{z}$ at centerline and 0.5[1] above the melt/solid interface (K/cm)	$\Delta T/\tilde{R}$ between centerline and radius at 0.5 above the melt/solid interface
V_m=3.1416			
No Control [4.33a]	-90.8	-46.5	-10.1
(R:Pe) [4.33e]	-99.1	-47.5	-9.7
$(R,\Delta:Pe,\Theta_{a,b})$ [4.36a]	-99.1	-47.5	-9.7
$(R,\Delta:Pe,\Theta_c)$ [4.36a]	-99.1	-47.5	-9.7
$(R,\Delta:\Theta_{a,b},\Theta_c)$ [4.36a]	-99.1	-47.5	-9.7
V_m=2.6			
No Control [4.33b]	-82.4	-45.1	-10.5
(R:Pe) [4.33f]	-100.3	-48.1	-9.7
$(R,\Delta:Pe,\Theta_{a,b})$ [4.36b]	-98.9	-47.3	-9.7
$(R,\Delta:Pe,\Theta_c)$ [4.36e]	-98.0	-47.3	-10.1
$(R,\Delta:\Theta_{a,b},\Theta_c)$ [4.36h]	-98.8	-47.3	-9.7
V_m=2.4			
No Control [4.33c]	-75.1	-43.7	-10.6
(R:Pe) [4.33g]	-95.2	-47.2	-9.9
$(R,\Delta:Pe,\Theta_{a,b})$ [4.36c]	-95.4	-47.3	-10.0
$(R,\Delta:Pe,\Theta_c)$ [4.36f]	-95.6	-47.3	-9.9
$(R,\Delta:\Theta_{a,b},\Theta_c)$ [4.36i]	-98.4	-47.2	-9.7
V_m=1.8			
No Control [4.33d]	-64.3	-43.9	-10.5
(R:Pe) [4.33h]	-68.9	-44.6	-10.3
$(R,\Delta:Pe,\Theta_{a,b})$ [4.36d]	---	---	---
$(R,\Delta:Pe,\Theta_c)$ [4.36g]	-84.7	-48.4	-10.3
$(R,\Delta:\Theta_{a,b},\Theta_c)$ [4.36j]	-92.1	-48.1	-9.9

[1] 3.5 cm above melt/solid interface

interface did decrease drastically with lowering melt volume when the radius or the interface deflection were not controlled so that the temperature field near the interface was allowed to change. This is an important result because it indicates that the simultaneous control of the interface shape and temperature gradients needed for controlling dislocation generation is not possible without introducing still more control parameters into the algorithm.

The calculations presented here can be used as a rough basis for evaluating the success of the three strategies for setting crystal radius and interface deflection (R,Δ). The strategy based on varying Pe and $\Theta_{a,b}$ is not effective since it is only workable over a limited range of melt volumes. The second strategy, based on Pe and Θ_c, is also not optimal since a large region of undercooled melt forms at the bottom of the crucible as the melt drops, thus limiting crystal pulling. This leaves the simultaneous control of heater temperature Θ_c and the use of a bottom heater $(\Theta_{a,b})$ as the most attractive choice; this algorithm was able to handle the entire range of melt volumes and tended to produce the lowest radial temperature gradients. It is interesting to note that this strategy is similar to that chosen by Watanabe et al. (1984) for the controlled low-gradient LEC growth of gallium arsenide.

Obviously, the calculations presented and the conclusions based on them are limited due to the qualitative nature of the conduction-dominated model used here. However, the concept of using a model for determining processing strategies is important, especially in controlling process features which are not directly observable, such

as the shape of the melt/solid interface. With the development of more quantitative heat transfer models, real-time simulation-based strategies will be possible and will lead to on-line processing strategies based on predictive model calculations.

Chapter 5. Linear Stability and Transient Results

In the following sections, the stability and dynamics of the CZ process are explored through calculations for a prototype of an experimental silicon growth system. The calculations presented here are the first to feature the dynamic interactions of heat transfer and crystal shape in a batch system with a crucible, liner, and dropping melt level. The details of the evolution of the crystal radius from the tri-junction and the mathematical features introduced by its addition to the thermal-capillary model were discussed in Chapters 2 and 3.

Section 5.1 introduces the quasi-steady-state calculations which are used as a basis for the ensuing analyses. In Section 5.2, the inherent stability of the CZ process is addressed through a linear stability analysis. Nonlinear dynamic results and a fully transient growth simulation follow in Section 5.3. The implementation of control strategies for setting crystal shape in a batch simulation is presented in Section 5.4.

5.1 Quasi-Steady Operating States

A schematic diagram of the transient model is shown in Fig. 5.1. For all of the calculations presented in this section, the ambient temperature Θ_a is taken to be uniform for all crystal, melt, and liner surfaces and for the inside, bottom, and top of the crucible. Heat enters the outer crucible side from a surrounding heater which has the constant temperature Θ_h. The heater temperature Θ_h enters the mathematical model in the flux boundary condition for the outer crucible surface. The system geometry and process parameters for the following calculations were chosen to match an experimental system in the Department of Materials Science and Engineering at the Massachusetts Institute of Technology and are listed in Tables 5.1 and 5.2 (also in Appendix A).

The parameters presented in Table 5.2 are used to define three reference quasi-steady operating states. The state for the high-gradient conditions of Θ_a=0.85 and Θ_h=1.1497 is shown in Fig. 5.2 along with an additional solution calculated for a higher pull rate of V^*=2.8 with all other parameters identical to those used for the high-gradient reference case. The isotherms in Fig. 5.2 and all subsequent plots in this chapter are spaced in 15K increments about the melting point of the system.

A series of tests were performed for the conditions depicted by the solutions shown in Fig. 5.2 to ensure that the numerical calculations were relatively free from error and that the height of the top of the crystal above the surface of the melt was sufficiently great so that heat transfer end effects were absent. First, a series

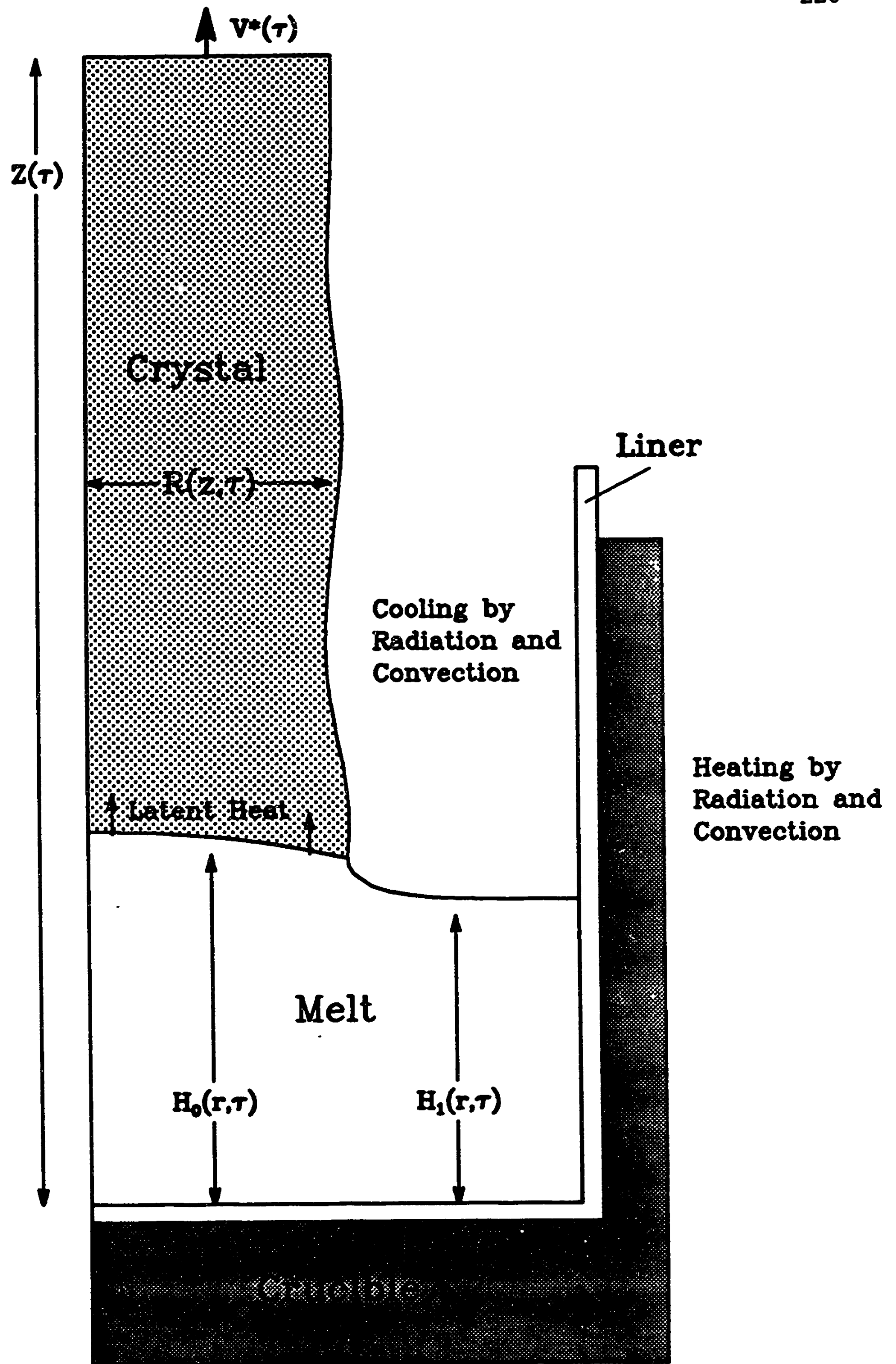

Fig. 5.1 Schematic diagram of prototype CZ system for calculations of Chapter 5.

Table 5.1 Thermophysical properties and parameters used for CZ silicon calculations of Chapter 5.

Property	Si
<u>Melt</u>	
Density, ρ_m (g/cm3)	2.42
Emissivity, ε_m	0.3
Specific heat, Cp_m (J/gK)	1.00
Thermal conductivity, k_m (W/cmK)	0.64
<u>Crystal</u>	
Density, ρ_s (g/cm3)	2.30
Emissivity, ε_s	0.7
Specific heat, Cp_s (J/gK)	1.00
Thermal conductivity, k_s (W/cmK)	0.22(1683K/T)
<u>Interfaces</u>	
Equilibrium growth angle, ϕ_0 (°)	11
Heat of fusion, ΔH_f, (J/g)	1800
Melting temperature, T_f (K)	1683
Meniscus surface tension, σ_m (dyn/cm)	720
<u>Parameters</u>	
Crucible geometry:	
Inner radius, R_c (cm)	7.3025
Outer radius (cm)	8.5725
Inner depth (cm)	11.7475
Bottom thickness (cm)	2.8575
Liner thickness (cm)	0.3175
Heat transfer coefficient, h_j (W/cm^{2}K)	10^{-3}
Pull rate, V_p (cm/hr)	5.

Property	Graphite	SiO_2
Density, ρ_c,ρ_ℓ (g/cm3)	1.6	2.2
Emissivity, $\varepsilon_c,\varepsilon_\ell$	0.8	0.35
Specific heat, Cp_c,Cp_ℓ (J/gK)	2.1	1.3
Thermal conductivity, k_c,k_ℓ (W/cmK)	0.6	0.06

Table 5.2 Operating parameters and dimensionless groups used in reference cases for CZ silicon quasi-steady and transient continuous-processing calculations of Chapter 5.

Operating Parameter	Dimensional Value	Dimensionless Value
High-Gradient Case:		
Ambient temperature, Θ_a	1430 K	0.85
Heater temperature, Θ_h	1935 K	1.1497
Medium-Gradient Case:		
Ambient temperature, Θ_a	1473 K	0.875
Heater temperature, Θ_h	1898 K	1.1278
Low-Gradient Case:		
Ambient temperature, Θ_a	1599 K	0.95
Heater temperature, Θ_h	1765 K	1.0486
Biot number, Bi	-	0.033
Bond number, Bo	-	176.
Crystal top location, Z	29.21 cm	4.0
Crystal pull rate, V^*	5.0 cm/hr	1.0
Peclet numbers, Pe_i		
melt	-	0.038
crystal	-	0.11
liner	-	0.48
crucible	-	0.057
Radiation numbers, Ra_i		
melt	$\varepsilon=0.3$	0.27
crystal	$\varepsilon=0.7$	0.63
liner	$\varepsilon=0.35$	0.31
crucible	$\varepsilon=0.8$	0.72
Stefan number, S	-	1.07
Thermal conductivity ratios, $K_i(\Theta)$		
melt	-	2.9
crystal	-	$1./\Theta$
liner	-	0.27
crucible	-	2.7
Volume of melt, V_m	1,360 cm^3 (3.44 kg)	3.5

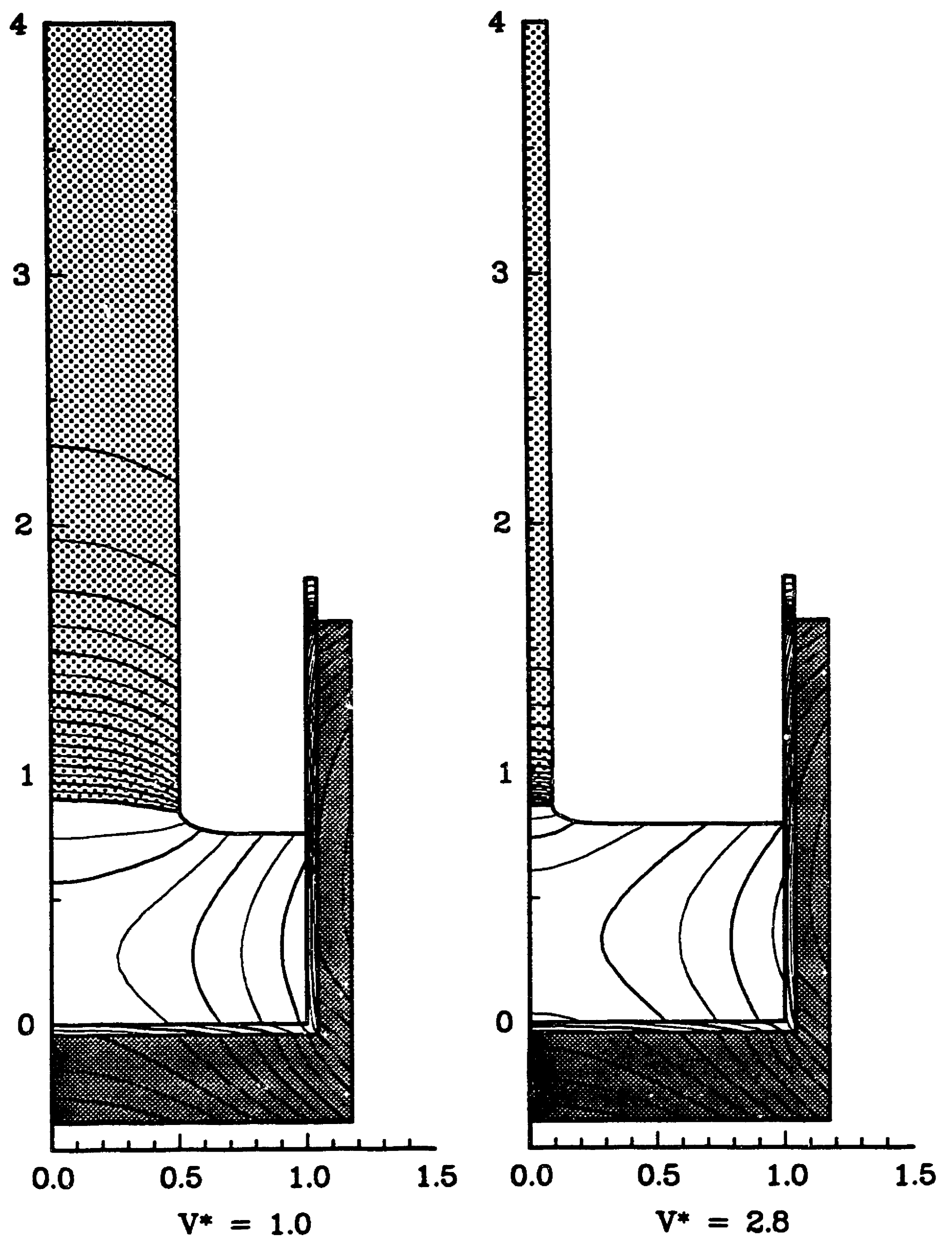

Fig. 5.2 Isotherms and interface shapes for reference case of $V^*=1.0$ (parameters listed in Tables 5.1 and 5.2) and case with identical operating parameters except $V^*=2.8$. Isotherms for all plots of Chapter 5 are incremented by 15K with alternating thin and thick contours.

of calculations was carried out on three different meshes to assess the accuracy of the finite element solutions for these two cases which span a wide range in system geometries. The finite element meshes used in this analysis are shown in Fig. 5.3 for the quasi-steady solution obtained for a crystal pull rate of $V^*=1.0$. Three meshes, denoted M1, M2, and M3, were used in this analysis with 151 biquadratic rectangular elements with 741 total unknowns, 315 elements with 1455 unknowns, and 604 elements with 2681 unknowns, respectively. Mesh M1 was the smallest used in these calculations, and mesh M2 consisted of roughly 50 percent more elements in the radial and axial directions with approximately double the elements. Mesh M3 contained twice the number of elements of mesh M1 in each linear direction, four times as many overall.

Each mesh was constructed so that there were nearly evenly spaced elements throughout each domain except for several extra elements set along the meniscus in the radial direction near the tri-junction. This extra interpolating power was needed to accurately approximate the curvature of the meniscus there. The configurations of the three meshes for a smaller crystal radius are represented in Fig. 5.4 for the quasi-steady solution with $V^*=2.8$. The elements in this mesh have rearranged themselves in the radial direction so that those in the crystal are compressed and those in the melt under the meniscus are expanded. For this solution, the extra elements in the melt near the crystal were especially necessary for an accurate approximation to the shape of the meniscus.

The crystal radii and interface heights obtained from these calculations are given in Table 5.3 for the solutions with each mesh for

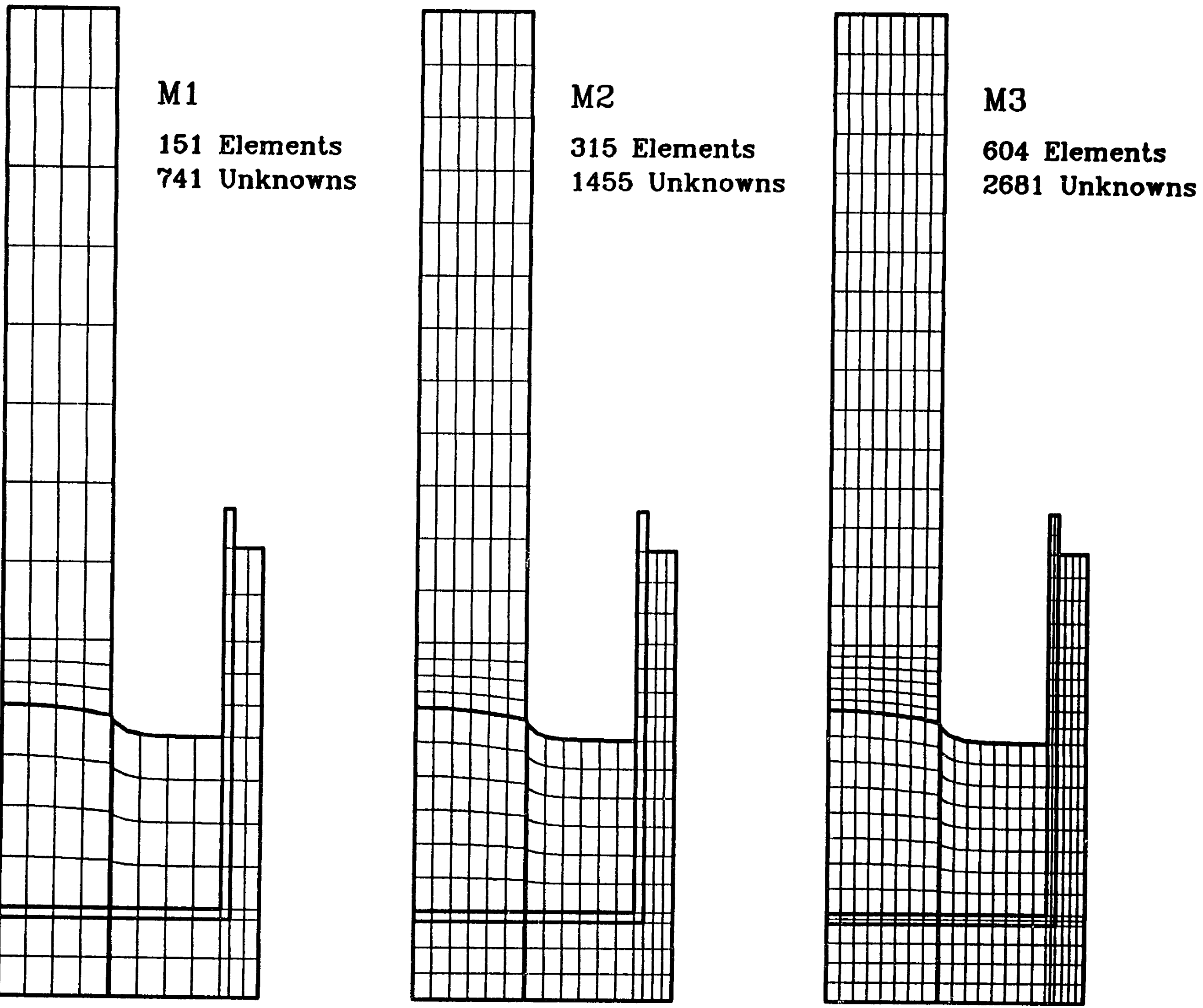

Fig. 5.3 Biquadratic finite element meshes used for CZ silicon calculations of Section 5.1 for case of pull rate V*=1.0.

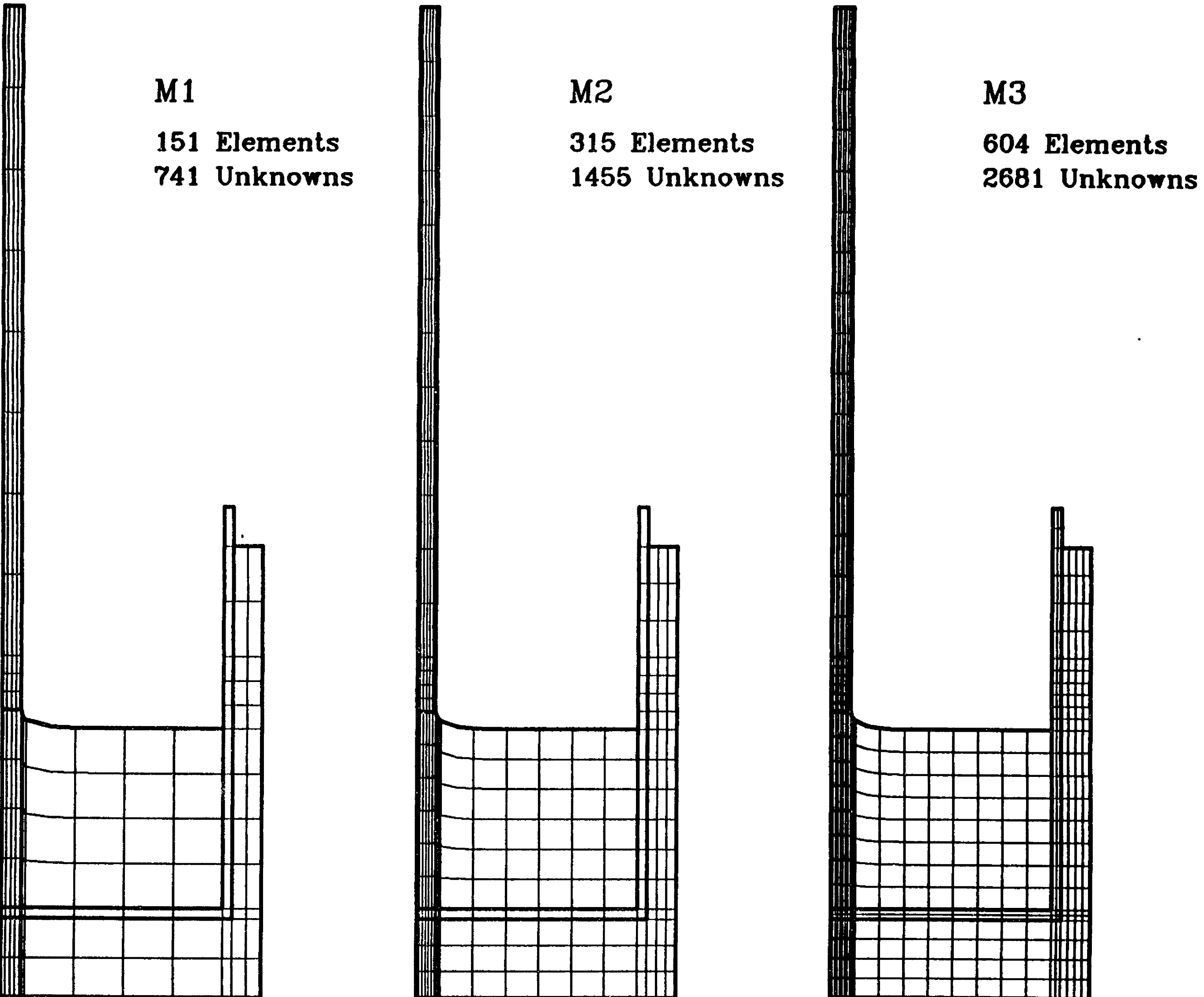

Fig. 5.4 Biquadratic finite element meshes used for CZ silicon calculations of Section 5.1 for case of pull rate $V^*=2.8$.

the conditions of $V^*=1.0$ and $V^*=2.8$. For the moderate diameter crystal of the $V^*=1.0$ solution, the reliability of the finite element approximations was evident by errors of less than one percent for the quasi-steady-state radius and interface heights on the smaller meshes with respect to those calculated with mesh M3. The greatest error in the smaller meshes occurred in approximating the deflection of the melt/crystal interface with errors of 9.6 and 2.2 percent for meshes M1 and M2, respectively. This error is quite reasonable since it represents a small quantity calculated by the difference in two interface heights, $H_0(0)-H_0(R)$.

There was more error in the finite element solutions for the small crystal resulting from increasing the pull rate to $V^*=2.8$, but mesh M2 still approximated the radius and interface locations with a maximum error of only 3.8 percent. Mesh M1 also did reasonably well with a maximum error of 6.4 percent in estimating the crystal radius. Again, the error of approximating the melt/crystal interface deflection was greater than that for the other quantities compared in Table 5.3, with 16 percent error for the solution obtained with M2 and 61 percent error with mesh M1. This error was not disturbing since the melt/crystal interface deflection was a very small quantity in this quasi-steady solution. The signs of the error in the small-crystal solution ($V^*=2.8$) are opposite for meshes M1 and M2 for the radius and the position of the melt meniscus at the crucible wall. This points out the balance between approximating the two-dimensional temperature field and the one-dimensional interface shapes. Uniformly decreasing the size of the elements did not uniformly decrease the

Table 5.3 Results of mesh refinement for the quasi-steady solutions shown in Fig. 5.2 and the meshes displayed in Figs. 5.3 and 5.4.

Quantity	Meshes for $V^*=1.0$			Meshes for $V^*=2.8$		
	M1	M2	M3	M1	M2	M3
Crystal Radius, R	0.4924 (-0.0187)	0.5000 (-0.0036)	0.5018	0.0841 (-0.0635)	0.0932 (+0.0379)	0.0898
Melt/Solid Interface, $H_0(0)$	0.9014 (-0.0013)	0.9024 (-0.0002)	0.9026	0.8741 (+0.0015)	0.8748 (+0.0023)	0.8728
Deflection of M/S Interface, $\Delta=H_0(0)-H_0(R)$	-4.521×10^{-2} (-0.0956)	-4.889×10^{-2} (-0.0220)	-4.999×10^{-2}	9.719×10^{-4} (-0.6187)	-2.140×10^{-3} (-0.1605)	-2.549×10^{-3}
Meniscus Height, $H_1(R)$	0.8561 (+0.0041)	0.8535 (+0.0011)	0.8526	0.8751 (+0.0056)	0.8727 (+0.0029)	0.8702
Meniscus Height, $H_1(1)$	0.7624 (+0.0018)	0.7612 (+0.0003)	0.7610	0.7942 (+0.0001)	0.7940 (-0.0001)	0.7941
CPU time per iteration on Cray-XMP	1.5 sec	3.8 sec	8.7 sec			

Note: Numbers in parentheses are relative differences between results for smaller meshes and mesh M3, computed as (M1-M3)/M3 and (M2-M3)/M3.

errors incurred in approximating both temperature field and interface location in the thermal-capillary model.

Computation times on the Cray-XMP at Bell Laboratories for the meshes M1, M2, and M3 are also shown in Table 5.3. The CPU execution time per model iteration has decreased by almost two orders-of-magnitude from the initial runs shown in Chapter 4, Table 4.4. This reduction has been achieved by streamlining the FORTRAN program and by using a more efficient Gaussian elimination routine for arrow-shaped matrices (Thomas and Brown, 1986). Mesh M2 with 315 elements and 1455 unknowns was used in all ensuing calculations since it represented a good balance in terms of solution accuracy and computational effort. Approximately 15 to 25 CPU seconds were needed on the Cray-XMP for a typical calculation requiring 4 to 6 Newton iterations.

The next concern for calculating the quasi-steady operating states was that the length of the crystal needed to be long enough to ensure that heat transfer end effects from the top of the crystal were minimal. The length of the crystal used in the analysis is set by the distance of the top of the crystal, Z, from the bottom of the crucible, as depicted in Fig. 5.1, and on the height of the melt level, which is determined by the volume of the melt, V_m. Figure 5.5 shows the quasi-steady crystal radius obtained from calculations performed for different values of the crystal height, Z. For values of crystal height Z greater than approximately 2.5, the radius does not change appreciably. This is also pointed out in Fig. 5.6 by the isotherms and system geometries for the solutions denoted by the solid circles in Fig. 5.5. The crystal was essentially isothermal at the ambient temperature for lengths

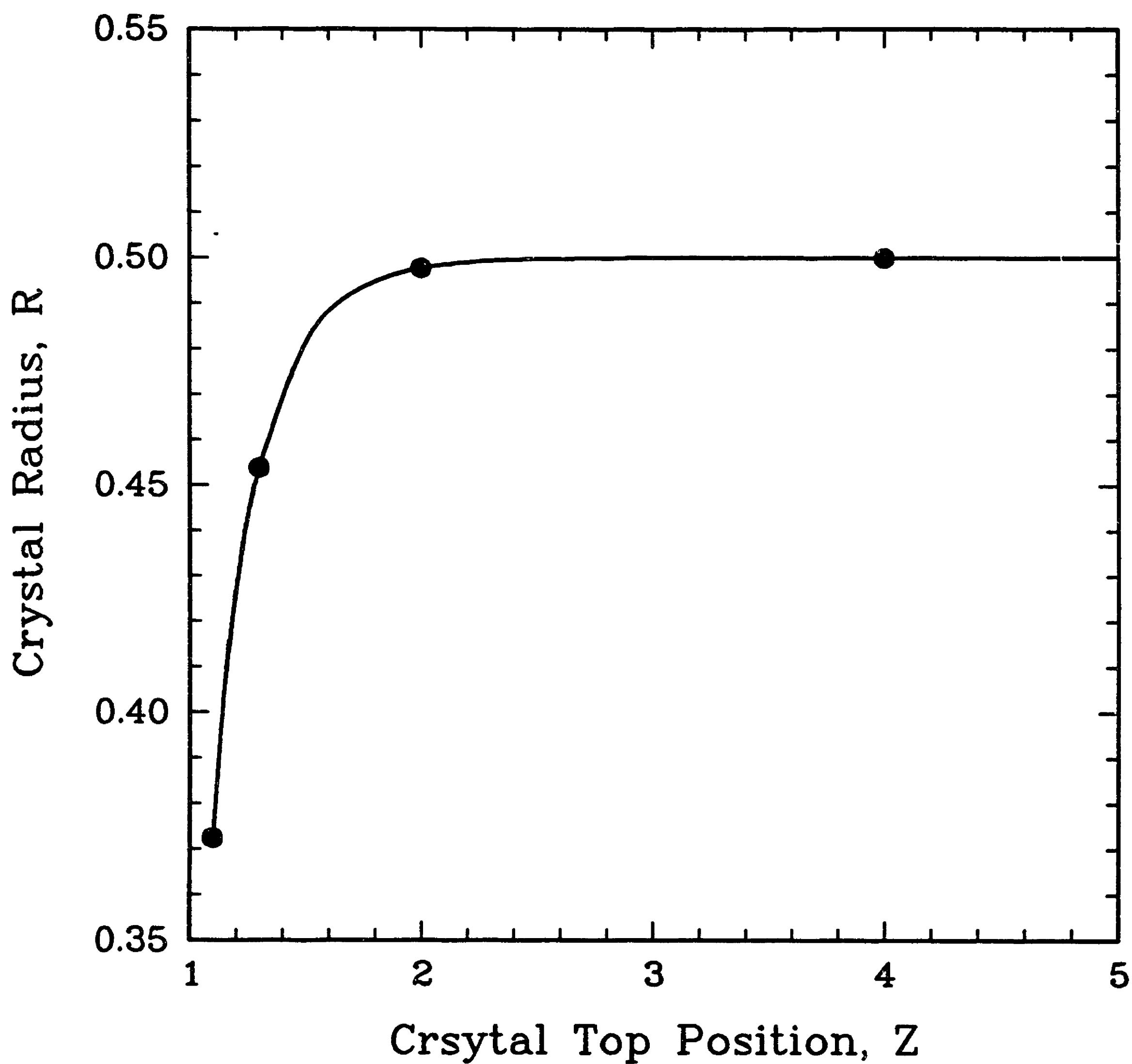

Fig. 5.5 Quasi-steady crystal radius as a function of crystal top position for the high-gradient reference case parameters listed in Tables 5.1 and 5.2 for CZ growth of silicon. Solutions at solid points on curve are shown in Fig. 5.6.

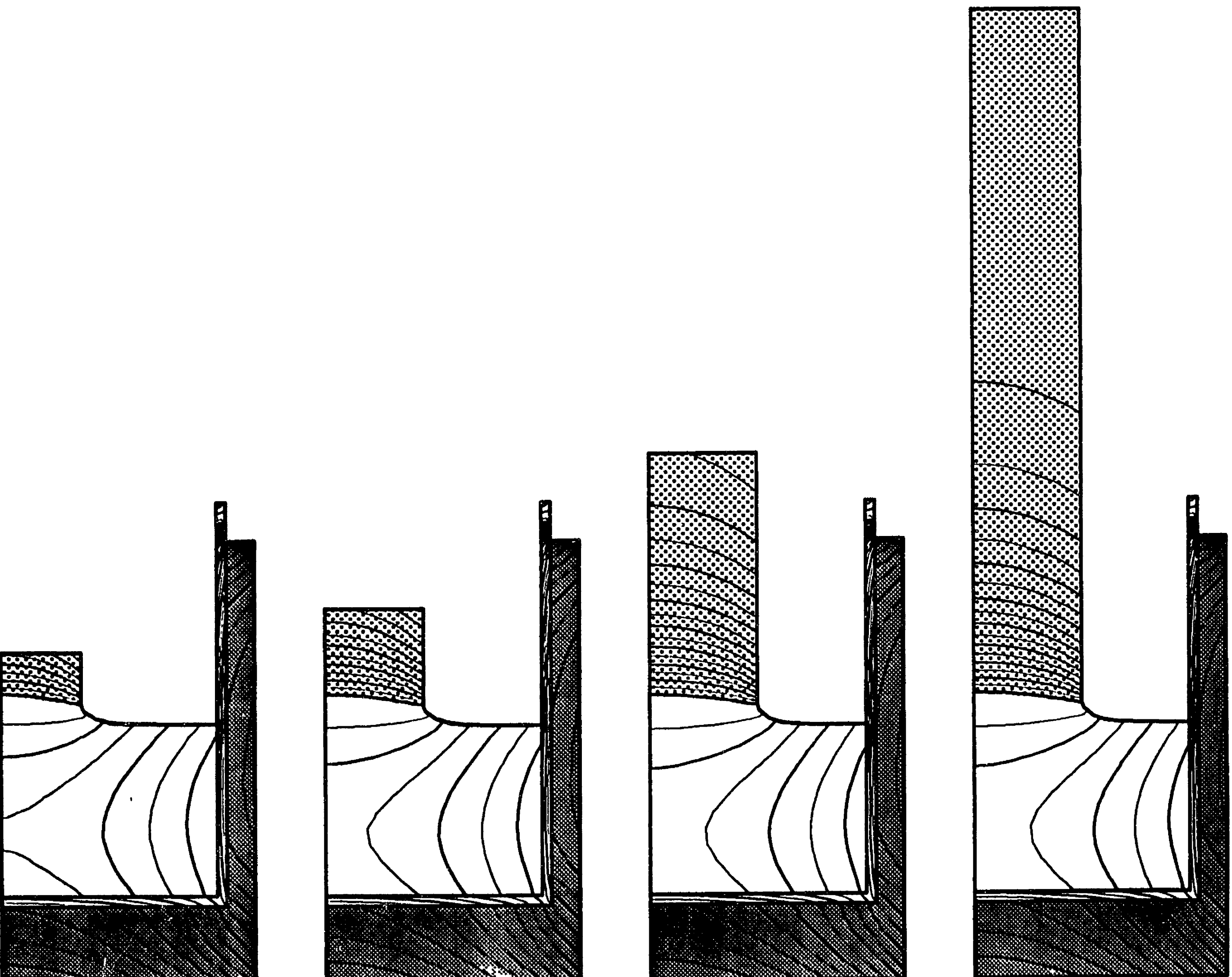

Fig. 5.6 Changes in quasi-steady isotherms and interface shapes with increasing crystal top position for CZ growth of silicon. All other parameters are held fixed at those of the high-gradient reference case.

greater than two crucible radii above the melt/solid interface. These results are not surprising since a one-dimensional heat transfer analysis indicates that the temperature field in the crystal should have a length scale of $Bi^{-1/2}$ (Jasinski et al., 1983; Carslaw and Jaeger, 1947). This length is approximately $Bi^{*-1/2} = 0.98$ crucible radii in this analysis where Bi^* is a linearized radiation Biot number based on the crystal radius and the parameters listed in Table 5.2, $Bi^* = R\ \{Bi + Ra(\Theta^2+\Theta_a^2)(\Theta+\Theta_a)\} \approx 1.04$ with $R \approx 0.5$, $Bi=0.033$, $Ra=0.63$, $\Theta \approx 1.0$, and $\Theta_a=0.85$. The case of crystal height $Z=4.0$ (crystal length ≈ 3.1) was chosen for use in all subsequent quasi-steady-state calculations.

5.1.1 Pull Rate

Figure 5.7 shows solutions obtained from the quasi-steady-state thermal-capillary model as operating curves plotted with the crystal radius as a function of pull rate. Three curves are presented for different heater-ambient temperature conditions. For the first point on each operating curve, the ambient temperature Θ_a was chosen as one of the values 0.85,0.875, or 0.95, the pull rate was set to $V^*=1.0$, and the heater temperature Θ_h was determined by augmenting the thermal-capillary equation set with the constraint for a quasi-steady crystal radius value of $R=0.5$, as performed in the previous chapter for the processing strategy calculations of Section 4.3. Once the heater temperature was set, the pull rate was varied with all other quantities held constant, and the states along each operating curve were calculated.

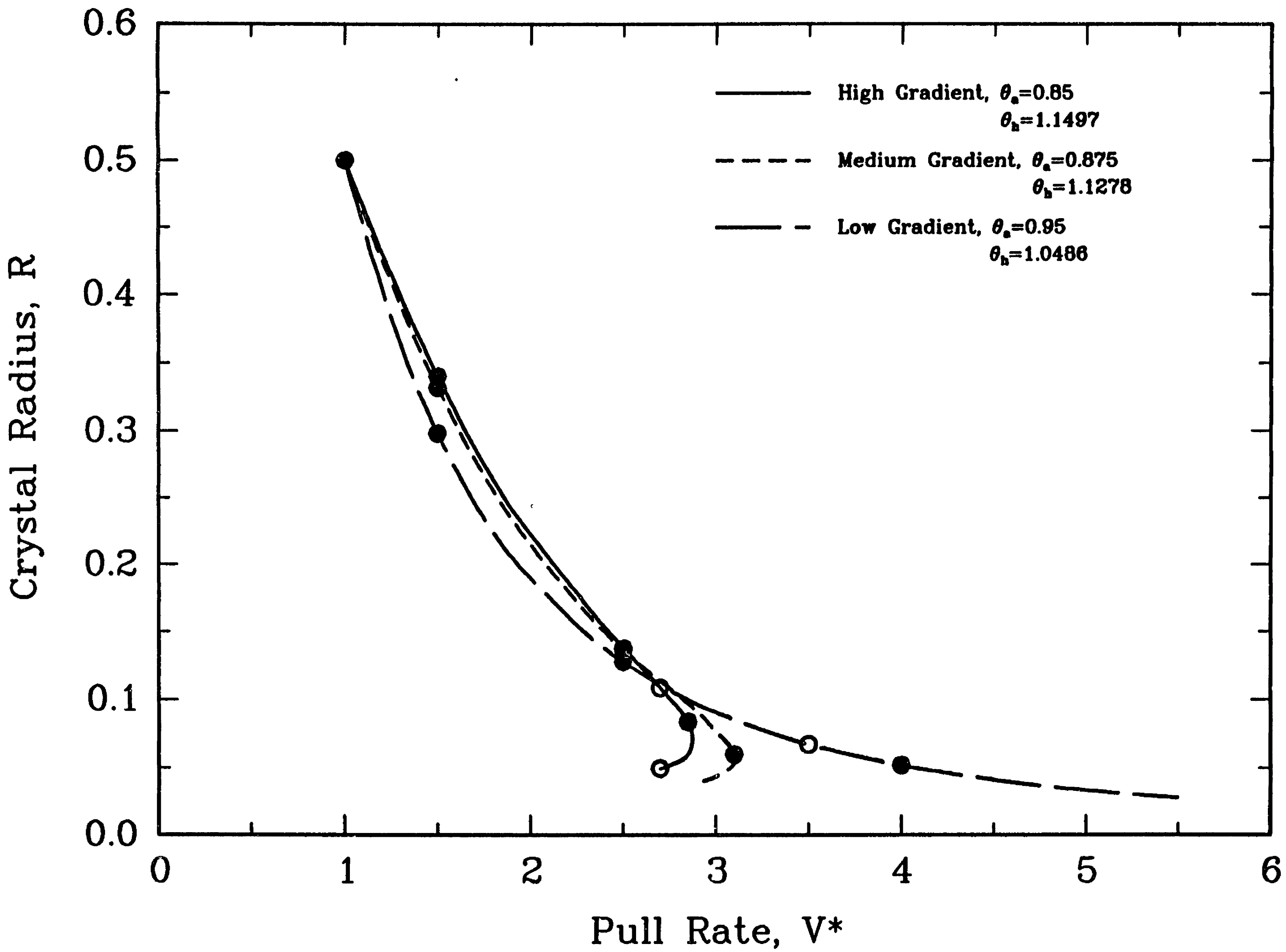

Fig. 5.7 CZ silicon growth quasi-steady operating curves of crystal radius as a function of pull rate for three heater-ambient temperature settings. All parameters except pull rate were held fixed at the reference values listed in Tables 5.1 and 5.2. The solutions at the points denoted by solid circles are shown in Figs. 5.8-5.10; results of linear stability analyses are given in Fig. 5.18 for the states denoted by the open circles.

Hereafter, each set of calculations will be referred to as the high-, medium-, or low-gradient operating curve, denoting the temperature difference between the heater and ambient temperature, for the conditions of (Θ_a=0.85,Θ_h=1.1497), (Θ_a=0.875,Θ_h=1.1278), and (Θ_a=0.95,Θ_h=1.0486), respectively. Note that the terms low-, medium-, and high-gradient do not refer to the radial temperature gradients present in the crystal for these different conditions, but only to the temperature difference between the heater and the ambient.

As in the calculations presented in Chapter 4, the quasi-steady radius decreased as the pull rate was increased and latent heat generation intensified at the melt/crystal interface. The most striking features for the high- and medium-gradient calculations were the limit points occurring at a critical pull rates $V_c^*\cong 2.85$ and 3.1, respectively. For pull rates greater than these values, no steady solutions were found for either set of operating conditions. The limit point shifted to higher values of V_c^* as the temperature difference between heater and ambient was decreased and vanished for the low-gradient conditions, where the pull rate was increased without the loss of existence of steady-state solutions. For the low-gradient calculations, the crystal radius reached unrealistically small values before any limit point could be detected. The quasi-steady solutions corresponding to the solid circles on the operating curves of Fig. 5.7 are shown as plots of system geometry and isotherms in Figs. 5.8, 5.9, and 5.10 for the cases of high-, medium-, and low-gradient conditions, respectively.

The existence of the limit points is explained by examining the evolution of the temperature fields along each operating curve as

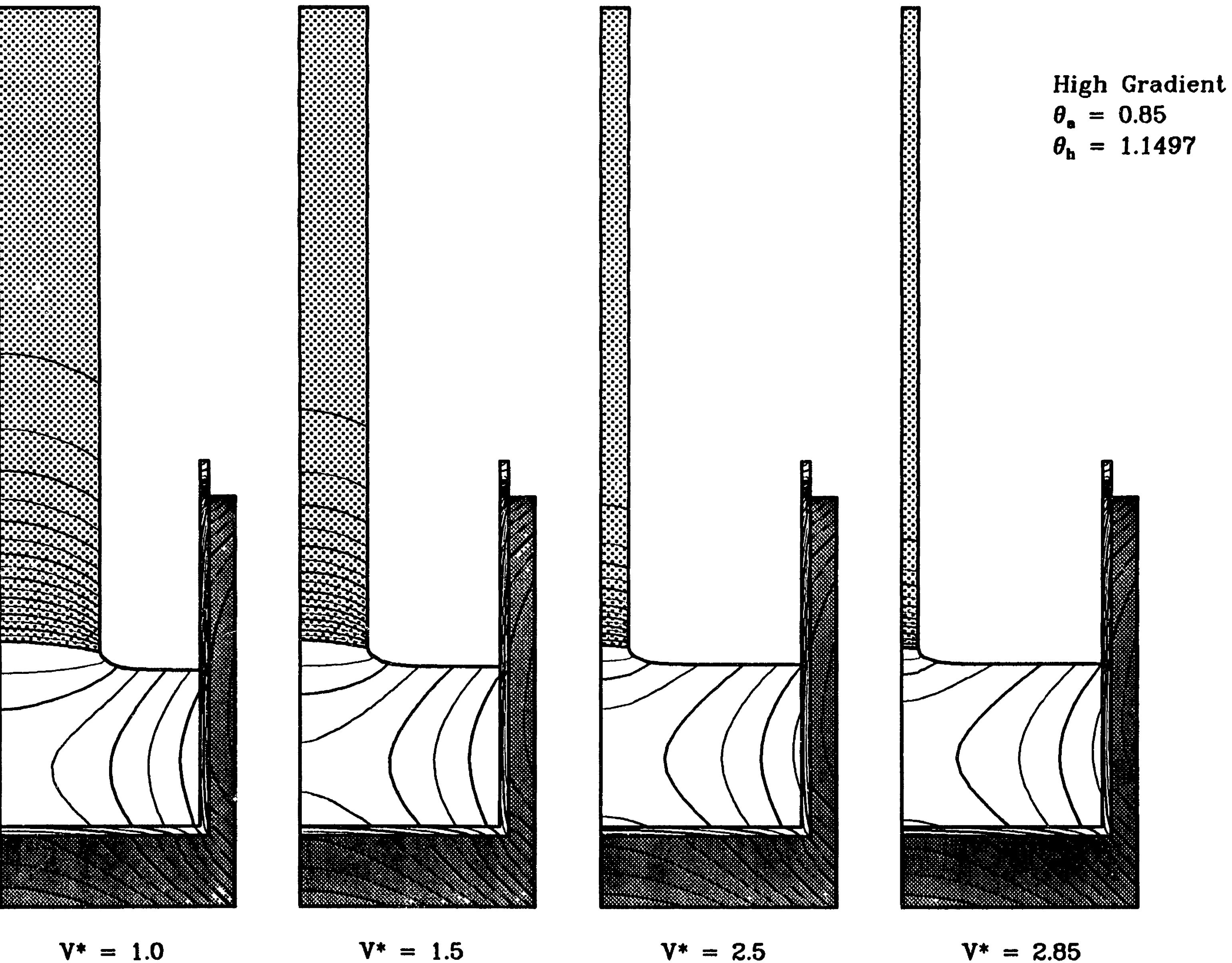

Fig. 5.8 Changes in isotherms and interface shapes with increasing pull rate for CZ silicon growth with Θ_a=0.85 and Θ_h=1.1497 corresponding to the solid circles on the high-gradient operating curve of Fig. 5.7. All other parameters are held fixed at those listed in Tables 5.1 and 5.2.

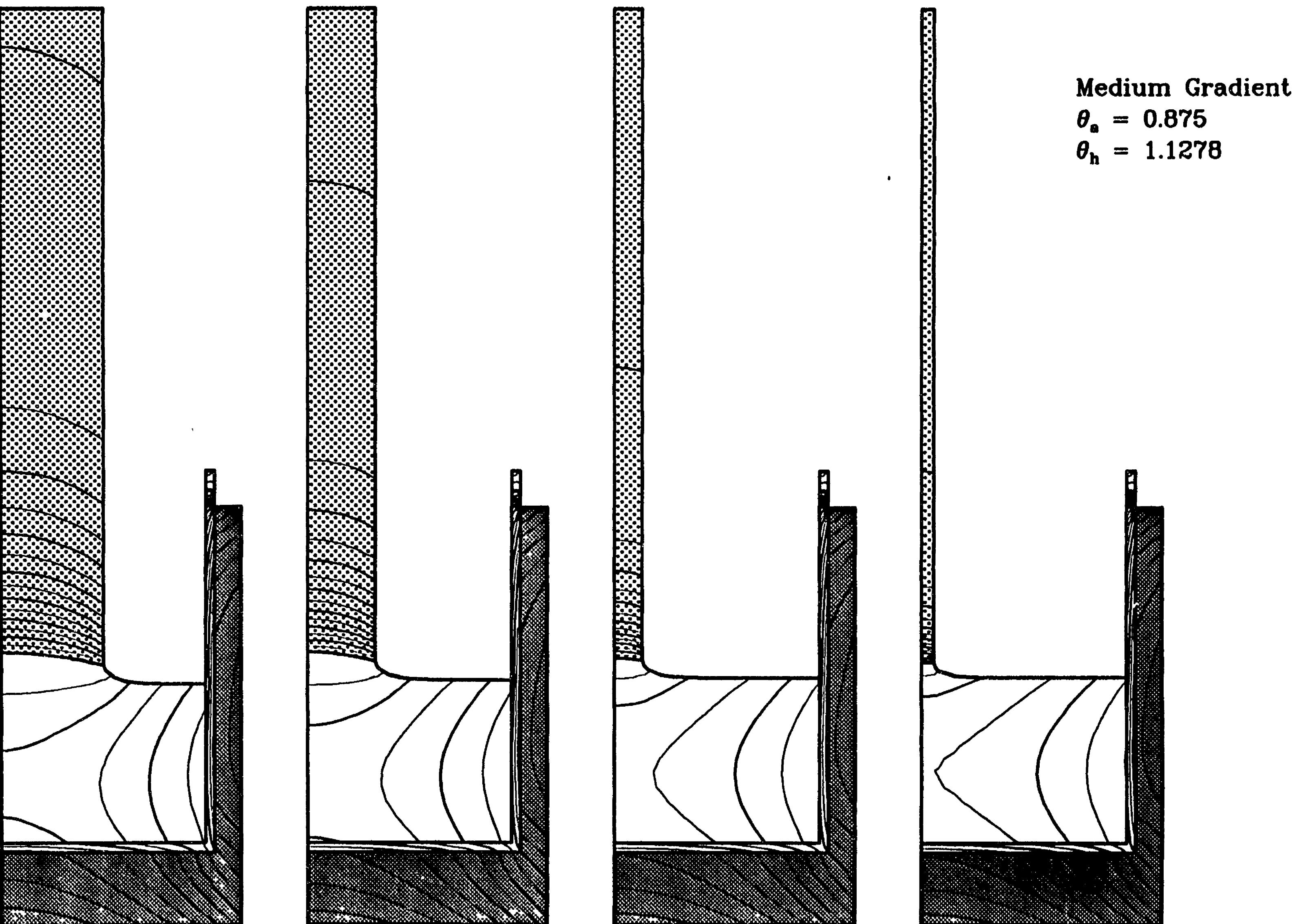

Fig. 5.9 Changes in isotherms and interface shapes with increasing pull rate for CZ silicon growth with Θ_a=0.875 and Θ_h=1.1278 corresponding to the solid circles on the medium-gradient operating curve of Fig. 5.7. All other parameters are held fixed at those listed in Tables 5.1 and 5.2.

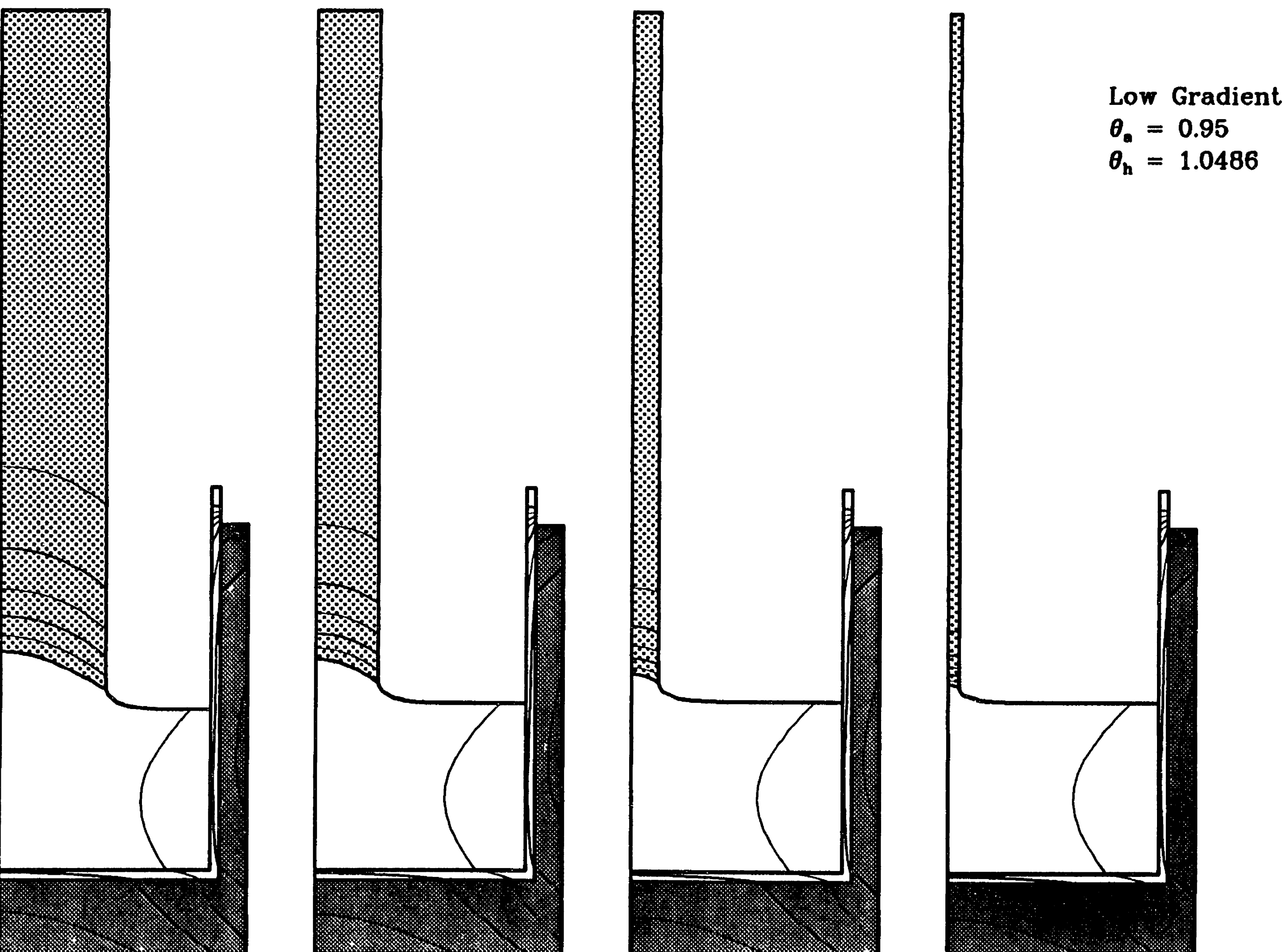

Fig. 5.10 Changes in isotherms and interface shapes with increasing pull rate for CZ silicon growth with Θ_a=0.95 and Θ_h=1.0486 corresponding to the solid circles on the low-gradient operating curve of Fig. 5.7. All other parameters are held fixed at those listed in Tables 5.1 and 5.2.

the pull rate is increased. Latent heat generation at the melt/solid interface intensifies at higher pull rates, and the system responds by decreasing the quasi-steady radius and increasing the axial temperature gradient in the crystal. However, the dissipation of the latent heat originating at the solidification interface eventually reaches a limiting value, and a turning point in the solution occurs. The cause for the limit point is qualitatively similar to that observed by Thomas et al. (1986) in calculations for the growth of thin silicon sheets by the Edge-Defined Film-Fed Growth (EFG) process.

The movement and eventual disappearance of the limit point is understood by comparing the shape of the melt/solid interface near the limit point on each curve. An expanded view of the region around the solidification interface is shown in Fig. 5.11 for solutions near the limit point on the high- and medium-gradient operating curves and for a solution with a comparable quasi-steady radius value on the low-gradient curve. Two factors are immediately obvious for the low-gradient case; the axial temperature gradient in the crystal is much smaller than that in the high-gradient and medium-gradient calculations and the melt/solid interface curvature is much greater. The lower axial temperature gradient is caused by the lower difference between the melting point and the ambient temperature and is not a major factor in the disappearance of the limit point. However, the increased curvature of the solidification front facilitates the removal of heat from that interface since there is greater surface area over which the latent heat is released. This enhancement of latent heat removal as a function of interface shape caused the limit point to

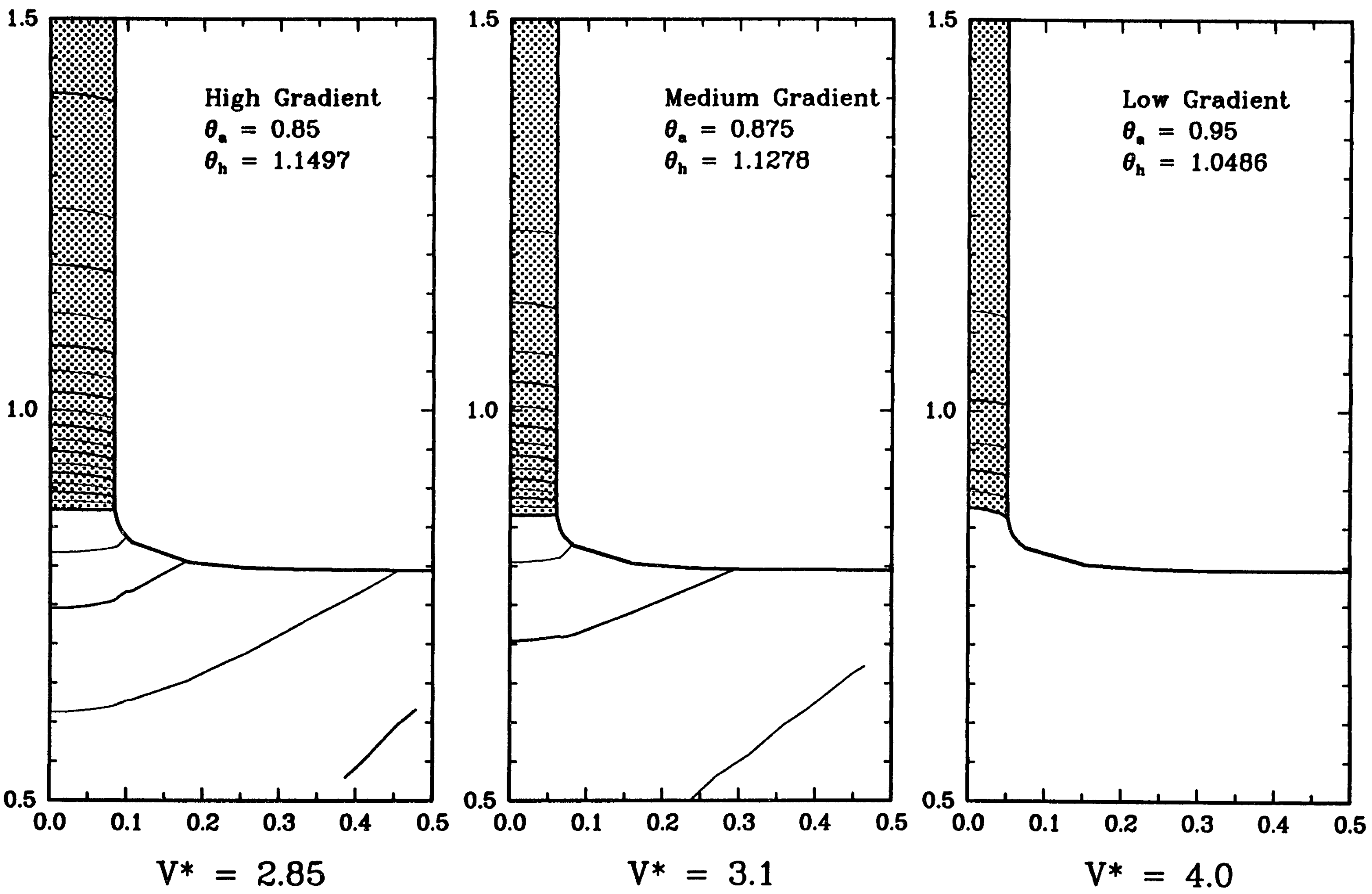

Fig. 5.11 Expanded view of region near melt/crystal interface for solutions near the limit point on the operating curves of Fig. 5.7.

shift to higher pull rates and eventually vanish as the difference between the heater and ambient temperature was increased.

Any change in the heat transfer environment which affects the shape of the melt solid interface is expected to shift the position of the limit point.

5.1.2. Heater Temperature

Quasi-steady calculations for varying heater temperatures with all other parameters held constant are shown in Fig. 5.12. Two operating curves which start with the initial points (R=0.5) on the high-gradient and low-gradient operating curves of the previous section (see Fig. 5.7) are highlighted. Limit points were found for each curve although the shapes of the curves differed for the low-temperature ambient (θ_a = 0.85) and the high-temperature ambient (θ_a = 0.95). The high-temperature ambient calculations shown by the dashed curve of Fig. 5.12 was shallower in shape than the low-temperature ambient curve. The solutions on the high-temperature ambient curve were therefore more sensitive to changes in heater temperature.

The isotherms and interface shapes for the solid points on the operating curves of Fig. 5.12 are shown in Figs. 5.13 and 5.14 for the high- and low-temperature ambients, respectively. The last two cases shown in Figs. 5.13 and 5.14 are for solutions at the same pull rate which bracket the limit point. As in the solutions in the previous section, the limit point occurs when the temperature gradient in the crystal increases and the melt/crystal isotherm is flattened so that

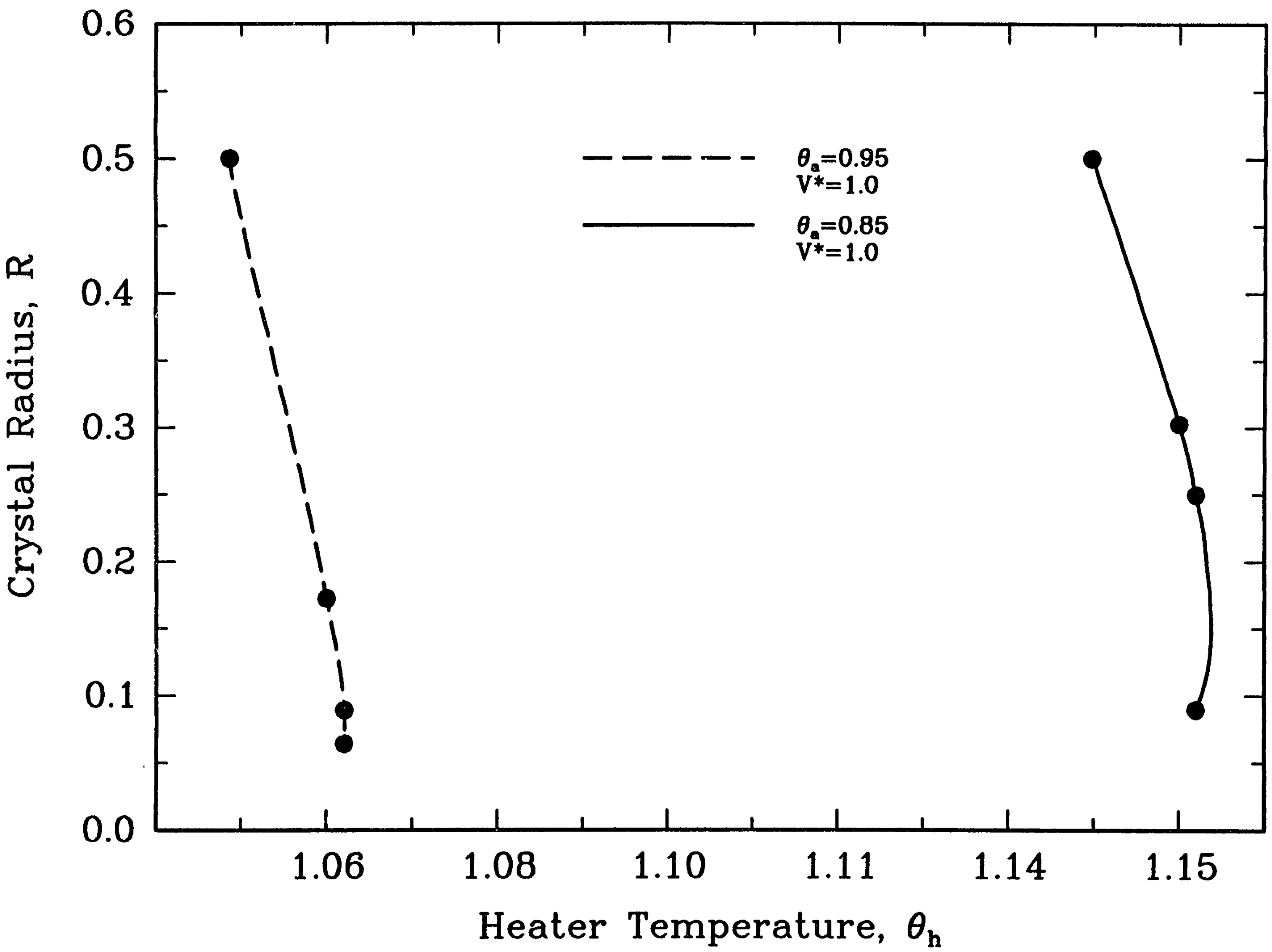

Fig. 5.12 Quasi-steady CZ silicon growth operating curves of crystal radius as a function of heater temperature for pull rate $V^*=1.0$ and two ambient temperature settings. Initial points (R=0.5) on operating curves are the same states represented on the pull rate operating curve of Fig. 5.7. All parameters except heater temperature were held fixed at the reference values listed in Tables 5.1 and 5.2. The solutions at the points denoted by solid circles are shown in Figs. 5.13 and 5.14.

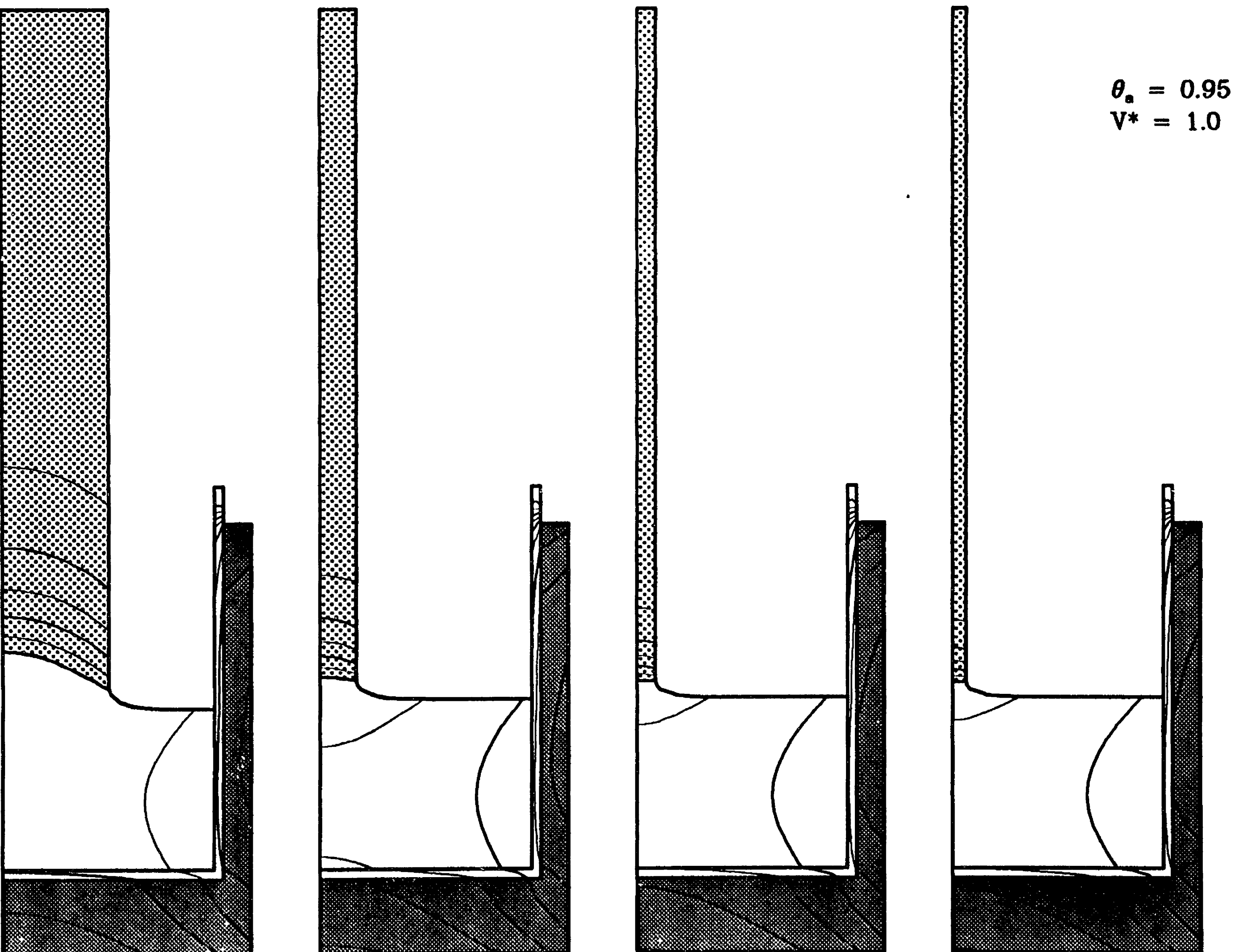

Fig. 5.13 Changes in isotherms and interface shapes with increasing heater temperature for CZ silicon growth with Θ_a=0.95 and V^*=1.0 corresponding to the solid circles on the dashed operating curve of Fig. 5.12. All other parameters are held fixed at those listed in Tables 5.1 and 5.2.

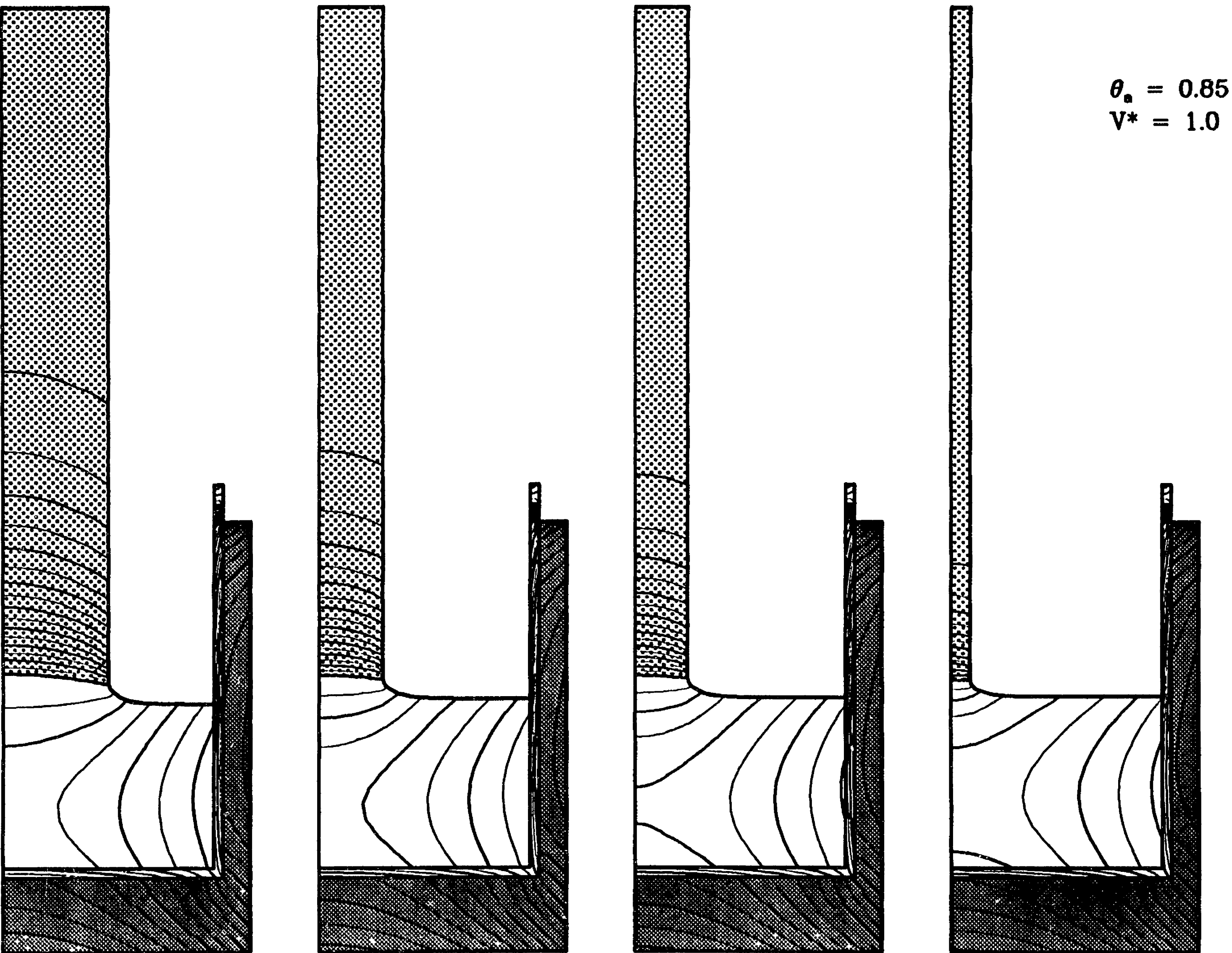

Fig. 5.14 Changes in isotherms and interface shapes with increasing heater temperature for CZ silicon growth with Θ_a=0.85 and V^*=1.0 corresponding to the solid circles on the solid operating curve of Fig. 5.12. All other parameters are held fixed at those listed in Tables 5.1 and 5.2.

latent heat cannot be conducted effectively to the crystal surface.

5.1.3. Ambient Temperature

The ambient temperature was varied keeping all other operating parameters constant at those listed in Table 5.2. The resulting operating curves of crystal radius versus ambient temperature are shown in Fig. 5.15 for the same starting points as the curves in the previous sections, (R=0.5, Θ_a=0.85, and Θ_h=1.1497) and (R=0.5,Θ_a=0.95, and Θ_h=1.0486). Again, limit points were found on each operating curve.

The solid curve in Fig. 5.15 originates from the high-gradient initial point with the high-temperature heater and exhibits a limit point at a quasi-steady radius of approximately 0.15 while the limit point on the low-temperature heater curve occurred at a much smaller radius. The shape of the dashed low-temperature heater operating curve is less curved than the other curve. This is consistent with the results of the two previous sections where the low-gradient conditions produced solutions which were more sensitive to changes in parameters.

Isotherms and interface shapes are shown in Figs. 5.16 and 5.17 for the solutions represented by the solid circles on the operating curves for Θ_h=1.1497 and Θ_h=1.0486, respectively. In both figures, the two plots on the right represent solutions for the identical pull rate which lie on the upper and lower branches of each operating curve. The solutions near the limit points on each curve are characterized by nearly flat melt/crystal interfaces, as in the previous sections, and therefore are likely to be caused by the same limitation on the

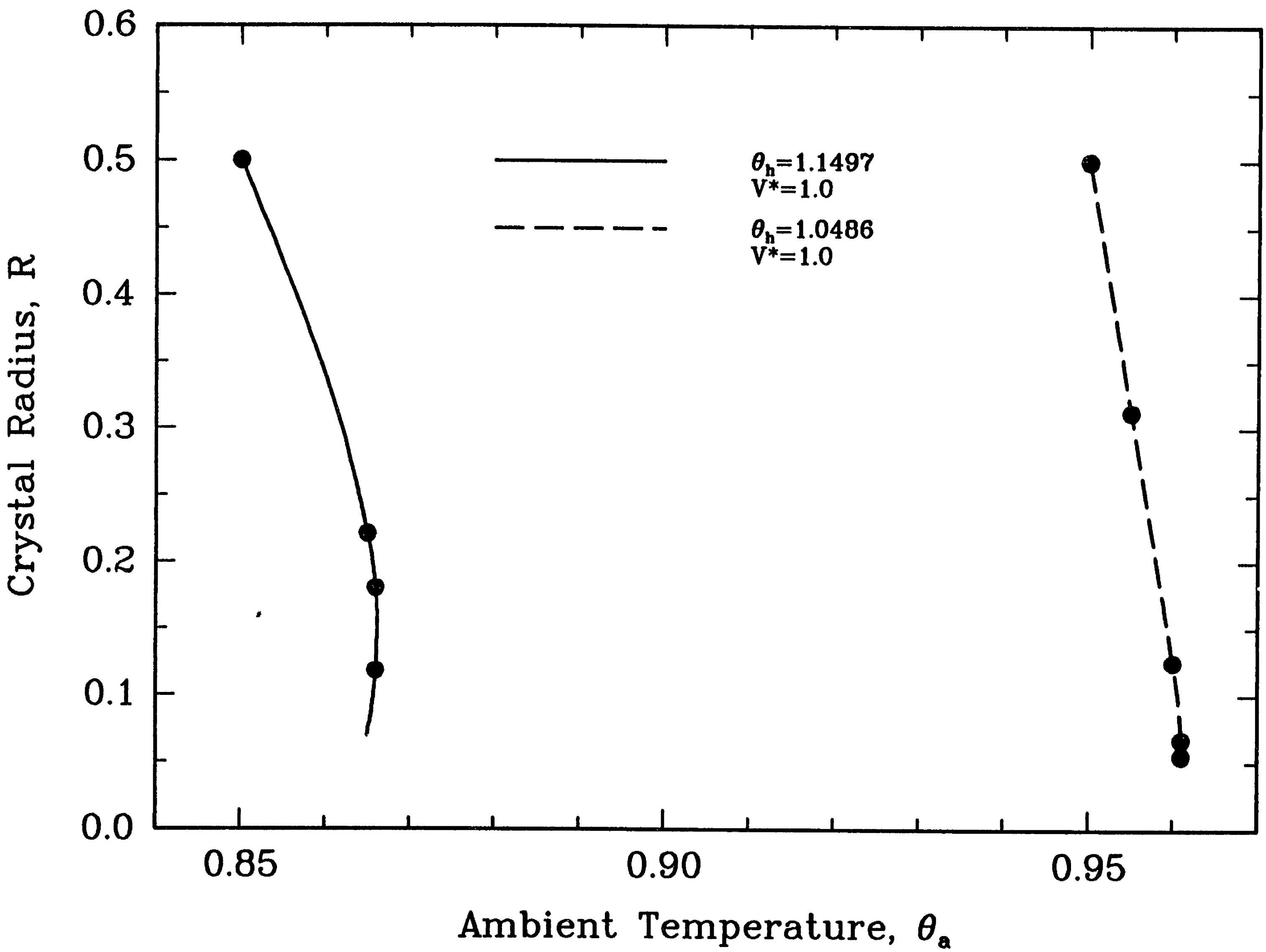

Fig. 5.15 Quasi-steady CZ silicon growth operating curves of crystal radius as a function of ambient temperature for pull rate $V^*=1.0$ and two heater temperature settings. Initial points ($R=0.5$) on operating curves are the same states represented on the pull rate operating curve of Fig. 5.7. All parameters except ambient temperature were held fixed at the reference values listed in Tables 5.1 and 5.2. The solutions at the points denoted by solid circles are shown in Figs. 5.16 and 5.17.

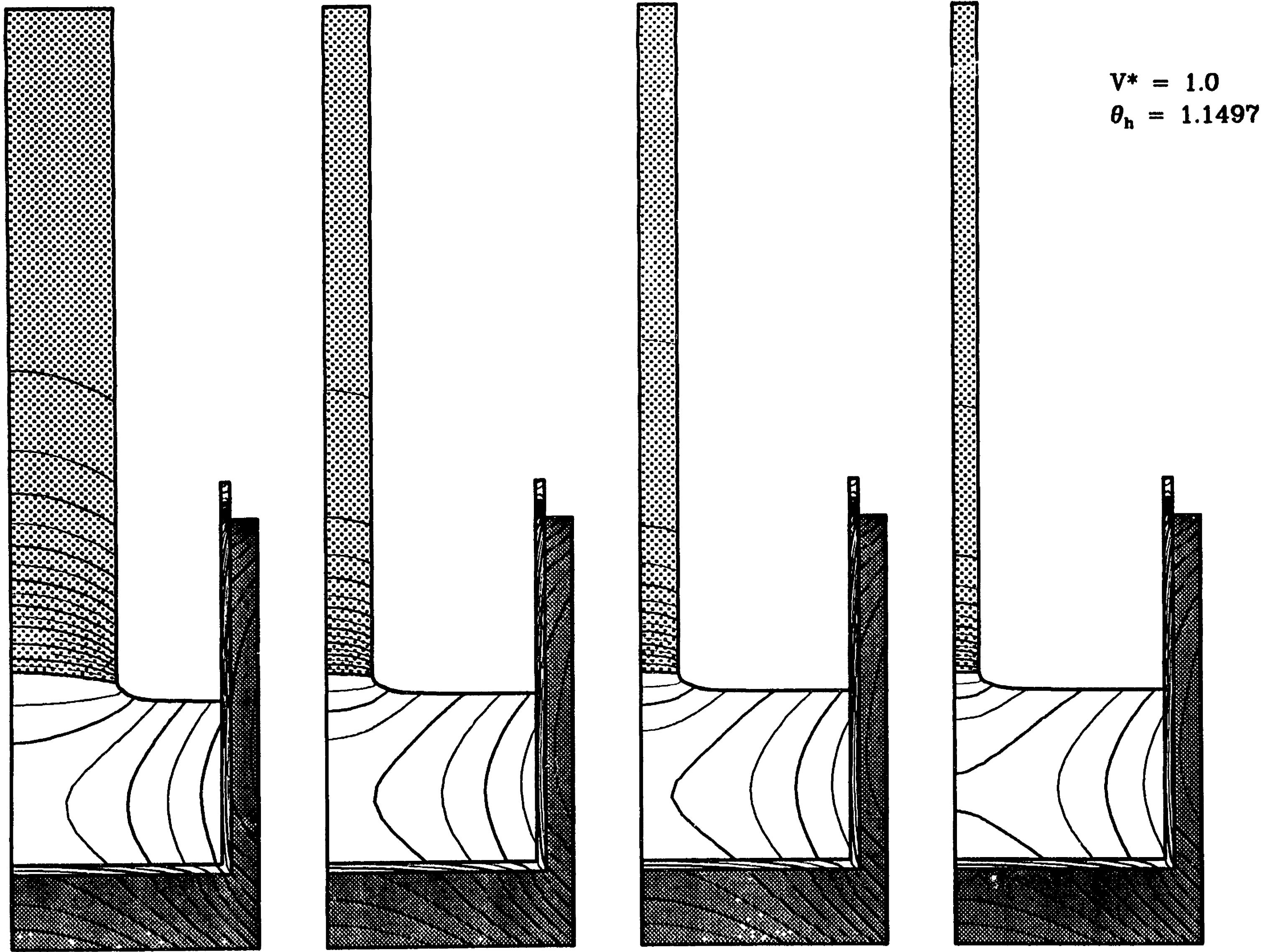

Fig. 5.16 Changes in isotherms and interface shapes with increasing ambient temperature for CZ silicon growth with Θ_h=1.1497 and V^*=1.0 corresponding to the solid circles on the solid operating curve of Fig. 5.15. All other parameters are held fixed at those listed in Tables 5.1 and 5.2.

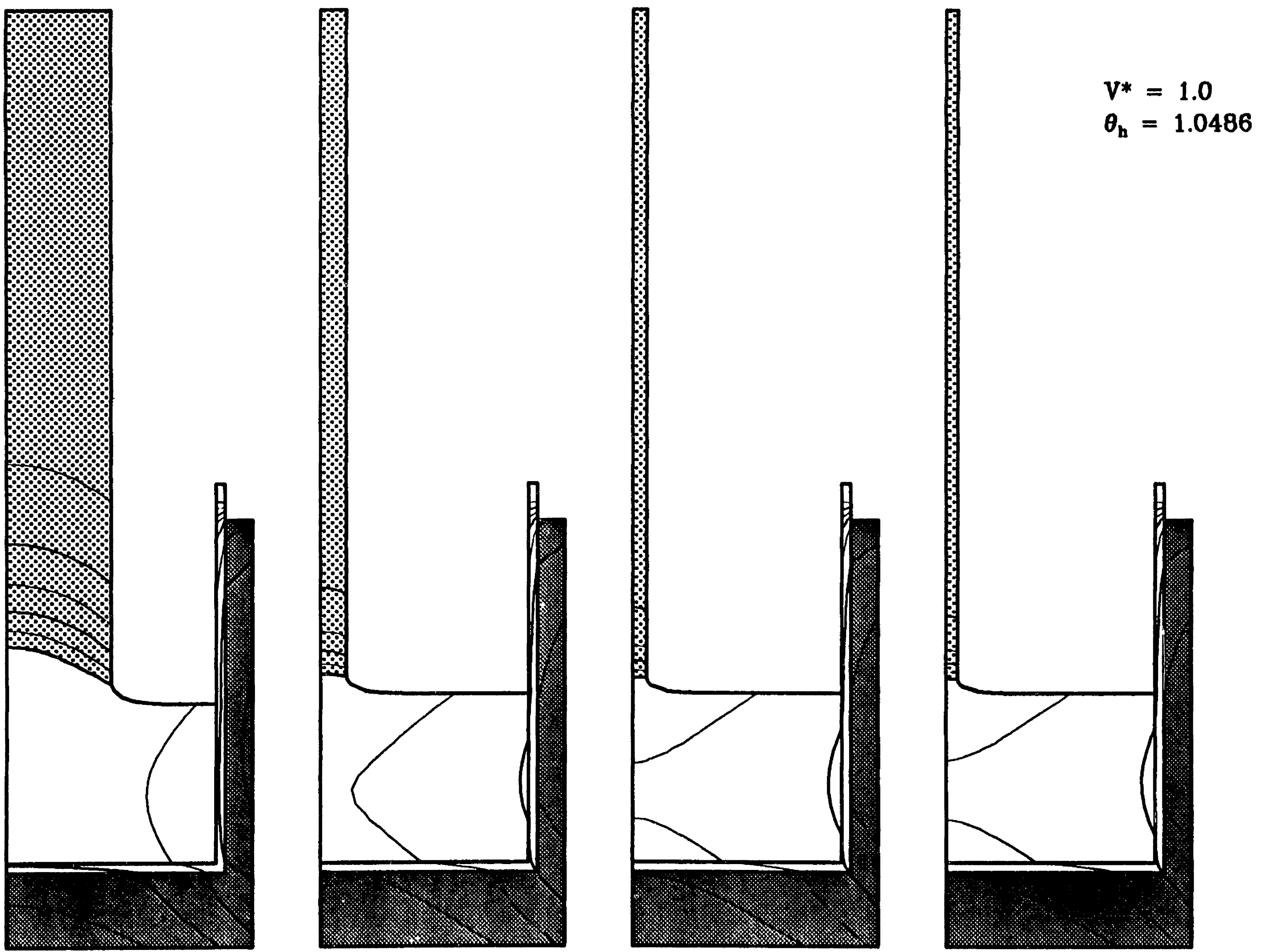

Fig. 5.17 Changes in isotherms and interface shapes with increasing ambient temperature for CZ silicon growth with Θ_h=1.0486 and V^*=1.0 corresponding to the solid circles on the dashed operating curve of Fig. 5.15. All other parameters are held fixed at those listed in Tables 5.1 and 5.2.

conduction of heat through the crystal.

5.2 Linear Stability

Linear stability analyses were performed for the operating states denoted by the open circles on the high- and low-gradient operating curves of Fig. 5.7. In these calculations, a small initial disturbance comprising random fluctuations was imposed on the steady state and monitored in time, as outlined in Chapter 3. The elements of the initial disturbance vector $\mathbf{x}_0$ were chosen so that aphysical disturbances to the steady operating state were not allowed. Specifically, the shape of the solid crystal above the melt remained unaltered. While these results required more computational effort than the quasi-steady calculations, they usually took less than 2 CPU minutes per run on the Cray-XMP at Bell Laboratories.

The results of this analysis are presented in Fig. 5.18 where the Euclidian norm of the disturbance vector divided by its initial value, $\|\mathbf{x}\|/\|\mathbf{x}_0\|$, is plotted as a function of time for the three operating states in the left column. Semi-log plots for the same analyses are shown in the right column. The disturbance to the solution on the upper branch of the operating curve for the high-gradient calculations (V^*=2.7, R=0.1088) decays with time with the final transient falling exponentially, as seen by the linear portion of the semi-log plot. However, the disturbance to the steady state on lower branch of the same operating curve (V^*=2.7, R=0.0495) grows exponentially. As expected for a any steady solution family with a limit point, there is an exchange

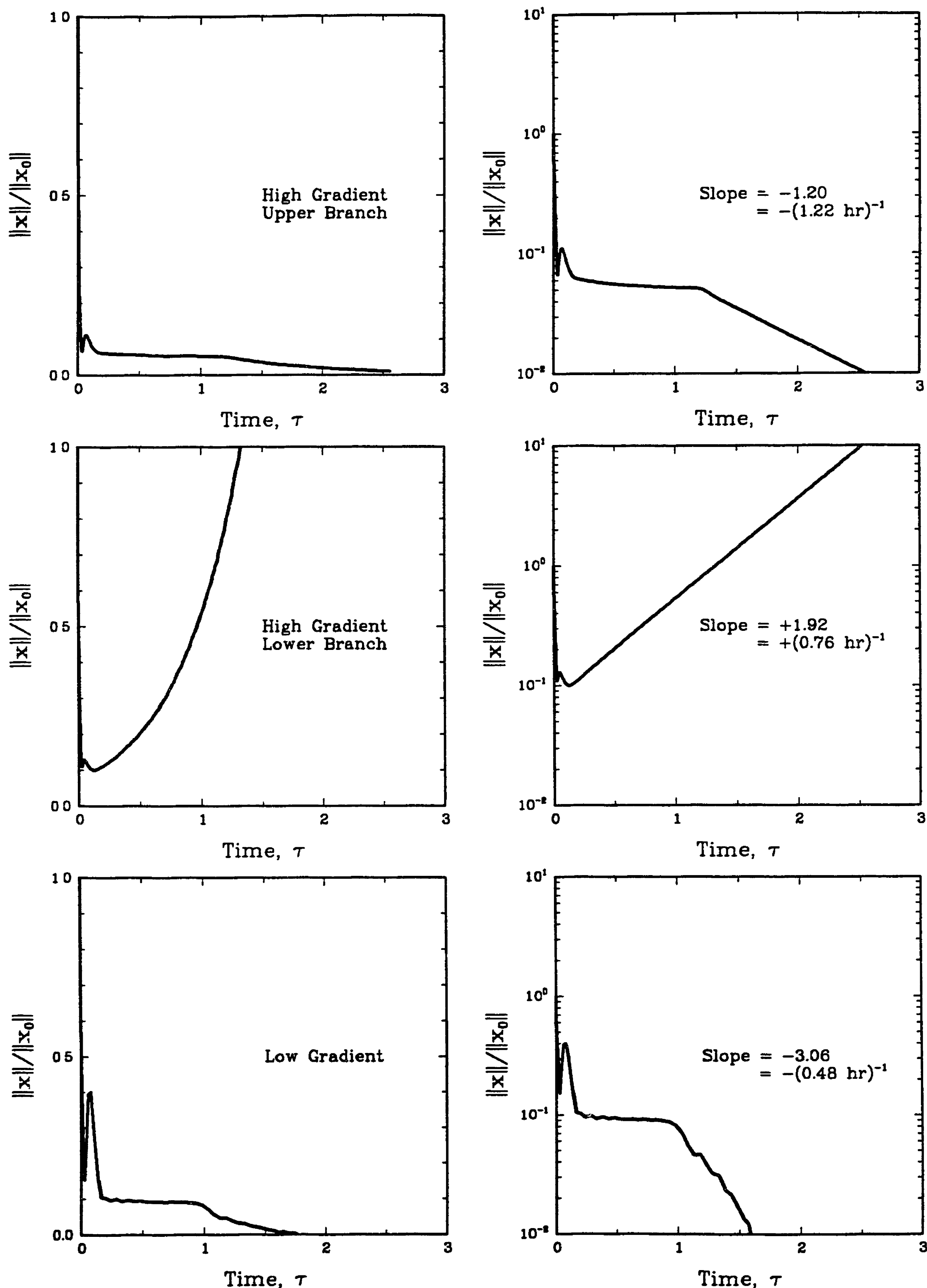

Fig. 5.18 Results of linear stability analyses performed for the states denoted by the open circles on the operating curves of Fig. 5.7. Left column plots show disturbance evolution for each case; right column shows semi-log plots for the same disturbance.

of stability between the solutions on the upper branch and those on the lower branch (Iooss and Joseph, 1980). However, the important result of this analysis is that the CZ process is inherently stable for most operating conditions. Time constants calculated from the final slope of the curves in the semi-log plots are $-(1.22\ hr)^{-1}$ and $+(0.76\ hr)^{-1}$ for the upper and lower branches, respectively.

The norm of the disturbance vector for the low-gradient solution (V^*=3.5, R=0.0673) is shown as the bottom row of plots in Fig. 5.18. This curve falls to zero with a time constant of approximately $-(0.48\ hr)^{-1}$, indicating an inherently stable system; in addition, oscillations are observed in the disturbance vector. These oscillations are the manifestation of imaginary components in some of the system's eigenvalues. This conclusion is also supported by the observation of oscillations in the decay of the disturbance to the crystal radius at the tri-junction. The amplitude of the oscillations is probably much too small to allow direct experimental observation of this type of system response to a small disturbance. However, their existence is important since this response could possibly be excited by a larger disturbance or by a controller and thus lead to detectable oscillations in the temperature field and the crystal radius.

The real component of the maximum eigenvalue, $Re(\sigma_{max})$, was calculated from a least-squares fit to the final slope of the semi-log plot of the norm of the disturbance vector versus time. This value is displayed as a function of pull rate V^* in Fig. 5.19 for the quasi-steady solutions on each of the operating curves of Fig. 5.7. Analyses which exhibited oscillations in the disturbance are denoted by the open circles along

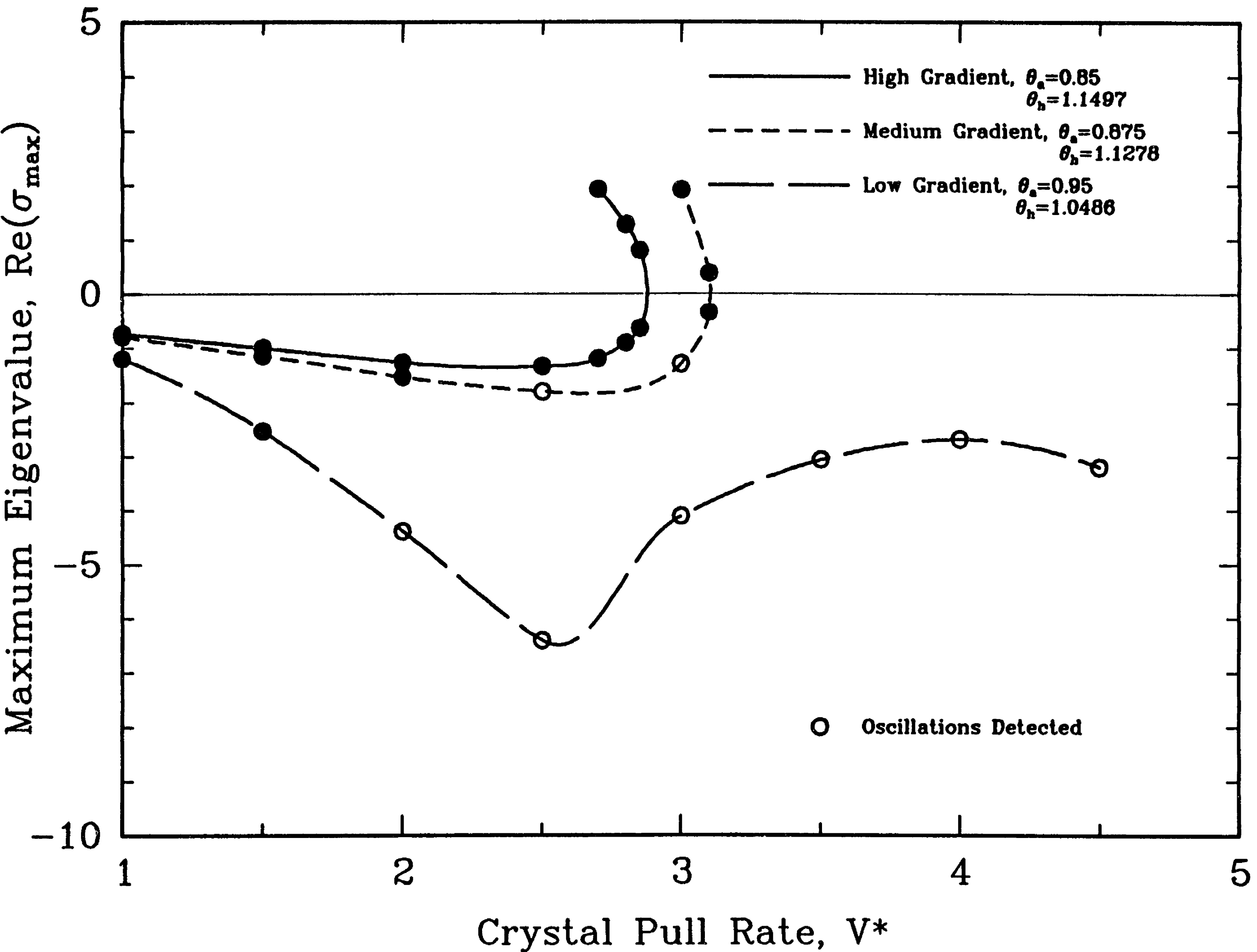

Fig. 5.19 Real part of maximum system eigenvalue as a function of pull rate for the three operating curves of Fig. 5.7. Crossings of zero axis indicate exchange of stability between solutions; negative values represent inherently stable solutions. Oscillations in disturbance vector evolution are seen in states denoted by open circles.

each curve.

The limit points of the high- and medium-gradient operating curves are seen in this plot as crossings of the zero axis by the maximum eigenvalue at some critical pull rate. Obviously, there is a change in the stability of the steady-state solutions as this crossing occurs, from stable solutions with a negative value of the real part of the maximum eigenvalue to unstable for those with a positive real value. The magnitude of the maximum eigenvalue was difficult to calculate for the low-gradient operating states due to the presence of oscillations in the evolution of the disturbance, and the error in calculating these values was considerable. However, there was no doubt that the real part of the maximum eigenvalue was negative, thus indicating stable solutions for these operating conditions.

The appearance of oscillations in the disturbance to the steady-state solutions followed a pattern. Oscillations were detected for stable solutions at moderate to small radius values for the lower-gradient systems. The appearance of these oscillations indicates imaginary components of the system's eigenvalues, and there is a possibility that a true oscillatory solution is present somewhere in parameter space. This time-periodic solution would occur at a Hopf bifurcation point from a steady-state operating curve (Iooss and Joseph, 1980). Time-periodic solutions were not searched for extensively, but one attempt is described in the calculations of Section 5.3.1 on the nonlinear dynamics of the system.

5.3 Transient Simulation

Results for the fully transient thermal-capillary model are presented in the following sections. These calculations represent the first comprehensive simulation of a transient CZ system. Crowley (1983) also solved for a transient system, but her model required experimentally measured fluxes for inputs and did not account for the batchwise nature of the process by allowing for decreasing melt depth and increasing crystal length, as is done here.

The dynamics of a hypothetical steady-state continuous-processing system are computed for imposed step changes in the crystal pull rate in Section 5.3.1. The results of Section 3.2.2 introduce the batchwise elements of CZ growth by allowing for an increasing crystal length and decreasing melt volume.

5.3.1 Dynamic Transitions between Steady States

The analysis presented in the previous section demonstrated the local stability of the quasi-steady operating states with respect to infinitesimally small disturbances. The nonlinear stability and dynamics of the quasi-steady system are addressed in this section by imposing a step change in the pull rate and integrating the full nonlinear transient equation set in time. This calculation models a true continuous-processing system where the melt volume remains constant in time and the top of the crystal is far from the melt. This is achieved in the transient model by arbitrarily setting the

density ratio of solid to liquid to zero in the differential equation (eq. 2.30 and 3.61) which describes the melt volume $V_m(\tau)$ and by keeping the top of the crystal $Z(\tau)$ at a constant value so that the crystal is pulled vertically through the plane defined by $z=Z(\tau)$ as if it was entering a sleeve above this point.

The results of three calculations are shown in Fig 5.20 for the dynamic response of the crystal radius at the tri-junction to a step change in pull rate. The initial state for each calculation was the quasi-steady-state solution calculated for the high-gradient condition at $V^*=2.7$. This is the same initial state used in the linear stability analysis of the previous section and is denoted in Fig. 5.7 as the open circle on the upper branch of the high-gradient operating curve.

When the pull rate was stepped to $V^*=3.0$, a pull rate beyond the critical pull rate V_c^* marking the position of the limit point on the operating curve, the radius decreased uniformly as the crystal steadily melted away. There was no evidence of any time periodic stationary state in this region of parameter space, as discussed previously in Section 5.2. For the step decreases in pull rate, to $V^*=2.5$ and $V^*=2.0$, the radius rose monotonically to the same values calculated from the quasi-steady model.

The solutions at the solid points on each curve of Fig. 5.20 are shown as system isotherm plots in Fig. 5.21. For each solution, the evolution of the radius is seen by the shape of the crystal. The decrease in the radius for the step increase in pull rate is seen from the downward taper of the crystal in the plot on the left. For the step decreases in pull rate shown in the middle and right cases

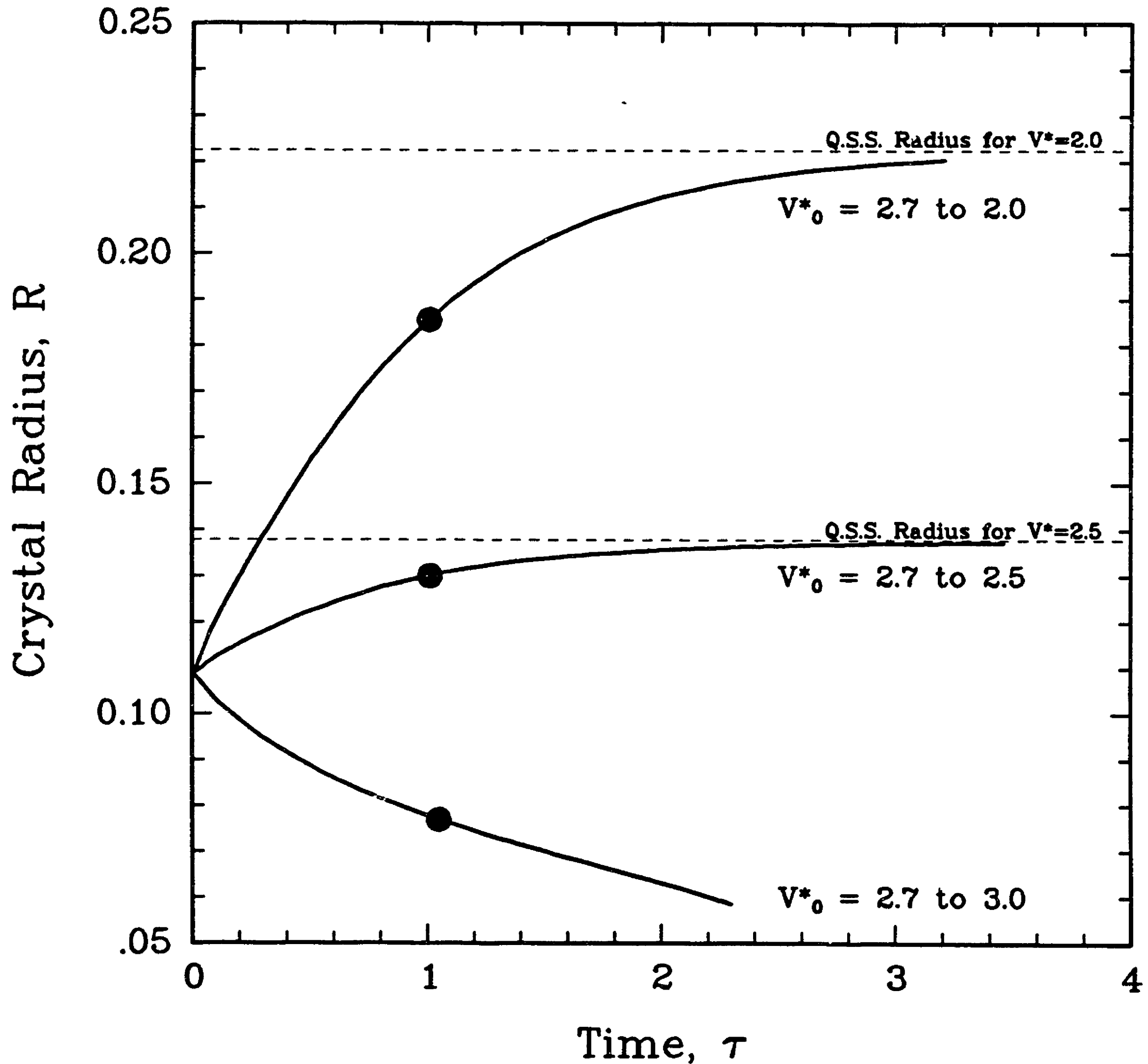

Fig. 5.20 Crystal radius at tri-junction as a function of time for dynamic response of quasi-steady solution to step change in pull rate. Results are shown for the initial state denoted by the open circle on the upper branch of high-gradient operating curve in Fig. 5.7, with Θ_a=0.85, Θ_h=1.1497, and V^*_0=2.7. At τ=0, the pull rate was stepped instantaneously to V^*=3.0, 2.5, or 2.0 with all other parameters are held fixed at those listed in Tables 5.1 and 5.2. Solutions at solid circles are shown in Fig. 5.21.

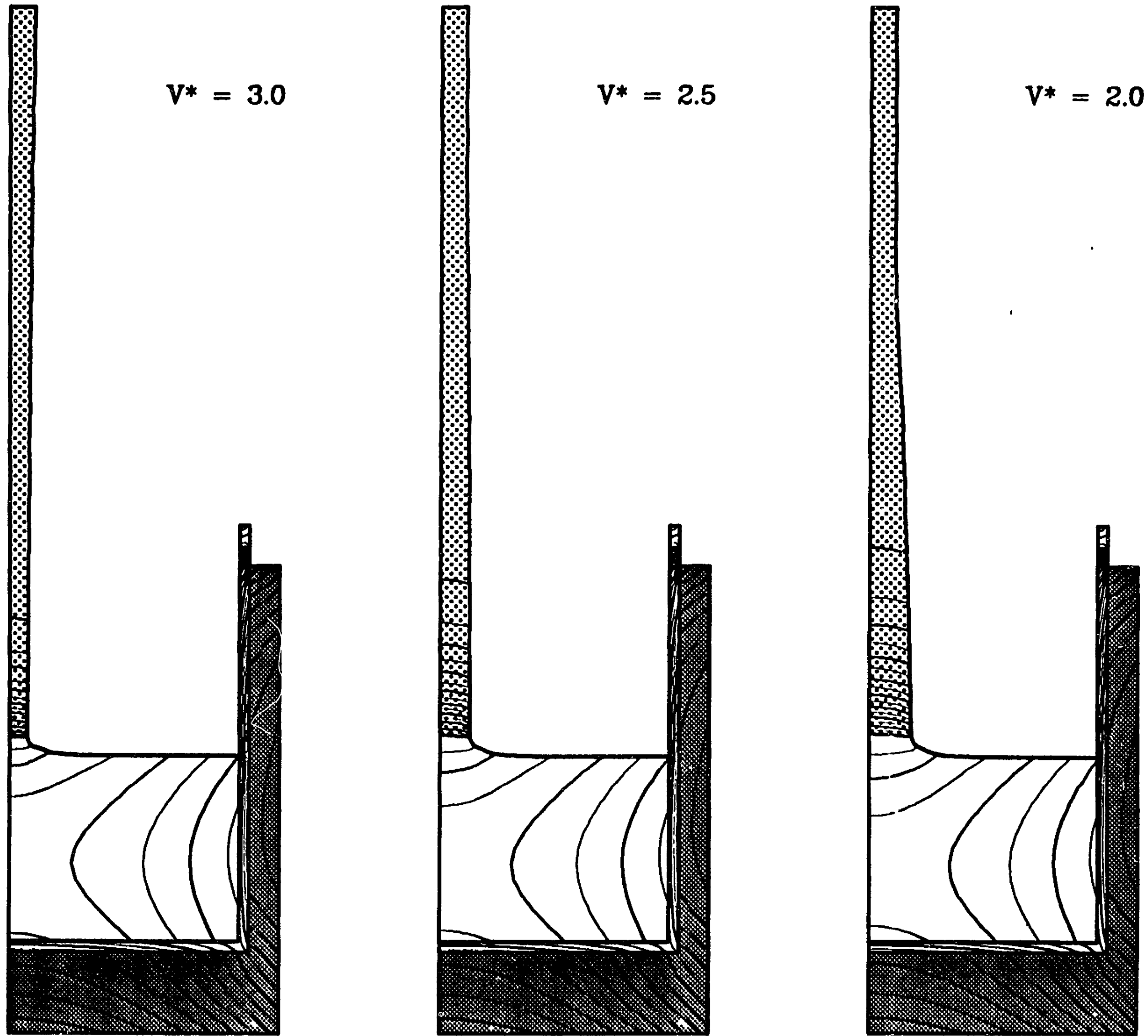

Fig. 5.21 Changes in isotherms and interface shapes for transient simulation of continuous-processing CZ silicon growth system with the high-gradient conditions of Θ_a=0.85 and Θ_h=1.1497. Solutions correspond with the solid circles on the curves of Fig. 5.20 and show response of system to initial step change of pull rate to value shown for each case. All other parameters are held fixed at those listed in Tables 5.1 and 5.2.

of Fig. 5.21, the crystal radius increases, as apparent from the enlarged lump in each crystal. The behavior of the full nonlinear system is consistent with the results of the linear stability analysis. The operating states are found to be stable to finite-amplitude disturbances, such as the pull rate changes imposed here, and each dynamic solution approaches the quasi-steady state defined by the new parameter values.

The next series of calculations was performed for the low-gradient operating state with $V^*=3.5$ as the initial solution. This solution correspond to the open circle on the low-gradient operating curve of Fig. 5.7 and was used in the linear stability analysis of the previous section. The response of the radius to two different decreases in pull rate is shown in Fig. 5.22. As in previous calculations, the radius approached the quasi-steady-state values for the new pull rate. However, the response of the radius to the small step change in pull rate ($V_0^*=3.0$) was not monotonic. In fact, there was an oscillation in the rate of change of the radius around the rise to the new steady-state value and a slight radius overshoot which was quickly damped. This feature was less obvious for the large step change in pull rate ($V_0^*=2.5$) where the radius evolution appears smoother. The states denoted by the solid points along the curves of Fig. 5.22 are shown in Fig 5.23. Here it obvious that oscillations occurred in the radius for both calculations as the new steady-state was approached.

The oscillatory behavior of the system in these transient calculations was expected from the linear stability analysis of the previous section for this initial state (R=0.0673, $V^*=3.5$ on the low-gradient

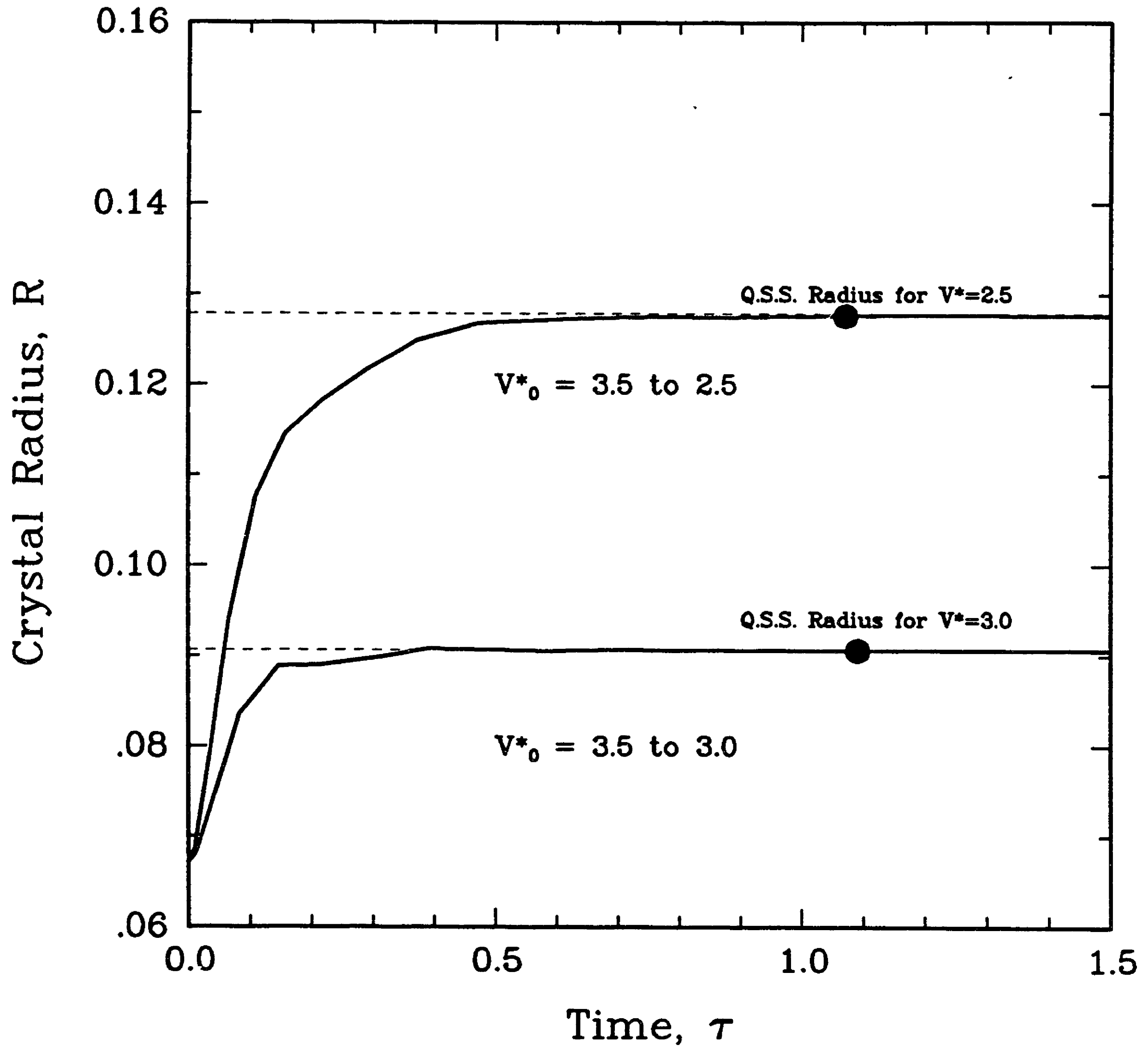

Fig. 5.22 Crystal radius at tri-junction as a function of time for dynamic response of quasi-steady solution to step change in pull rate. Results are shown for the initial state denoted by the open circle on the low-gradient operating curve in Fig. 5.7, with Θ_a=0.95, Θ_h=1.9486, and V^*_0=3.5. At τ=0, the pull rate was stepped instantaneously to V^*=3.0 or 2.5 with all other parameters are held fixed at those listed in Tables 5.1 and 5.2. Solutions at solid circles are shown in Fig. 5.23.

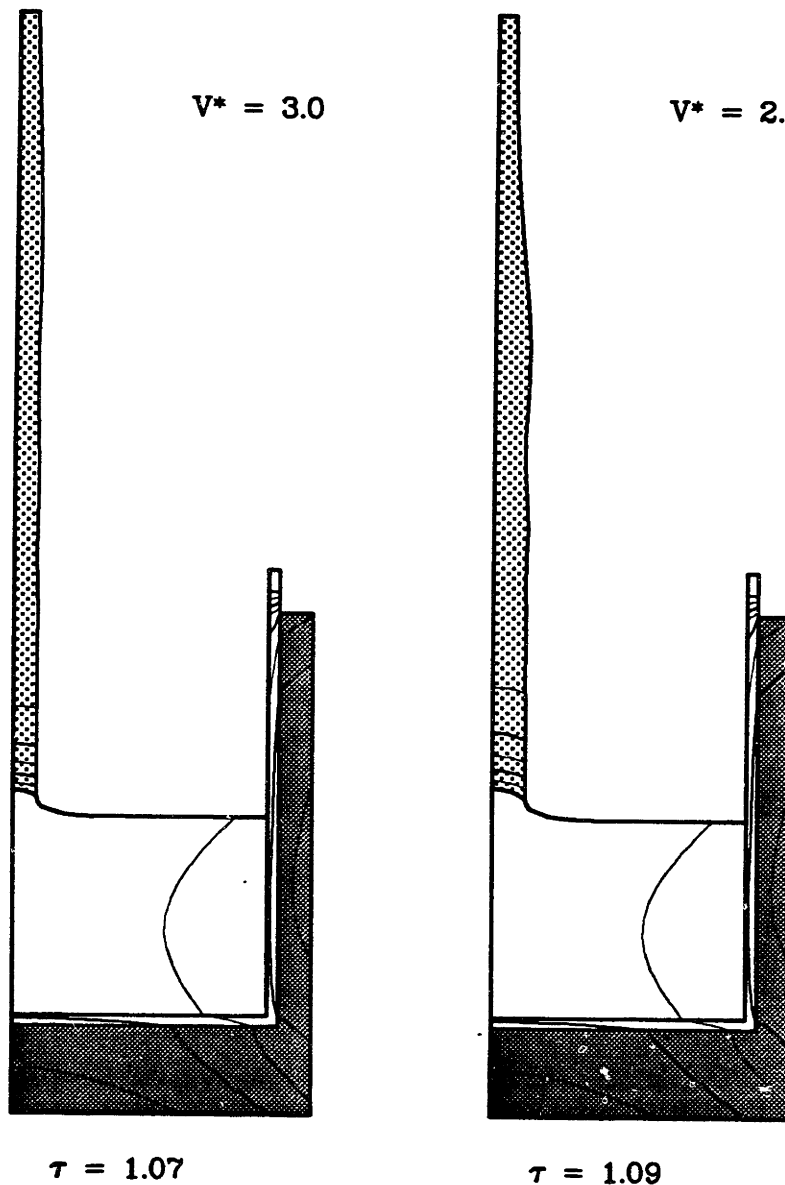

Fig. 5.23 Changes in isotherms and interface shapes for transient simulation of continuous-processing CZ silicon growth system with the low-gradient conditions of Θ_a=0.95 and Θ_h=1.0486. Solutions correspond with the solid circles on the curves of Fig. 5.22 and show response of system to initial step change of pull rate to value shown for each case. All other parameters are held fixed at those listed in Tables 5.1 and 5.2.

operating curve of Fig. 5.7). This low-gradient state is qualitatively similar to the situation produced by the thermal environment used in the current practice of LEC gallium arsenide growth, were low temperature gradients are desired to minimize the thermoelastic stresses in the crystal during growth. The results obtained here may explain the origins of oscillatory behavior observed in experimental LEC systems (Jordan et al., 1983; Elliot et al., 1984).

5.3.2 Dynamic Growth Simulation

The modeling of an entire CZ growth run is performed in the next series of calculations by integrating the transient thermal-capillary model equations, described previously in Chapters 2 and 3. These calculations represent the first complete transient simulation of the Czochralski process. An unconstrained growth run, where all operating parameters are held fixed throughout the simulation, was simulated for the initial configuration and the operating parameters listed in Table 5.4.

The evolution of crystal radius with time is plotted in Fig 5.24 for this batch simulation. The radius initially decreased and then increased monotonically as growth proceeded. The growth run was terminated when the pulled crystal encountered a growing region of undercooled melt at the bottom of the crucible. In experimental practice, this can occur and is known as crystal "bumping." The increase in the crystal radius with time was expected from the quasi-steady-state calculations of Chapter 4 for decreasing melt volume V_m. The amount

Table 5.4 Operating parameters and dimensionless groups characterizing the quasi-steady initial condition used for the dynamic CZ silicon simulations of batchwise growth in Chapter 5.

Operating Parameter	Dimensional Value	Dimensionless Value
Ambient temperature, Θ_a	1430 K	0.85
Biot numbers, Bi_j	-	0.033
Bond number, Bo	-	176.
Crystal top location, Z	10.95 cm	1.5
Crystal pull rate, V^*	5.0 cm/hr	1.0
Heater temperature, Θ_h	1890 K	1.1227
Peclet numbers, Pe_i		
melt	-	0.038
crystal	-	0.11
liner	-	0.48
crucible	-	0.057
Radiation numbers, Ra_j		
melt	ε=0.3	0.27
crystal	ε=0.7	0.63
liner	ε=0.35	0.31
crucible	ε=0.8	0.72
Stefan number, S	-	1.07
Thermal conductivity ratios, $K_i(\Theta)$		
melt	-	2.9
crystal	-	$1./\Theta$
liner	-	0.27
crucible	-	2.7
Volume of melt, V_m	1,460 cm^3 (3.7 kg)	3.75

of heat flowing into the melt decreases as the conduction path of surface area in contact with the crucible lessens with the dropping the melt level. This factor coupled with the crystal cooling to a uniform ambient allowed the radius to grow out as the run proceeded.

The length of the crystal boule increased as it was pulled from the melt, and the greater surface area of the crystal facilitated the cooling of the boule. This effect also promoted an increase in the crystal radius, as shown by the calculations discussed previously in Section 5.1, where the quasi-steady crystal radius increased for greater values of the quasi-steady crystal height Z.

It should be emphasized here that this simulation did not include radiative heat transfer between the crystal and the crucible wall, as would be experienced in an experimental system. Including radiative exchange would eventually cause the crystal radius to decrease during a growth run if no changes were made in the operating parameters. This effect is caused by exposing the hot crucible wall to the crystal as the melt level drops during batch growth, as was shown qualitatively in the calculations of Chapter 4 and Derby and Brown (1986b, 1986c).

Although the results of the present analysis do not include the details of radiative heat transfer discussed above, the calculation of the macroscopic changes in the crystal and interface shapes for this batch simulation is a major accomplishment and lays the basis for including these additional effects. A comprehensive treatment of the batch-induced changes caused by radiation heat transfer is given in Atherton et al. (1986) for an extension of the thermal-capillary model presented in this thesis.

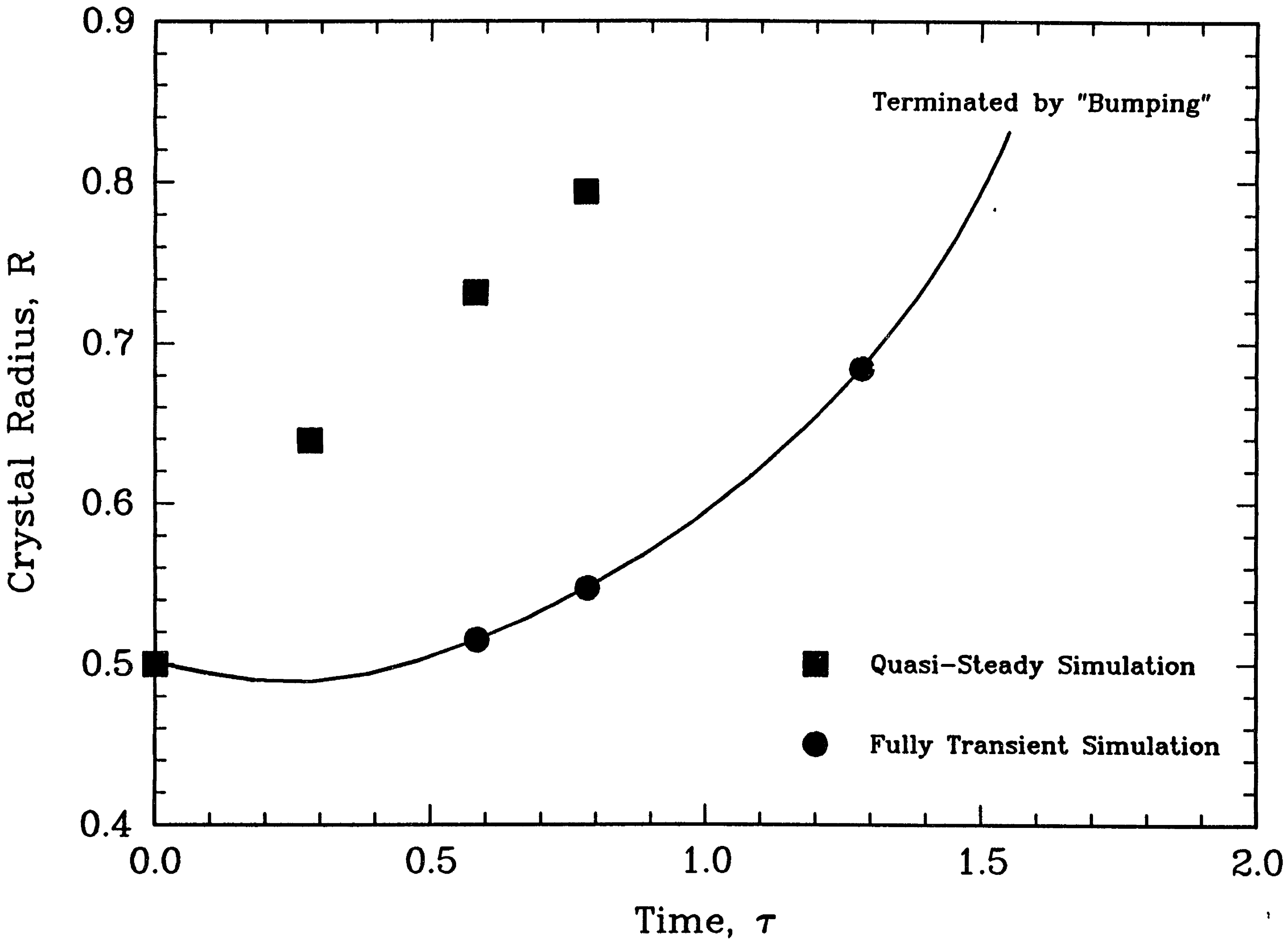

Fig. 5.24 Crystal radius as a function of time for the dynamic simulation of batchwise CZ silicon growth. Results are shown for the tri-junction radius in a fully transient run with all parameters held fixed at those listed in Table 5.4 and for the quasi-steady radius obtained by steady-state calculations. Solutions corresponding to the solid points are shown in Figs. 5.25 and 5.26 for the fully transient simulation and the quasi-steady calculations, respectively.

The initial decrease in the crystal radius seen in Fig. 5.24 was unexpected but is explained by a reexamination of the heat transfer boundary condition at the melt/solid interface,

$$K_m(\mathbf{n}\cdot\nabla\Theta)_m - K_s(\mathbf{n}\cdot\nabla\Theta)_s = Pe_s S[V^*(\tau) - \frac{\partial H_o}{\partial\tau}](\mathbf{n}\cdot\mathbf{e}_z) , \qquad (5.1)$$

where the conductive fluxes are shown on the left-hand side of the equation and the latent heat release on the right. The growth velocity of the solidifying interface, the quantity within the square brackets, differs from the crystal pull rate by the term $\partial H_o/\partial\tau$. For the quasi-steady-state calculations, this time derivative is set to zero. However, this rate of interface height change is significant in the growth velocity of the melt/crystal interface in this batch process.

The overall importance of batch effects on the growth rate of the solidification interface is estimated as follows. The time-dependent mass balance for the melt during a batch growth run is

$$\frac{\partial V_m}{\partial\tau} = -2\pi\int_0^R \frac{\rho_s}{\rho_m}[V^*(\tau) - \frac{\partial H_o}{\partial\tau}]r\,dr , \qquad (5.2)$$

where the quantity inside the integral on the right-hand side of the equation represents the flux of material leaving the melt through the melt/solid interface. If we assume that the shapes of the crystal and meniscus are flat, above relation is approximated by the following equation,

$$\frac{\partial V_m}{\partial\tau} \approx -(\frac{\rho_s}{\rho_m})\,\pi R^2 V_g , \qquad (5.3)$$

where V_g is the growth rate of the melt/crystal interface and is given by,

$$V_g = V^*(\tau)/[1-(\frac{\rho_s}{\rho_m}) R^2] , \qquad (5.4)$$

where $V^*(\tau)$ is the crystal pull rate, ρ_s and ρ_m are the densities of solid and melt, respectively, and R is the radius of the crystal at the tri-junction. For a crystal radius of R=0.5, the overall interface growth velocity V_g is approximately 32 percent greater than the value of $V^*=1.0$ used to obtain the initial quasi-steady solution. When this quasi-steady solution is used as an initial condition for the transient simulation, there is an immediate acceleration of the melt/crystal interface to the greater growth rate present in the batch run. This initial acceleration causes extra latent heat to be generated, and the crystal radius decreases.

The predictions of radius versus melt volume obtained from calculations with the quasi-steady-state model are shown as the solid squares plotted in Fig. 5.24. These calculations were performed for the $Z(\tau)$ and $V_m(\tau)$ values obtained at selected times along the transient solution curve. As growth proceeded, the quasi-steady-state predictions got progressively worse. Eventually, the quasi-steady radius grew out to the crucible wall, and the quasi-steady growth simulation was terminated after a much shorter time (corresponding to a greater melt volume, V_m) than that achieved by the fully transient run.

This mismatch between the quasi-steady predictions for the crystal radius and the transient values was a direct result of two effects. The increase of the growth rate at the melt/crystal interface over

the pull rate becomes more important as the crystal radius increases, as described above by eq. (5.4), and the extra latent heat released at the interface opposes the increase in crystal radius. In addition, the dynamic crystal shape cannot be calculated by the quasi-steady model, where the crystal is assumed to be cylindrical. Since a cylinder has a greater surface area than a cone, the cooling of the crystal to the ambient is overstated in the quasi-steady-state calculations. Both of these effects cause the quasi-steady model to over-predict the the crystal radius.

The isotherms and interface shapes of the states denoted by the circles on the transient curve of Fig. 5.24 are shown in Fig. 5.25. The cone-shaped crystal produced by the steadily increasing radius is apparent in the solution at $\tau=1.28$, and a small portion of undercooled melt is also shown by the shaded region at the bottom of the crucible. Eventually, this region of undercooled melt grows until the pulled crystal bumps against it, thereby terminating the growth run. The quasi-steady solutions for the squares in Fig. 5.24 are shown in Fig. 5.26. In this series of calculations, the crystal radius increases to nearly fill the crucible before any undercooling is detected in the melt.

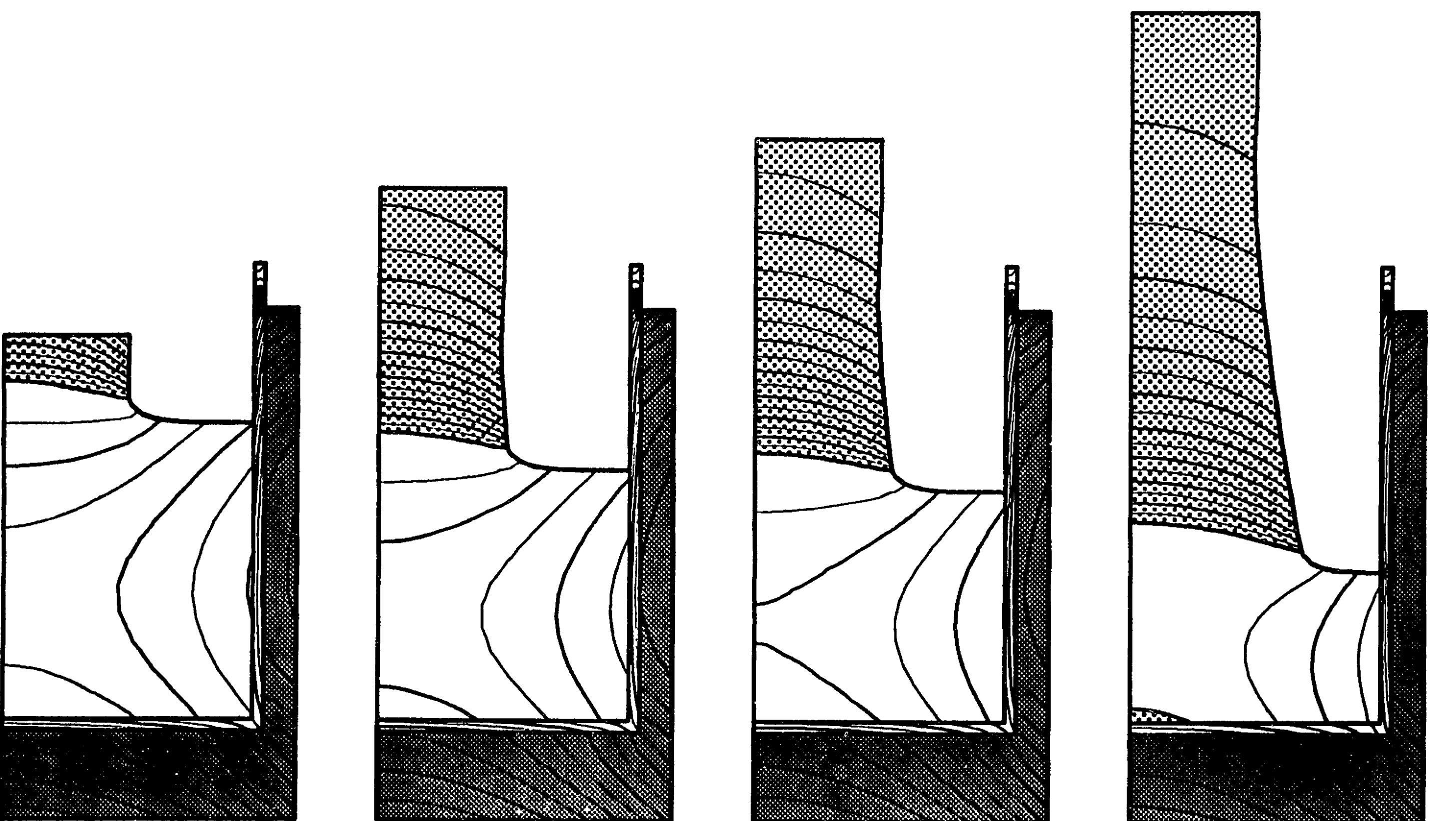

Fig. 5.25 Changes in isotherms and interface shapes with time for the fully transient CZ silicon batch growth simulation. Solutions correspond to the solid circles shown in Fig. 5.24. All parameters are held fixed through the run at those listed in Table 5.4.

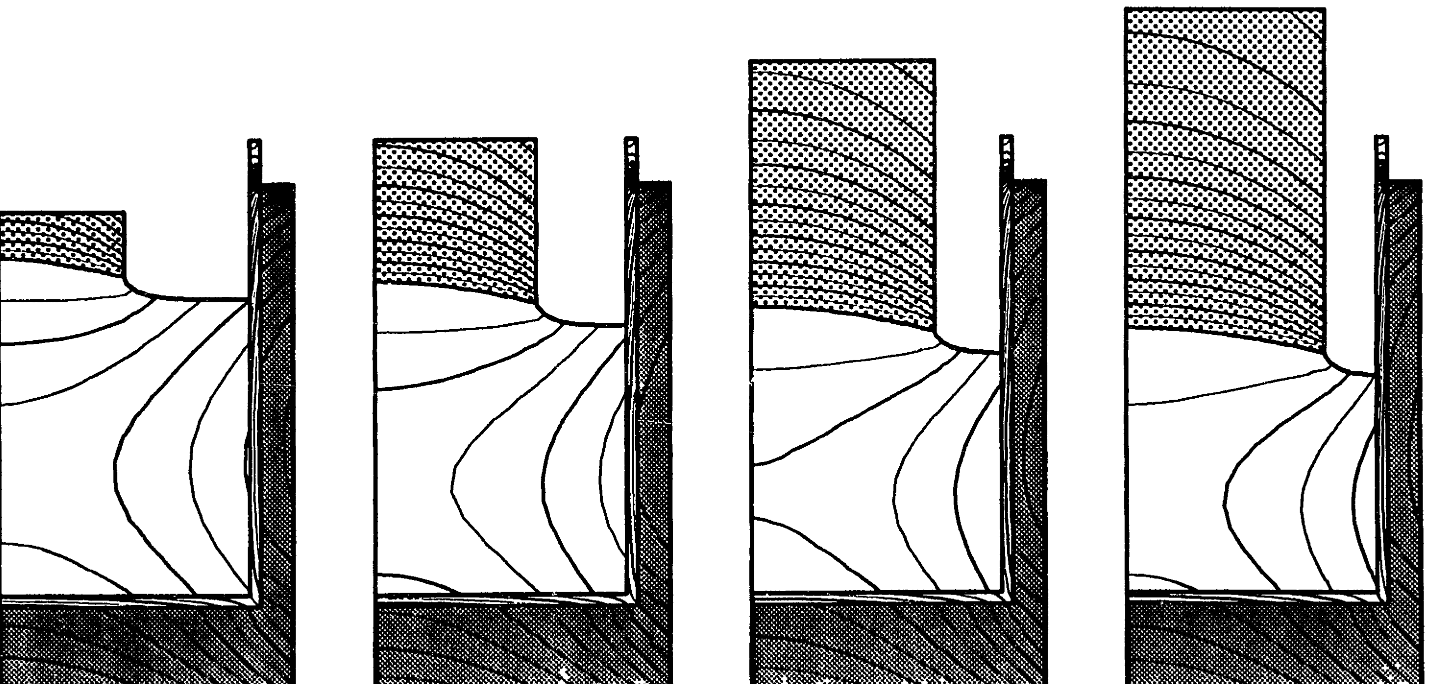

Fig. 5.26 Changes in isotherms and interface shapes with time for the quasi-steady-state CZ silicon batch calculations. Solutions correspond to the solid squares shown in Fig. 5.24. At each time shown, crystal top position and melt volume were obtained from the values obtained from the fully transient simulation. All parameters except crystal top and melt volume are held fixed through the run at those listed in Table 5.4.

5.4 Dynamics of Control

In the calculations of this section, several control strategies are employed in an attempt to maintain a constant crystal radius throughout a batch growth run. These calculations represent the first controlled batch simulations of the CZ growth process and point out the power of the transient thermal-capillary model as a test bed for different control stràtegies. Radius control strategies which adjust the heater temperature during the growth process are implemented in a manner analogous to the quasi-steady processing strategy calculations of Section 4.3, except that a transient servo-controller equation is added to the existing thermal-capillary model equations instead of a quasi-steady constraint.

For a true steady-state process a heater controller for keeping a constant crystal radius would be employed with the following relation,

$$\Theta_h - \Theta_{h,set} = g_p(R - R_{set}) + g_i \int_0^{\tau} (R - R_{set})dt \, , \qquad (5.5)$$

where Θ_h is the heater temperature, R is the radius of the crystal at the tri-junction point, $\Theta_{h,set}$ and R_{set} are the set point values for heater temperature and crystal radius, and g_p and g_i are the controller gains for proportional and integral control, respectively. The set point heater temperature $\Theta_{h,set}$ is a constant, and equation (5.5) is differentiated with respect to time to obtain

$$\frac{\partial \Theta_h}{\partial \tau} = g_p \frac{\partial R}{\partial \tau} + g_i(R - R_{set}) \, . \qquad (5.6)$$

This controller equation is used in the next series of calculations to change the heater temperature in time as a response to deviations in the radius from its set point value.

Since CZ crystal growth is a batch process, the set point for the heater temperature, $\Theta_{h,set}$ of eq. (5.5) above, is actually not constant but a slowly varying function of time which compensates for the changes in heat transfer as the melt level drops. This time-dependent set point is the quantity calculated by the quasi-steady processing strategies of Section 4.3. Equation (5.6) is employed as a servo-controller so that it calculates changes to the heater temperature in time and effectively updates the heater temperature to the new set point value. This type of control is often used in practice (Bardsley et al., 1977a,b) where the deviation quantity $R\text{-}R_{set}$ is determined by an analysis of the weight gain of the crystal, as monitored by a load cell connected to the pull rod, and the power input to the heater, which is represented here as the heater temperature Θ_h, is adjusted accordingly.

Three cases are presented below for different choices of controller gains g_p and g_i which represent proportional (P), integral (I), and proportional-integral (PI) control schemes. The initial condition for all of these runs was chosen to be the same solution as that used in the batch simulation of the previous section, and the operating parameters for this initial solution are given in Table 5.4. Except for the heater temperature, which is determined by equation (5.6) with $R_{set}=0.5$, all operating parameters are held constant during the growth simulation.

5.4.1 Proportional Control

In this series of calculations, the results of employing a proportional (P) controller are shown by setting $g_i=0$ in equation (5.6) above to obtain

$$\frac{\partial \Theta_h}{\partial \tau} = g_p \frac{\partial R}{\partial \tau} \bigg|_{z=H_0(R,\tau)} . \tag{5.7}$$

This controller is implemented by augmenting the transient equation set, described previously in Chapter 3, with eq. (5.7); the term involving the time derivative of the radius at the tri-junction is an additional contribution to the mass matrix **M**. The results of this strategy used with different controller gains g_p are shown in a plot of radius versus time in Fig. 5.27 for the control of the batch simulation described above.

For $g_p=0.5$, the control strategy succeeded in preventing the crystal bumping which occurred for the uncontrolled growth run and maintained growth until the crucible was very nearly empty. However, the crystal radius still increased substantially through the run. Increasing the gain for the controller succeeded in bringing the crystal radius closer to the set point through the run, but the crystal radius was still almost 10 percent greater than the desired value of R=0.5 at the end of the growth simulation for $g_p=2.0$. It is expected that better results could be obtained with higher proportional gain values. However, a finite amount of offset in the crystal radius is always expected from this type of control scheme (Coughanowr and Koppel,

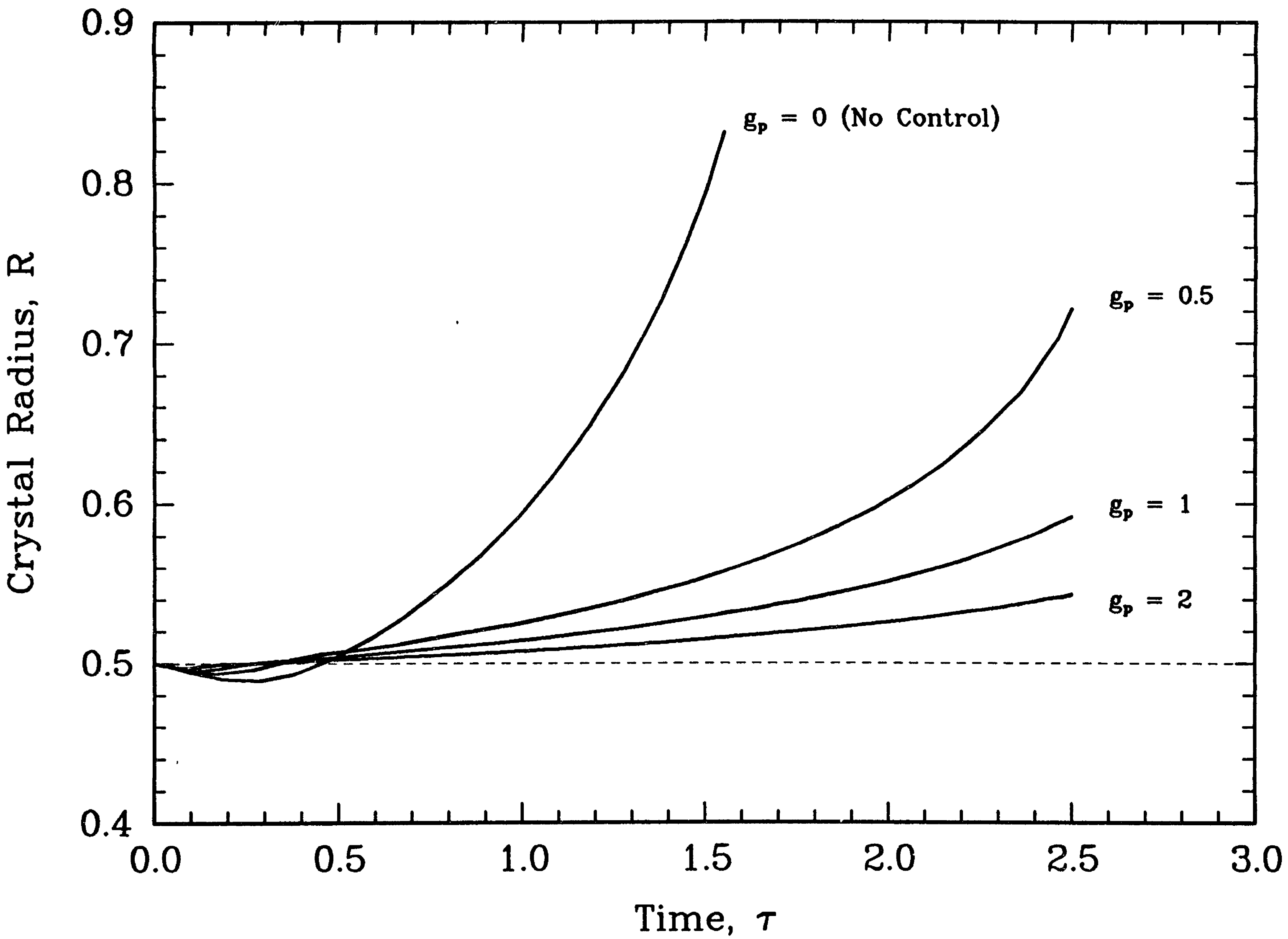

Fig. 5.27 Crystal radius at tri-junction as a function of time for fully transient batchwise growth simulations. Results of proportional (P) control strategies with different gain values are shown. Strategies use eq. (5.7) to adjust heater temperature in an attempt to maintain a constant crystal radius of R=0.5 throughout the run.

1965), and increases in controller gain may adversely affect the dynamics of the system (Chang and Chen, 1984).

5.4.2 Integral Control

In the next runs, The heater temperature Θ_h is varied in an attempt to maintain a constant crystal radius with the following servo-controller,

$$\frac{\partial \Theta_h}{\partial \tau} = g_i (R(H_0,\tau) - R_{set}) , \tag{5.8}$$

where g_i is the gain of the controller, $R(H_0,\tau)$ is the crystal radius at the tri-junction, and R_{set} is the set-point value for the radius. This controller acts in an integral mode, and we expect that it will affect the nonlinear dynamics of the system (see Chang and Chen, 1984) as the set point heater temperature evolves to counter the batchwise changes in process heat transfer.

The evolution of the radius with time is shown for four growth simulations in Fig. 5.28 with different controller gain values, g_i. The radius evolution which resulted with the servo-controller employed with different gains show the oscillatory response of the system to this simple control strategy. Several features are apparent from the shapes of these curves. Although increasing the gain of the controller did help to keep the radius in check, it also caused the frequency of the radius oscillations to increase. In fact, as the gain was doubled, the frequency also nearly doubled. Increasing the integral controller gain g_i alone was not an effective strategy for producing constant-diameter crystals.

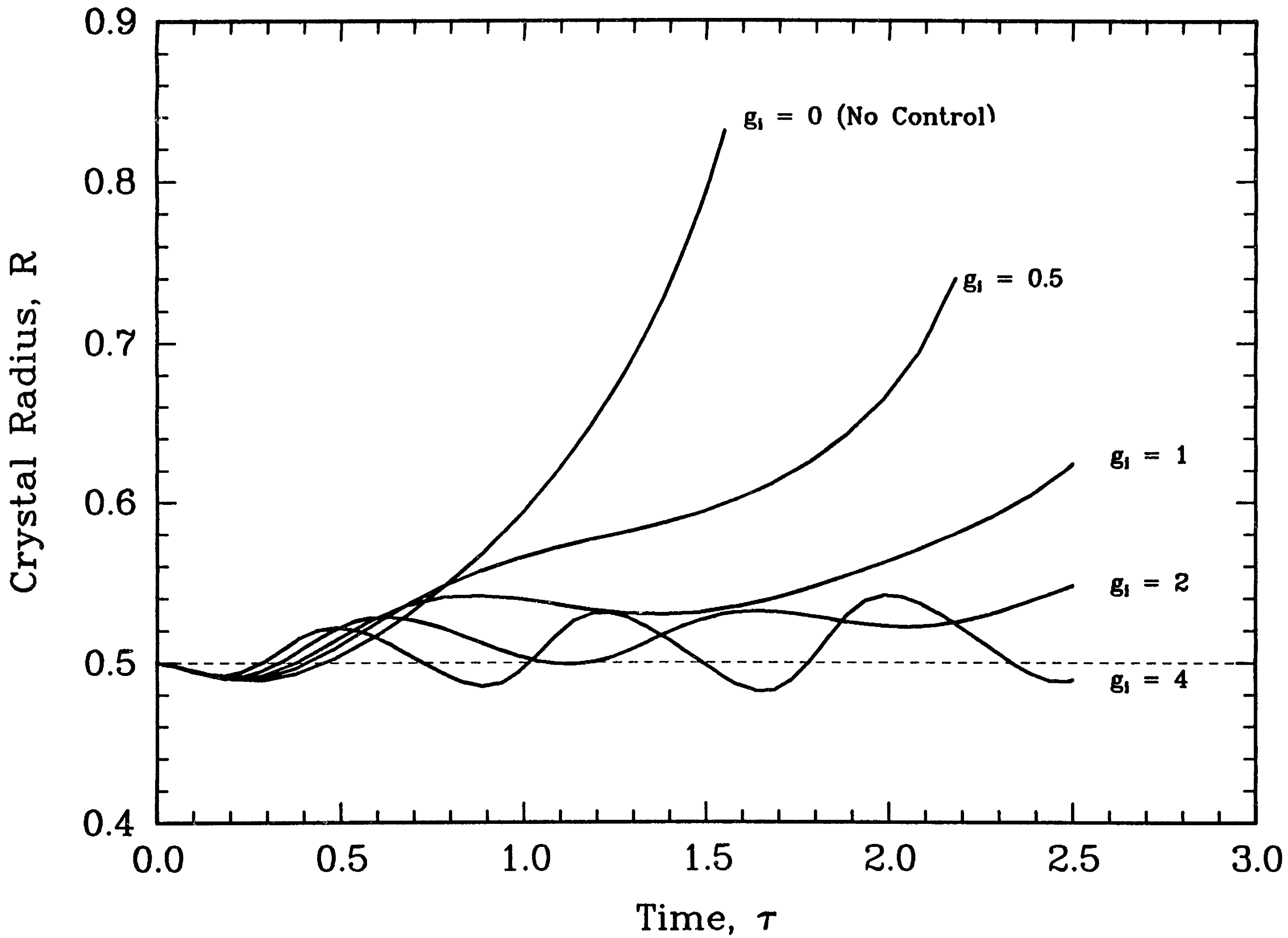

Fig. 5.28 Crystal radius at tri-junction as a function of time for fully transient batchwise growth simulations. Results of integral (I) control strategies with different gain values are shown. Strategies use eq. (5.8) to adjust heater temperature in an attempt to maintain a constant crystal radius of R=0.5 throughout the run.

The isotherms and interface shapes for the simulation with g_i=4.0 are shown in Fig. 5.29. The crystal radius oscillations are clearly seen by the undulating shape of the grown crystal. This crystal shape is similar to those observed experimentally for systems where the control action was inappropriate (Bardsley et al., 1977b). The power of the fully transient thermal-capillary model for calculating non-uniform interface shapes is seen in this example, and the meshes produced for the stages of growth shown in Fig. 5.29 are presented in Fig. 5.30. Approximately 8 CPU minutes on a Cray-XMP were needed to run this growth simulation, and this time was typical for all other batch growth calculations.

The transient history of the heater temperature is presented in Fig. 5.31 along with the radius history for the case of controller gain g_i=4.0. The overall rise in the heater temperature with time is a direct result of the batch-induced changes in the thermal environment caused by the dropping melt level. The excursions of the heater temperature around this overall rise attempted to keep the radius in check, but there was a lag in the response of the radius to the heater which resulted in continuing oscillations in the crystal shape.

The oscillations in the heater temperature and crystal radius for the controlled growth simulations occur on a much shorter time scale than the longer batch transient. For the simulation with g_i=4.0, the batch transient occurred over a time scale of approximately 3.7 hours whereas the frequency of the radius oscillations was approximately 1.1 hours. This discrepancy in time scales leads to the conclusion that this oscillatory state is a controller-induced phenomenon which

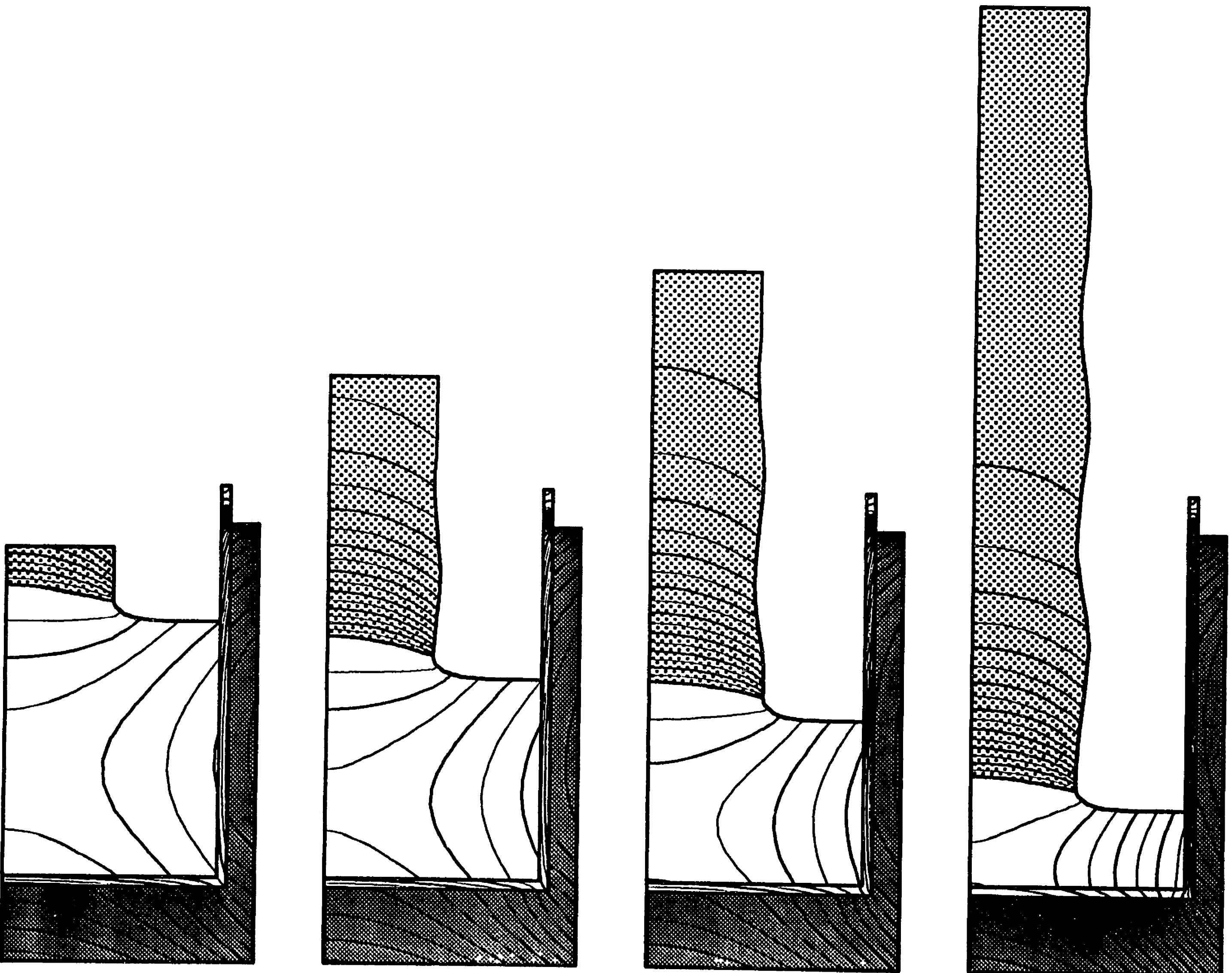

Fig. 5.29 Isotherms and interface shapes for transient simulation of a controlled CZ silicon batch growth system with the integral controller of eq. (5.8) employed with gain g_i=4.0. Solutions are shown at various points during growth run. All parameters except for heater temperature are held fixed at those listed in Table 5.4.

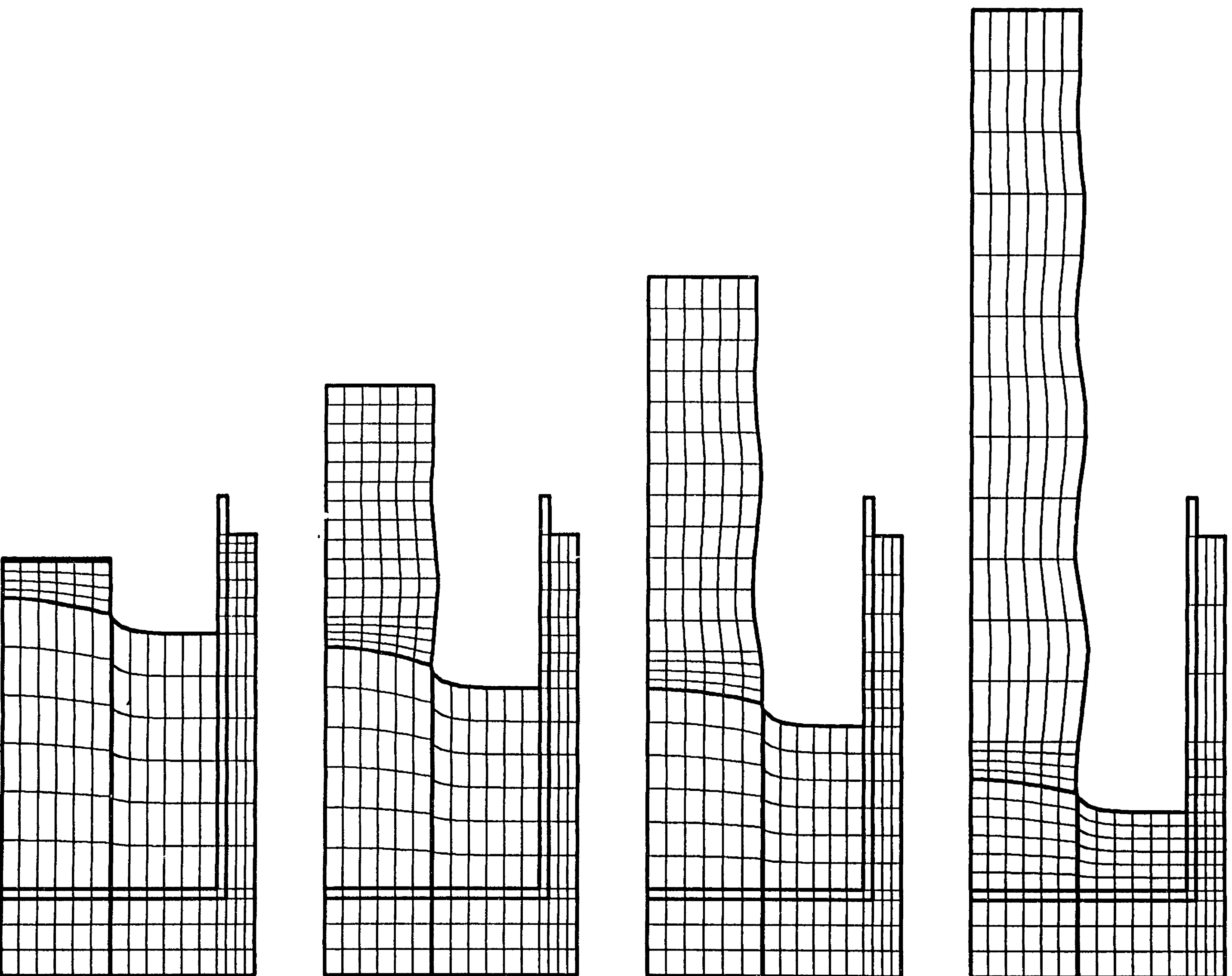

Fig. 5.30 Finite element meshes for the isotherms and interface shapes shown in Fig. 5.29.

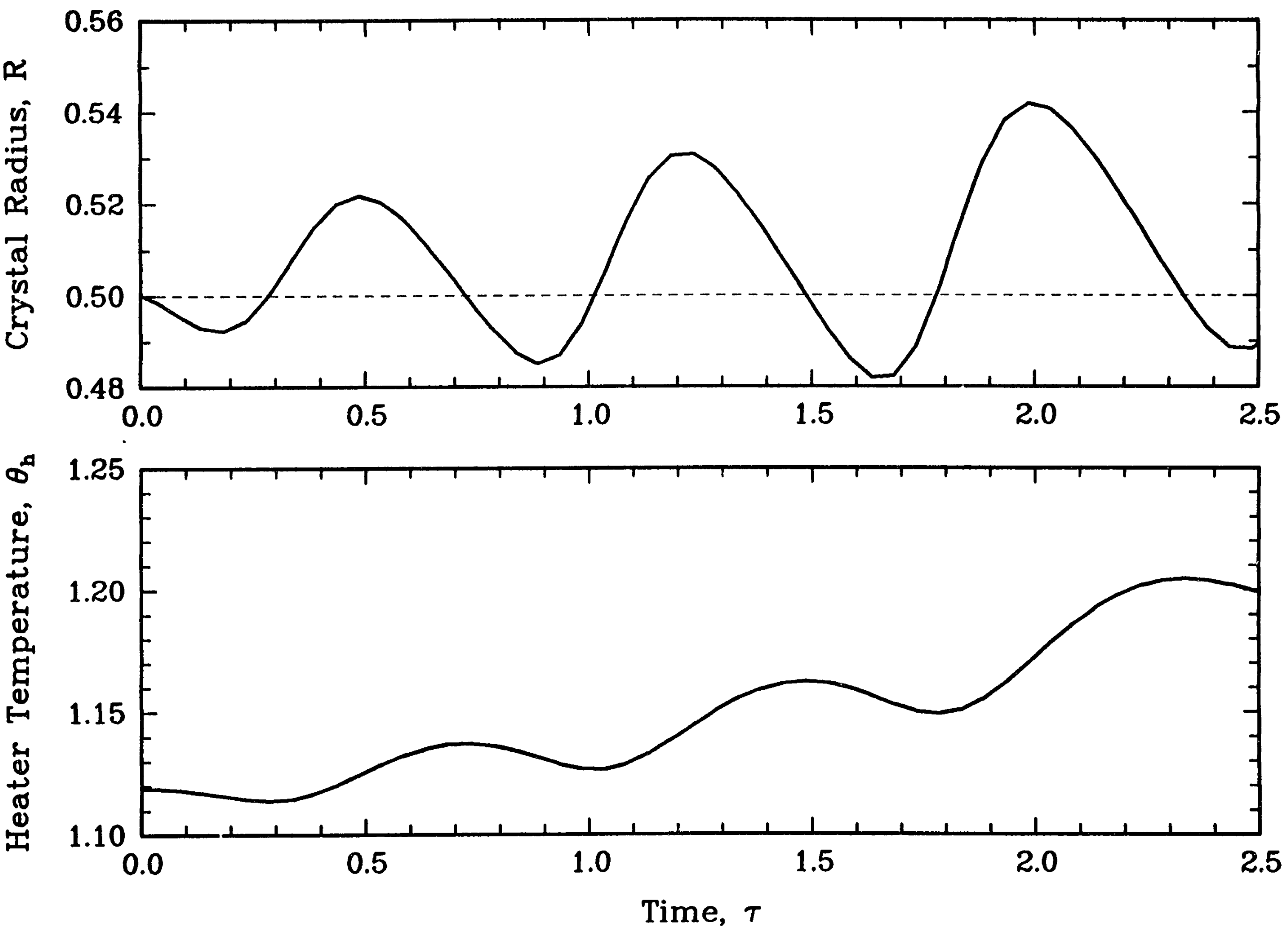

Fig. 5.31 Crystal radius at tri-junction and heater temperature as functions of time for the dynamic simulation of a CZ silicon batch growth run with the integral controller of eq. (5.8) employed with the gain set at g_i=4.0. All parameters except heater temperature are held fixed at those listed in Table 5.4.

is independent of the batch features of CZ growth. The batch-induced change in the heat transfer environment is not the primary cause of these oscillations, and this phenomenon will most likely prevail when the details of radiative exchange and its effects on batchwise heat transfer are included.

The presence of a controller-induced oscillatory state is supported by radius oscillations seen in the nonlinear transient analysis of a controlled continuous-processing system similar to that employed in the calculations of Section 5.3.1. These radius oscillations are shown along with the heater temperature in Fig. 5.32 for the high-gradient reference case of Table 5.2 integrated in time with an initial step decrease in heater temperature. This calculation enables us to eliminate the batch transient from the system and observe only the dynamic response of the system to the controller. The quantities shown in Fig. 5.32 oscillate around their set point values with approximately the same frequency as the oscillations in the batch run, and the heater temperature does not exhibit any rise in time since batch effects are absent.

The dynamics of this nonlinear system can be addressed through a bifurcation analysis with the controller gain as the bifurcation parameter (Chang and Chen, 1984). From the results shown above, there is evidence that a critical integral gain value exists at which a Hopf bifurcation to a time-periodic solution from the steady-state solution occurs (Iooss and Joseph, 1980). This would explain the dependence of the frequency of the radius oscillation with g_i, as seen previously in Fig. 5.28, and the time-periodic solution depicted

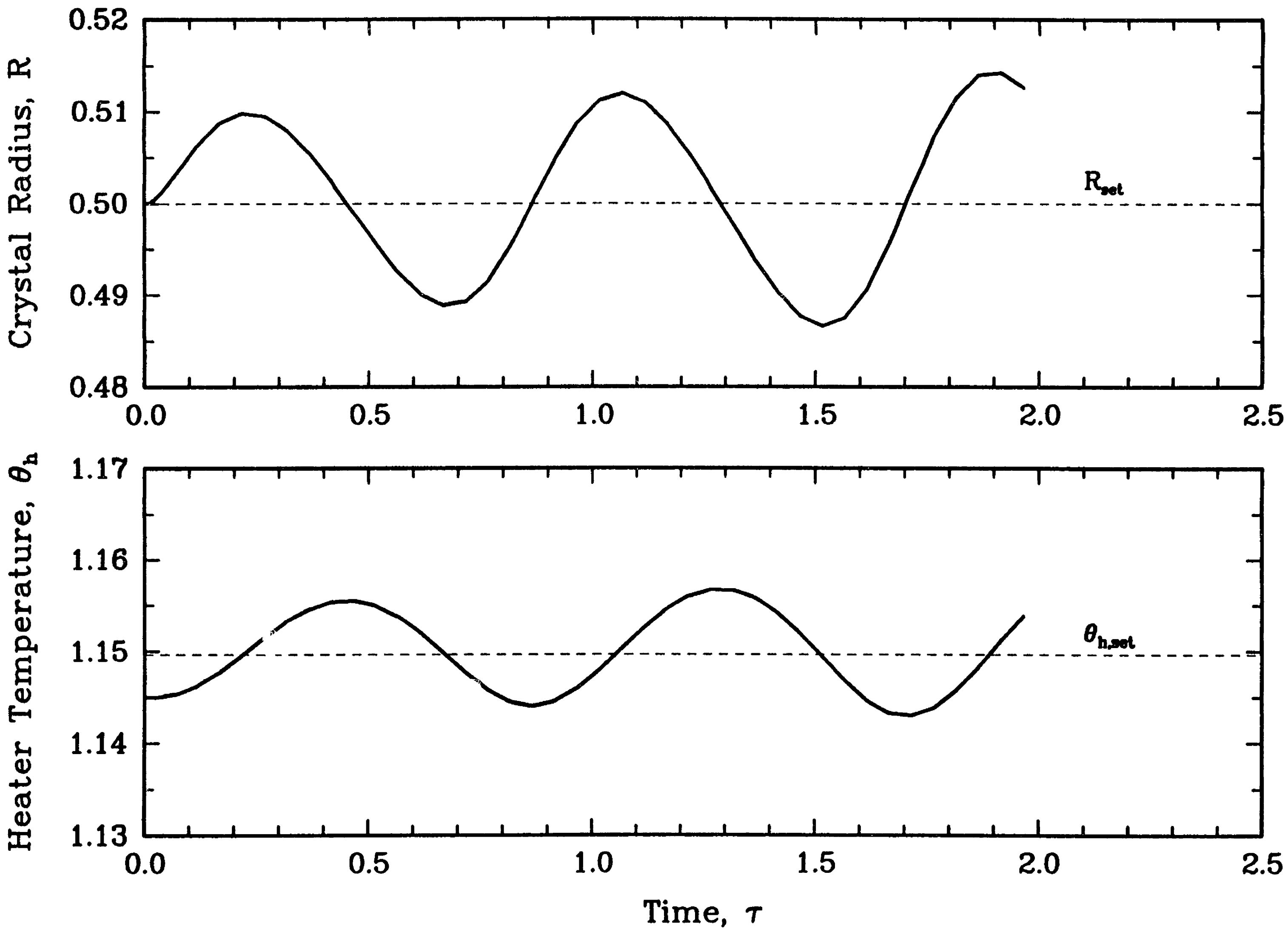

Fig. 5.32 Crystal radius at tri-junction and heater temperature as functions of time for the transient simulation of a continuous-processing CZ silicon run with a constant melt volume. The integral controller of eq. (5.8) was employed with the gain set at g_i=4.0. All parameters except heater temperature are held fixed at those listed in Tables 5.1 and 5.2 for the high-gradient reference case. A small step decrease in heater temperature was imposed initially.

in Fig. 5.32 obtained for the continuous-processing system with integral control.

5.4.3 Proportional-Integral Control

Both proportional and integral control are employed in the next series of growth simulations. In these cases, both terms of eq. (5.6) are used in an attempt to control the crystal radius, and the servo-controller is described by

$$\frac{\partial \Theta_h}{\partial \tau} = g_p \frac{\partial R}{\partial \tau} + g_i (R - R_{set}) \ . \tag{5.9}$$

Two series of computations are presented for proportional gains of g_p=1.0 and g_p=2.0 with values of integral gain g_i=0.5-10.0. In Fig. 5.33, the cases for g_p=1.0 are exhibited, and runs for g_p=2.0 are shown in Fig. 5.34.

In both sets of calculations, increasing the amount of integral gain produced more uniform diameter crystals. Predictably, the strategies with the proportional controller gain of g_p=2.0 produced better results than those with gain g_p=1.0. The oscillations in crystal radius were absent from all curves utilizing PI control, even when the integral gain was set to values far in excess of those used in the calculations of Section 5.4.2.

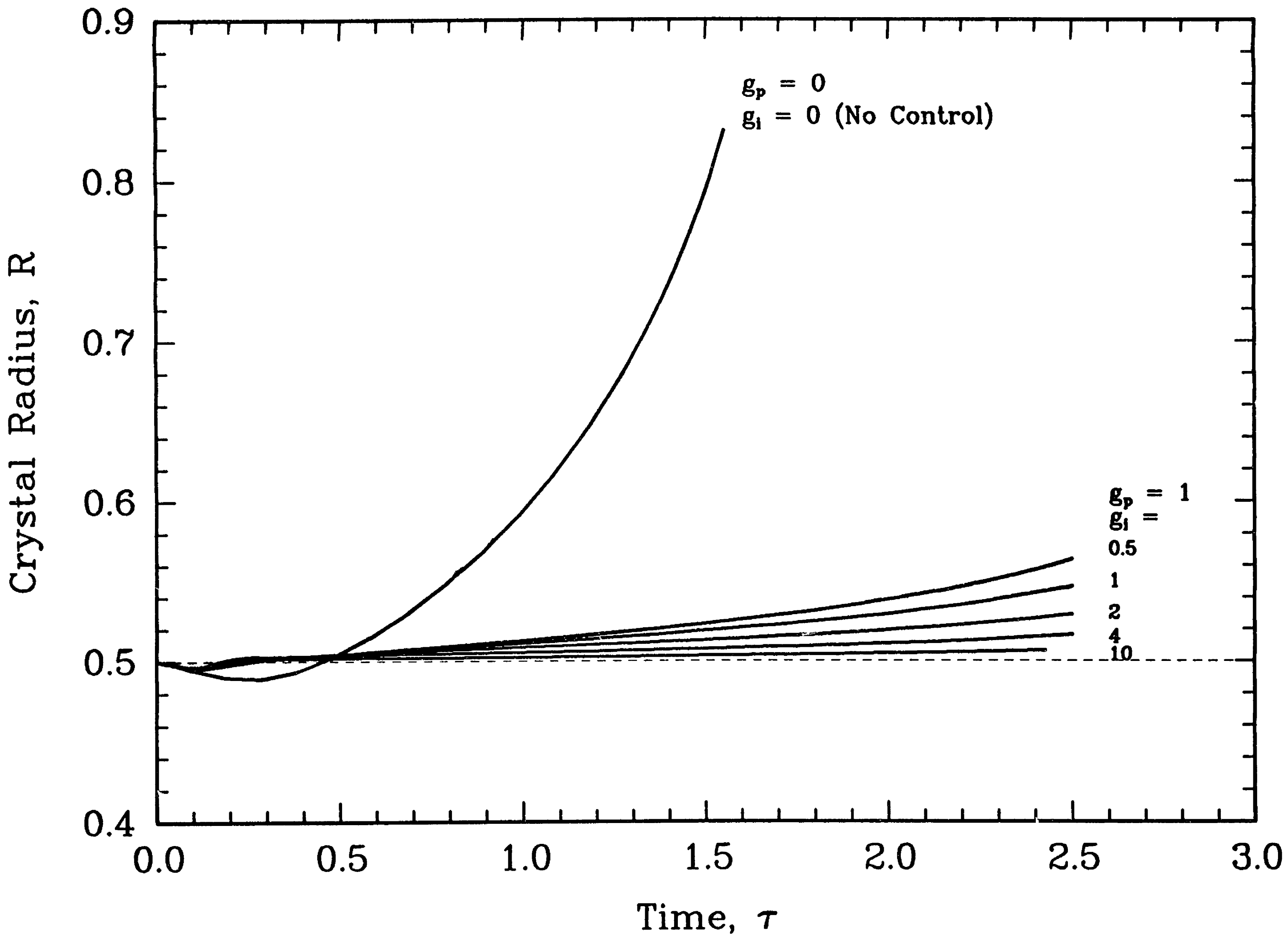

Fig. 5.33 Crystal radius at tri-junction as a function of time for fully transient batchwise growth simulations. Results of proportional-integral (PI) control strategies with different gain values are shown. Strategies use eq. (5.9) to adjust heater temperature in an attempt to maintain a constant crystal radius of R=0.5 throughout the run.

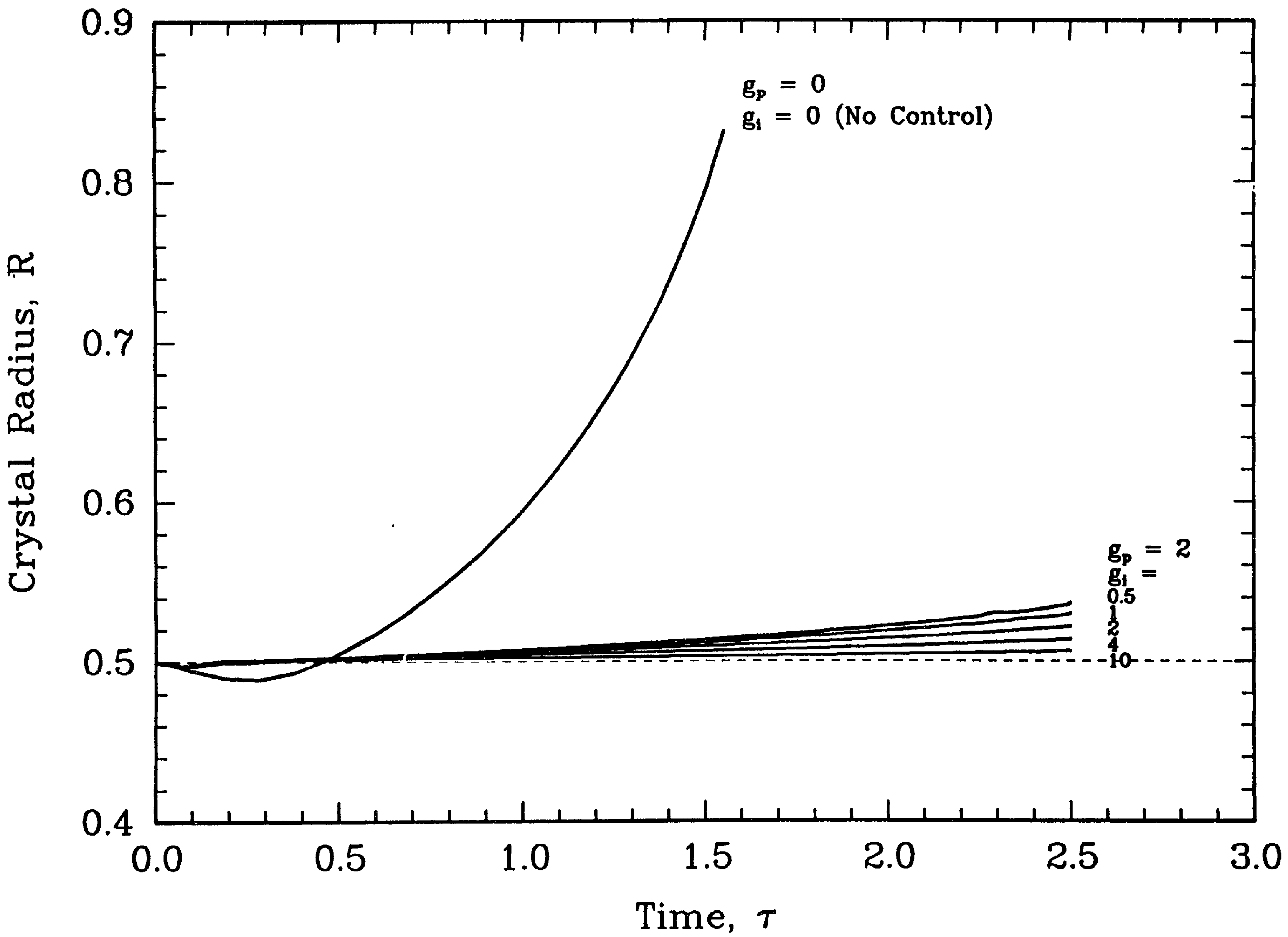

Fig. 5.34 Crystal radius at tri-junction as a function of time for fully transient batchwise growth simulations. Results of proportional-integral (PI) control strategies with different gain values are shown. Strategies use eq. (5.9) to adjust heater temperature in an attempt to maintain a constant crystal radius of R=0.5 throughout the run.

5.4.4 Quasi-Steady Processing Results

If the transient servo-controller employed in the fully transient calculations was effective in keeping the crystal radius near its set point value, the transient change in the heater temperature should follow the set points predicted by the processing calculations of the augmented quasi-steady-state model. This postulate was tested by performing calculations similar to those in Section 4.3 for this system using $R_{set}=0.5$ and adjusting heater temperature as a processing variable. Starting with the initial steady state, quasi-steady processing calculations were carried out for the crystal height $Z(\tau)$ and melt volume $V_m(\tau)$ values which follow the transient history which would characterize a batch run with a constant-diameter crystal.

The results of heater temperature as a function of time for these processing runs are plotted along with the continuous profile generated by the most successful control algorithm of the previous section ($g_p=2.0$, $g_i=10.0$) in Fig. 5.35. The initial wiggles in the controller-generated temperature history resulted from the mismatch in the initial solution and the batch-induced solidification rate of the melt/solid interface, as described previously in Section 5.3.2. The processing results fall near the transient curve but tend away from it as growth proceeds, with the final heater temperature value calculated for $\tau=2.5$ being approximately 2 percent too high. The pull rate used in the quasi-steady calculations was increased to match the melt/crystal interface growth rate by setting the batch-corrected pull rate $V_b^*=V_g$, calculated from eq. (5.4) with $V^*=1.0$ and $R=0.5$, and the results are shown in

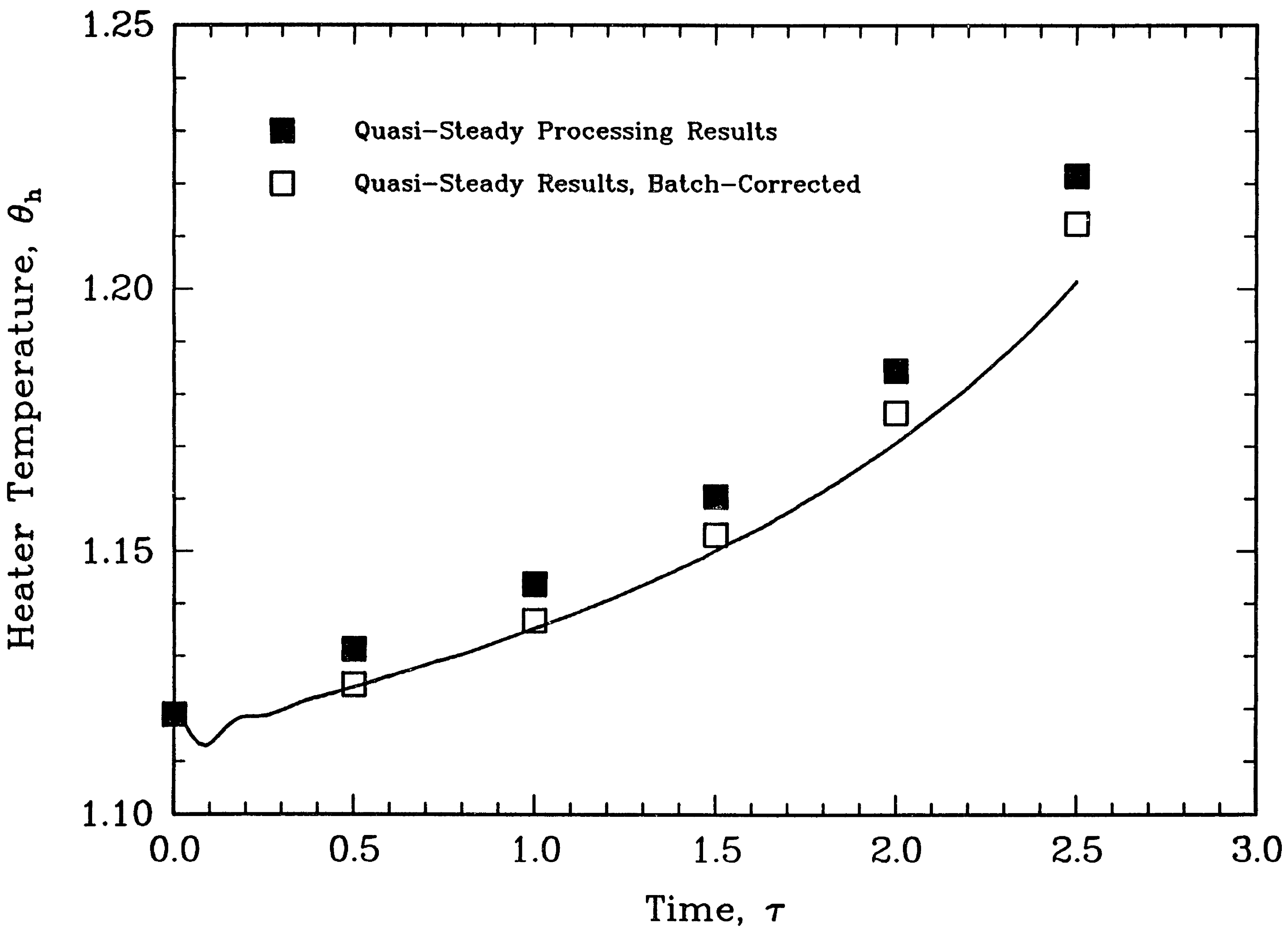

Fig. 5.35 Heater temperature as a function of time for fully transient batchwise growth simulation with PI control (g_p=2.0, g_i=10.0) compared with results obtained by quasi-steady processing calculations. Open squares denote processing calculations in which an approximate correction for the batch-induced increase in the melt/crystal interface growth rate was made. Solutions at selected times are shown for the transient simulation and the quasi-steady calculations in Figs. 5.36 and 5.37, respectively.

Fig. 5.35 as open squares. Although the batch-corrected heater temperatures fall closer to the transient curve, they still slightly over-predict the transient results.

Isotherms and interface shapes for selected points along the transient curve of Fig. 5.35 are shown in Fig. 5.36. The crystal radius remained quite constant for this transient simulation. The same points are represented with the quasi-steady solutions produced by the processing strategy calculations in Fig. 5.37 and are very similar to the solutions from the dynamic growth run. The results of this analysis indicate that the processing strategy calculations perform an adequate job of predicting the set point changes needed to control the batch transient process.

5.5 Discussion

The calculations performed in this chapter comprise the first comprehensive analysis of the inherent stability of the CZ process and the first fully transient simulation of Czochralski crystal growth. The results presented here show the power of the transient thermal-capillary model for determining the influence of process parameters on the evolution and control of crystal shape. The important conclusions drawn from the results of this chapter are discussed below.

Steady-state temperature fields and crystal shapes calculated for the idealized growth of silicon from a melt of constant volume and a long crystal are stable for a wide range of operating parameters. These operating conditions form a range which is bound by a locus

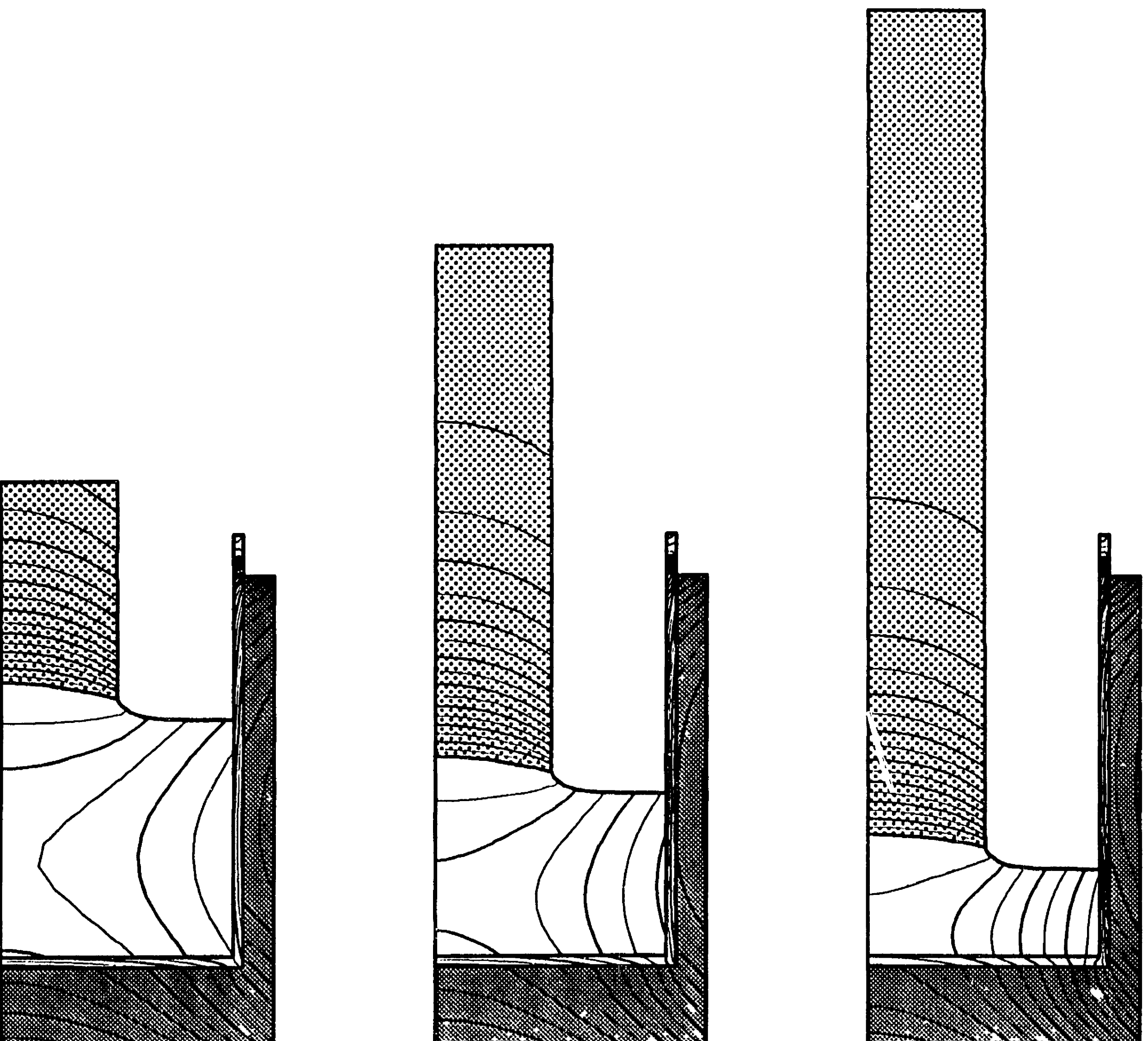

Fig. 5.36 Changes in isotherms and interface shapes with time for a fully transient CZ silicon batch growth simulation with effective PI control on heater temperature. Solutions correspond to the selected points along the solid curve of Fig. 5.35.

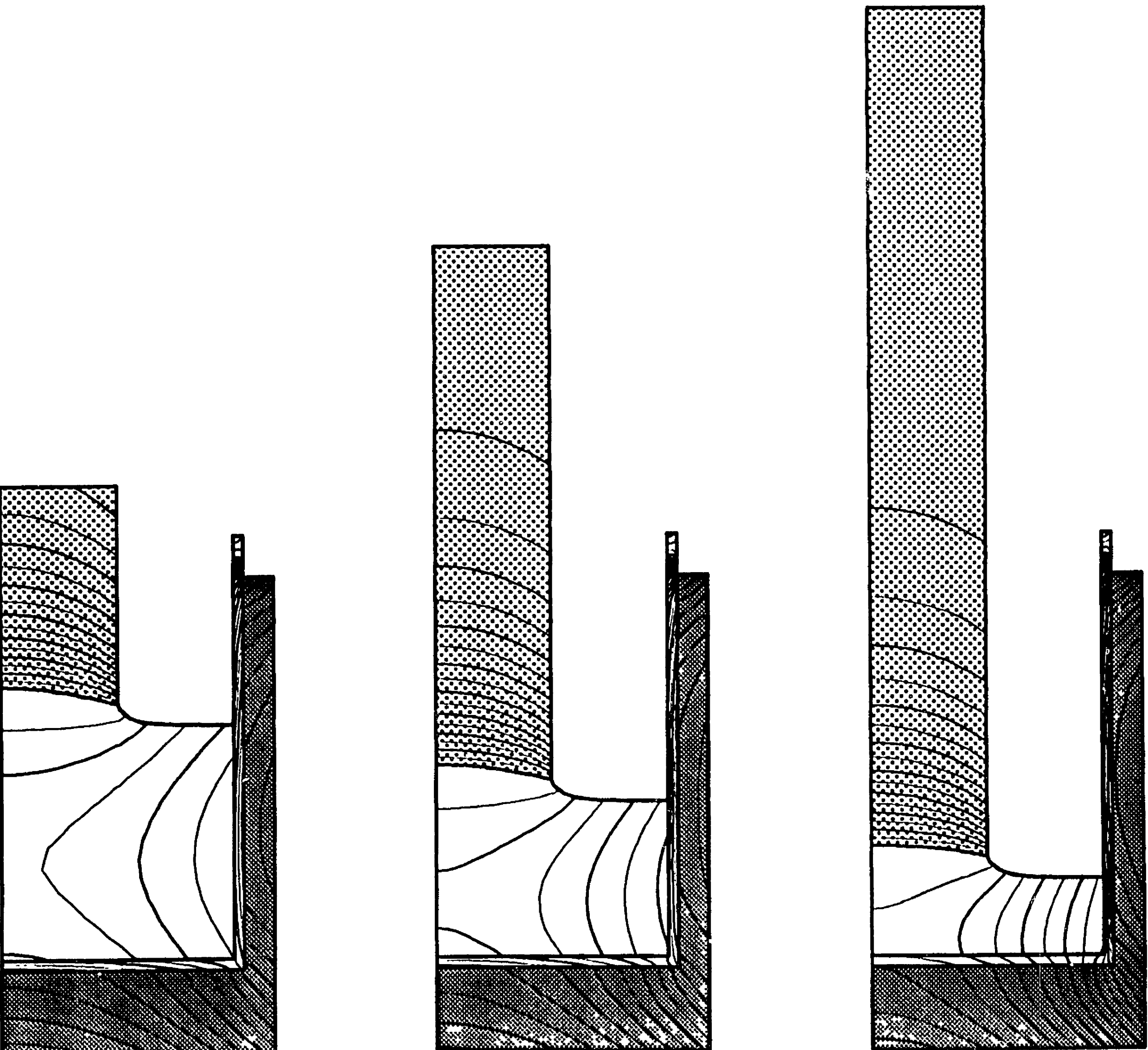

Fig. 5.37 Isotherms and interface shapes for the quasi-steady CZ silicon processing strategies calculated for crystal top position and melt volume corresponding to the batch growth time shown. Solutions are shown for the batch-corrected calculations at selected open squares plotted in Fig. 5.35.

that marks limit points in the steady-state operating curves; steady-state operation at parameter values beyond these critical values is not possible. In physical terms, these limit points mark operating states at which the rate of generation of latent heat at the solidifying interface exceeds that which can be removed by conduction through the crystal. These limit points have been calculated for changes in pull rate, heater temperature, and ambient temperature, but they are expected to exist for any parameter which influences the value of the steady-state crystal radius and the curvature of the melt/crystal interface.

The time constants obtained through linear stability analyses and the dynamic response of the full nonlinear model to finite-amplitude changes in operating parameters show that changes in crystal shape occur on a time scale which is long with respect to heat transfer in the system but short in comparison to the transients introduced by the batchwise nature of the CZ process. There are at least three disparate time scales in the system, a short time scale for heat conduction, a long transient caused by the dropping melt level with concomitant changes in the heat transfer environment, and an intermediate time scale corresponding to the meniscus-controlled changes in the shape of the crystal. Since the time scale for changes in the crystal shape is quite different from those associated with the heat transfer processes in the system, the details of convective heat transfer in the melt and radiation heat transfer caused batch-induced changes in geometry probably do not strongly affect the dynamics of crystal shape evolution calculated here.

Radius oscillations in CZ crystal growth arise due to two different phenomena. In low-gradient conditions, there are inherent oscillatory modes in the system, which were evident in the linear stability analyses, and these can affect the shape of the growing crystal, as shown in the nonlinear calculations for the system response to step changes in the crystal pull rate. Induced oscillations can be caused by an integral controller operating at a gain higher than some critical value, and the frequency of the radius oscillations is a function of the controller gain. Both of these situations can be understood as Hopf bifurcations from steady-state solution families. In the first case, the steady-state family is the uncontrolled, open-loop system and the relevant parameters are those which affect the temperature gradients in the system. For the controlled CZ process, the appropriate bifurcation parameter is the gain of the integral controller.

The processing strategies calculated by the augmented quasi-steady-state model for setting a constant radius with changes in the heater temperature closely matched the transient history of the heater temperature produced by successful servo-control in a fully transient simulation. These results justify the calculation of processing strategies a priori with the quasi-steady-state model and show that the resultant strategies mimic the time-dependent set points of the process parameters which vary continuously as the melt level slowly drops. This result is not surprising since the CZ system was determined to be inherently stable and is an example of the quasi-steady-state approximation successfully decoupling the short time scale for heat transfer from the longer transient caused by batchwise changes in the melt level.

Chapter 6. Final Remarks

The analytical and numerical tools needed to describe the CZ and LEC systems have been successfully developed in the thermal-capillary model described in this thesis. In mathematical terms alone, this is a significant accomplishment since this work represents one of the most sophisticated models ever put forth to solve an extremely complex moving-boundary problem. Although certain aspects of the problem were not addressed by the work presented here, specifically the details of radiative heat transfer and fluid flow, these aspects can be included in the framework developed for the solution of this model. Some important results obtained from the thermal-capillary model are reiterated below.

6.1 Quasi-Steady-State Results

The first modeling goal of this research was to better understand heat transfer and the effects of operating parameters on the temperature field in the crystal. This goal has been largely accomplished, with the exception of detailed radiative heat transfer effects, which are noted later in this discussion. Realistic temperature fields, interface shapes, and crystal radii have been efficiently calculated by the

quasi-steady-state thermal-capillary model. The response of the quasi-steady crystal radius to the crystal pull rate obtained from model calculations is well described by the experimental correlation of Kim et al. (1983), and the importance of other operating parameters on the quasi-steady temperature field in the CZ and LEC systems has been assessed through model predictions. Several crucial factors needed for the accurate description of the CZ and LEC systems have been identified, the most important being the interactions of capillarity and heat transfer through the shape of the melt meniscus. In quasi-steady calculations, the model proved sensitive to changes in the constant-diameter wetting angle Φ_0, and neglecting this angle by assuming flat interfaces produced markedly different modeling results.

The success in better understanding the physics involved in the CZ and LEC processes through the quasi-steady calculations is evident and, furthermore, the features which make the LEC growth of gallium arsenide much more difficult than the conventional CZ growth of silicon have been clarified. The difference in the thermal conductivity of the two crystals causes greater temperature gradients to occur in the LEC GaAs crystal during growth. This, coupled with the lower critical resolved shear stress of gallium arsenide (Jordan et al., 1980), facilitates the generation of crystalline defects caused by thermal stresses in the pulled boule. In addition, the radiative character of the B_2O_3 encapsulant strongly affects the heat transfer and interface shapes in the LEC growth system. The melt/crystal interface shapes calculated for an opaque encapsulant were very similar to those observed experimentally by Muller et al. (1983), and, for this case,

the geometrical interactions of the encapsulant volume and depth strongly affected heat transfer. This caused the system to be very sensitive to changes in other operating parameters which affected the system geometry and is probably one reason why LEC growth has proven much more difficult to control than CZ systems. It is not surprising that the extrapolation of CZ silicon technology to LEC GaAs growth has failed.

A method of understanding the system transients introduced by the batch nature of the process was introduced through the use of the augmented quasi-steady thermal-capillary model for the calculation of processing strategies as functions of melt volume, $V_m(\tau)$. In these calculations, different control strategies were assessed in a rational manner, and features of the growth system inaccessible through experimental observation, such as the shape of the melt/crystal interface, were monitored and controlled.

6.2 Stability and Transient Results

The second major objective of this work was to determine the inherent stability of the CZ process and to gain insight into the dynamic behavior of the system. This goal required understanding two major aspects of the problem which are associated with different time scales, the long-term batch transients of the system and the time scales inherent in crystal shape evolution.

The inherent stability of the system and the dynamics of crystal shape evolution could not be assessed through the quasi-steady model.

A transient analysis of CZ silicon growth discovered that the process is inherently stable, in contrast to many previous results (Surek, 1976; Crowley, 1983) and against the intuition of many practitioners of CZ growth. Unstable operating conditions do exist, however, and there are regions in parameter space where no quasi-steady solutions are found, as shown by the calculation of limit points for the radius-pull rate operating curves. In addition, there is evidence from the linear stability analysis that oscillatory modes exist in the system.

These inherent oscillatory responses to disturbances imposed on the system were observed for small crystals in low-gradient growth simulations. The parallels between the oscillations observed in the low-gradient CZ silicon simulation and those observed experimentally in low-gradient LEC gallium arsenide systems are revealing. In Fig. 6.1, the silicon crystal shape obtained by simulation of a step decrease in pull rate, such as might occur in the transition from seed to full crystal, is compared with a photograph of gallium arsenide crystals grown by LEC under low gradient conditions by Elliot et al. (1984). Although the length scales and materials differ, the crystal shapes are similar, and the oscillations in both systems may have a common origin. For the first time, oscillations in crystal shape similar to those observed experimentally have been achieved in model calculations (Jordan et al., 1983; Elliot et al., 1984).

The transient thermal-capillary model also served as a vehicle to examine the dynamics associated with the batch nature of the CZ and LEC processes and controller-induced phenomena. There was a significant effect on the solidification rate of the melt/crystal interface

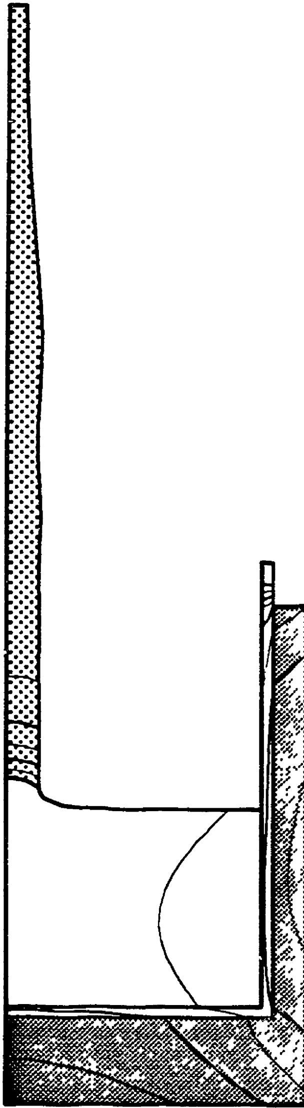

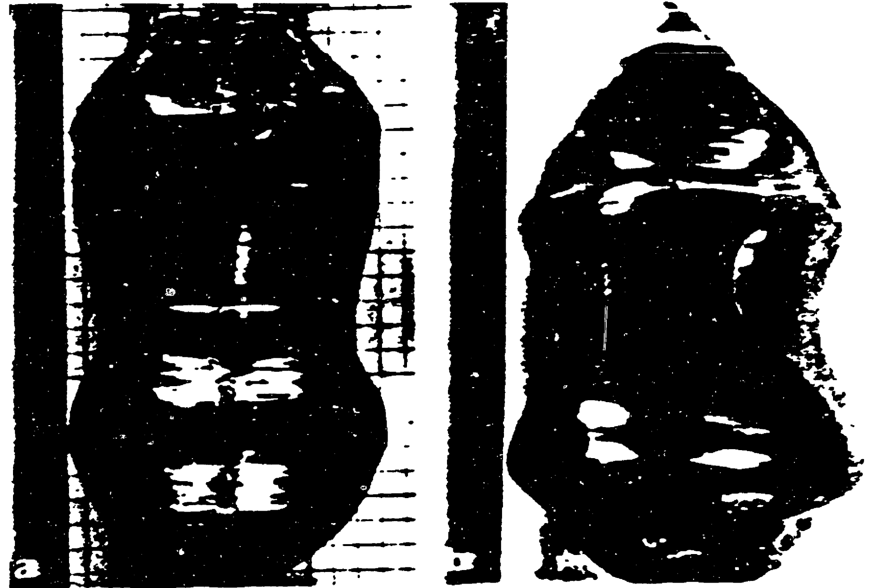

Fig. 6.1 Comparison of crystal shape resulting from transient simulation of CZ silicon growth under low temperature gradient conditions to experimentally grown gallium arsenide by LEC method under similar conditions (Elliot et al., 1984). Undulating crystal shapes caused by inherent oscillatory responses in system are seen.

caused by the batchwise decrease of melt volume in time, and this caused the radius predicted by the quasi-steady-state model to be much greater than that obtained in the transient simulation of batch growth. Proportional (P) control was fairly effective for maintaining a constant-diameter radius through a batch simulation, but proportional-integral (PI) control produced the best results. An integral (I) servo-controller caused macroscopic oscillations in the shape of the crystal which were similar to those reported by experimental investigators. A crystal shape obtained from the batch simulation with integral control is shown with photographs of two CZ-grown germanium crystals, one of which exhibits controller-induced radius oscillations (Bardsley et al., 1977b), in Fig. 6.2. The crystal materials and the length scales differ in this comparison, but the fundamental phenomena which produce these crystal shapes are qualitatively the same for both the simulation and the experimental system.

Another conclusion drawn from the controlled batch simulations was that the processing strategies calculated by the augmented quasi-steady-state thermal-capillary model were virtually the same as those produced by a successfully controlled transient system. In this situation, where the crystal radius is relatively constant through the growth run, the quasi-steady assumption is valid and can be successfully exploited to decouple the short heat transfer time scale from the long time scale of the batch transients in the system. The processing strategy calculations are valid and can be used to predict, a priori, actions needed to produce desired features in CZ and LEC growth.

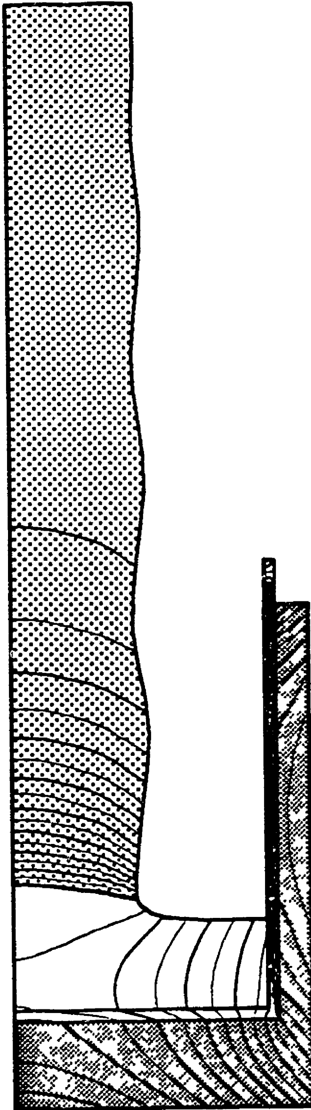

From Fig. 5.29

BARDSLEY et al. (1977)
Royal Signals and Radar Establishment

Fig. 6.2 Crystal resulting from a transient simulation of batchwise CZ silicon growth using an integral controller and an experimentally grown CZ germanium crystal in a system exhibiting servo-loop instability (Bardsley et al., 1977b)). Oscillating crystal radius in both systems is the result of controller-induced dynamics.

6.3 Future Research Directions

Although this work has succeeded in qualitative and semi-quantitative modeling of the CZ and LEC systems and has shed light on the fundamental interactions of heat transfer and capillarity, further efforts are needed to quantitatively describe these systems. After the development of a quantitative model, the direct influence of system design and process control is possible. There are two major areas which need to be addressed in future modeling efforts, radiative heat transfer and fluid mechanics.

6.3.1 Radiation

Radiation is the predominant heat transfer mechanism in the CZ and LEC systems. A quantitative approach to modeling radiative exchange among all surfaces in the system calls for the application of enclosure theory to the crystal and melt surfaces and all surrounding system surfaces (Wouters, 1985; Ramachandran and Dudukovic, 1985). Development of the thermal-capillary model presented here is currently under way to include these effects (see Atherton et al., 1986).

A major complication in the quantitative modeling of the LEC system is the accurate accounting of radiative heat transfer in the encapsulant layer. More experimental work is needed to experimentally characterize radiation in molten B_2O_3, and this knowledge must be incorporated into heat transfer models. The importance of this knowledge is pointed out by the dramatic changes in heat transfer which occur

for the limiting cases of radiatively transparent and opaque encapsulant layers, as shown by the calculations of Chapter 4.

6.3.2 Fluid Flow

The calculation of fluid flow is necessary if mass transfer in the melt and the resultant distribution of solutes in the crystal is desired. Flows in the melt and encapsulant are also required to quantitatively model heat transfer in the CZ and LEC systems, especially large-scale systems (crucible radius ~10cm or larger) where buoyancy-driven convection is a major component of heat transfer in the melt. This limitation could be addressed by including detailed fluid dynamic calculations, yet even though the formulation of the complete problem with fluid flow is straightforward, the computational aspects are overwhelming. The increase in the number of unknowns in the equation set increases by a factor of four to five with the addition of velocity and pressure variables at every node in the melt, and the number of elements required to resolve the flow is much greater than needed to solve for the temperature field due to the complex structure of the thermally-driven flows of low Prandtl number fluids. These aspects were addressed in the steady-state modeling of intense laminar flows in semiconductor melts of the Bridgman-Stockbarger crystal growth system by Adornato (1986).

However, much information about overall heat transfer and crystal shape evolution can be obtained from the conduction-dominated model. The time scales for macroscopic geometrical changes, such as crystal

shape variation during growth, are found in model calculations to be much longer than the time scale for thermal transients in the system. In this case, the details of heat transfer in the melt may not strongly affect the dynamics of macroscopic crystal shape evolution.

An issue which is not yet resolved is the importance of heat transfer caused by chaotic or turbulent flows in the melt on the inherent stability of the CZ and LEC systems and on the dynamics of crystal shape evolution. It is well known that this type of convective heat transfer affects the dynamics of the melt/crystal interface (Carruthers and Witt, 1975; Kim et al., 1972; Hurle, 1983). However, a comprehensive simulation which couples the macroscopic aspects of crystal shape determination, as is done here, with the microscopic details of these phenomena is probably beyond the computational capabilities of any computer in use today.

6.4 Postscript

The ultimate objective of this research was the quantitative description of the CZ and LEC systems. This ambitious objective has not been attained, but some degree of success has been achieved through the qualitative or near-quantitative modeling results of the thermal-capillary model. This partial success cannot be viewed as a failure since much insight into the workings of the real systems have been obtained, and the results calculated here can lend direction to the solution of specific problems or toward attaining desired objectives in experimental systems. In the following abbreviated recommendations,

we attempt to spell out the significance of the results of this research to practitioners of the "art and science" of Czochralski and liquid encapsulated Czochralski crystal growth of semiconductors.

1) Capillarity is a crucial component in determining the behavior of the CZ and LEC systems. The importance of this statement is not obvious since only changes in heat transfer are accessible through the manipulation of operating parameters, such as pull rate and heater power, in experimental systems. However, this important piece of physics should be emphasized for the following reasons. Intuitive notions about heat transfer in one dimension will lead to great error in describing the two-dimensional interaction of the temperature filed with the meniscus shape. This was shown in the results presented in Chapter 4 for the quasi-steady crystal radius as a function of pull rate where the one-dimensional analysis of Billig (1955) failed to accurately describe the behavior of the system. In addition, the meniscus-controlled nature of CZ and LEC growth leads to time scales for crystal shape changes which are much longer than those associated with heat transfer, as pointed out in the linear stability and transient analyses of Chapter 5. Experimental control of crystal shape relies on understanding the time scales of several phenomena, as is discussed in item 4.

2) The encapsulant rules in LEC growth. Based on the calculations of Chapter 4 and the assumption that the radiative character of the encapsulant is very nearly opaque, as is consistent with the experimental results of Muller et al. (1983) for interface shape and the results of Jordan (1984) for temperature gradients in the encapsulant layer, the thickness of the encapsulant layer predominantly influences the behavior of the system. The results calculated for an opaque encapsulant are so totally different from those with a transparent encap-

sulant and from those for CZ growth that LEC should be considered a fundamentally different growth process as far as heat transfer is concerned, and intuition or rules-of-thumb developed from experience with CZ growth should be viewed with much caution when using the LEC method.

3) The CZ process is inherently stable. If batch effects could be eliminated from the CZ process, the resulting continuous-growth process would be stable, and the diameter of the crystal would tend to self-correct in response to disturbances to the system.

4) The CZ process is a batch process. Until features such as automatic melt replenishment are developed and put into practice, the practical crystal grower must contend with the transient nature of a batch system for CZ and LEC growth. However, the situation should not be viewed as hopeless since, as noted above, the process is inherently stable. One must understand at least three differing time scales in the system. Changes in heat transfer occur over a relatively short time scale, on the order of a few minutes. Crystal shape evolution occurs on a time scale determined by the rate at which the meniscus shape responds to changes imposed by altering the heat transfer in the system, and this depends on capillarity, as discussed in item 1 above. This time scale is on the order of an hour. Batch transients occur in the system and the overall heat transfer environment as the melt level drops, occurring on the time scale of several hours.

5) Oscillations in crystal shape are produced by two fundamentally different mechanisms. As pointed out by the transient calculations of Chapter 5, oscillations in the shape of a growing crystal are caused either by an inherent oscillatory response to a disturbance in the system or from dynamics

introduced by a controller. The inherent system oscillations are only observed when the overall temperature gradients in the system are small, such as might occur in the growth of low-dislocation GaAs boules by the LEC method. Controller-induced oscillations may arise in any situation when an integral controller is used.

Major advances in modeling and understanding the Czochralski and liquid encapsulated Czochralski processes have been achieved through this work. In addition, the groundwork for future models which can address the shortcomings of this work have been laid. In this sense, the major objectives of this research have been fulfilled.

References

Adornato, P.M., 1986, Ph.D. thesis, Department of Chemical Engineering, Massachusetts Institute of Technology, Cambridge, Massachusetts.

Arizumi, T. and N. Kobayashi, 1969, The solid-liquid interface shape during crystal growth by the Czochralski method, Jap. J. Appl. Phys. 8(9), 1091-1097.

Arizumi, T. and N. Kobayashi, 1972, Theoretical studies of the temperature distribution in a crystal being grown by the Czochralski method, J. Crystal Growth **13/14**, 615-618.

Arthur, J.R., 1967, Vapor pressures and phase equilibria in the Ga-As system, J. Phys. Chem. Solids **28**, 2257-2267.

Atherton, L.J., J.J.Derby, and R.A. Brown, 1986, Radiative heat exchange in Czochralski crystal growth, J. Crystal Growth, in preparation.

AuCoin, T.R., R.L. Ross, M.J. Wade, and R.O. Savage, 1979, Liquid encapsulated compounding and Czochralski growth of semi-insulating gallium arsenide, Solid State Tech. January, 59-62,67.

Bachmann, K.J., H.J. Kirsch, and K.J. Vetter, 1970, Programmed Czochralski growth of metals, J. Crystal Growth **7**, 290-295.

Bardsley, W., F.C. Frank, G.W. Green, and D.T.J. Hurle, 1974, The meniscus in Czochralski growth, J. Crystal Growth **23**, 341-344.

Bardsley, W., D.T.J. Hurle, and G.C. Joyce, 1977a, The weighing method of automatic Czochralski crystal growth I. Basic theory, J. Crystal Growth **40**, 13-20.

Bardsley, W., D.T.J. Hurle, G.C. Joyce, and G.C. Wilson, 1977b, The weighing method of automatic Czochralski crystal growth II. Control equipment, J. Crystal Growth **40**, 21-28.

Bell, A.E., 1977, Thermal analysis of single-crystal silicon ribbon growth processes, RCA Rev. **38**, 109-138.

Berzhatyy, V.I. and F.F. Lezhenin, 1973, Study of thermal conductivity of boric oxide, Fl. Mech-Sov. Res. 2(1), 123-126.

Billig, E., 1955, Growth of monocrystals of germanium from an undercooled melt, Proc. R. Soc. Lond. A. **229**, 346-363.

Bird, R.B., W.E. Stewart, and E.N. Lightfoot, 1960, Transport Phenomena, John Wiley & Sons, Inc., New York.

Boomgaard, J. van den, and K. Schol, 1957, The P-T-x phase diagrams of the systems In-As, Ga-As and In-P, Philips Res. Rep. **12**, 127-140.

Borodin, V.A., L.B. Davidova, V.N. Erofeev, A.V. Shdanov, S.A. Startsev, and V.A. Tatarchenko, 1979, The effect of the solidification front shape on the temperature distribution in the crystal, J. Crystal Growth **46**, 757-762.

Boucher, E.A. and H.J. Kent, 1977, Capillary phenomena III. Properties of rotationally symmetric fluid bodies with one asymptote — holms, Proc. R. Soc. Lond. A **356**, 61-75.

Bourret, E.D., J.J. Derby, and R.A. Brown, 1985, Dynamics of Bridgman-Stockbarger growth of non-dilute binary alloys, J. Crystal Growth **71**, 587-596.

Brice, J.C., 1968, Analysis of the temperature distribution in pulled crystals, J. Crystal Growth **2**, 395-401.

Brooks, A.N. and T.J.R. Hughes, 1982, Streamline upwind/Petrov-Galerkin formulations for convection dominated flows with particular emphasis on the incompressible Navier-Stokes equations, Comput. Meths. Appl. Mech. Engrg. **32**, 199-259.

Brown, R.A., L.E. Scriven, and W.J. Silliman, 1980, Computer-aided analysis of nonlinear problems in transport phenomena, New Approaches to Nonlinear Problems in Dynamics, ed. by P.J. Holmes, SIAM, Philadelphia.

Buckley-Golder, I.M. and C.J. Humphreys, 1979, A theoretical study of temperature distributions during Czochralski crystal growth, Phil. Mag. A **39**(1), 41-57.

Burmeister, R.A., 1983, GaAs Technology: A Perspective, during Workshop on the Electronic Materials Program, Lawrence Berkeley Laboratory, Berkely, CA (October 10-12).

Carslaw, H.S. and J.C. Jaeger, 1947, Conduction of Heat of Solids, first edition, Oxford University Press, Amen House, London.

Carruthers, J.R., 1967, Radial solute segregation in Czochralski growth, J. Electrochem. Soc. **114**(9), 959-962.

Carruthers, J.R., 1976, Flow transitions and interface shapes in the Czochralski growth of oxide crystals, J. Crystal Growth **36**, 212-214.

Carruthers, J.R., 1977, Thermal convection instabilities relevant to crystal growth from liquids, Preparation and Properties of Solid State Materials, Vol. 3, ed. by W.R. Wilcox and R.A. Lefever, Marcel Dekker, New York.

Carruthers, J.R., 1983, GaAs Bulk Crystal Growth, Workshop on the Electronics Materials Program, Lawrence Berkeley Laboratory, Berkely, CA (October 10-12), 7-9.

Carruthers, J.R. and K. Nassau, 1968, Nonmixing cells due to crucible rotation during Czochralski crystal growth, J. Appl. Phys. **39**(11), 5205-5214.

Carruthers, J.R. and A.F. Witt, 1975, Transient segregation effects in Czochralski growth, Crystal Growth and Characterization, ed. by R. Ueda and J.B. Mullin, North-Holland Publishing Company, Amsterdam.

Chang, C.J., 1982, A study of natural convection and its effects on melt crystal growth, Ph.D. thesis, Department of Chemical Engineering, Massachusetts Institute of Technology, Cambridge, Massachusetts.

Chang, C.J. and R.A. Brown, 1983a, Finite element calculations of buoyancy-driven convection near a melt/solid phase boundary, Numerical Properties and Methodologies in Heat Transfer, ed. by T.M. Shih, Hemisphere Publishing Corporation, Washington.

Chang, C.J. and R.A. Brown, 1983b, Radial segregation induced by natural convection and melt/solid interface shape in vertical Bridgman growth, J. Crystal Growth **63**, 343-364.

Chang, H. and L. Chen, 1984, Bifurcation characteristics of nonlinear systems under conventional PID control, Chem. Eng. Sci. **39**(7/8), 1127-1142.

Ciszek, T.F., 1976, Maximum growth rates for melt-grown ribbon-shaped crystals, J. Appl. Phys. **47**(2), 440-442.

Cockayne, B., B. Lent, and J.M. Roslington, 1976, Interface shape changes during the Czochralski growth of gadolinium gallium garnet single crystals, J. Mater. Sci. **11**, 259-263.

Cole, M., R.M. Ware, and M.A. Whitaker, 1976, presentation at ECCG-1, Zurich.

Coughanowr, D.R. and L.B. Koppel, 1965, Process Systems Analysis and Control, McGraw-Hill, New York.

Crochet, M.J., P.J. Wouters, F.T. Geyling, and A.S. Jordan, 1983, Finite-element simulation of Czochralski bulk flow, J. Crystal Growth **65**, 153-165.

Crowley, A.B., 1983, Mathematical modelling of heat flow in Czochralski crystal pulling, IMA J. Appl. Math. **30**, 173-189.

Czochralski, J., 1917, Ein neues verfahren zur messung der kristallisationsgeschwindigkeit der metalle, (in German), Z. Physik. Chemie **92**, 219-221.

Dahlquist, G. and A. Bjorck, 1974, Numerical Methods, translated by N. Anderson, Prentice-Hall, Inc., Englewood Cliffs, New Jersey.

Dash, W.C., 1959, Growth of silicon crystals free from dislocations, J. Appl. Phys. **30**, 459-474.

Denn, M.M., 1975, Stability of Reaction and Transport Processes, Prentice-Hall, Inc., Englewood Cliffs, New Jersey.

Derby, J.J. and R.A. Brown, 1986a, A fully implicit method for simulation of the one-dimensional solidification of a binary alloy, Chem. Eng. Sci. **41**(1), 37-46.

Derby, J.J. and R.A. Brown, 1986b, Thermal-capillary analysis of Czochralski and liquid encapsulated Czochralski crystal growth: 1. Simulation, J. Crystal Growth in press.

Derby, J.J. and R.A. Brown, 1986c, Thermal-capillary analysis of Czochralski and liquid encapsulated Czochralski crystal growth: 2. Processing Strategies, J. Crystal Growth in press.

Derby, J.J. and R.A. Brown, 1986d, Dynamic analysis of Czochralski crystal growth, AIChE J. submitted.

Derby, J.J., R.A. Brown, F.T. Geyling, A.S. Jordan, and G.A. Nikolakopoulou, 1985, Finite elemnt analysis of a thermal-capillary model for liquid encapsulated Czochralski growth, J. Electrochem. Soc. **132**, 470-482.

Duseaux, M., 1983, Temperature profile and thermal stress calculations in GaAs crystals growing from the melt, J. Crystal Growth **61**, 576-590.

Elliot, A.G., 1984, private communication.

Elliot, A.G., C. Wei, R. Farraro, G. Woolhouse, M. Scott, and R. Hiskes, 1984, Low dislocation density, large diameter, liquid encapsulated Czochralski growth GaAs, J. Crystal Growth **70**, 169-178.

Ettouney, H.M., 1983, Heat, Mass and Momentum Transfer in Edge-Defined Film-Fed Crystal Growth, Ph.D. thesis, Department of Chemical Engineering, Massachusetts Institute of Technology, Cambridge, Massachusetts.

Ettouney, H.M., J.P. Kalejs, and R.A. Brown, 1984, Comparison of finite element calculations and experimental measurements in edge-defined film-fed growth of silicon sheets, J. Crystal Growth **70**, 306-313.

Ettouney, H.M. and R.A. Brown, 1983, Finite-element methods for steady solidification problems, J. Comp. Phys. **49**, 118-150.

Finlayson, B.A., 1972, The Method of Weighted Residuals and Variational Principles, Academic Press, New York.

Finlayson, B.A., 1980, Nonlinear Analysis in Chemical Engineering, McGraw-Hill, New York.

Foster, L.M., 1977, The preparation of III-V semiconductor alloys, Preparation and Properties of Solid State Materials, Vol. 3, ed. by W.R. Wilcox and R.A. Lefever, Marcel Dekker, New York.

Francis, J.G.F., 1961-62, The QR transformation—a unitary analogue to the LR transformation, Comput. J. 4, 265-271, 332-345.

Gallagher, R.H., J.T. Oden, C. Taylor, and O.C. Zienkiewicz, editors, 1975, Finite Elements in Fluids, vols. 1-3, John Wiley & Sons, London.

Gear, C.W., 1971a, Numerical Initial Value Problems in Ordinary Differential Equations, Prentice-Hall, Inc., Englewood Cliffs, New Jersey.

Gear, C.W., 1971b, Simultaneous numerical solution of differential-algebraic equations, IEEE Trans. Circuit Theory **CT-18**, 89-95.

Ghandhi, S.K., 1983, VLSI Fabrication Principles, John Wiley & Sons, New York.

Glazov, V.M., S.N. Chizhevskaya, and N.N. Glagoleva, 1969, Liquid Semiconductors, Plenum Press, New York.

Gresho, P.M., R.L. Lee, and R.L. Sani, 1980, On the time-dependent solution of the incompressible Navier-Stokes equations in two and three dimensions, Recent Advances in Numerical Methods in Fluids, Vol. 1, ed. by C. Taylor and K. Morgan, Pineridge Press, Swansea, 27-81.

Gaule, G.K. and J.R. Pastore, 1961, in Metallurgy of Elemental and Compound Semiconductors, ed. by R. Grubel, Interscience, New York.

Herring, C., 1951, The Physics of Powder Metallurgy, ed. by W.E. Kingston, McGraw-Hill, New York.

Hughes, T.J.R. and T.E. Tezduyar, 1984, Finite element methods for first-order hyperbolic systems with particular emphasis on the compressible Euler equations, Comput. Meths. Appl. Mech. Engrg. **45**, 217-284.

Hurle, D.T.J., 1977, Control of diameter in Czochralski and related crystal growth techniques, J. Crystal Growth **42**, 473-482.

Hurle, D.T.J., 1983, Convective transport in melt growth systems, J. Crystal Growth **65**, 124-132.

Iooss, G. and D.D. Joseph, 1980, Elementary Stability and Bifurcation Theory, Springer-Verlag, New York.

Jackson, K.A. and D.A. Kurtze, 1985, Instability in radiatively melted silicon films, J. Crystal Growth **71**, 385-390.

Jasinski, T.J., W.M. Rohsenow, and A.F. Witt, 1983, Heat transfer analysis of the Bridgman-Stockbarger configuration for crystal growth. Part I. Analytical treatment of the axial temperature distribution, J. Crystal Growth **61**, 339.

Johnson, C., U. Navert, and J. Pitkaranta, 1984, Finite element methods for linear hyperbolic problems, Comput. Meths. Appl. Mech. Engrg. **45**, 285-312.

Jordan, A.S., 1980, An evaluation of the thermal and elastic constants affecting GaAs crystal growth, J. Crystal Growth **49**, 631-642.

Jordan, A.S., 1985, Estimated thermal diffusivity, Prandtl number and Grashof number of molten GaAs, InP, and GaSb, J. Crystal Growth **71**, 551-558.

Jordan, A.S., 1984, personal communication at ACCG-6/ICVGE-6, Atlantic City, NJ.

Jordan, A.S., R. Caruso, and A.R. Von Neida, 1980, A thermoelastic analysis of dislocation generation in pulled GaAs crystals, Bell System Tech. J. **59**(4), 593-637.

Jordan, A.S., R. Caruso, and A.R. Von Neida, 1983, An analysis of the derivative weight-gain signal from measured crystal shape: Implications for diameter control of GaAs, Bell System Tech. J. **62**(2), 477-498.

Kalejs, J.P., H.M. Ettouney, and R.A. Brown, 1983, Comparison of growth characteristics of sapphire and silicon ribbon produced by EFG, J. Crystal Growth **65**, 316-323.

Kashkooli, I.Y., Z.A. Munir, and L. Williams, 1974, The influence of substrate characteristics on the contact angles between liquid gallium and gallium arsenide crystals, J. Mater. Sci. **9**, 538-542.

Kim, K.M., A. Kran, P. Smetana, and G.H. Schwuttke, 1983, Computer simulation and controlled growth of large diameter Czochralski silicon crystals, J. Electrochem. Soc. **130**(5), 1156-1160.

Kim, K.M., A.F. Witt, and H.C. Gatos, 1972, Crystal growth from the melt under destabilizing thermal gradients, J. Electrochem. Soc. **119**(9), 1218-1226.

Kobayashi, N., 1978, Computational simulation of the melt flow during Czochralski growth, J. Crystal Growth **43**, 357-363.

Kobayashi, N., 1981, Heat transfer in Czochralski crystal growth, Preparation and Properties of Solid State Materials, Vol. 6, ed. by W.R. Wilcox, Marcel Dekker, Inc., New York, 119-253.

Kobayashi, N. and T. Arizumi, 1970a, The numerical analyses of the solid-liquid interface shapes during the crystal growth by the Czochralski method, Jap. J. Appl. Phys. **9**(4), 361-367.

Kobayashi, N. and T. Arizumi, 1970b, The numerical analyses of the solid-liquid interface shapes during the crystal growth by the Czochralski method Part II. Effects of crucible rotation, Jap. J. Appl. Phys. **9**(10), 1255-1259.

Kuo, V.H.S., and W.R. Wilcox, 1972, Influence of crystal dimensions on the interfacial temperature gradient, J. Crystal Growth **12**, 191-194.

Lamprecht, R., D. Schwabe, A. Scharmann, and E. Schultheiss, 1983, Experiments on buoyant, thermocapillary, and forced convection in Czochralski configuration, J. Crystal Growth **65**, 143-152.

Landau, H.G., 1950, Heat conduction in a melting solid, Quart. Appl. Math. **8**, 81-94.

Langlois, W.E., 1980, Digital simulation of Czochralski bulk flow in microgravity, J. Crystal Growth **48**, 25-28.

Langlois, W.E., 1981, Convection in Czochralski growth melts, Physicochem. Hydrodynamics 2(4), 245-261.

Langlois, W.E. and C.C. Shir, 1977, Digital simulation of flow patterns in the Czochralski crystal pulling process, Comput. Meths. Appl. Mech. Engrg. 12, 145-152.

Levinson, J., 1959, U.S. Patent No. 2,908,004 (October 6, 1959).

Lorenzini, R.E., F.S. Neff, D.J. Blair, 1974, An overview of silicon crystal growing processes, Solid State Tech. February, 33-36,55.

Lynch, D.R., 1982, Unified approach to simulation on deforming elements with application to phase change problems, J. Comp. Phys. **47**(3), 387-411.

Lynch, D.R. and J.M. Sullivan, 1985, Heat conservation in deforming element phase change simulation, J. Comp. Phys. **57**(2), 303-317.

Matsumoto, K., H. Morishita, M. Sasaki, S. Nishine, M. Yokogawa, M. Sekinobu, K. Tada, and S. Akai, 1984, Proceedings of the Semi-insulating III-V Materials Conference, Kah-nee-tah, WA, ed. by D.C. Look, G.S. Blakemore, Shiva Publishing, Ltd.

Metz, E.P.A., R.C. Miller, and R. Mazelsky, 1962, A technique for pulling single crystals of volatile materials, J. Appl. Phys. **33**(6), 2016-2017.

Mihelcic, M., C. Schrock-Pauli, K. Wingerath, H. Wenzl, W. Uelhoff, and A. Van der Hart, 1982, Numerical simulation of free and forced convection in the classical Czochralski method and in CACRT, J. Crystal Growth **57**, 300-317.

Mika, K. and W. Uelhoff, 1975, Shape and stability of menisci in Czochralski growth and comparison with analytical approximations, J. Crystal Growth **30**, 9-20.

Mil'vidskii, M.G. and B.I. Golovin, 1961, The from of the crystallization front in semiconducting single crystals grown from the melt by the Czochralski method, Soviet Physics-Solid State 3(4), 737-739.

Moler, C.B. and G.W. Stewart, 1973, An algorithm for generalized matrix eigenvalue problems, SIAM J. Numer. Anal. **10**(2), 241-256.

Muller, G. and G. Neumann, 1983, Tenfold growth rates in the travelling heater method of GaSb crystals by forced convection on a centrifuge, J. Crystal Growth **63**, 58-66.

Muller, G., J. Volkl, and E. Tomzig, 1983, Thermal analysis of LEC InP growth, J. Crystal Growth **64**, 40-47.

Nanishi, Y., S. Ishida, T. Honda, H. Yamazaki, and S. Miyazawa, 1982, Inhomogeneous GaAs FET threshold voltages related to dislocation distribution, Jap. J. Appl. Phys. **21**(6), L335-L337.

Neuberger, M., editor, 1971, III-V semiconducting compounds, Handbook of Electronic Materials, Volume 2, IFI/Plenum, New York, NY, 45-63.

Patzner, E.J., R.G. Dessauer, and M.R. Poponiak, 1967, Automatic diameter control of Czochralski crystals, SCP and Solid State Tech. **10**(10), 25-30.

Patera, A.T. and A.V. Tangborn, 1986, Direct numerical simulation of bulk flow in Czochralski crystal growth, SIAM Fall Meeting, October 28-30, Arizona State University, Tempe, Arizona.

Peters, G. and J.H. Wilkinson, 1970, Eigenvectors of real and complex matrices by LR and QR triangularizations, Numer. Math. **16**, 181-204.

Petzold, L., 1982, Differential/algebraic equations are not ODE's, SIAM J. Sci. Stat. Comput. 3(3), 367-384.

Ramachandran, P.A., and M.P. Dudukovic, 1985, Simulation of temperature distributions in crystals grown by Czochralski method, J. Crystal Growth **71**, 399-408.

RASA Industries, Ltd., 1981, Technical Brochure, Tokyo, Japan.

Raymond, W.H. and A. Garder, 1976, Selective damping in a Galerkin method for solving wave problems with variable grids, Monthly Weather Rev. **104**, 1583-1590.

Rea, S.N., 1981, Czochralski silicon pull rate limits, J. Crystal Growth **54**, 267-274.

Richman, D., 1963, Dissociation pressures of GaAs, GaP and InP and the nature of III-V melts, J. Phys. Chem. Solids **24**, 1131-1139.

Robertson, D.S. and I.M. Young, 1975, Observations on the unrestrained growth of germanium crystals, J. Phys. D: Appl. Phys. **8**, L59-L61.

Robinson, A.L., 1983, GaAs readied for high-speed microcircuits, Science **219**, 275-277.

Rode, A.G. and J.G. Roper, 1985, Gallium Arsenide digital IC processing — a manufacturing perspective, Solid State Tech. February, 209-215.

Rosenberger, F., 1979, Fundamentals of Crystal Growth I Macroscopic Equilibrium and Transport Concepts, Springer-Verlag, Berlin.

Saito, H.L. and L.E. Scriven, 1981, Study of coating flow by the finite element method, J. Comput. Phys. **42**, 53-76.

Schmaker, P., A. Kramer, and W. Stahlin, 1976, presentation at EECG-1, Zurich.

Schwabe, D., 1981, Marangoni effects in crystal growth melts, Physicochem. Hydrodynamics 2(4), 263-280.

Shpil'rain, E.E., K.A. Yakimovich, and A.F. Tsitsarkin, 1972, Investigation of the surface tension of liquid boron oxide to 2000°C by the cylinder pulling method, High Temp.-High Press. **4**, 67-76.

Shpil'rain, E.E., K.A. Yakimovich, A.F. Tsitsarkin, D.N. Kagan, L.S. Barkhatov, V.A. Fomin, and Y.U. Tsigenkhagen, 1974, Comprehensive investigation of the thermophysical properties of molten boron oxide, Fl. Mech-Sov. Res. **3**(4), 29-36.

Srivastava, R.K., P.A. Ramachandran, and M.P. Dudukovic, 1985, Interface shape in Czochralski grown crystals: Effect of conduction and radiation, J. Crystal Growth **73**, 487-504.

Steel, G.K. and M.J. Hill, 1975, Analysis of the transfer function governing crystal growth in the Czochralski process, J. Crystal Growth **30**, 45-53.

Stepanov, A.V., 1959, New method of producing articles (sheets, tubes, rods, various sections, etc.) directly form liquid metal I., Soviet Phys.-Techn. Phys. **4**, 339-348.

Strang, G. and G.J. Fix, 1973, An Analysis of the Finite Element Method, Prentice-Hall, Inc., Englewood Cliffs, New Jersey.

Surek, T., 1976, Theory of shape stability in crystal growth from the melt, J. Appl. Phys. **47**(10), 4384-4393.

Surek, T. and B. Chalmers, 1975, The direction of growth of the surface of a crystal in contact with its melt, J. Crystal Growth **29**, 1-11.

Surek, T., S.R. Coriell, and B. Chalmers, 1980, The growth of shaped crystals from the melt, J. Crystal Growth **50**, 21-31.

Takagi, K., T. Fukazawa, and M. Ishii, 1976, Inversion of the direction of the solid-liquid interface on the Czochralski growth of GGG crystals, J. Crystal Growth **32**, 89-94.

Teal, G.K. and E. Buehler, 1952, Growth of silicon single crystals and of single crystal silicon p-n junctions, Phys. Rev. **87**, 190.

Teal, G.K. and J.B. Little, 1950, Growth of germanium single crystals, Phys. Rev. **78**, 647.

Thomas, P.D. and R.A. Brown, 1986, In-core solution of an augmented block-banded matrix, Int. J. Num. Meth. Engrg., submitted.

Thomas, P.D., H.M. Ettouney, and R.A. Brown, 1986, A thermal-capillary mechanism for a growth rate limit in Edge-Defined Film-Fed growth of silicon sheets, J. Crystal Growth, submitted.

Thomas, P.D., 1987, , Ph.D. thesis, Department of Chemical Engineering, Massachusetts Institute of Technology, Cambridge, Massachusetts.

Touloukian, Y.S. and C.Y. Ho, editors, 1970, Thermophysical Properties of Matter, Vol. 1-13, IFI/Plenum, New York.

Ungar, L.H. and R.A. Brown, 1986, Finite-element methods for unsteady solidification problems arising in prediction of morphological structure, J. Comp. Phys., submitted.

Van der Hart, A. and W. Uelhoff, 1981, Macroscopic Czochralski growth I. Theoretical investigation, heat flow and growth model, J. Crystal Growth **51**, 251-266.

Viskanta, R. and E. Anderson, 1975, Heat transfer in semi-transparent solids, Advances in Heat Transfer, vol. 11, 318-441.

Wargo, M.J., 1982, The effect of direct current on crystal growth from the melt: InSb, Ph.D. thesis, Department of Materials Science and Engineering, Massachusetts Institute of Technology, Cambridge, Massachusetts.

Wargo, M.J., 1984, Maximization of growth rates during Czochralski pulling, Proceedings of the Flat-Plate Solar Array Project Research Forum on the High-Speed Growth and Characterization of Crystals for Solar Cells, 25-27 July 1983, Port St. Lucie, Florida, JPL Publication 84-23.

Watanabe, M., T. Fujii, S. Washizuka, S. Yashiro, J. Ushizawa, and S. Matsumura, 1984, LEC grown GaAs crstals with low dislocation density, presentation at ACCG-6/ICVGE-6, Atlantic City, NJ (July 15-20, 1984).

Whiffin, P.A.C., T.M. Bruton, and J.C. Brice, 1976, Simulated rotational instabilities in molten Bismuth Silicon Oxide, J. Crystal Growth **32**, 205-210.

Wilcox, W.R. and R.L. Duty, 1966, Macroscopic interface shape during solidification, J. Heat Transfer **88c**, 45-51.

Williams, G. and W.E. Reusser, 1983, Heat transfer in silicon Czochralski crystal growth, J. Crystal Growth **64**, 448-460.

Wouters, P.J., 1985, Simulation numerique des echanges thermiques et application a la croissance des cristaux semi-conducteurs, Ph.D. thesis (in French), Universite Catholique de Louvain, Louvain-la-Neuve, Belgium.

Yamaguchi, Y., C.J. Chang, and R.A. Brown, 1984, Multiple buoyancy-driven flows in a vertical cylinder heated from below, Phil. Trans. R. Soc. Lond. A **312**, 519-552.

Zienkiewicz, O.C., 1971, The Finite Element Method in Engineering Science, McGraw-Hill, New York.

Zulehner, W., 1983, Czochralski growth of silicon, J. Crystal Growth **65**, 189-213.

Appendix A.

Table A.1 Nomenclature.

Table A.2 Thermophysical properties for gallium arsenide.

Table A.3 Thermophysical properties for silicon.

Table A.4 Thermophysical properties for boric oxide (B_2O_3), graphite and quartz (SiO_2).

Table A.1 Nomenclature.

Roman Symbols

Bi_j,	Biot number = $h_j R_c / k_s$ for surface j
Bo_i,	Bond number = $g R_c^2 \Delta\rho_i / \sigma_i$ for surface i
$\mathbf{C}$,	vector of constraints used in processing strategies
Cp,	heat capacity [cal/gK]
Ca,	Capillary number = $\mu V / \sigma$
$\mathbf{e}_r$,	unit radial vector
$\mathbf{e}_z$,	unit axial vector
$\mathbf{F}$,	residuals vector for quasi-steady-state model
g,	gravitational constant [cm/s²]
g_i,	gain for integral controller
g_p,	gain for proportional controller
h_j,	heat transfer coefficient for surface j [W/cm²K]
$\tilde{H}_i$,	height of interface i from bottom of crucible [cm]
H_i,	dimensionless interface heights
$\mathcal{H}_i$,	mean curvature of interface i
$\mathbf{J}$,	Jacobian matrix
J_e,	elemental Jacobian of transformation
k,	thermal conductivity [W/cmK]
K_i,	thermal conductivity ratio = $k_i(T)/k_s$ for region i
L,	length scale [cm]
$\mathbf{M}$,	Mass matrix
$\mathbf{n}$,	normal vector to surface
N_Θ,	number of temperature unknowns

Table A.1 Nomenclature (continued).

N_i,	number of unknowns for interface i
p,	vector of parameters in thermal-capillary model
p_i°,	datum pressure for interface i [dyne/cm²]
Pe_i,	Peclet number = $V_0 R_c \rho_i C p_i / k_s$ (in quasi-steady-state model, $V_0 = V_p$)
Pr,	Prandtl number = ν/α
$\tilde{r}$,	radial coordinate measued from center of crucible [cm]
r,	dimensionless radial coordinate = $\tilde{r}/R_c$
$\tilde{R}$,	crystal radius [cm]
R,	dimensionless crystal radius = $\tilde{R}/R_c$
R_c,	crucible radius [cm]
Ra_j,	Radiation number = $\sigma^* \varepsilon_j R_c T_f^3 / k_s$ for surface j
Re,	Reynolds number = VL/ν
S,	Stefan number = $\Delta H_f / Cp_s T_f$
t,	time [s]
T,	temperature [K]
T_f,	solidification temperature [K]
V,	fluid velocity [cm/s]
V_0,	nominal crystal pull rate [cm/s]
V^*,	dimensionless crystal pull rate = V_p/V_0
$\tilde{V}_e$,	volume of encapsulant [cm³]
V_e,	dimensionless volume of encapsulant = $\tilde{V}_e/R_c^3$
$\tilde{V}_g$,	axial component of melt/crystal interface growth velocity [cm/s]
V_g,	dimensionless growth rate of melt/crystal interface = $\tilde{V}_g/V_0$
$\tilde{V}_m$,	volume of melt [cm³]

Table A.1 Nomenclature (continued).

V_m, dimensionless volume of melt = $\tilde{V}_m/R_c^3$

V_p, crystal pull rate [cm/s]

v^e, elemental velocity due to movement of mesh

$\mathbf{x}$, disturbance vector

$\mathbf{X}$, vector of nodal coordinates

$\mathbf{y}$, solution vector of all unknowns

$\tilde{z}$, axial coordinate measured from bottom of crucible [cm]

z, dimensionless axial coordinate = $\tilde{z}/R_c$

$\tilde{Z}$, position of crystal top [cm]

Z, dimensionless crystal height = $\tilde{Z}/R_c$

Greek Symbols

$\boldsymbol{\alpha}$, vector of finite element temperature unknowns

α, thermal diffusivity [cm²/s]

$\boldsymbol{\beta}$, vector of finite element interface height and radius unknowns

$\boldsymbol{\delta}$, correction vector used in Newton-Raphson method

Δ, deflection of melt/crystal interface = $H_0(R)-H_0(0)$

ΔH_f, heat of fusion [cal/g-mole]

$\Delta\tau_n$, time step n

$\Delta\rho_i$, density difference across interface i [g/cm³]

ϵ_j, emissivity of surface j

η, axial coordinate in unit element

Θ, dimensionless temperature = T/T_f

λ_i, dimensionless reference pressure for interface i = $p_i^\circ/\Delta\rho_i g R_c$

μ, viscosity [g/cm s]

Table A.1 Nomenclature (continued).

ν,	kinematic viscosity [cm^2/s]
ξ,	radial coordinate in unit element
ρ,	density [g/cm^3]
σ,	surface tension for interface [dyne/cm]
σ^*,	Stefan-Boltzmann constant [W/cm^2K^4]
σi,	eigenvalues
τ,	dimensionless time = V_0t/R_c
ϕi,	two-dimensional finite element basis function in unit element
Φi,	two-dimensional finite element basis function in global element
ψi,	one-dimensional finite element basis function in unit element
Ψi,	one-dimensional finite element basis function in global element
$\tilde{\phi}$,	equilibrium wetting angles [°]

<u>Mathematical Symbols</u>

dS,	differential surface area element
dt,	differential unit of time
dV,	differential volume element
D_i,	Domain i
$\Re^n$,	real n-dimensional space
Re( ),	real part of
∇,	Gradient operator = $(\partial/\partial r)\mathbf{e}_r + (\partial/\partial z)\mathbf{e}_z$
$\partial/\partial x$,	Partial derivative with respect to x
∂D_i,	surface i
$\|\ \|$,	vector norm
ε,	small number

Table A.1 Nomenclature (continued).

$\sum$,	summation

Subscripts

o,	reference, equilibrium, or initial
a,	ambient
c,	crucible or critical
e,	encapsulant
h,	heater
i,j,k,	indeces denoting region, surface, or numeral
(i),	index in unit element
ℓ,	liner
m,	melt
n,	time step number
s,	solid
set,	set point value

Superscripts

aug,	augmented set for processing strategies
i,j,	index for basis functions
(k),	iteration number
∞,	far above crucible

Table A.2 Thermophysical properties for gallium arsenide.

Property	Value	Reference
Melt		
Density, ρ_m (g/cm3)	5.71	Glazov et al. (1969)
Emissivity, ε_m	0.55	Jordan (1980)
Specific heat, Cp_m (J/gK)	0.42	Jordan (1983)
Thermal conductivity, k_m (W/cmK)	0.14	Jordan (1983)
Crystal		
Density, ρ_s (g/cm3)	5.17	Glazov et al. (1969)
Emissivity, ε_s	0.55	Jordan (1980)
Specific heat, Cp_s (J/gK)	0.42	Jordan (1980)
Thermal conductivity, k_s (W/cmK)	0.07	Jordan (1980)
Interfaces		
Equilibrium growth angle, $\tilde{\phi}_o$ (°)	15	Kashkooli et al. (1974), Jordan et al. (1983)
Heat of fusion, ΔH_f, (J/g)	726	Glazov et al. (1969), Jordan (1980)
Melting temperature, T_f (K)	1511	Neuberger (1971)
Meniscus surface tension, σ_m (dyn/cm)	700	estimated

Table A.3 Thermophysical properties for silicon.

Property	Value	Reference
Melt		
Density, ρ_m (g/cm^3)	2.42	Touloukian and Ho (1970)
Emissivity, ε_m	0.64 0.3	Touloukian and Ho (1970) Jackson and Kurtze (1985)
Specific heat, Cp_m (J/gK)	1.00	Touloukian and Ho (1970)
Thermal conductivity, k_m (W/cmK)	0.64	Touloukian and Ho (1970),
Crystal		
Density, ρ_s (g/cm^3)	2.30	Touloukian and Ho (1970)
Emissivity, ε_s	0.64 0.7	Touloukian and Ho (1970) Jackson and Kurtze (1985)
Specific heat, Cp_s (J/gK)	1.00	Touloukian and Ho (1970)
Thermal conductivity, k_s (W/cmK)	0.22* (1683K/T)	Touloukian and Ho (1970), Bell (1977)
Interfaces		
Equilibrium growth angle, $\tilde{\phi}_o$ (°)	11	Surek and Chalmers (1985)
Heat of fusion, ΔH_f, (J/g)	1800	Touloukian and Ho (1970)
Melting temperature, T_f (K)	1683	Touloukian and Ho (1970)
Meniscus surface tension, σ_m (dyn/cm)	720	Touloukian and Ho (1970)

Table A.4 Thermophysical properties for boric oxide (B_2O_3), graphite, and quartz (SiO_2).

Property	B_2O_3	Reference
Density, ρ_e (g/cm3)	1.51	Shpil'rain et al. (1974)
Emissivity, ε_e	0. or 1.[1]	assumed
Thermal conductivity, k_e (W/cmK)	0.02	Berzhatyy and Lezhenin (1973)
Meniscus surface tension, σ_e (dyn/cm)	100	Shpil'rain et al. (1972)
Wetting angle, $\tilde{\phi}_e$ (°)	5	estimated

[1] For transparent or opaque encapsulant, respectively.

Property	Graphite	Reference
Density, ρ_c (g/cm3)	1.6	Touloukian and Ho (1970)
Emissivity, ε_c	0.8	Touloukian and Ho (1970)
Specific heat, Cp_c (J/gK)	2.1	Touloukian and Ho (1970)
Thermal conductivity, k_c (W/cmK)	0.6	Touloukian and Ho (1970)

Property	SiO_2	Reference
Density, ρ_ℓ (g/cm3)	2.2	Touloukian and Ho (1970)
Emissivity, ε_ℓ	0.35	Touloukian and Ho (1970)
Specific heat, Cp_ℓ (J/gK)	1.3	Touloukian and Ho (1970)
Thermal conductivity, k_ℓ (W/cmK)	0.06	Touloukian and Ho (1970)

Appendix B.

Reprinted with permission from Chemical Engineering Science Vol. 41, No. 1, pp. 37-46, Jeffrey J. Derby and Robert A. Brown, "A Fully Implicit Method for the Simulation of the One-dimensional Solidification of a Binary Alloy," 1986, Pergamon Press, Ltd.

Chemical Engineering Science Vol 41 No 1 pp 37–46 1986
Printed in Great Britain

A FULLY IMPLICIT METHOD FOR SIMULATION OF THE ONE-DIMENSIONAL SOLIDIFICATION OF A BINARY ALLOY

JEFFREY J. DERBY and ROBERT A. BROWN
Department of Chemical Engineering and the Materials Processing Center, Massachusetts Institute of Technology, Cambridge, MA 02139, U.S.A

(*Received* 25 *October* 1984)

Abstract—A finite difference method is developed which overcomes the difficulties of the disparate time scales and small solute diffusion layers inherent to one-dimensional models for the solidification of binary alloys The boundary immobilization method applied with a coordinate transformation which stretches the solute boundary layer adjacent to the interface is combined with centred difference approximations to generate a set of ordinary differential equations for the solute and temperature fields and the melt/solid interface location Numerical integration by a variable step-size fully-implicit trapezoid method is compared to an explicit Adams–Bashforth predictor–corrector technique The implicit method is found to be from two to twelve times more efficient when the Lewis number (the ratio of mass to thermal diffusivities) is small, as is typically the case for metals and semiconductors

1. INTRODUCTION

Numerical modelling of alloy solidification systems is a formidable task involving the time-integration of moving-boundary problems which describe the conservation of heat and species through melt and solid phases and across the melt/solid interface. Even when the effects on convective mass and heat transfer of bulk flow in the melt caused by buoyancy differences are neglected, solution of the resulting diffusion-controlled models is hindered by two major complications. First, at even moderate solidification rates, the relatively low diffusivities of solutes in the melt cause steep gradients ahead of the interface which are difficult to approximate in any numerical formulation. During steady-state solidification, the extent of this layer scales as D/V, where D is the mass diffusivity of the species and V is the translation rate of the interface. This distance is represented in dimensionless form by the inverse of the Peclet number for mass transfer. $Pe_m^{-1} = D/VR$, where R is the radius of the ampoule.

Second, the widely disparate diffusivities between heat and mass in a typical metal or semiconductor system lead to greatly varying time scales for these two transport processes and to numerical stiffness in the set of ordinary differential equations which results from any numerical discretization. The Lewis number, $Le = D/\alpha_l$ (where α_l is the thermal diffusivity of the liquid) is a measure of the ratio of thermal to solutal time scales and, hence, of the stiffness of the system.

The purpose of this paper is to present a fully-implicit, finite difference time-integration scheme for solving a one-dimensional alloy solidification problem with steep concentration gradients and to demonstrate the efficiency of this method relative to more conventional integration procedures.

Many finite difference and finite element methods have been previously presented for solving problems involving a change-of-phase in one or two spatial dimensions (Crowley and Ockendon, 1979; Ettouney and Brown, 1983; Fix, 1978; Rubinsky, 1983, Ungar and Brown, 1984; Yoo and Rubinsky, 1983); however, few of these methods address the problems specific to numerical solution of the problem for a binary alloy. Rubinsky (1983) solved a one-dimensional solidification problem similar to the one solved here using a finite element algorithm that accounted for the steep concentration gradients by using small elements adjacent to the interface. The ordinary differential equations resulting from a conventional Galerkin finite element discretization were solved by splitting the coupled set into equations for the composition, temperature fields and interface location. Although the field variables were computed from linear equations by an implicit integration procedure, the coupling of the field variables to the interface was only treated explicitly. Rubinsky's decoupling is explained later in our framework for a fully-implicit integration scheme.

Our approach follows the development of Newton iteration schemes for free-boundary (time-independent) solidification problems (Ettouney and Brown, 1983) and concentrates on explicit representation of the nonlinearities associated with the unknown interface location. We do this by transforming the moving-boundary problem to one with a fixed domain, as originally done by Landau (1950). The coordinate stretching needed for adequate representation of the solute diffusion layer is introduced as part of this transformation. Centred difference approximations applied to the transformed coordinates reduce the field equations and boundary conditions to a set of coupled ordinary differential equations. The stiffness of the original transport problem caused by the small Lewis number is manifested in this set, and we show that explicit integration techniques are inadequate for their solution. The implicit integration method used here is similar to that developed by Gresho *et al.* (1980).

Our results are presented in the context of a one-dimensional model for the solidification of $Hg_{1-x}Cd_xTe$, an important alloy used in infrared detectors. The solidification model is for a vertical Bridgman growth furnace, as described elsewhere (Wang *et al.*, 1985, Bourret *et al.*, 1986) for the solidification of this material. The phase diagram and representative thermophysical properties for HgCdTe are presented by Bourret *et al.* (1986), and are reported here only in terms of the dimensionless groups in the model Because HgCdTe forms an isomorphous mixture between the pseudo-binary components HgTe and CdTe across the entire phase diagram, we solve only for the concentration of CdTe in the melt. We neglect the diffusion of either species in the solid so that the composition there is completely specified by the species balance at the interface at the time of solidification

2. ONE-DIMENSIONAL SOLIDIFICATION MODEL

Our model for the heat-pipe vertical Bridgman furnace of Wang *et al.* (1985) is shown schematically in Fig 1. The furnace consists of a cylindrical cavity lined with isothermal hot and cold zones separated by an adiabatic region. A cylindrical ampoule of length $\tilde{L}$ and radius R holds the solidifying alloy as it is lowered from rest through the furnace

We model heat and mass transfer inside the ampoule using the equations appropriate for a long, thin ampoule with only slow variations of temperature along its length. These so-called "fin equations" are written in terms of a dimensionless axial coordinate $z \equiv \tilde{z}/R$ which moves with the ampoule translation rate V, a dimensionless time scale is defined as $\tau \equiv tV/R$ so that one unit represents the time necessary for the ampoule to traverse one radius. Dimensionless temperatures in the melt (θ_l) and solid (θ_s), and concentration are defined by $\theta_j \equiv (T_j - T_c)/(T_h - T_c)$ and $C \equiv c/c_0$, respectively, where c_0 is the initial concentration of the melt, and T_c and T_h are the cold and hot zone temperatures. We assume constant thermophysical properties and write the field equations in the form

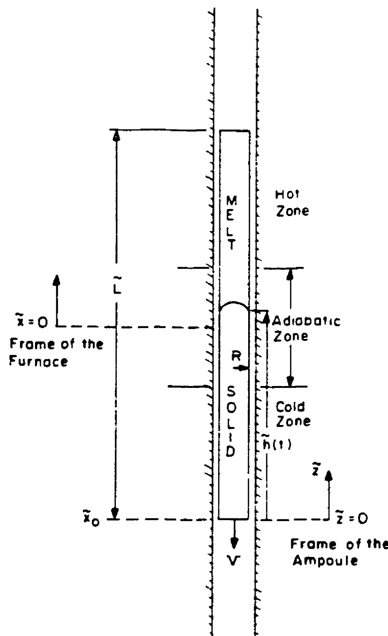

Fig. 1. Model for the heat-pipe vertical Bridgman furnace of Wang *et al.* (1985)

$$Pe_s\frac{\partial\theta_s}{\partial\tau} = \frac{\partial^2\theta_s}{\partial z^2} - 2Bi_sU(z,\tau)\,[\theta_s - \theta_a(z,\tau)], \quad (1)$$

$$Pe_l\frac{\partial\theta_l}{\partial\tau} = \frac{\partial^2\theta_l}{\partial z^2} - 2Bi_lU(z,\tau)\,[\theta_l - \theta_a(z,\tau)], \quad (2)$$

$$Pe_m\frac{\partial C}{\partial\tau} = \frac{\partial^2 C}{\partial z^2}, \quad (3)$$

where $\theta_a(z,\tau)$ is the ambient temperature distribution along the wall of the furnace and $U(z,\tau)$ is a dimensionless heat-transfer coefficient appropriate for the three-zone furnace The Peclet (Pe_j) and Biot (Bi_j) numbers are defined in Table 1

We model the heat exchange between the furnace and ampoule with analytical expressions for $\theta_a(z,\tau)$ and $U(z,\tau)$:

$$\theta_a(z,\tau) = \frac{1}{2}(1 + \tanh[B_1(z - \tau + x_0)]), \quad (4)$$

$$U(z,\tau) = \frac{\tilde{U}(z,t)}{\tilde{U}_0} = 1 + \frac{1}{2}(\tanh[B_2\{(z-\tau+x_0) - B_3\}] + \tanh[-B_2\{(z-\tau+x_0)+B_3\}]), \quad (5)$$

where x_0 is a reference point relating a fixed point in the furnace to the initial position of the ampoule coordinate system, and the coefficients $\{B_1, B_2, B_3\}$ set the shape of each profile. These expressions are time-dependent because the coordinate system is attached to the moving ampoule. The values of the coefficients used in this work are given in Table 2 and the profiles of the ambient temperature and heat-transfer coefficient at the initiation of the growth experiment are shown as Fig. 2.

At the melt/solid interface $H(\tau) \equiv \tilde{h}(t)/R$, the boundary conditions for energy and mass conservation and for local equilibrium are

$$\theta_s(H(\tau),\tau) = \theta_l(H(\tau),\tau) = F(C(H(\tau),\tau)), \quad (6)$$

$$Pe_lS\frac{dH}{d\tau} = K\frac{\partial\theta_s}{\partial z}\bigg|_{H(\tau)} - \frac{\partial\theta_l}{\partial z}\bigg|_{H(\tau)}, \quad (7)$$

$$Pe_mC(k-1)\frac{dH}{d\tau} = \frac{\partial C}{\partial z}\bigg|_{H(\tau)}, \quad (8)$$

where the Stefan number S represents a dimensionless heat of fusion, K is the ratio of the thermal conductivity of the solid with respect to that of the liquid, and $F(C)$ and $k(C)$ are expressions for the melting temperature and segregation coefficient taken from the phase diagram for the alloy material. These are most

Table 1 Definitions of dimensionless groups and numerical values used in the solidification model for HgCdTe

Parameter	Definition	Value
Biot numbers	$Bi_j \equiv \frac{\tilde{U}_0 R}{\tilde{k}_j}$	$Bi_l = 0.3$ $Bi_s = 0.1875$
Lewis number	$Le \equiv \frac{D}{\alpha_l}$	$Le = 7.36 \times 10^{-3}$, for HgCdTe $Le = 1$, for test case
Peclet number, heat transfer	$Pe_j \equiv \frac{VR}{\alpha_j}$	$Pe_l = 9.58 \times 10^{-4}$, 1.92×10^{-3}, 3.83×10^{-3}, for HgCdTe $Pe_l = 0.833$, for test case $Pe_s = 1.53 \times 10^{-3}$, 3.07×10^{-3}, 6.13×10^{-3}, for HgCdTe $Pe_s = 0.833$, for test case
Peclet number, mass transfer	$Pe \equiv \frac{VR}{D}$	$Pe_m = 0.208$, 0.417, 0.833, for HgCdTe $Pe_m = 0.833$, for test case
Stefan number	$S \equiv \frac{\Delta H_f}{Cp_l T_f}$	$S = 6.3$
Thermal conductivity ratio	$K \equiv \frac{\tilde{k}_s}{\tilde{k}_l}$	$K = 1.6$

Table 2. Coefficients specifying furnace configuration and phase diagram for the HgCdTe system

System equation	Coefficient values
Dimensionless overall heat-transfer coefficient	$B_1 = 1.0$ $B_2 = 1.0$ $B_3 = 2.0$
Interfacial equilibrium temperature	$a_0 = 670.1$ $a_1/c_0 = 686.5$ $a_2/c_0^2 = -465.4$ $a_3/c_0^3 = 191.8$
Equilibrium distribution coefficient	$b_0 = 3.983$ $b_1/c_0 = -6.867$ $b_2/c_0^2 = 1.135$ $b_3/c_0^3 = 14.90$ $b_4/c_0^4 = -20.20$ $b_5/c_0^5 = 8.054$

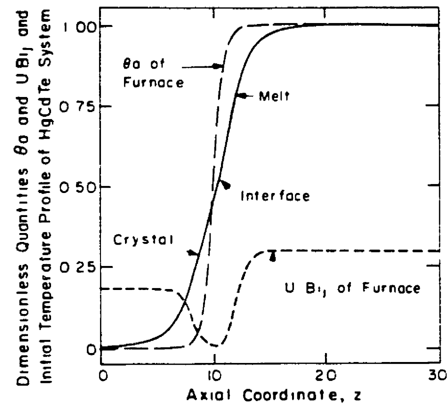

Fig 2 Temperature profile of charge (—) in a static ($Pe_m = 0$) ampoule which results from the furnace temperature (— —) Dimensionless heat-transfer coefficient (- - -) profiles are also shown.

easily expressed in terms of polynomials in the temperature and concentration at the interface as

$$F(C) = \frac{\sum_{i=0}^{3} a_i C^i - T_c}{T_h - T_c}, \tag{9}$$

$$k(C) = \sum_{i=0}^{5} b_i C^i, \tag{10}$$

where the coefficients appropriate for the HgCdTe system are given in Table 2.

We assume that no heat or mass exits from the ends of the ampoule:

$$\left.\frac{\partial \theta_s}{\partial z}\right|_{z=0} = \left.\frac{\partial \theta_l}{\partial z}\right|_{z=L} = \left.\frac{\partial C}{\partial z}\right|_{z=L} = 0. \tag{11}$$

The specification of the moving-boundary problem dictated by eqs (1)–(11) is completed by setting initial solute and temperature profiles and an interface location at $\tau = 0$. We have chosen these to be the solution of the free-boundary problem for the ampoule at rest ($V = 0$, $Pe_j = 0$), so that the computed transient corresponds to the step change in the pull rate that occurs at the onset of solidification. The concentration profile for an ampoule at rest is constant everywhere, $C(z, 0) \equiv 1$, and the temperature profile $\theta_j(z, 0)$ and interface position $H(0)$ are shown in Fig. 2 for the furnace configuration and thermophysical properties used in these calculations.

3. NUMERICAL METHOD

The moving-boundary problem represented by eqs (1)–(11) was mapped to a fixed domain using two

different transformations: the one originally proposed by Landau (1950) and a bilinear mapping that accounts for the solute diffusion layer adjacent to the interface. The transformation used by Landau is

$$\xi = \begin{cases} \dfrac{z}{H(\tau)}, & 0 \leqslant z \leqslant H(\tau) \\ \dfrac{z-H(\tau)}{L-H(\tau)}+1, & H(\tau) \leqslant z \leqslant L. \end{cases} \tag{12}$$

The bilinear mapping is applied only to the solutal field equation of the melt [eq. (3)] and takes the form

$$\xi = \frac{Az+E}{Gz+J}, \qquad H(\tau) \leqslant z \leqslant L \tag{13}$$

where the coefficients $\{A, E, G, J\}$ are functions of the interface position $H(\tau)$ and a characteristic distance from the interface s:

$$A = -2H(\tau)+2L-3s, \tag{14}$$

$$E = 2H^2(\tau)-2H(\tau)L+2H(\tau)s+Ls, \tag{15}$$

$$G = -H(\tau)+L-2s, \tag{16}$$

$$J = H^2(\tau)-H(\tau)L+H(\tau)s+Ls \tag{17}$$

Both mappings fix the interface at $\xi = 1$ and the ends of the ampoule at $\xi = 0$ and $\xi = 2$. In addition, the bilinear mapping transforms the point $H(\tau)+s$ in real space to a fixed point in the mapped coordinate, $\xi = 3/2$. This additional feature allows for an expansion of a region of the melt adjacent to the interface into a large region in the mapped system and is responsible for the increased accuracy of the steep concentration gradients in the diffusion layer. We have taken s to be the characteristic length for mass diffusion, Pe_m^{-1}.

The field equations for temperature and concentration, eqs (1)–(3), and the distinguished condition for the melt/solid interface, eq. (5), are transformed into the ξ-coordinate system This technique of tracking the moving solidification front is analogous to the energy–flux method for the solution of steady-state problems, as discussed by Ettouney and Brown (1983). The mapped domain is discretized into evenly spaced segments, and a centred-difference formulation is used to transform the partial differential eqs (1)–(3) into a set of ordinary differential equations. The interfacial heat and mass transfer conditions, eqs (5) and (6), are discretized using a second-order accurate, one-sided differencing formula, which is consistent with the centred difference approximations (Finlayson, 1980)

The complete set of ordinary differential equations takes the form of the following vector equation.

$$\mathbf{M}(\mathbf{y}, \tau)\frac{\partial \mathbf{y}}{\partial \tau} = \hat{\mathbf{f}}(\mathbf{y}), \tag{18}$$

where $\mathbf{y}$ represents the unknown set of nodal values for temperature and concentration resulting from the difference approximations and the interface position. The nonlinear vector function $\hat{\mathbf{f}}(\mathbf{y})$ arises from the finite difference discretization, and $\mathbf{M}(\mathbf{y}, \tau)$ is the mass matrix which naturally occurs for discretizations of initial value problems. For finite difference approximations to the heat equation on fixed domains, the mass matrix is diagonal and so is trivially inverted to yield a conventional set of ordinary differential equations. Either of the mappings of the moving-boundary proposed here adds to the complexity of the mass matrix by introducing new time-derivatives into the interfacial heat and mass flux equations according to

$$\frac{\partial \hat{y}(z,\tau)}{\partial \tau} = \frac{\partial y(\xi,\tau)}{\partial \tau} + \frac{\partial y(\xi,\tau)}{\partial \xi}\frac{\partial \xi}{\partial \tau}, \tag{19}$$

where $\hat{y}$ is a variable in the original coordinate system and y is the corresponding quantity in the mapped coordinate system. Since the mapped coordinate system depends on the location of the moving solidification interface, ξ is implicitly a function of time and the second term of the above equation includes $\partial\xi/\partial\tau$. The time-derivative of ξ is obtained from the mapping eqs (12) and (13). For the Landau transformation,

$$\frac{\partial \xi}{\partial \tau} = \begin{cases} -\dfrac{\xi}{H(\tau)}\dfrac{\mathrm{d}H}{\mathrm{d}\tau}, & 0 \leqslant \xi \leqslant 1 \\ \dfrac{\xi-2}{L-H(\tau)}\dfrac{\mathrm{d}H}{\mathrm{d}\tau}, & 1 \leqslant \xi \leqslant 2 \end{cases} \tag{20}$$

and for the bilinear mapping,

$$\frac{\partial \xi}{\partial \tau} = \frac{\left(\dfrac{\partial G}{\partial \tau}J - G\dfrac{\partial J}{\partial \tau}\right)\xi^2 + \left(\dfrac{\partial E}{\partial \tau}G - E\dfrac{\partial G}{\partial \tau} + A\dfrac{\partial J}{\partial \tau} - \dfrac{\partial A}{\partial \tau}J\right)\xi + \dfrac{\partial A}{\partial \tau}E - A\dfrac{\partial E}{\partial \tau}}{EG-AJ}, \tag{21}$$

where the coefficients are given in eqs (14)–(17).

For this one-dimensional problem, $\mathbf{M}(\mathbf{y}, \tau)$ is composed of a single diagonal and one filled column. If we order the unknown vector so that the interface position is the final component, $\mathbf{y}^T = \{\theta_i, C_i, H(\tau)\}$, the mass matrix takes the form

$$\mathbf{M}(\mathbf{y},\tau) = \begin{bmatrix} 1 & 0 & 0 & \cdot & & & X_1 \\ 0 & 1 & 0 & \cdot\, 0\, \cdot & & & X_2 \\ 0 & 0 & 1 & \cdot & & & X_3 \\ & & & \ddots & & & \vdots \\ & & \cdot & & 1 & 0 & X_{N-2} \\ & & \cdot\, 0\, \cdot & & 0 & 1 & X_{N-1} \\ & & \cdot & & 0 & 0 & X_N \end{bmatrix}, \tag{22}$$

where $X_i(\mathbf{y}, \tau)$ are relations derived from eqs (20) and (21). This matrix is inverted analytically to yield an ordinary differential equation set

$$\frac{\partial \mathbf{y}}{\partial \tau} = \mathbf{M}^{-1}\hat{\mathbf{f}}(\mathbf{y}) = \mathbf{f}(\mathbf{y}), \tag{23}$$

where the inverse of **M** is still sparse and the product of the inverse mass matrix and $\hat{\mathbf{f}}$ is denoted as **f**. Either generalizing this formulation to multiple space dimensions or switching the distinguished condition for locating the interface shape to the isotherm equation, as suggested by Ettouney and Brown (1983), will prevent the analytical inversion of **M**. In the first case, the mass matrix will be too complex to invert analytically; in the second, no time-derivatives will appear in the residual equations for the interface shape and the mass matrix will be singular. In these cases, explicit integration schemes are not feasible, as discussed at length by Ungar and Brown (1985b).

Two integration techniques with second-order accuracy in time were employed to solve eq. (23)—an explicit Adams–Bashforth predictor followed by a single-step Adams–Moulton corrector and the fully-implicit trapezoid rule. The predictor–corrector scheme was carried out with a predictor step,

$$\mathbf{y}_{n+1}^{P} = \mathbf{y}_n + \frac{\Delta\tau_n}{2}\left[\left(2+\frac{\Delta\tau_n}{\Delta\tau_{n-1}}\right)\mathbf{f}(\mathbf{y}_n) - \frac{\Delta\tau_n}{\Delta\tau_{n-1}}\mathbf{f}(\mathbf{y}_{n-1})\right], \quad (24)$$

followed by a single corrector step,

$$\mathbf{y}_{n+1} = \mathbf{y}_n + \frac{\Delta\tau_n}{2}\left[\mathbf{f}(\mathbf{y}_n)+\mathbf{f}(\mathbf{y}_{n+1}^{P})\right], \quad (25)$$

where $\Delta\tau$ is the time step and the subscripts n and $n+1$ refer to quantities at the nth and $n+1$st time step. This is an explicit method since the predictor $\mathbf{y}^P$ of eq. (24) is used for the value of $\mathbf{y}_{n+1}$ on the left-hand side of eq. (25). The trapezoid method employs only the fully-implicit version of the corrector, eq. (25),

$$\mathbf{y}_{n+1} = \mathbf{y}_n + \frac{\Delta\tau_n}{2}\left[\mathbf{f}(\mathbf{y}_n)+\mathbf{f}(\mathbf{y}_{n+1})\right], \quad (26)$$

where now $\mathbf{y}_{n+1}$ is used on the left- and right-hand sides of the equation. We start both methods with a single forward Euler time step,

$$\mathbf{y}_1 = \mathbf{y}_0 + \Delta\tau_0\mathbf{f}(\mathbf{y}_0), \quad (27)$$

where $\mathbf{y}_0$ is the initial steady solution for the system at rest and $\Delta\tau_0$ is the first time step, which is taken to be very small (10^{-8}) in order to minimize the initial error.

We solve the implicit equation set, eq. (26), iteratively at each time step by a pseudo-Newton's method. A correction vector $\boldsymbol{\delta}$ is used to update the guess for $\mathbf{y}_{n+1}$ as

$$\mathbf{y}_{n+1}^{(k+1)} = \mathbf{y}_{n+1}^{(k)} + \boldsymbol{\delta}^{(k+1)}, \quad (28)$$

where the superscripts denote iteration number and $\boldsymbol{\delta}^{(k+1)}$ is determined from

$$\mathbf{J}\boldsymbol{\delta}^{(k+1)} = \mathbf{y}_n - \mathbf{y}_{n+1}^{(k)} + \frac{\Delta\tau_n}{2}\left[\mathbf{f}(\mathbf{y}_n)+\mathbf{f}(\mathbf{y}_{n+1}^{(k)})\right]. \quad (29)$$

The formulation for the matrix **J** is as follows:

$$\mathbf{J} = \mathbf{I} + \frac{\Delta\tau_n}{2}\left.\frac{\partial\mathbf{f}}{\partial\mathbf{y}}\right|_{\mathbf{y}=\mathbf{y}_{n+1}^{P}}, \quad (30)$$

where **I** is the identity matrix and $\partial\mathbf{f}/\partial\mathbf{y}\ \{\partial f_i/\partial y_j\}$ is a sensitivity matrix for **f** evaluated at the predictor value of $\mathbf{y}_{n+1}^{P}$ as given in eq. (24). The matrix **J** is updated only when the procedure has failed to converge in four iterations; thus the same **J** may be carried along for several time steps.

The strategies for varying the step-size $\Delta\tau$ are based on local error estimation for both schemes. Truncation error in the second-order time expansions is proportional to the lowest-order neglected term, i.e. the third-order term in the expansion, $\partial^3\mathbf{y}/\partial\tau^3$. The estimated local errors $\Delta\mathbf{y}$ are given for the explicit method as

$$\Delta\mathbf{y} = \frac{\Delta\tau_n^3}{12}\left(2+3\frac{\Delta\tau_{n-1}}{\Delta\tau_n}\right)\frac{\partial^3\mathbf{y}}{\partial\tau^3} = \frac{1}{12}\left(2+3\frac{\Delta\tau_{n-1}}{\Delta\tau_n}\right)\left[\Delta\tau\,\mathbf{f}(\mathbf{y}_n) - (\Delta\tau_n+\Delta\tau_{n-1})\mathbf{f}(\mathbf{y}_{n-1}) + \Delta\tau_{n-1}\mathbf{f}(\mathbf{y}_{n-2})\right], \quad (31)$$

and for the implicit method as

$$\Delta\mathbf{y} = \frac{\Delta\tau_n^3}{12}\frac{\partial^3\mathbf{y}}{\partial\tau^3} = \frac{\mathbf{y}_{n+1}-\mathbf{y}_{n+1}^{P}}{3\left(1+\frac{\Delta\tau_{n-1}}{\Delta\tau_n}\right)}, \quad (32)$$

where again the predictor of eq. (24) is used. These estimates of local truncation error are used to project a step size for the next step which will result in local error proportional to a parameter, here represented as ε:

$$\Delta\tau_{n+1} = \Delta\tau_n\left(\frac{\varepsilon}{\|\Delta\mathbf{y}\|}\right)^{1/3}, \quad (33)$$

where $\|\Delta\mathbf{y}\|$ is the L_2-Euclidean norm of the vector quantity $\Delta\mathbf{y}$. We accept the new step size $\Delta\tau_{n+1}$ if it is greater than the old step size $\Delta\tau_n$ or if it is less than $0.8\Delta\tau_n$. If $\Delta\tau_{n+1}$ is greater than $0.8\Delta\tau_n$ and less than $\Delta\tau_n$, the step size is not changed. For every run, the error criterion ε was chosen as 10^{-4} so that the error at each time step was proportional to 0.01%.

The explicit algorithm also included a provision to limit the step size near the onset of numerical instability. When errors accumulated to the degree that the calculations diverged, the entire explicit run was repeated with a maximum step size determined by the last successful step in the aborted run. Measurements of computer time were also restarted so reported CPU times are only those for each successful run.

Details of the fully-implicit method and heuristic guidelines for choosing step size are found in the paper by Gresho *et al.* (1980). A discussion of the Adams predictor–corrector and other explicit methods is included in the work by Finlayson (1980).

4. NUMERICAL RESULTS

Fortran computer programs were written for solution of the model problem, using formulations based on the Landau and the bilinear mappings for interface immobilization and on the explicit and implicit integration schemes. All results are reported for calculations performed in double-precision arithmetic on

the Data General MV4000 computer in the Department of Chemical Engineering. The calculations presented here are for thermophysical properties and growth conditions appropriate for solidification of the alloy semiconductor $Hg_{1-x}Cd_xTe$ system treated as a pseudo-binary alloy CdTe–HgTe with CdTe as the solute. The dimensionless groups, furnace configuration and other coefficients are those listed in Tables 1 and 2, unless stated otherwise. The ampoule translation rates used in the calculations vary and are given in terms of the appropriate mass-transfer Peclet number; the Peclet numbers for heat transfer were also changed to be consistent with these values.

4.1. *Length scales: effect of* Pe_m

The effect of the steep concentration gradients on the accuracy of the finite difference solutions is demonstrated in Fig. 3 by profiles of the solute concentration in both melt and crystal at various solidification rates and at the dimensionless time $\tau = 10$ when the ampoule has been lowered ten radii The calculations were performed with ten finite-difference segments in the melt and the solid which yielded a set of 32 ordinary differential equations in the form of eq. (23)

For each translation rate, the solute concentration in the crystal decreased uniformly to the steady-state value of $C = 1$ as the solute was selectively partitioned into the solid during solidification. The sudden decrease in the composition at the melt/solid interface was due to the segregation coefficient being greater than unity. The diffusion layer in the melt adjacent to the interface was visible in each of the calculations. The numerical calculations with the Landau and bilinear mappings were very similar for the lowest two translation rates, but differed significantly at the highest value $Pe_m = 0.833$. The uniform Landau mapping lead to a spurious wiggle in the concentration profile in the solid and to loss of mass conservation between the two phases. These problems were absent in the results from the bilinear mapping.

The concentration profile at $\tau = 10$ is shown again in Fig. 4 for $Pe_m = 0.833$ and calculations performed with 100 grid points for the Landau mapping and only 20 points with the bilinear technique. The latter calculation was accurate to within a few per cent of the finer mesh result.

The velocity of the solidification interface is plotted in Fig. 5 as a function of time for $Pe_m = 0.833$. The results using the Landau mapping showed the same wiggle observed above in the concentration profile. These oscillations are due solely to the numerical solution of the solute balance equation, since both methods treat the heat balances and interface equation identically. Both discretizations yielded interface velocities which differed from the results for the finer (100

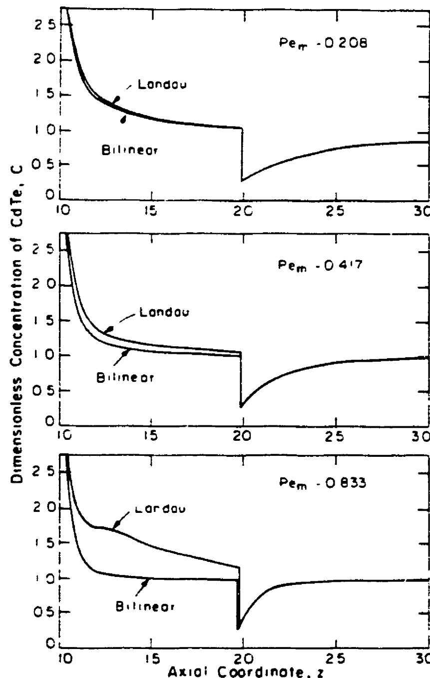

Fig 3 Solute profiles calculated with both the Landau and the bilinear mapping for three different Peclet numbers All profiles are after the ampoule has translated 10 radii.

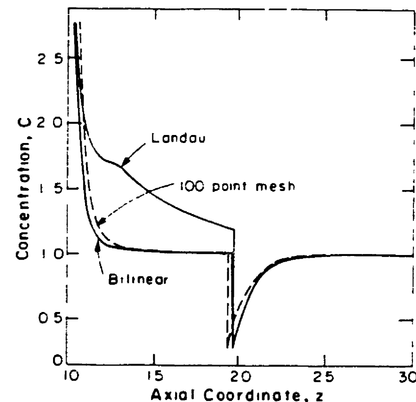

Fig 4 Concentration profiles computed for $Pe_m = 0.833$ using the Landau transformation with 20 and 100 segments and the bilinear mapping with 20 segments Results are for $\tau = 10$

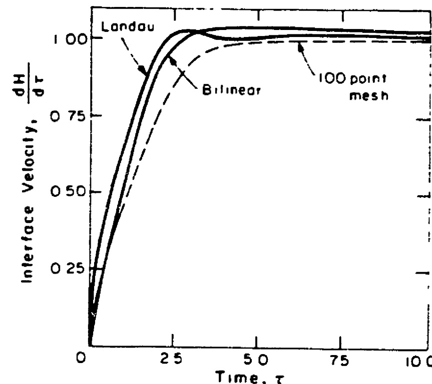

Fig 5 Velocity of the solidification interface for $Pe_m = 0.833$ as a function of time for the same discretizations used in Fig 4.

grid point) mesh. This difference was due to the approximation error in the temperature field near the interface.

As is evident from the results in Figs 3 and 4, the errors in the formulation using the Landau mapping were most severe during the initial transient. This point was emphasized by examining the concentration profiles produced using both mappings at times both during ($\tau = 0.833$) and after this transient ($\tau = 10$), as shown in Fig 6 At the early time the bilinear mapping placed eight grid points within the boundary layer, whereas the uniform mapping had only two points approximating the entire gradient and the accuracy of the solute balance at the interface suffered At the longer time the concentration boundary layer expanded to fill more of the melt and involved enough grid points to resolve the diffusion layer.

4.2. *Time scales. effect of* Le

The effects of numerical stiffness caused by the widely disparate time scales, as measured by the Lewis number, were examined by calculations for the Lewis number appropriate for the HgCdTe system (7.36×10^{-3}) and $Le = 1$. Both the explicit predictor–corrector technique and the implicit formulation described above were used. All calculations were performed for integration over one unit of the characteristic time for mass transfer $\tau^* \equiv \tau/Pe_m = Dt/R^2$

The calculations for $Le = 1$ were accomplished by scaling the value of the liquid-phase thermal diffusivity to that of the solutal diffusivity, with all other parameters remaining the same. The effect of this rescaling is shown in Fig. 7. The concentration field and interface velocity are driven to a steady state by the rapid response of the thermal field to the motion of the ampoule for the case of $Le = 7.36 \times 10^{-3}$. The results for $Le = 1$ show the effect of a relatively slowly changing temperature field on the concentration field and interface. The calculations for $Le = 7.36 \times 10^{-3}$ are numerically stiff since the thermal field has a much smaller characteristic time for change than that of the concentration field and interface. The case of $Le = 1$ is not stiff since all quantities are changing in time at nearly the same rate.

The execution times for the explicit and implicit integration methods and different Lewis numbers are plotted in Fig. 8 as a function of the number of variables in the ordinary differential equation set. Two points are obvious The implicit method was more efficient for a given size problem than the explicit technique for both Lewis numbers. Also, this difference was most pronounced for the extreme value $Le = 7.36 \times 10^{-3}$, where the implicit formulation consumed only approximately 25% of the computer time of the explicit method The savings of the implicit method were a direct result of the large increase in time step $\Delta\tau^*$ over the explicit formulation, which more than compensated for the extra computer time needed to solve iteratively the implicit equations generated at each time step The temporal histories of the time steps taken for calculations with $Le = 7.36 \times 10^{-3}$ and 32 equations (10 segments in each phase) are shown as Fig. 9. While the step size for the predictor–corrector

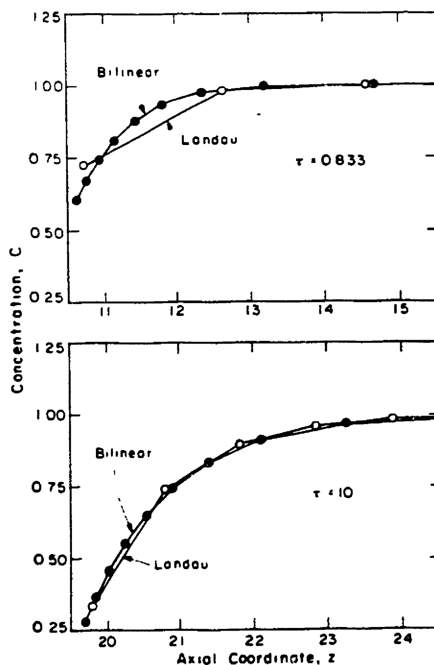

Fig. 6. Concentration profiles in the melt adjacent to the interface for $\tau = 0.833$ and $\tau = 10$. Calculations are for 20 total segments using both the Landau and the bilinear mapping. Only nodes falling within the concentration boundary layer are shown.

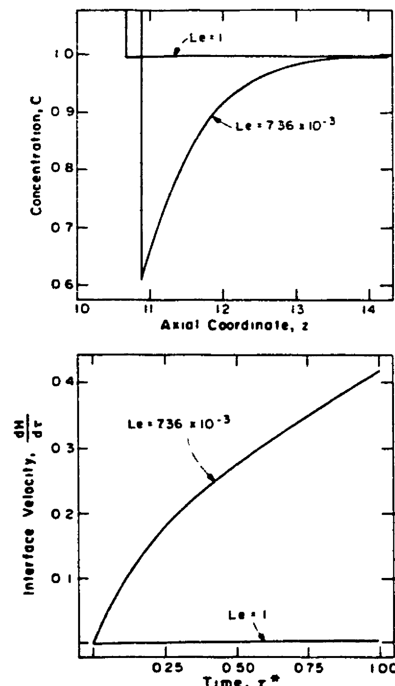

Fig. 7. (a) Concentration profiles in the melt adjacent to the interface at time $\tau^* = 1$. (b) Interface velocity as a function of time τ^* for Lewis numbers of 1 and 7.36×10^{-3}.

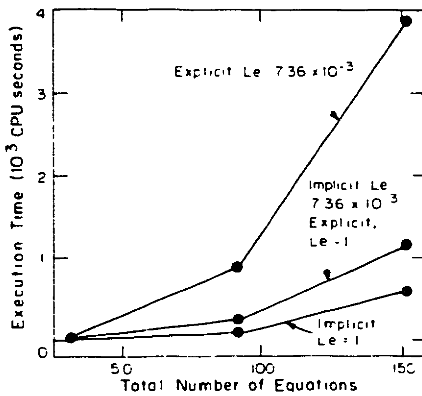

Fig 8. Computational times for integration to $\tau^* = 10$ using both the explicit and implicit techniques for Lewis numbers of 1 and 7.36×10^{-3}.

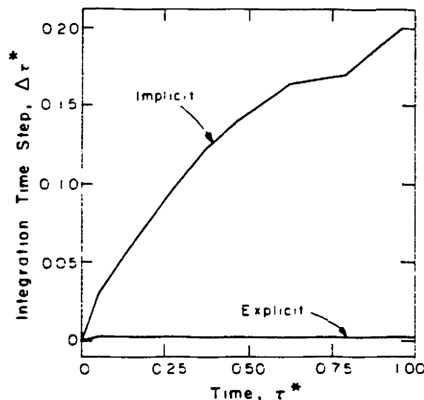

Fig 9. Step size as a function of time for implicit and explicit integration schemes Calculations are shown for $Le = 7.36 \times 10^{-3}$ and 32 equations

technique reached a plateau within $\tau^* \approx 0.1$, the step size for the implicit method increased throughout the run.

The savings in execution time realized by using implicit integration are even more dramatic for longer integration times. Execution times for the calculations involving the 32-equation set are listed in Table 3 for both Lewis numbers and two integration times. The differences between the two methods were largest for the longer integration time because the implicit formulation is able to use very large time steps as the system approaches steady state while the explicit scheme is still limited by the numerical stability of the equation set

5. DISCUSSION

Combining the bilinear mapping for the accommodation of the steep diffusion layer adjacent to the interface with the fully-implicit time integration scheme is an efficient and accurate strategy for solving the coupled heat and mass transfer problems arising in modelling solidification systems. The bilinear mapping results in finite difference approximations similar in spirit to those derived from the mesh grading used in finite element algorithms (Rubinsky, 1983; Ungar and Brown, 1984) and is essential for accurate prediction of transients. This scheme carries over to two- and three-dimensional interfaces that are not so deformed from a plane that the concept of a diffusion layer in the melt ahead of the growing interface is lost, as is the case in very deformed cellular and dendritic surfaces (Woodruff, 1973). For deep cells, the concentration gradients in the deep grooves of the interface are controlled by diffusion in both directions and finite difference or finite element approximations must be constructed appropriately (Ungar and Brown, 1985a, b).

The increase in efficiency obtained using the implicit integration method is dramatic and is crucial for simulation of systems with the small Lewis numbers realistic for metal and semiconductor alloys. The quasi-implicit splitting technique used by Rubinsky accounted for the two time scales in the solution of the actual field equations, but only updated the location of the interface explicitly. We feel that implicit handling of the interface position is crucial for efficient calculations, especially when the melting temperature and segregation coefficient, $F(C)$ and $k(C)$, strongly couple the temperature and concentration fields at the interface. This is certainly the case for HgCdTe, where the separation between the liquidus and solidus curves can exceed 80 K.

The implicit integration methods will undoubtedly be necessary when melt flow driven by thermosolutal convection is present to introduce another time scale for solute and heat transport, the bulk convection rate. As has been described for small-scale solidification

Table 3. Execution time calculations with discretizations resulting in 32 equations

Conditions		Integration time (CPU seconds) Explicit	Implicit	Ratio of times explicit/implicit
$\tau = 0.833$	$Le = 1$	9.8	5.3	1.8
($\tau^* = 1$)	$Le = 7.36 \times 10^{-3}$	40.4	15.6	2.6
$\tau = 10$	$Le = 1$	104.3	16.0	6.5
	$Le = 7.36 \times 10^{-3}$	473.3	40.6	11.7

systems (Chang and Brown, 1983; Brown *et al.*, 1984), the small Lewis number typical for semiconductors causes heat transfer to remain conduction-dominated, whereas solute transport is primarily by convection, except in boundary layers near solid surfaces.

Acknowledgements—We are grateful to the Microgravity Sciences and Space Applications Program of the National Aeronautics and Space Administration for support of this research and to A. N Beris for valuable discussions on the development of the bilinear mapping

NOTATION

- a constant in interfacial temperature function
- A constant in bilinear mapping
- b constant in distribution coefficient function
- B constant in furnace temperature and heat-transfer coefficient profiles
- Bi Biot number
- c concentration of CdTe, mol %
- C dimensionless concentration
- Cp heat capacity, J/kg K
- D solutal diffusivity of CdTe in melt, m^2/s
- E constant in bilinear mapping
- $\hat{\mathbf{f}}$ vector function for finite difference equations
- $\mathbf{f}$ vector function, $\mathbf{M}^{-1}\hat{\mathbf{f}}$
- F dimensionless equilibrium temperature at the interface
- G constant in bilinear mapping
- $\tilde{H}$ interface position, m
- H dimensionless interface position
- $\mathbf{I}$ identity matrix
- J constant in bilinear mapping
- $\mathbf{J}$ matrix used in iterative solution
- k dimensionless equilibrium distribution coefficient
- $\tilde{k}$ thermal conductivity, W/mK
- K dimensionless thermal conductivity ratio
- $\tilde{L}$ length of ampoule, m
- L dimensionless ampoule length
- Le Lewis number
- $\mathbf{M}$ mass matrix
- Pe Peclet number
- R radius of ampoule, m
- s parameter in bilinear mapping
- S Stefan number
- t time, s
- T temperature, K
- $\tilde{U}$ overall heat-transfer coefficient, $W/m^2 K$
- U dimensionless overall heat-transfer coefficient
- V ampoule translation rate, m/s
- $\tilde{x}$ coordinate in furnace reference frame, m
- x dimensionless coordinate in furnace reference frame
- X entry in mass matrix
- $\mathbf{y}$ vector of finite difference unknowns
- y component of $\mathbf{y}$ in transformed coordinate system (ξ, τ)
- $\hat{y}$ component of $\mathbf{y}$ in original coordinate system (z, τ)
- $\tilde{z}$ axial coordinate measured from bottom of ampoule, m
- z dimensionless axial coordinate

Greek letters

- α thermal diffusivity, m^2/s
- $\boldsymbol{\delta}$ correction vector used in iterative solution method
- ΔH_f heat of fusion, J/kg
- $\Delta\tau$ time step in integration method
- $\Delta\tau^*$ time step size in units of τ^*
- $\Delta\mathbf{y}$ local truncation error estimate of $\mathbf{y}$
- ε error parameter used in step size calculations
- θ dimensionless temperature
- ξ axial coordinate in mapped frame
- τ dimensionless time scaled with velocity
- τ^* dimensionless time scaled with solutal diffusion

Subscripts

- a ambient
- c furnace cold zone
- f at melting point
- h furnace hot zone
- i numerical index
- j index denoting phase (s, l) or solutal (m) quantity
- l liquid phase
- m pertaining to mass transfer
- n index denoting time step
- s solid phase
- x atom fraction
- 0 reference value

Superscripts

- (k) iteration number
- p predictor

REFERENCES

Bourret, E. D., Derby, J. J. and Brown, R A., 1986, Dynamics of Bridgman-Stockbarger growth of non-dilute binary alloys *J. Crystal Growth* (in press).

Brown, R A., Chang, C. J. and Adornato, P. M., 1984, Finite element analysis of directional solidification of dilute and concentrated binary alloys. In *Modeling of Casting and Welding Processes* (Edited by Dantzig, J. A. and Berry, J. T.), pp. 95–115. AIME, Philadelphia.

Chang, C. J. and Brown, R. A., 1983, Radial segregation induced by natural convection and melt solid interface shape in vertical Bridgman growth *J. Crystal Growth* **63**, 343–364

Crowley, A B and Ockendon, J. R., 1979, On the numerical solution of an alloy solidification problem. *Int J Heat Mass Transfer* **22**, 941–947.

Ettouney, H M. and Brown, R. A., 1983, Finite-element methods for steady solidification problems. *J. comp. Phys* **49**, 118–150.

Finlayson, B. A., 1980, *Nonlinear Analysis in Chemical Engineering* McGraw-Hill, New York

Fix, G. J., 1978, Numerical methods for alloy solidification problems. In *Moving Boundary Problems* (Edited by Wilson, D. G., Solomon, A. D. and Boggs, P. T.), pp 109–128. Academic Press, New York

Gresho, P. M., Lee, R. L and Sani, R. L., 1980, On the time-dependent solution of the incompressible Navier-Stokes equations in two and three dimensions. In *Recent Advances*

in *Numerical Methods in Fluids* (Edited by Taylor and Morgan). Pineridge Press, London

Landau, H. G., 1950, Heat conduction in a melting solid *Quart appl Math* **8**, 81–94

Rubinsky, B., 1983, Solidification processes in saline solutions *J Crystal Growth* **62**, 513–523.

Ungar, L H. and Brown, R A., 1984, Cellular interface morphologies in directional solidification—I. The one-sided model. *Phys Rev. B* **29**, 1367–1380

Ungar, L H and Brown, R A., 1985a, Cellular interface morphologies in directional solidification—IV The formation of deep cells. *Phys Rev B* **31**, 5931–5940

Ungar, L. H and Brown, R. A., 1985b, Finite-element methods for unsteady solidification problems arising in the prediction of morphological structure *J comp Phys.* (submitted)

Wang, C. A., Witt, A. F. and Carruthers, J A., 1985, *J. Crystal Growth* (submitted).

Woodruff, D. P., 1973, *The Solid–Liquid Interface.* Cambridge University Press, London

Yoo, J. and Rubinsky, B., 1983, Numerical computation using finite elements for the moving interface in heat transfer problems with phase transformation *Numer Heat Transfer* **6**, 209–222.